Opvolgen van het vervormingsgedrag van
vezelversterkte composieten in meerdere richtingen
met behulp van ingebedde, sterk dubbelbrekende, Bragg-sensoren

Multi-Axial Strain Monitoring of
Fibre Reinforced Thermosetting Plastics
Using Embedded Highly Birefringent Optical Fibre Bragg Sensors

Geert Luyckx

Promotoren: prof. dr. ir. J. Degrieck, prof. dr. ir. W. De Waele
Proefschrift ingediend tot het behalen van de graad van
Doctor in de Ingenieurswetenschappen

Vakgroep Toegepaste Materiaalwetenschappen
Voorzitter: prof. dr. ir. J. Degrieck
Faculteit Ingenieurswetenschappen
Academiejaar 2009 - 2010

UNIVERSITEIT
GENT

ISBN 978-90-8578-322-0
NUR 971, 968
Wettelijk depot: D/2009/10.500/80

ACKNOWLEDGEMENTS

De verhalen en stoten die je tegenkomt op weg naar een doctoraatstitel zouden kunnen opgetekend worden in een apart boek. Uiteraard met heel veel foto's die te pas en te onpas werden gemaakt tijdens dit doctoraat. Op deze foto's staan heel wat mensen die je gedurende de looptijd van je doctoraat ontmoet hebt en waarvan je iets hebt opgestoken (al laten die foto's dikwijls iets anders uitschijnen). Een beknopt verslag van de feiten zul je hier niet terugvinden maar wel een overzicht van de mensen waarbij ik (zoals ze zelf wellicht weten) in het krijt sta. Hoe kan ik jullie ooit bedanken? Wel ik doe een poging:

In de eerste plaats dank ik mijn promotoren (Joris en Wim DW) die me de kans hebben gegeven om mijn eigen onderzoek te laten voeren en die me waar nodig hebben bijgestuurd. Ook dank ik hen voor het aanvragen van het MASSFOS-project, waar dit werk op steunt. Voor de technische ondersteuningen tijdens dit werk) dank ik ook FOS&S, XenIC's en ESA (met in het bijzonder Iain McKenzie en Andreas Obst voor de gepaste en terecht kritische ondersteuning).

Op familie kun je altijd rekenen: Sofie, beter bekend als moksje, bedankt voor het samenzijn tot nog toe en voor het opvangen van onze twee keppedozen van kinderen, Seppe en Zita. "Papa moet nu werken" was de laatste maanden een veelgedraaide plaat tijdens het weekend, die we nu wel eventjes in de kast laten. Die paar maanden zijn zo weer ingehaald! Mijn ouders bedank ik voor het vertrouwen in mij en voor de financiële steun tijdens mijn studies. Samen met mijn schoonouders bedank ik hen tevens voor het opvangen van de kinderen wanneer nodig (in het verleden maar ook in de toekomst)!

Vrienden en/of collega's zijn ook gegeerde onderwerpen in een dankwoordje en dat is bij mij niet anders: dank aan 'bob de bouwers' Wim VP en Patricia voor de vele bouwkundige gesprekken. Wim, ooit komt de dag dat ik in onze 'groene energie discussies' harde bewijzen vind die je zullen overhalen tot het andere kamp (leve de zonnepanelen). 'Dakenloper' Eli, bedankt voor 't gezever onderweg en vooral voor de ondersteuning in het labo (fibre optics rules!). Rudy 'brainwasher' verhelses bedankt voor de druppels muziek en voor de rest kan je er natuurlijk dik in! Bedankt 'soulsaver' Ebrahim. Diepgaande gesprekken zijn je specialiteit wat uitermate werd geapprecieerd. Ik kijk er echt naar uit om verder samen te werken ;-). 'Schunnige moppentapper' Luc, je beseft het niet (of wel) maar jij bent één van de grote krachten van dit team. Jij maakt het mogelijk om gisteren iets gedaan te krijgen wat ik vandaag nog moet vragen (e magico!). 'Recto verso' Martine (en ik kan waarschijnlijk nog duizenden bijnamen verzinnen), oe is da toch mogelijk! Bedankt voor sfeer en koffie, voor spaghetti en BBQ, voor SAP en "mechanica van materialen en constructieee". Bedankt ook aan Gohua Han, my best and only chinese friend, the asian connection (Reddy, Siva, Shreda and Ali), Tai chi Ives, wees zen met jezelf (hierbij één woord: informatie en …!), Nuchtere Stijn voor je

cynische kijk op deze werkelijkheid, de mannen van het labo Soete Johan, Chris en Hans en natuurlijk de andere collega's die ik nog niet persoonlijk ken (Stefan, Diederik, Jesus,…). Al zijn we daar aan het werken.
Ex-collega's laten altijd hun sporen na op georganiseerde uitjes en andere events: Glen, Jochen, Filip, Nico, Joost, Antoine, Julien, en Chris. Aaaach, dat waren nog eens collega's…

PUBLICATION LIST

Publications in international journal of the Science Citation Index (a1)

[1] Luyckx, G., De Waele, W., Degrieck, J., Van Paepegem, W., Vlekken, J., Van Damme, S., Chah, K.. Deformation Monitoring of Composite Structures: Three dimensional strain and temperature monitoring of composite laminates. INSIGHT, 2007, 49(1): p. 10-16.

[2] Geernaert, T., Luyckx, G., Voet, E., Nasilowski, T., Chah, K., Becker, M., Bartelt, H., Urbanczyk, W., Wojcik, J., De Waele, W., Degrieck, J., Terryn, H., Berghmans, F., and Thienpont, H.. Transversal Load Sensing With Fiber Bragg Gratings in Microstructured Optical Fibers. Ieee Photonics Technology Letters, 2009. 21(1-4): p. 6-8.

[3] De Baere, I., Luyckx, G., Voet, E., Van Paepegem, W. and Degrieck, J.. On the feasibility of optical fibre sensors for strain monitoring in thermoplastic composites under fatigue loading conditions. Optics and Lasers in Engineering, 2009, 47: p403–411

[4] Luyckx, G., Voet, E., Geernaert, T., Nasilowski, T., Chah, K., Becker, M., Bartelt, H., Urbanczyk, W., Wojcik, J., De Waele, W., Degrieck, J., Terryn, H., Berghmans, F., and Thienpont, H.. Response of FBGs in Microstructured and Bow Tie Fibers Embedded in Laminated Composite. Ieee Photonics Technology Letters, 2009. 21(18): p. 1290-1292.

Publications in ISI proceedings (p1)

[1] Luyckx, G., De Waele, W., Van Paepegem, W., Degrieck, J., Soete, L., Vlekken, J., Chah, K.. Measurement of multi-axial stress/strain in composite elements with Bragg sensors. in Proceedings of the 3rd European Workshop on Structural Health Monitoring. 2006. Granada, SPAIN.

[2] De Baere, I., Luyckx, G., Van Paepegem, W., Degrieck, J., Voet, E., Vlekken, J.. The use of optical fibers for fatigue testing of fiber-reinforced thermoplastics. in Proceedings of the 4th International Conference on Emerging Technologies in Non-Destructive Testing. 2007. Stuttgart, GERMANY.

[3] Luyckx, G., De Waele, W., Degrieck, J., Van Paepegem, W., Vlekken, J., Verbeke, T.. Feasibility study of an embedded Multi-Axial fibre bragg grating sensor. in Proceedings of the Conference on Optical Sensing Technology and Applications. 2007. Prague, CZECH REPUBLIC.

[4] Luyckx, G., Degrieck, J., De Baere, I., De Waele, W., Van Paepegem, W., Verbeke, T.. Monitoring of a curved beam test structure using Bragg sensors. in

Proceedings of the 4th International Conference on Emerging Technologies in Non-Destructive Testing. 2007. Stuttgart, GERMANY.

[5] Luyckx, G., Degrieck, J., De Waele, W., Van Paepegem, W., Vlekken, J., Verbeke, T.. Non-destructive evaluation of composite structures using an innovative Bragg sensor. in Proceedings of the 4th International Conference on Emerging Technologies in Non-Destructive Testing. 2007. Stuttgart, GERMANY.

[6] Luyckx, G., Voet, E., De Waele, W., Van Paepegem, W., Degrieck, J., Vlekken, J.. Strain monitoring of FRP elements using an embedded fibre optic sensor. in Proceedings of the 3rd International Conference on Smart Materials, Structures and Systems. 2008. Acireale, ITALY.

[7] Voet, E., Luyckx, G., De Baere, I., Degrieck, J., Vlekken, J., Jacobs, E., Bartelt, H.. High Strain monitoring during Fatigue Loading of Thermoplastic Composites using imbedded Draw Tower Fibre Bragg Grating Sensors. in Proceedings of the 3rd International Conference on Smart Materials, Structures and Systems. 2008. Acireale, ITALY.

Chapters in books (b2)

[1] Van Paepegem, W., De Baere, I., Lamkanfi, E., Luyckx, G. and Degrieck, J. (2008). Numerical modelling of fatigue in textile polymer composites. Accepted chapter for Pavlou D.G. (ed.) Computational & experimental analysis of damaged materials. Research Signpost, India (http://www.ressign.com). Invited contribution

[2] Van Paepegem, W., De Baere, I., Lamkanfi, E., Luyckx, G. and Degrieck, J. (2008). Research directions in the fatigue testing of polymer composites. Accepted chapter for Durand L.G. (ed.) Composite Materials Research Progress. Nova Science Publishers, Inc., new York, United States of America (http://www.novapublishers.com). Invited contribution.

Publications in conference proceedings (c1)

[1] Luyckx, G., Degrieck, J., De Waele, W., Van Paepegem, W., Measuring multi-axial stress and strain in composite elements with Bragg sensors. In Proceedings of the 5th PHD-symposium Ghent university. 2004. Ghent, BELGIUM.

[2] Luyckx, G., De Waele, W., Degrieck, J., Van Paepegem, W., Health Monitoring of composites by means of an innovating Fibre Bragg Grating Sensor. 2005. In Proceedings of the 6th PHD-symposium Ghent university. Ghent, BELGIUM.

[3] Luyckx, G., De Waele, W., Degrieck, J., Multi-axial stress and strain sensing with Bragg-sensors: a theoretical study. In Proceedings of ACOMEN. 2005. Ghent, BELGIUM.

[4] Luyckx, G., De Waele, W., Degrieck J., Vlekken, J., Chah, K.. Theoretical study of feasibility for discriminating axial and transverse stress/strain components with Bragg sensors. Lecture at the second OPTIMESS workshop. 2005. Ghent, BELGIUM.

[5] Luyckx, G., Degrieck, J., De Waele, W., Van Paepegem, W., Van Roosbroeck, J., Chah, K., Vlekken, J., McKenzie, I., Obst, A.. Feasibility study on measuring axial and transverse stress/strain components in composite materials using Bragg sensors. In proceedings of ICSO. 2006. Estec Noordwijk, THE NETHERLANDS.

[6] Luyckx, G., De Waele, W., Degrieck, J., Van Paepegem, W., Vlekken, J., Chah, K.. Multi-axial Fiber Bragg sensors for monitoring purposes . In Proceedings of ECCM12. 2006. Biarritz, FRANCE.

[7] Luyckx, G., De Waele, W., Degrieck, J., Van Paepegem, W., Vlekken, J., Chah, K.. Fiber optic sensing system for discriminating multi-axial strain components in composite elements. In Proceedings of OFS18. 2006. Cancun, MEXICO.

[8] Luyckx, G., De Waele, W., Van Paepegem, W., Degrieck, J., Vlekken, J., Van Damme, S., Measurement of multi-axial stress/strain in composite elements with Bragg sensors. Lecture at the autumn SAMPE Benelux meeting (Sabena Technics). 2006. Zaventem, BELGIUM.

[9] Degrieck, J., Van Paepegem, W., Cnudde, V., De Baere, I., De Baets, P., Declercq, N., Luyckx, G., Masschaele, B., Moentjens, A., Quintelier, J., Sol, H., Van Hemelrijck, D., Vlekken, J.. Monitoring of Fatigue, Impact and Wear in Cetex TPC. From Scratch to Flight proceedings of the first Cetex conference. 14 june 2006. TUDelft, THE NETHERLANDS

[10] Luyckx, G., De Baere, I., De Waele, W., Degrieck, J., Van Paepegem, W., Vlekken, J., Verbeke, T.. Analysis of a curved composite test specimen with Fiber Bragg Gratings. In Proceedings of the OPTIMESS 2007 Workshop. 2007. Leuven, BELGIUM.

[11] De Baere, I., Voet, E., Luyckx,G., Van Paepegem, W., Vlekken, J., Cnudde, V., Masschaele, B., Degrieck, J., 'On the feasibility of optical fibre sensors for strain monitoring in thermoplastic composites under fatigue loading conditions', In Proceedings of the OPTIMESS2007 Workshop. 2007. Leuven, BELGIUM.

[13] Voet, E., Luyckx, G., De Baere, I., Degrieck, J., Bartelt, H., Vlekken, J., Jacobs, E., High strain measurements during fatigue cycling in fibre reinforced

thermoplastic composites using imbedded draw tower fibre Bragg grating sensors. In Proceedings of the 13th European Conference on Composite Materials (ECCM-13). 2008. Stockholm, SWEDEN.

[14] Geernaert, T., Luyckx, G., Voet, E., Nasilowski, T. A., Chah, K., Becker, M., Bartelt, H., Urbanczyk, W., Wójcik, J., De Waele, W., Degrieck J., Berghmans, F., Thienpont, H., "Fiber Bragg gratings in microstructured optical fibers for stress Monitoring", In proceedings of the SPIE conference on optics and opto-electronics. 2009. Praag, CZECH REPUBLIC.

[15] Geernaert, T., Luyckx, G., Voet, E., Nasilowski, T. A., Chah, K., Becker, M., Bartelt, H., Urbanczyk, W., Wójcik, J., De Waele, W., Degrieck, J., Berghmans, F., Thienpont, H., "Fiber Bragg gratings in microstructured optical fibers for stress Monitoring", In Proceeding of Sensor + Test. 2009. Nurnburg, GERMANY.

[16] Luyckx, G., Voet, E., Geernaert, T., Nasilowski, T., Chah, K., Becker, M., Bartelt, H., Urbanczyk, W., Wojcik, J., De Waele, W., Degrieck, J., Terryn, H., Berghmans, F., and Thienpont, H., Benchmarking the response of Bragg gratings written in micro-structured and bow-tie fiber embedded in composites. In the Proceedings of OFS20. 2009. Edinburgh, UK.

[17] Voet, E., Luyckx, G., Degrieck, J.. Response of embedded fibre Bragg gratings: strain transfer effects. In the Proceedings of OFS20. 2009. Edinburgh, UK.

Aan mijn liefste Vrouw

Sofie

en

Onze twee schatten van kinderen

Zita en Seppe

TABLE OF CONTENTS

NEDERLANDSTALIGE SAMENVATTING

Inleiding

Er is groeiende interesse in het gebruik van hoogwaardige vezelversterkte kunststoffen (VVK'en) voor verschillende toepassingen, waarbij het gewicht beperkt moet blijven en de sterkte toch voldoende hoog moet zijn. Men moet er zich terdege van bewust zijn dat dergelijke materialen een ander mechanisch gedrag hebben dan de conventionele isotrope constructiematerialen. Schade (zoals matrixscheuren, vezelbreuk en delaminatie) kan al ontstaan na een paar honderd belastingscycli. En door het anisotropisch gedrag van VVK'en kan een mechanische belasting, die slechts een laag rekniveau veroorzaakt in de vezelrichting, rekken veroorzaken loodrecht op de vezel die groot genoeg zijn om schade te berokkenen. Hoewel de initiatie van schade niet levensbedreigend is voor vezelversterkte materialen, is het nuttig deze regelmatig te inspecteren om de evolutie van de schade op te volgen. Standaard inspectiemethodes (zoals visueel onderzoek, ultrasoon onderzoek en radiografie) laten niet toe om de constructie op te volgen tussen twee inspectie-intervallen. Het continu opvolgen van constructies zou een groot inzicht moeten verschaffen in hun structureel gedrag op lange termijn. De terugkoppeling van de gemeten krachten, rekken en temperatuur van onderdelen van de constructie zou moeten leiden tot belangrijke informatie op het vlak van het ontwerp. Optische vezelsensoren zijn uitermate geschikt voor deze taken en hebben een aantal (welgekende) voordelen ten opzichte van conventionele sensoren (zoals rekstrookjes). Een aantal daarvan zijn hun ongevoeligheid voor elektromagnetische straling, hun kleine afmetingen en gewicht, de mogelijkheid tot het plaatsen van meerdere sensoren in 1 lijn en hun weerstand tegen corrosie. Het vaakst worden deze optische vezelsensoren verlijmd op het oppervlak van de op te volgen constructie en meten ze enkel en alleen de rek volgens de langsrichting van de vezel. In dit boek worden dubbelbrekende vezels met Bragg-sensoren gebruikt om het rekveld in met koolstofvezel versterkte thermohardende kunststoffen in meerdere richtingen op te volgen.

Geavanceerde rekmetingen

Een Bragg rooster is een verandering van de brekingsindex van de kern van de optische vezel volgens een bepaalde periode. Wanneer breedbandig licht in de vezel met Bragg-sensor wordt gekoppeld, wordt slechts een deel van dat licht teruggekaatst. Het weerkaatste spectrum is gecentreerd rond de Bragg golflengte. Figuur 1 toont verschillende types optische vezel waarin een Bragg-sensor kan worden geschreven, met hun respectievelijke Bragg spectrum.

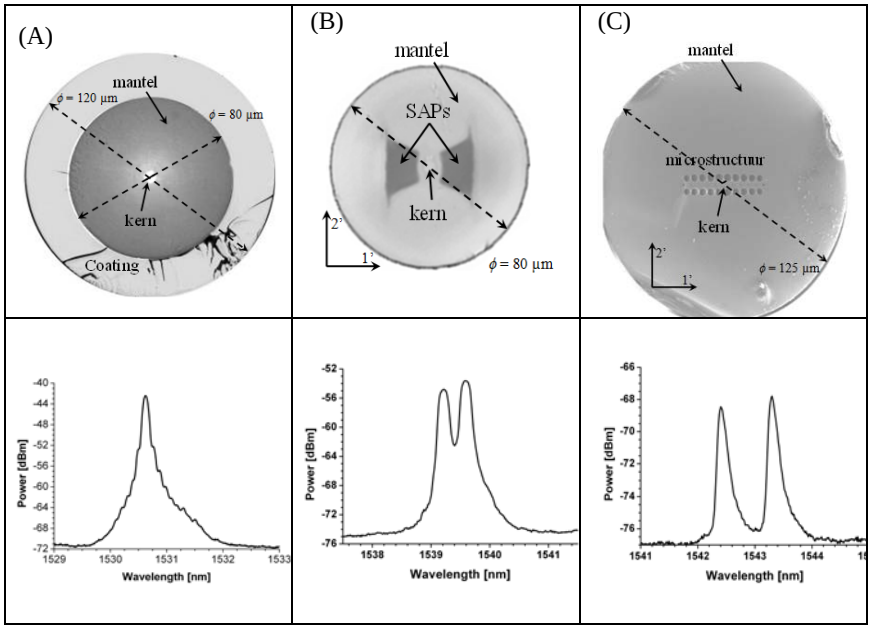

Figuur 1: Een typische doorsnede van verschillende optische vezeltechnologieën waarin een Bragg-sensor kan geschreven worden (A: niet dubbelbrekende vezel, B: sterk dubbelbrekende bow-tie vezel en (C) sterk dubbelbrekende microstructuurvezel) met hun Bragg spectrum (onderaan).

Het foto-elastisch effect relateert de rek in een vezel aan de verandering van zijn brekingsindex. Dit effect kan gebruikt worden om de wijziging in de Bragg golflengtes ten gevolge van een willekeurig rekveld te bepalen:

$$\frac{\Delta\lambda_{B,1'}}{\lambda_{B,0}} = \varepsilon_{3'} - \frac{1}{2} n_{eff,1'}^2 \left[p_{11}\varepsilon_{1'} + p_{12}\left(\varepsilon_{2'} + \varepsilon_{3'}\right)\right]$$
$$\frac{\Delta\lambda_{B,2'}}{\lambda_{B,0}} = \varepsilon_{3'} - \frac{1}{2} n_{eff,2'}^2 \left[p_{11}\varepsilon_{2'} + p_{12}\left(\varepsilon_{1'} + \varepsilon_{3'}\right)\right] \quad \textbf{1}$$

Hierin zijn $\varepsilon_{1'}$, $\varepsilon_{2'}$, en $\varepsilon_{3'}$ de hoofdrekken van de vezel volgens het assenstelsel gedefinieerd in Figuur 1, de 3' richting bevindt zich loodrecht op het blad. Ten gevolge van een verschil in brekingsindex zal de golflengteverschuiving anders zijn voor het licht dat zich voortplant langsheen de twee hoofdassen (*1'* and *2'*). Deze golflengteverschuivingen worden volledig bepaald door de foto-elastische coëfficiënten (p_{11} en p_{12}). Om deze coëfficiënten te bepalen, kan men een experimentele kalibratie uitvoeren waarbij de optische vezel in transversale richting wordt belast. Deze procedure zorgt voor een eenvoudige rektoestand (twee transversale rekcomponenten) in de kern van de vezel (Figuur 2). De auteur van dit

werk stelt voor om een uni-axiale Bragg-sensor waarvan de kern exact dezelfde eigenschappen heeft als van het dubbelbrekend exemplaar transversaal te kalibreren. Bij de start van de proef zal slechts 1 Bragg piek zichtbaar zijn (het zwarte spectrum in Figuur 3). Een zekere minimale kracht is nodig om genoeg differentiële transversale rek te induceren zodat het Bragg spectrum splitst in twee afzonderlijke pieken (van het rode naar het groene naar finaal het blauwe spectrum in Figuur 3). Vanaf dat moment zijn beide pieken duidelijk zichtbaar en kan een transversale kalibratie uitgevoerd worden.

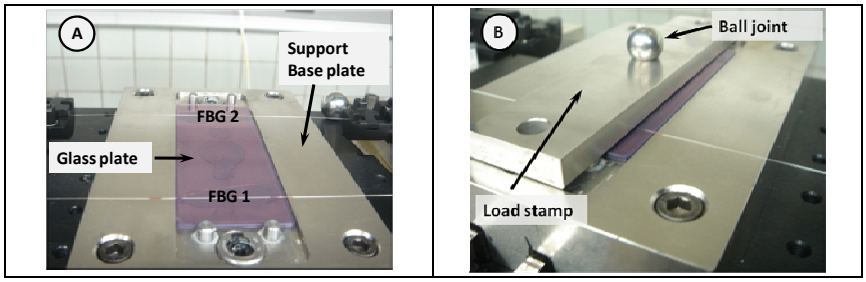

Figuur 2: Transversale rekkalibratie met een stempel die twee optische vezels gelijktijdig belast.

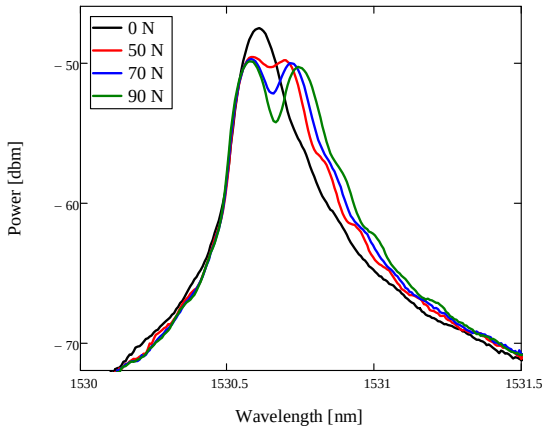

Figuur 3: Spectrum van een diametraal belaste, niet dubbelbrekende vezel met Bragg-sensor.

Voor de rekoptische coëfficiënten zijn waarden gevonden die vergelijkbaar zijn met literatuurgegevens: p_{11} = 0.111 ± 0.008 en p_{12} = 0.247±0.017.

Multi-axiale reksensor

Meerassige rekmetingen van een constructie uit VVK onder belasting, zou het inzicht en het vertrouwen in het langdurig gebruik van dergelijke materialen sterk moeten verbeteren. Sterk dubbelbrekende Bragg-sensoren kunnen hierin een belangrijke rol vervullen. Het ontwerpen van een dergelijke sensor moet echter voldoen aan een aantal voorwaarden die als volgt kunnen worden opgesomd: een hoge gevoeligheid, een voldoend onderscheidend vermogen voor alle rekcomponenten, een minimale verstoring van het materiaal, en de sensor moet het productieproces van VVK'en en de ruwe en moeilijke omgevingscondities waarin ze gebruikt worden, overleven.

De beschreven multi-axiale sensorconfiguraties zijn stuk voor stuk gebaseerd op sterk dubbelbrekende vezels die commercieel beschikbaar zijn. De dubbelbreking van Bragg-sensoren in dergelijke vezels zal niet beïnvloed worden door een pure axiale rek of temperatuursverandering. Het volledige spectrum verschuift homogeen naar hogere of lagere golflengtes. Een verandering in transversale rek leidt wel tot een verandering van de dubbelbreking wat zich zal uiten in een wijziging van de afstand tussen de twee Bragg pieken (Figuur 4). Al naargelang de richting en de oriëntatie van de transversale rek, zal dit leiden tot een toename of afname van de tussenafstand.

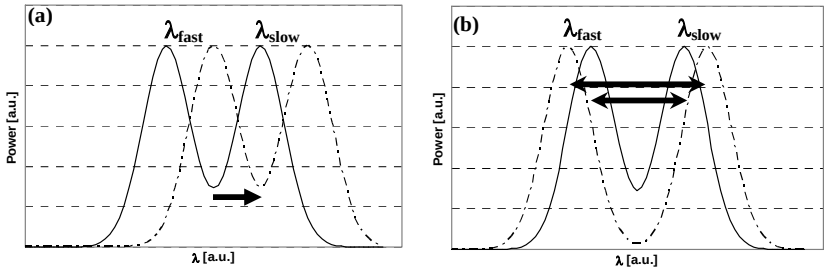

Figuur 4: Wijziging van het spectrum van de Bragg-sensor onder invloed van (a) axiale rek en/of temperatuur en (b) transversale rek.

Wanneer twee Bragg roosters gecombineerd worden in één en dezelfde sensor, dan beschikken we over vier golflengteverschuivingen. Als deze op een voldoend verschillende manier reageren op een externe sollicitatie van de constructie (zoals axiale en transversale rek), ontstaat een multi-axiale sensor.

Het verband tussen de golflengteverschuiving ($\Delta\lambda_B$) en de aanwezige rek ($\Delta\varepsilon$) in de kern van de vezel kan als volgt genoteerd worden:

$$\begin{bmatrix} \Delta\lambda_{B1,1'} \\ \Delta\lambda_{B1,2'} \\ \Delta\lambda_{B2,2'} \end{bmatrix} = K \begin{bmatrix} \Delta\varepsilon_{1'} \\ \Delta\varepsilon_{2'} \\ \Delta\varepsilon_{3'} \end{bmatrix} \quad \textbf{2}$$

Hierin is K gelijk aan:

$$K = \begin{bmatrix} K_{11} & K_{12} & K_{13} \\ K_{21} & K_{22} & K_{23} \\ K_{31} & K_{32} & K_{33} \end{bmatrix} \quad \textbf{3}$$

De coëfficiënten van de K-matrix zijn afhankelijk van de gebruikte sensor (vezeltype en configuratie). De rekcomponenten in de kern van de vezel kunnen berekend worden door de K-matrix te inverteren en te vermenigvuldigen met de golflengteverschuivingen.

Om de optimale sensor te definiëren, werden verschillende configuraties onderzocht waarbij twee Bragg-sensoren gecombineerd worden tot één enkele sensor. Door één van de Bragg-sensoren in het finaal concept te omgeven met een capillair hebben de transversale rekken een verschillende invloed op beide sensoren. De eerste is blootgesteld aan alle spanningscomponenten terwijl de tweede is afgeschermd van de transversale spanningen binnenin het composiet (Figuur 5). Bijgevolg zal de axiale rek resolutie gelijk zijn aan deze van een niet ingebedde uni-axiale Bragg-sensor. De resolutie van de transversale rek kan als zeer goed beschouwd worden in het finaal concept (Tabel 1)

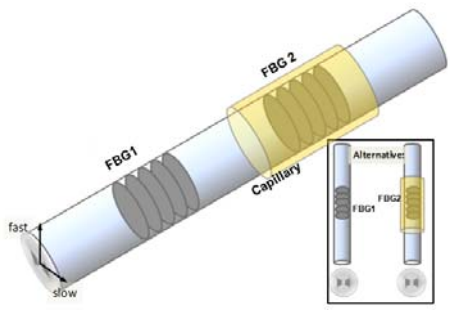

Tabel 1: Gevoeligheidsanalyse

	Fout-analyse	Standaard afwijking
$\delta\varepsilon_{1'}$ [με]	>6.9	±4.3
$\delta\varepsilon_{2'}$ [με]	>6.9	±4.3
$\delta\varepsilon_{3'}$ [με]	>0.9	±0.9

Figuur 5: Het concept waarbij het tweede Bragg rooster is omgeven door een glazen capillair.

Een aantal veronderstellingen werden gemaakt en gevalideerd om deze uitstekende resolutie te bekomen. De eerste is de volledige afscherming van de transversale spanningen voor de Bragg-sensor in het capillair. De tweede aanname is de complete overdracht van de longitudinale structurele rek naar de sensor in het capillair.

Ingebedde Bragg-sensoren

Het inbedden van een optische vezel in een VVK zou zo eenvoudig mogelijk moeten zijn. De volgende zijn hierbij van belang. Een robuuste inleiding van de vezel in het composiet moet voorzien worden. De plotse overgang van de behoorlijk buigbare vezel in het eerder stijve materiaal is zonder voorzorg een zeer breekbaar punt. In dit werk werden Kapton® folie en kleine Teflon buisjes gebruikt ter bescherming van de vezel (Figuur 6). De Teflon buisjes laten zelfs toe om de uitvloei van overtollig hars te verwijderen.

Figuur 6: Bescherming van de ingang van de optische vezel door middel van een Teflon buisje.

Omdat in dit werk gebruik wordt gemaakt van dubbelbrekende vezels, is het noodzakelijk om een correcte oriëntatie te garanderen tijdens het inbedden. Bijvoorbeeld zal een verkeerde oriëntatie (θ in Figuur 7) leiden tot een aanzienlijke fout op de transversale rekcomponenten.

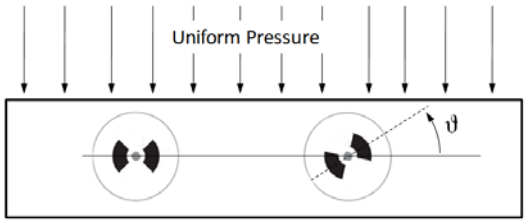

Figuur 7: Voorbeeld van twee ingebedde dubbelbrekende vezels met verschillende oriëntatie.

Niettegenstaande de afwezigheid van een harsrijke zone rond de ingebedde vezel kan deze toch een zekere invloed hebben op de mechanische eigenschappen en sterkte van de constructies waarin ze zijn ingebed. In de literatuur en eigen werk werd aangetoond dat dit niet het geval is wanneer de vezel parallel met de versterkingsvezels wordt ingebed.
De mechanische eigenschappen van de sensor (glasvezel) en de constructies (VVK) zijn erg verschillend, waardoor er een rekoverdrachtsmatrix (*TC*-matrix) moet

berekend worden die het verband tussen de rek in beide materialen beschrijft. Deze matrix is afhankelijk van de mechanische eigenschappen van de sensor en de constructie waarin ze is ingebed.
Deze interactie is complex en daardoor niet eenvoudig te beschrijven. In zijn meest algemene vorm kan de volgende matrix-vergelijking opgesteld worden:

$$\begin{bmatrix} \varepsilon_1^c \\ \varepsilon_2^c \\ \vdots \\ \varepsilon_6^c \end{bmatrix} = \begin{bmatrix} TC_{11} & TC_{12} & \cdots & TC_{16} \\ TC_{21} & TC_{22} & \cdots & TC_{26} \\ \vdots & \vdots & \ddots & \vdots \\ TC_{61} & TC_{62} & \cdots & TC_{66} \end{bmatrix} \begin{bmatrix} \varepsilon_1^s \\ \varepsilon_2^s \\ \vdots \\ \varepsilon_6^s \end{bmatrix} \quad \textbf{4}$$

Hierin zijn ε_i^c ($i = 1,\ldots,6$) de rekken van het composiet op de plaats van de sensor in de veronderstelling dat er geen sensor aanwezig is. Het rekveld in de kern van de optische vezel wordt beschreven door ε_i^s ($i = 1,\ldots,6$). In allebei de gevallen refereert het subscript $i = 1,\ldots,6$ naar de componenten van de rek in verkorte notatie.
De beste methode om een dergelijke *TC*-matrix op te stellen, is gebruik te maken van de eindige elementen methode. Omwille van symmetrieredenen wordt slechts één achtste van het laminaat gemodelleerd. De afmetingen van het model zijn 10 mm x 1.2 mm x 10 mm, waarbij het laminaat in totaal uit 24 prepreg lagen bestaat (Figuur 8).

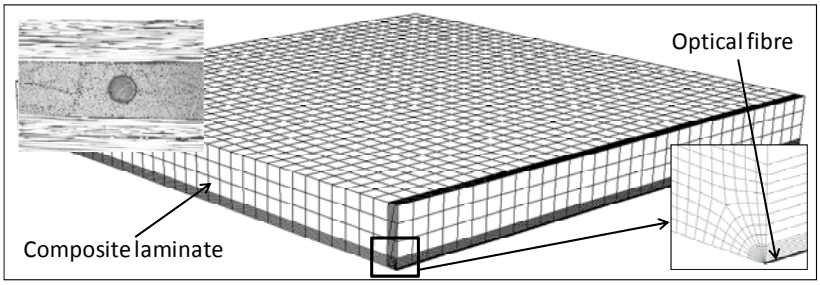

Figuur 8: Eindig elementen model dat gebruikt werd bij het berekenen van de rekoverdrachtsmatrix tussen het laminaat en de ingebedde vezel.

Door dit eindig elementen model op verschillende manieren te belasten kan men de *TC*-matrix bepalen. Als de mechanische eigenschappen van sensor en/of constructie aangepast worden, kan men de invloed van die eigenschappen op de *TC*-matrix begroten. Volgende eigenschappen werden bestudeerd: de mechanische eigenschappen van het composiet, de stapeling van het laminaat, de positie van de sensor in een enkelvoudige laag, en de grootte van de sensor en het type sensor.
De aldus bepaalde *TC*-matrix voor een uni-axiale Bragg-sensor ingebed in een uni-directioneel koolstof epoxy laminaat werd tevens experimenteel gevalideerd.

Hiervoor werd een proefopstelling gebruikt die een gekende transversale kracht oplegt aan het oppervlak van een composiet plaatje. Een aantal proefstukken (16 lagen dik) met ingebedde 80µm uni-axiale Bragg-rooster werden getest. De proefstukken ondergingen een maximale druk van 92 MPa (Figuur 9). Een gesimuleerd experiment ($\Delta\varepsilon_{xx}$, $\Delta\varepsilon_{yy}$, $\Delta\varepsilon_{zz}$) werd gebruikt om referentiewaarden van de rekken in de dwarse richting te bepalen. De meetresultaten van deze proef komen goed overeen met de referentierekken (Figuur 9) en bewijzen de juistheid van de berekende *TC*-matrix voor een ingebedde uni-axiale Bragg-sensor.

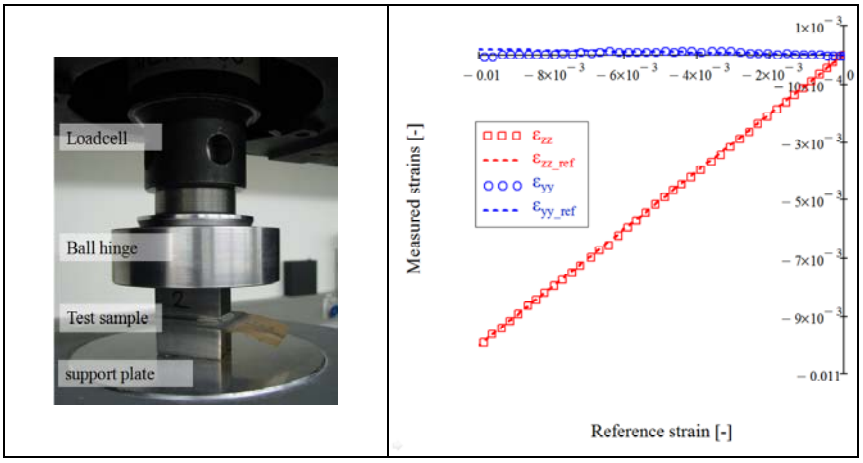

Figuur 9: De opstelling voor het uitvoeren van een transversale drukproef (links). De gemeten en gesimuleerde transversale rek componenten ($\Delta\varepsilon_{yy}$ and $\Delta\varepsilon_{zz}$) in het proefstuk in functie van hun respectieve referentiewaarden.

De resolutie van de ingebedde vezel is anders dan als deze niet is ingebed, en kan beschouwd worden als de mogelijkheid om de verschillende componenten van het rekveld van de structuur waarin ze is ingebed te onderscheiden. Door de theoretische *TC*-matrix en *K*-matrix te combineren, berekent men een resolutie die ~10 maal kleiner is dan deze van de niet ingebedde vezel.

Experimentele validatie van een ingebedde MAxS-sensor

Een groot aantal proefstukken met ingebedde MAxS-sensor werden getest door het opleggen van gekende krachten en dito rekvelden (longitudinale trek, transversale druk, vierpuntsbuiging, schuifrek en temperatuurscyclus). De met de MAxS-sensor gemeten rekwaarden worden gerelateerd met referentiemetingen op basis van extensometer, verplaatsing, kracht, extern verlijmde Bragg-rooster of eindige elementen simulaties. Eén van de proeven om de bruikbaarheid van de MAxS-sensor te bewijzen, wordt hieronder in detail uitgelegd. De werkwijze is geldig voor

alle proefstukken. De berekeningsprocedure wordt als volgt samengevat. In Figuur 10 wordt de golflengteverschuiving van een ingebedde MAxS-sensor in een $[0°]_{48}$ laminaat onder transversale drukbelasting getoond. De afstand tussen beide pieken vergroot het meest voor de eerste Bragg-sensor. De tweede Bragg-sensor, omgeven door een capillair, vertoont een kleine negatieve golflengteverschuiving.

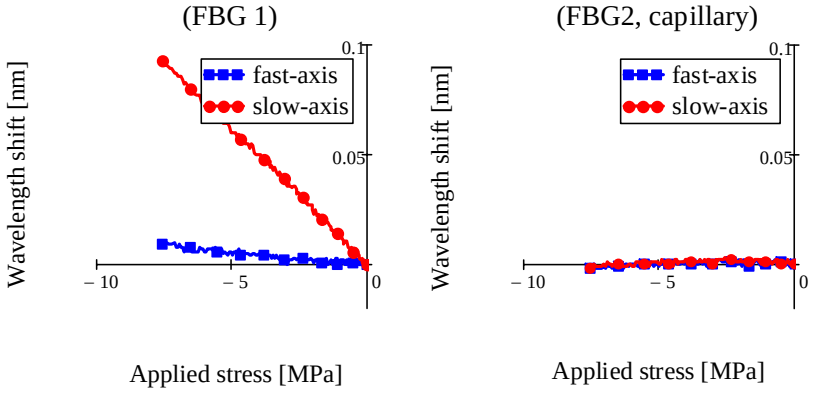

Figuur 10: De golflengteverschuivingen van de twee Bragg roosters van de MAxS-sensor.

Door gebruik te maken van de *K*-matrix en vergelijking 2, kan het rekveld in de kern van de optische vezel bepaald worden (Figuur 11).

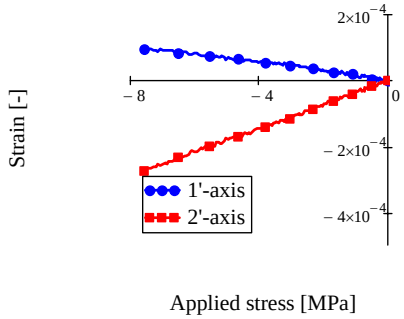

Figuur 11: Het gemeten rekveld in de kern van de ingebedde optische vezel (MAxS-sensor).

Het rekveld in het composiet wordt gevonden door het rekveld in de kern van de optische vezelsensor te vermenigvuldigen met de inverse van de *TC*-matrix (Figuur 12, links). De berekende rekken in het composiet zijn een stuk groter dan de referentiewaarden (tot zelfs een factor 2 verschil voor de rek door-de-dikte). Dit kan een gevolg zijn van een onderschatting van de bestaande rekoverdracht. Daarom

werd door middel van een uitgebreid proefprogramma de *TC*-matrix geoptimaliseerd. Met deze geoptimaliseerde *TC*-matrix zijn de gemeten rekcomponenten (volle lijn en symbool) in betere overeenstemming met hun respectievelijke referentiewaarden (gebroken lijn) (Figuur 12, rechts).

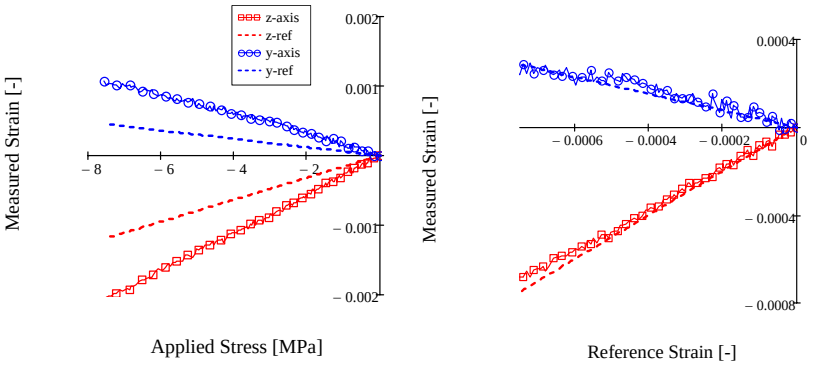

Figuur 12: De berekende rekwaarden in een composieten proefstuk door middel van een ingebedde vezel, met behulp van de theoretische (links) en experimenteel (rechts) bepaalde *TC*-matrix.

Mogelijke toepassingen voor een multi-axiale reksensor

De werking van de multi-axiale reksensor (MAxS-sensor) werd bewezen d.m.v. een uitgebreid testprogramma. In deze paragraaf worden een aantal voorbeelden gegeven van ‘reële’ toepassingen waarvoor een multi-axiale sensor een meerwaarde kan betekenen.

De eerste toepassing is het opvolgen van residuele rekken tijdens het productieproces van VVK elementen. Door het inbedden van de MAxS-sensor in een laminaat met een $[\pm 45_2, 0_2, 90_2]_s$ stapeling was het mogelijk om de effecten van axiale en transversale rek afzonderlijk in kaart te brengen gedurende het productieproces. De temperatuur, overdruk, vacuüm en de golflengteverschuivingen (MAxS-sensor) werden gemeten tijdens uitharden (Figuur 13).

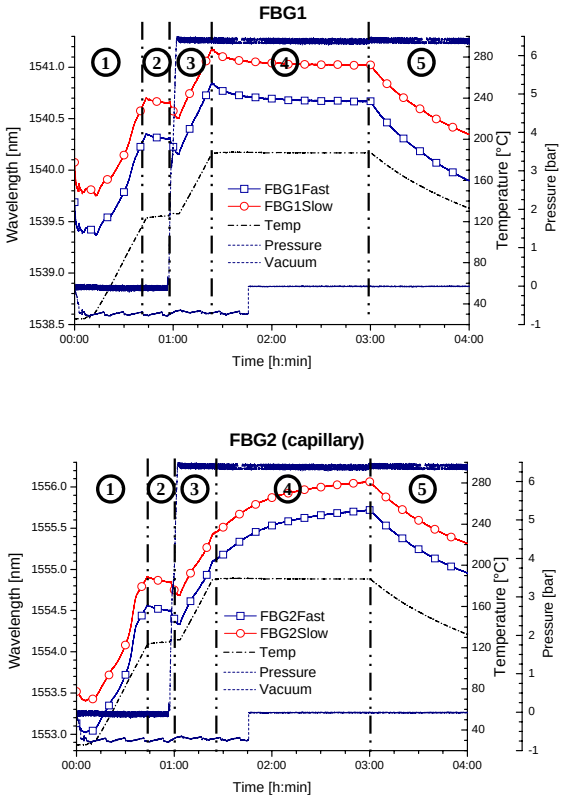

Figuur 13: Gemeten golflengteverschuiving, overdruk, vacuüm en temperatuur tijdens het productieproces van een $[\pm 45_2, 0_2, 90_2]_s$ laminaat.

Het productieproces kan in 5 stappen onderverdeeld worden (aangeduid op Figuur 13). In een eerste stap wordt de temperatuur verhoogd tot 120°C. Hierbij stijgen de golflengtes lineair met de temperatuur. In de tweede stap wordt de temperatuur constant gehouden op 120°C. Hierbij is er een lichte daling van de golflengtes zichtbaar door het zetten van de VVK onder invloed van het vacuüm. In de derde fase wordt er eerst 7 bar overdruk geplaatst op het proefstuk en bijna gelijktijdig stijgt de temperatuur naar 180°C. Opnieuw stijgen de golflengtes lineair met de temperatuur. In de vierde fase begint de eigenlijke uitharding. In deze fase is er een duidelijk zichtbaar verschil in de golflengteverschuivingen van beide Bragg-sensoren. In fase 5 wordt de verwarmingsplaat uitgeschakeld en koelt de autoclaaf op natuurlijke wijze af. Transversale residuele rekken manifesteren zich in het materiaal met een grotere afstand tussen de twee pieken van het spectrum van Bragg-rooster 1 tot gevolg.

Een tweede toepassing is het opvolgen van een schaalmodel van een verbindingsstuk in T-vorm (bvb. ter versteviging van vleugels of romp van een vliegtuig) (Figuur 14). Het model werd onderworpen aan een vierpuntsbuiging die aantoont (via eindige elementen simulaties) dat er een constant rekveld ontstaat op het plateau van de T-verbinding (Figuur 15). Daarvan werd gebruik gemaakt om de Bragg-sensoren te positioneren.

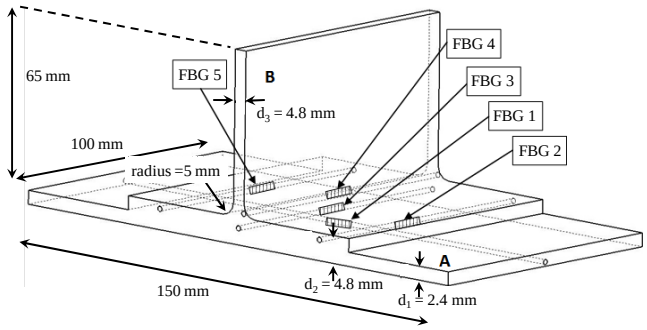

Figuur 14: De geometrie van het gefabriceerde schaalmodel.

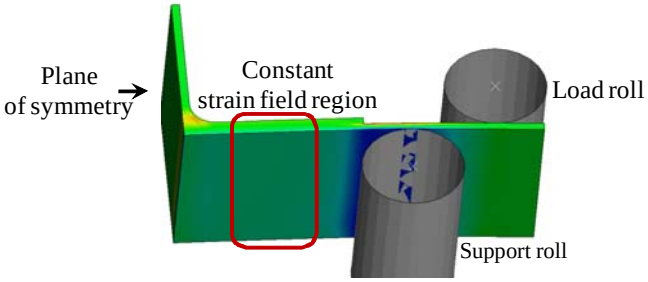

Figuur 15: Eindige elementen analyse van een T-vormig verbindingsstuk belast in vierpuntsbuiging.

In plaats van het gebruik van conventionele sterk dubbelbrekende vezels, kan men overstappen op microstructuurvezels. Bragg-sensoren in dergelijke vezels beloven een interessant alternatief te worden voor het opmeten van transversale rekken zonder de nodige temperatuurscompensatie. Die vezeltechnologieën met Bragg rooster (uni-axiale Bragg-sensor, bow-tie Bragg-sensor, en microstructuur Bragg-sensor, Figuur 1) werden experimenteel vergeleken door ze in te bedden in VVK proefstukken. De uni-axiale Bragg-sensor werd in de buigproeven als referentiewaarde gebruikt voor de twee andere technologieën. Drie verschillende belastingen werden gebruikt om de gevoeligheid van de verschillende sensoren met elkaar te vergelijken (een vierpuntsbuiging, een transversale drukproef en een temperatuurstest).

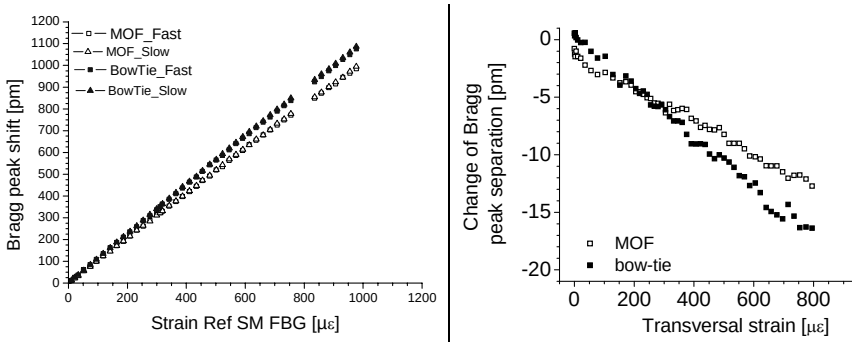

Figuur 16: Golflengteverschuiving gemeten tijdens een vierpuntsbuiging (links) en transversale test (rechts) voor de bow-tie en microstructuur Bragg-sensor.

Een gelijkaardig verloop werd gevonden voor de bow-tie en de microstructuur vezel in vierpuntsbuiging, waarbij de bow-tie iets sterker reageert (~8%) (Figuur 16, links). Merk op dat de bow-tie en de microstructuurvezel dezelfde oriëntatie hebben. Voor de transversale drukproef zien we een soortgelijke curve. De gevoeligheid (verbreding van het spectrum) is iets groter voor de bow-tie Bragg-sensor. Beide verschillen zouden te wijten kunnen zijn aan de iets grotere diameter van de microstructuurvezel.

Voor de temperatuurtest werden de proefstukken opgewarmd tot 120°C en dan langzaam afgekoeld. Tijdens het afkoelen werd de afstand tussen beide pieken (volgens de twee polarisatierichtingen van het licht) opgevolgd in functie van de temperatuur (Figuur 17).

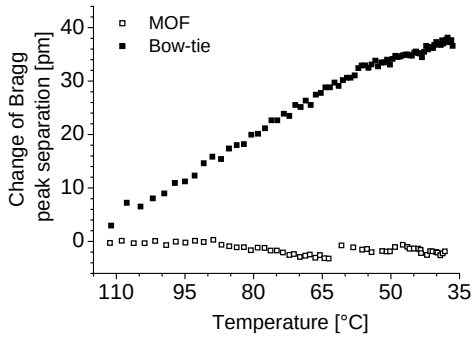

Figuur 17: Verandering van de piek verbreding voor de bow-tie en microstructuur Bragg-sensoren in functie van de temperatuur.

Een nagenoeg lineair verloop van de afstand tussen beide pieken werd vastgesteld voor beide sensoren. Voor de bow-tie Bragg-sensor is die gelijk aan -0.42 pm/°C en voor de microstructuur Bragg-sensor is die een stuk kleiner 0.026 pm/°C. Rekening houdende met deze resultaten kunnen we stellen dat een quasi onafhankelijke transversale rekmeting kan uitgevoerd worden met behulp van ingebedde microstructuur Bragg-sensoren.

Conclusies

In dit werk werden alle aspecten van het opvolgen van VVK constructies met ingebedde sensoren besproken. Hierbij werd de nadruk gelegd op het meten in meerdere richtingen en de interactie tussen de sensor en het materiaal waarin het is ingebed.

ENGLISH SUMMARY

Introduction

There is growing interest in the use of fibre reinforced plastics (FRPs) as high-grade construction material for various applications that need to be lightweight, yet strong in sometimes harsh loading conditions. Despite the growing popularity of structural composite materials, one has to realize that their mechanical behaviour is significantly different compared to conventional isotropic construction materials. Another major issue is the appearance and growth of damage (e.g. matrix cracks, fibre breakage, delamination, ...), which can already occur after a few hundred loading cycles. Due to the anisotropic and inhomogeneous nature of composites, mechanical loading that develops even little strain in the main fibre direction, may cause strain levels normal to the fibres or at the fibre/resin interface which are sufficiently high to cause damage. Although the initiation of damage in composite materials is not life-threatening, regular inspection of the damage status and of its evolution is necessary. Standard inspection methods (visual surveillance, ultrasonic inspection and radiography) do not allow collecting data in between two inspection intervals, i.e. they do not provide continuous and on-line information. Strain monitoring of an in-service structure should greatly enhance the insight and confidence in the (long-term) behaviour of high performance composite structures. The feedback from recorded loads, deformations and temperatures of (parts of) existing structures in real conditions, can lead to highly valuable information for design conditions. Structural health monitoring can already start by mapping residual strains during the production process.

For these applications, optical fibre sensors exhibit a number of well-known advantages over conventional electrical sensors including insensitivity to electromagnetic interference, small dimensions, light weight, multiplexing capabilities and resistance to corrosion. These fibre optic sensors are mostly used as surface mounted and single axial strain gauge to measure the in-plane strain of a structure's surface. In this dissertation, embedded highly birefringent optical fibres with Bragg gratings are used to reach the goal of multi-axial strain monitoring of carbon fibre reinforced thermosetting plastics.

Advanced strain sensing

A fibre Bragg grating (FBG) is a periodic refractive index variation in the core of a single mode optical fibre. When a broadband light spectrum is coupled into the fibre in which a Bragg grating is written, only a narrow part of the spectrum will be back-reflected. The reflected spectrum is centred on the Bragg-wavelength λ_B. Several types of optical fibres in which FBGs can be shot and their resulting spectrum are shown in Figure 1.

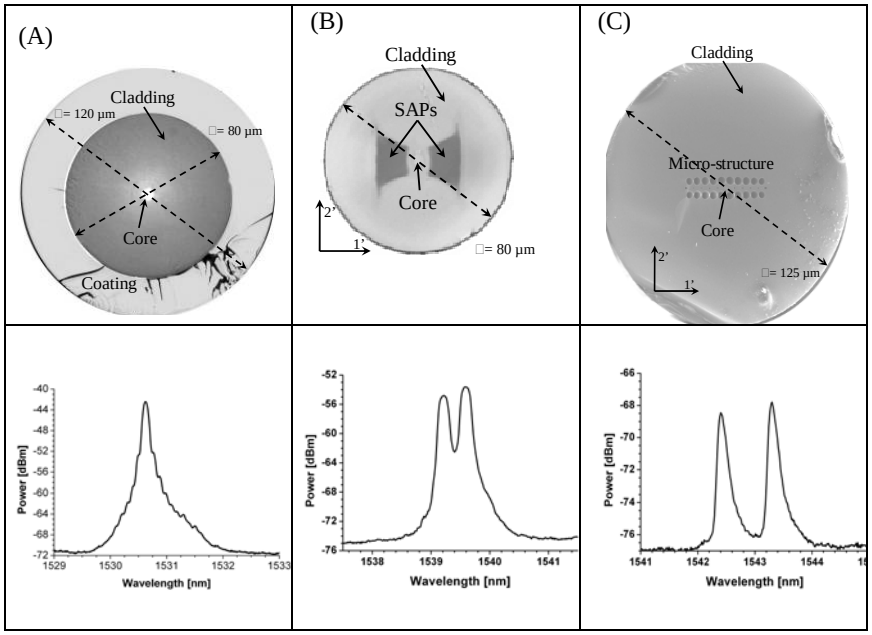

Figure 1: Typical cross sections of different optical fibre technologies (A: low birefringent, B: HiBi bow-tie, C HiBi micro-structured) and the spectral response of an FBG written in their core.

By using the photo-elastic effect, the spectral response of the fibre Bragg gratings to a random strain field can be determined as:

$$\frac{\Delta\lambda_{B,1'}}{\lambda_{B,0}} = \varepsilon_{3'} - \frac{1}{2} n_{eff,1'}^2 \left[p_{11}\varepsilon_{1'} + p_{12}\left(\varepsilon_{2'} + \varepsilon_{3'}\right)\right]$$
$$\frac{\Delta\lambda_{B,2'}}{\lambda_{B,0}} = \varepsilon_{3'} - \frac{1}{2} n_{eff,2'}^2 \left[p_{11}\varepsilon_{2'} + p_{12}\left(\varepsilon_{1'} + \varepsilon_{3'}\right)\right] \quad \textbf{1}$$

Where $\varepsilon_{1'}$, $\varepsilon_{2'}$, and $\varepsilon_{3'}$ are the principal strains of the fibre according to the coordinate system in Figure 1. The wavelength shift of light travelling according to both (*1'* and *2'*) axes will differ due to a different change of the refractive index induced by the strain field present at the core of the optical fibre. By determining the strain optic coefficients (p_{11} and p_{12}), the complete strain dependency of a fibre Bragg grating is defined (Equation 1). A transverse strain calibration method (Figure 2) inducing a simple strain state at the core of the fibre has been developed. The author suggests to calibrate uni-axial FBGs (shot in a low-birefringent SMF) with exactly the same fibre core properties (mechanical and optical) as for the HiBi optical fibre. As this is a uni-axial FBG, only one Bragg peak is back-reflected

(black spectrum in Figure 3). A certain preload is necessary to induce enough differential transverse strain to split up the spectrum (from red to green, and finally to the blue spectrum in Figure 3). From this moment on both Bragg peaks become distinguishable and the transverse load response can be determined.

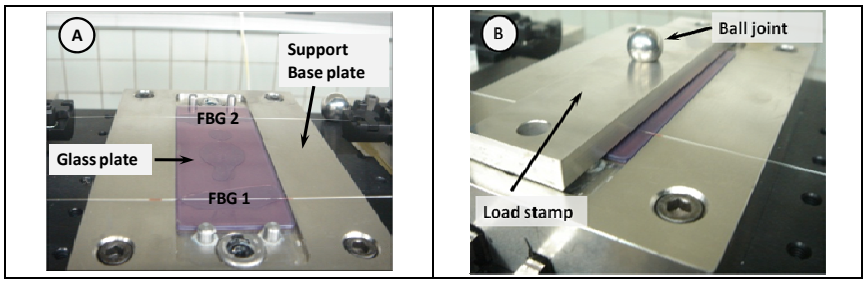

Figure 2: Transverse strain calibration device using a load stamp to simultaneously load two fibre Bragg gratings.

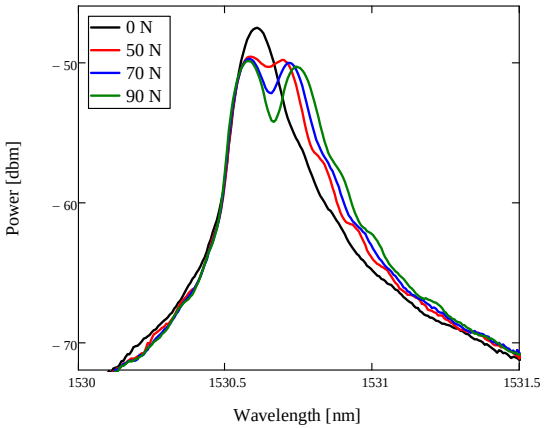

Figure 3: Spectra of a diametrically loaded uni-axial low birefringent fibre.

Good results were obtained for the coefficients p_{11} = 0.111 ± 0.008 and p_{12} = 0.247 ± 0.017 if compared to values mentioned in literature.

Multi-axial strain sensor

Structural health monitoring necessitates the possibility of measuring multi-axial strain fields. High birefringent optical fibres (HiBi-fibres) with Bragg grating can become a solution in this matter. Designing a multi-axial strain sensor based on optical FBGs should meet several basic requirements which could be summarized as: a high sensitivity for all strain components, resolving power which should be high enough to enable a distinction between the different strain components, no or

limited composite distortion, it should survive the composite manufacturing process, and it should be resistant to (harsh) loading conditions.
The multi-axial sensor configurations described are based on commercially available HiBi-fibre . For such FBGs, a change in axial strain or temperature will not affect the birefringence of the fibre, but will cause an overall shift of the Bragg spectrum towards higher or lower values. A change in transverse strain leads to a change of the birefringence of the fibre which results in a change of the peak separation, (Figure 4). Depending on the direction of the applied transverse strain with respect to the polarization axes of the fibre, the peak wavelength separation will increase or decrease.

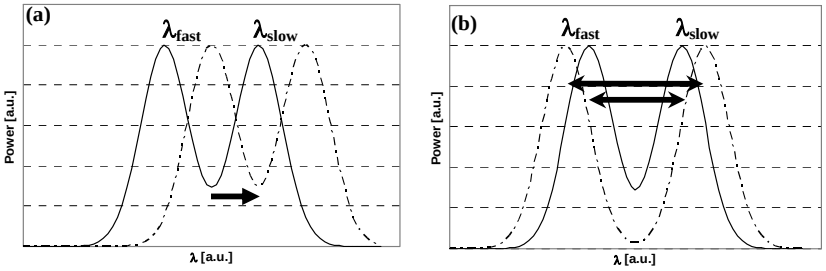

Figure 4: Effect on the spectral response of a HiBi-FBG due to (a) axial stress or uniform temperature change and (b) transverse stress.

By adding an extra FBG, 4 different wavelengths are obtained. If the two gratings respond differently to external perturbations like axial and transverse strain components, one can build a multi-axial strain sensor. The relation between wavelength shifts ($\Delta\lambda_B$) and change in strain components ($\Delta\varepsilon$) can be written in the following general form:

$$\begin{bmatrix} \Delta\lambda_{B1,1'} \\ \Delta\lambda_{B1,2'} \\ \Delta\lambda_{B2,2'} \end{bmatrix} = K \begin{bmatrix} \Delta\varepsilon_{1'} \\ \Delta\varepsilon_{2'} \\ \Delta\varepsilon_{3'} \end{bmatrix} \qquad \textbf{2}$$

in which K equals:

$$K = \begin{bmatrix} K_{11} & K_{12} & K_{13} \\ K_{21} & K_{22} & K_{23} \\ K_{31} & K_{32} & K_{33} \end{bmatrix} \qquad \textbf{3}$$

The coefficients K_{ij} depend on the used sensor configuration (fibre type and sensor combination). The strain components can be calculated by inverting Equation 2.

In order to define the optimal monitoring system, numerical analyses have been performed on three different sensor configurations. It was already mentioned that both gratings should have a diverse response on external loading. In the designed concept this goal is reached by decreasing the sensitivity to transverse stress of the second grating. The first grating stays exposed to longitudinal stress as well as transverse stress and the second one is shielded from transverse stress by covering the second grating with a capillary (Figure 5). The axial strain resolution is in this case equal to that of a uni-axial non embedded FBG. The obtained transverse strain resolutions are very good.

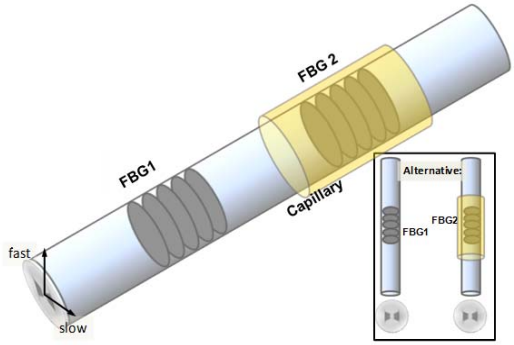

Figure 5: The capillary configuration consists of one fibre with two FBGs of which one grating is isolated from transverse stress through a glass capillary.

Table 1: Sensitivity analysis for the capillary configuration

Condition number = ~10		
	Error analysis	Standard deviation
$\delta\varepsilon_{1'}$ [με]	>6.9	±4.3
$\delta\varepsilon_{2'}$ [με]	>6.9	±4.3
$\delta\varepsilon_{3'}$ [με]	>0.9	±0.9

To obtain the resolution of the MAxS-sensor as described in Table 1, some assumptions need to be fulfilled. The FBG encapsulated in the capillary should be isolated from the transverse stresses existing inside the composite structure and a 100% longitudinal strain transfer from host structure to fibre core should exist.

Embedded fibre Bragg gratings

When embedding an optical fibre in a host material the embedding procedure should be as simple as possible. A robust entry point of the optical fibre in a composite component is needed for the successful cost-effective development of embedded

sensor technology. The sudden transition of the fibre surrounded by the stiff host material to the freely bendable fibre gives rise to in- and egress points which are prone to breaking. In this dissertation Kapton® foil and a Teflon tubing was used to protect the fibre outcome (Figure 6). The Teflon tubing is very flexible, which creates the opportunity to gently remove excessive resin flow at the edges of the laminate.

Figure 6: Optical fibre protection at the entry point by means of Teflon tubing (right)

Since HiBi-fibres are used, it is necessary to realize the correct orientation of the fibre when being embedded in a host material. It is shown that bad orientation of the fibre (illustrated by angle in Figure 7) could lead to big errors in the interpretation of measured values of strain.

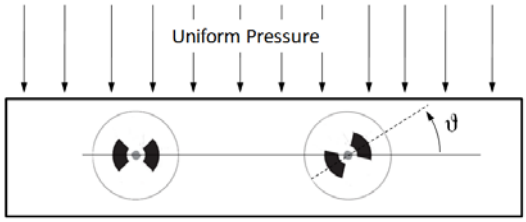

Figure 7: Example of two embedded PM optical fibres, one well-oriented and the other degrees misaligned.

It is well-known that an embedded optical fibre will cause a distortion of the material in which it is embedded. Notwithstanding the absence of a resin eye, embedded optical fibres can still have an effect on the mechanical behaviour of the structure in which they are embedded. Structural properties are, however, not affected when the fibre is embedded parallel to the reinforcement fibres.
In this work the embedded sensor is an optical fibre sensor and the host structure is a carbon fibre reinforced epoxy which has different material properties. As such, a strain transfer coefficient matrix (*TC*-matrix) needs to be defined which relates the strain of the sensor to the strain inside the structure as if no sensor would be present.

This *TC*-matrix depends on the elastic properties of the sensor as well as on those of the host material.

Due to the complex interaction between the host material and the embedded optical fibre sensors, the relationship between the strain present in the core of the sensor and in the host material is difficult to predict and can in general form be written as:

$$\begin{bmatrix} \varepsilon_1^c \\ \varepsilon_2^c \\ \vdots \\ \varepsilon_6^c \end{bmatrix} = \begin{bmatrix} TC_{11} & TC_{12} & \cdots & TC_{16} \\ TC_{21} & TC_{22} & \cdots & TC_{26} \\ \vdots & \vdots & \ddots & \vdots \\ TC_{61} & TC_{62} & \cdots & TC_{66} \end{bmatrix} \begin{bmatrix} \varepsilon_1^s \\ \varepsilon_2^s \\ \vdots \\ \varepsilon_6^s \end{bmatrix} \quad \textbf{4}$$

In which ε_i^c ($i = 1,\ldots,6$) is the strain of the composite material as if no optical fibre sensor was present, ε_i^s ($i = 1,\ldots,6$) is the strain field present at the core of the optical fibre sensor. In both cases the subscript $i = 1,\ldots,6$ refers to the components of strains in contracted notation.

The relationship of the strain field at the core of an optical fibre with the one present in the composite material, has been defined by finite element simulations. Because of symmetry reasons only 1/8 of an embedded fibre was modeled (Figure 8). The composite model is 10 mm x 1.2 mm x 10 mm for a 24 layer laminate.

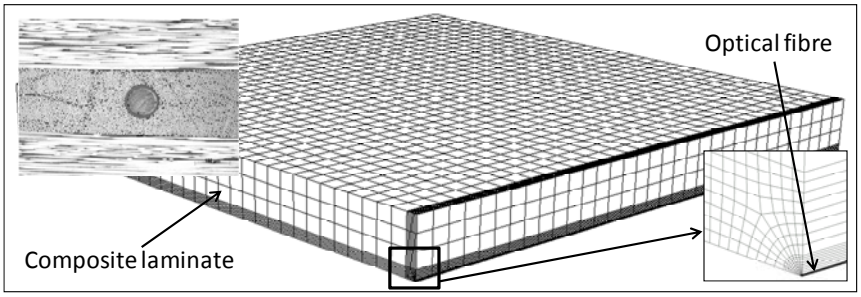

Figure 8: Finite element model used for simulation of the strain transfer between embedded optical fibre and CFRP laminate.

Using this finite element model one can, by changing several properties of sensor and/or host, examine their effect on the *TC*-matrix. The following parameters were considered: the mechanical properties of the host material, the lay-up of the composite laminate, the position of the sensor inside a certain layer of the host material and the properties of the sensor.

To validate the numerically determined *TC*-matrices a testing procedure was developed to introduce a well-defined homogeneous strain field inside a host material. Several 1.54 mm thick carbon fibre reinforced epoxy laminates were produced with at their mid-thickness an embedded 80 µm uni-axial FBG. Two metal

blocks (20 x 40 x 20 mm) were glued to the surfaces using a thin epoxy layer with a uniform thickness. The samples were loaded in the z-direction up to a maximum pressure of 92 MPa (Figure 9). The simulated (FEM) transverse strain (through-the-thickness) was used as reference strain measurement. In Figure 9 the three principal measured strains ($\Delta\varepsilon_{xx}$, $\Delta\varepsilon_{yy}$, $\Delta\varepsilon_{zz}$) of the laminate are plotted against the reference strain ($\Delta\varepsilon_{zz\_ref}$). The measured compressive strains correspond well with the reference through-the–thickness strain.

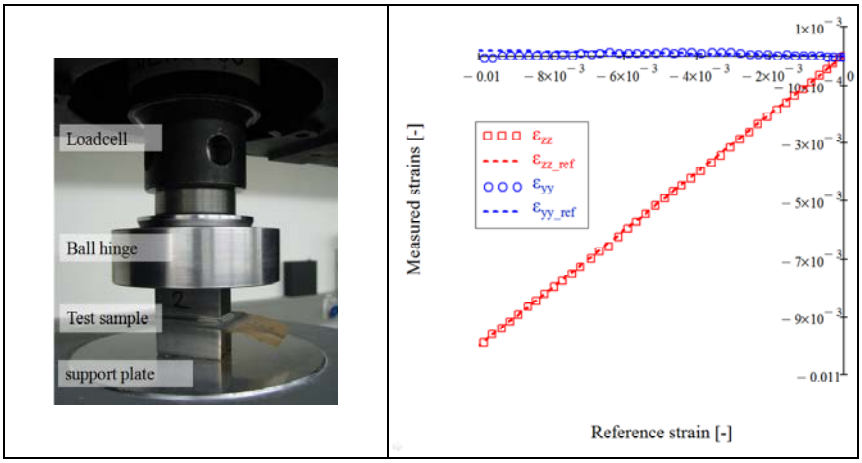

Figure 9: Picture of the test-set-up for transverse compression loading (left). The measured principal strain components ($\Delta\varepsilon_{xx}$, $\Delta\varepsilon_{yy}$ and $\Delta\varepsilon_{zz}$) in the composite laminate as a function of the simulated (FEM) reference strain $\Delta\varepsilon_{zz\_ref}$ (right).

Based on these results, one can state that a valid *TC*-matrix was obtained for a uni-axial FBG using the numerical calibration procedure.

The resolving power of an embedded sensor can be defined as the ability of this sensor to distinguish 3D-strain components of the material in which it is embedded. Using the simulated *TC*-matrix and the calibrated *K*-matrix one can determine that that the theoretical resolving power of the MAxS-sensor becomes ~10 times lower than the resolution of the non-embedded sensor.

Experimental validation of an embedded MAxS-sensor

Many CFRP-samples with embedded sensors were manufactured and tested under controlled loading conditions (tensile testing, transverse compression testing, four point bending testing, shear tensile testing, and thermal load testing). A selection of these tests were used to optimize the *TC*-matrix and thus prove the working principle of the MAxS-sensor. The measured strain values were compared with

reference measurements like extensometer, displacement, load, or surface attached FBG together with finite element simulations.

The strain calculation procedure is summarized in the following. In Figure 10 the response of a MAxS-sensor embedded in a laminate with a unidirectional lay-up ($[0°]_{48}$) is given. A high Bragg peak separation can be observed for FBG 1 while very small wavelength shifts and no Bragg peak separation can be observed for the encapsulated FBG.

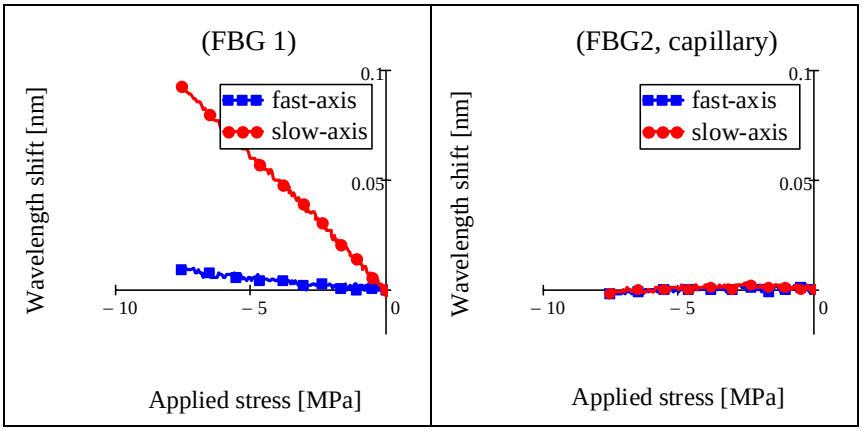

Figure 10: The MAxS-sensor's response under transverse compression.

Using the *K*-matrix one can calculate the strain field at the core of the optical fibre sensor from the measured wavelength shifts (Figure 11).

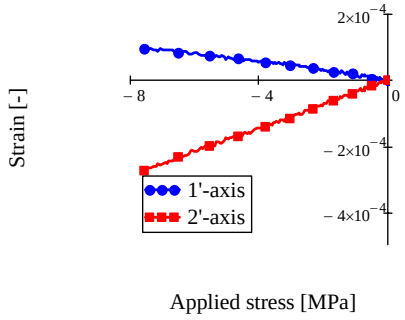

Figure 11: The measured strain at the core of the embedded MAxS-sensor during a transverse compression test

Using the transfer matrix, which is dependent on the mechanical properties of the sensor and the host material, one can calculate the strain field present in the host material (Figure 12, left).

Based on a comparison with reference strains, it can be concluded that the calculated strains are overestimated. This could be caused by an underestimation of the strain that is transferred from the host material to the core of the optical fibre. Therefore, several experimental results are combined to optimize the *TC*-matrix.

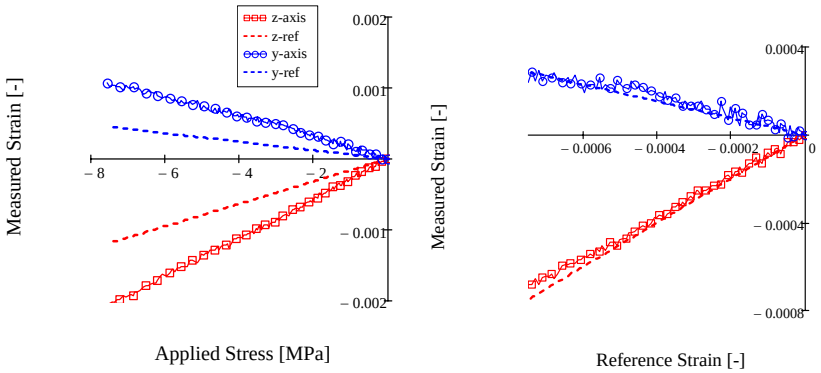

Figure 12: The calculated strain inside the host material during a transverse compressive test. On the left using the calculated *TC*-matrix, on the right, using the optimized *TC*-matrix.

By using the optimized *TC*-matrix, one can, once more, calculate the strain field present in the host material (Figure 12, right). The transverse strain components measured by the MAxS-sensor (full line with symbol) are compared with the reference strains (dashed lines) calculated using a finite element simulation.

Perspectives in multi-axial strain monitoring

The feasibility of the MAxS-sensor was studied by conducting tests on coupon level. In this paragraph some perspectives are given to use this sensor in “real-life” applications.

The first is following up the existence of **residual strains** in composite laminates and structures. By embedding the MAxS-sensor in a composite laminate $[\pm 45_2, 0_2, 90_2]_s$ (fabricated using the autoclave technique) it was possible to visualize the separate effects of axial strain and transverse strain components during the curing process. Temperature, pressure, vacuum, and wavelength shifts were measured in function of time (Figure 13). The cure cycle can be divided into five phases which is clearly indicated at the bottom of the figure. At first, the temperature is raised until it reaches 120°C (wavelengths change linearly with temperature). The second phase is the isothermal dwell phase (at 120°C), during which the wavelengths slightly decrease which corresponds to the settlement of the material

due to the vacuum.In the third phase, pressure is put on top of the sample which leads to a small drop of the wavelengths. In addition, temperature is raised up to 180°C (cure temperature). Again all wavelengths are equally raised as function of temperature. At that point we enter the fourth phase in which the epoxy curing starts. In this phase, a different wavelength behaviour is noticed for both FBGs. The fifth phase starts when the heating is stopped and the inside of the autoclave can cool down under atmospheric conditions. The residual strains appear in a peak separation of the spectrum of FBG 1.

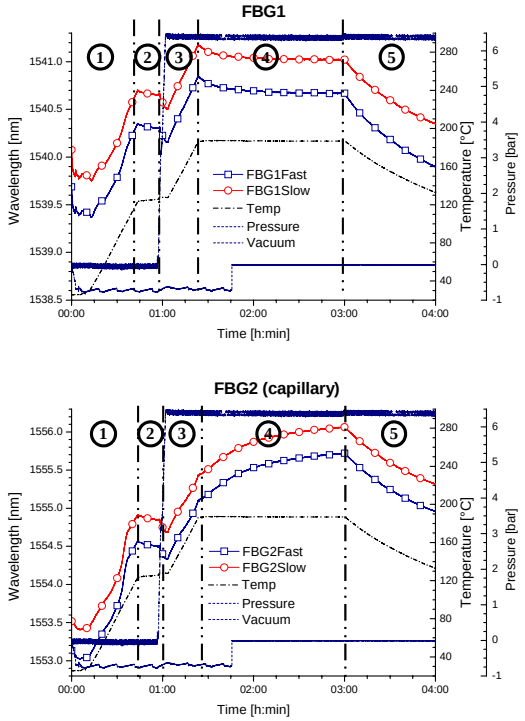

Figure 13: The measured temperature, pressure, vacuum, and Bragg wavelengths during the cure cycle of a $[\pm 45_2, 0_2, 90_2]_s$ laminate [15].

A second perspective is the monitoring of a scale model of a **T-joint structural element** (Figure 14). The scale model of the T-joint structure was first exposed to a four point bending experiment. As was shown in the FE- simulations (Figure 15), this experiment creates a constant strain field in the plateau of the structure. This property was used in determining the position of the different gratings.

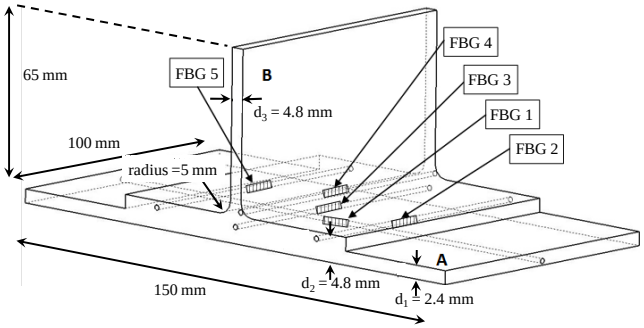

Figure 14: The geometry of the fabricated scale model of a T-joint structure

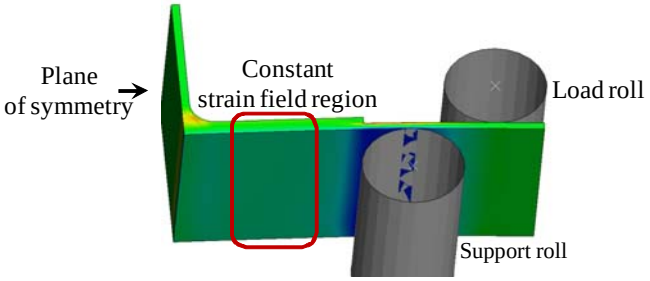

Figure 15: Finite element analysis of four point bending loading of a T-joint with indication of the principal strains

Instead of using the conventional HiBi-fibre to measure the transverse strain components, one can switch to **micro-structured fibre**. FBGs written in such a fibre hold a promising solution for transverse strain measurements without the necessary temperature compensations. Three FBG technologies with grating (conventional single mode FBG, bow-tie FBG, and micro-structured FBG, Figure 1) are experimentally compared by embedding them in composite test samples. The grating in the conventional single-mode fibre is used as reference sensor. The Bragg gratings have been embedded between the 2nd and the 3rd layer of a lay-up of 16 uni-directional prepreg layers (carbon/epoxy) with a total thickness of 1.54 mm. The slow axes of the micro-structured and bow-tie fibres were both oriented parallel to the surface of the composite panel. The actual orientation of the polarization axes has been checked afterwards in cross sections of the composite coupon.

Three different loading conditions were used to compare the response of the different sensors: a four point bending test, a transverse load test, and a thermal test.

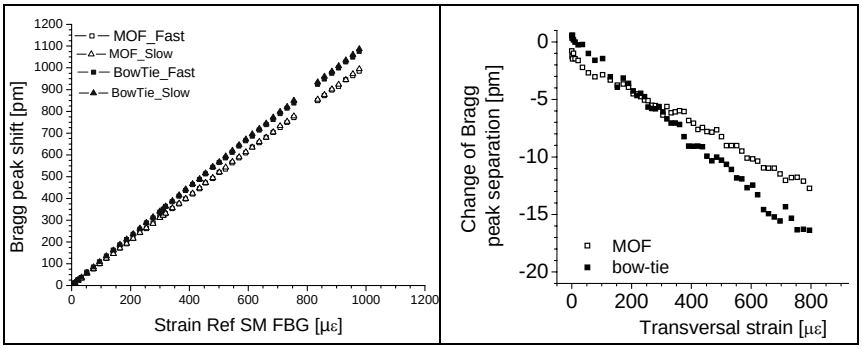

Figure 16: Wavelength shifts measured during the four point bending test (left) and the compression test (right) for the different embedded FBGs.

For the four point bending experiment, the curves show almost similar slopes for both sensors (Figure 16, left).

For the transverse compression experiment, the strain response of the two grating types shows moderate differences (Figure 16, right). The transverse sensitivities of the FBG in the bow-tie fibre are slightly higher. This difference can be partly attributed to the smaller cladding diameter of the bow-tie fibre.

For the thermal cycling, the composite samples were heated up to 120 °C and were then allowed to cool down slowly in a climate chamber. During the cooling phase the peak wavelength separation was monitored. Figure 17 shows that the linear change of the peak separation due to temperature is much smaller in the micro-structured fibre (0.026 pm/°C) than in the bow-tie fibre (-0.42 pm/°C). We can state that the Bragg peak separation in a highly birefringent micro-structured fibre provides a quasi temperature independent measurement for the transverse strain in the composite material.

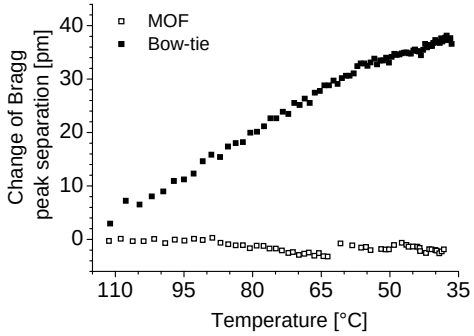

Figure 17: Change of the peak separation in the FBG in the MSF and bow-tie during cooling down phase (sample 1).

The results show that FBGs in MSF can be an alternative to FBGs in conventional birefringent fibres.

Conclusions

In this work all aspects of embedding optical fibre Bragg gratings were considered starting with the multi-axial strain calibration of these sensors and ending with the transfer of a strain field in a composite material onto the core of the optical fibre sensor. An extensive test program has proven the feasibility of a multi-axial strain sensor consisting of two Bragg-sensors.

Chapter 1 : INTRODUCTION

1. 1. PROBLEM STATEMENT

There is growing interest in the use of fibre reinforced plastics (FRPs) as high-grade construction material for various applications that need to be lightweight, yet strong in sometimes harsh loading conditions. Aerospace tails, wings, fuselages, and propellers can be made out of composite material. Figure 1-1 gives a historical overview of the used percentage of FRPs in civil aircrafts [1]. As much as 50% of the primary structure of the Boeing 787 Dreamliner - including fuselage and wings - is made of composite materials (Figure 1-2) [2]. Other examples are the A380 and the A350 of Airbus. Each Airbus A380 contains 20% composite materials and at the moment, the wings of the A350 will solely consist of composite materials [3].

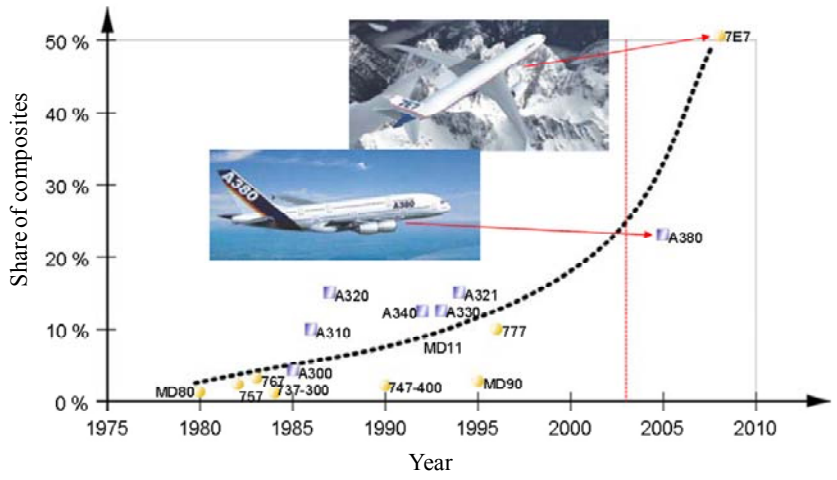

Figure 1-1: Development of composite aerospace applications over the last 40 years [1].

In space applications, these materials are used for solar panel substrates, antenna reflectors, yokes of spacecraft, and fuel tanks. For example in 2006, Microcosm Inc. successfully completed qualification tests on an all-composite cryogenic liquid oxygen tank (1 m diameter pressure vessel/ operating pressure ~40 bar) [4].

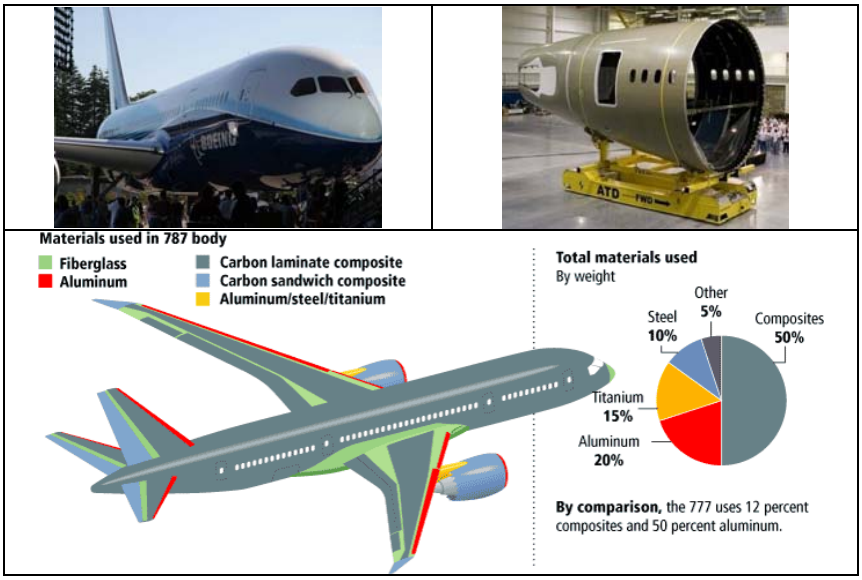

Figure 1-2: Example of an airplane in which 50% of the primary structure exists of composite materials [2].

In civil engineering applications, an all composite road bridge was built in Oxfordshire (UK) [5]. Other applications are the use of composites in boat and scull hulls, bicycle frames and race car bodies.

Despite the growing popularity of structural composite materials, one has to realize that their mechanical behaviour is significantly different compared to conventional isotropic construction materials. Another major issue is the appearance and growth of damage (e.g. matrix cracks, fibre breakage, delamination, ...), which can already occur after a few hundred loading cycles [6, 7]. Due to the anisotropic and inhomogeneous nature of composites, mechanical loading that develops even little strain in the main fibre direction, may cause strain levels normal to the fibres or at the fibre/resin interface, which are sufficiently high to cause damage [8]. Although the initiation of damage in composite materials is not life-threatening, regular inspection of the damage status and of its evolution is necessary. Standard inspection methods (visual surveillance, ultrasonic inspection and radiography) do not allow collecting data in between two inspection intervals, i.e. they do not provide continuous and on-line information.

Therefore, worldwide research is conducted on other evaluation techniques to measure strain and to detect damage in different types of materials and structures. Strain monitoring of an in-service structure should greatly enhance the insight and confidence in the (long-term) behaviour of high performance composite structures. The feedback from recorded loads, deformations and temperatures of (parts of)

existing structures in real conditions, can lead to highly valuable information for design conditions. Structural health monitoring can already start by mapping residual strains during the production process.

A major field of research concerns the application of optical fibre sensors [9-11], which have a number of well-known advantages including insensitivity to electromagnetic interference, small dimensions, light weight, multiplexing capabilities and resistance to corrosion [12]. These fibre optic sensors are mostly used as surface mounted and single axial strain gauge to measure the in-plane strain of a structure's surface. In this dissertation, we integrate these fibre sensors in FRPs, which brings along a number of challenges. A first challenge is to limit the mechanical distortion of the host material as well as the stress field disturbance caused by the embedded sensor. A second challenge is to develop suitable and accurate finite element models, which relate the (multi-axial) strain in the anisotropic material to the strain in the optical fibre sensor. The third challenge is to identify the transverse strain components, since measuring the axial strain alone will not be sufficient to judge the health condition of a structure. Although several attempts to design a multi-axial strain sensor have been published, these studies were mostly limited to the non embedded characterization of a sensor without taking the anisotropic behaviour of the host material into account [13, 14]. In the beginning of the MASSFOS project, and in consultation with Sonaca (industrial advisor) and the European Space Agency (ESA), strain measurement requirements were put forward for such a multi-axial strain sensor. A strain operating range of ±4000 με, a strain measurement resolution of ±5 με for the longitudinal and transverse strain components, and a temperature operating range of -175°C up to 200°C should be aimed for [15]. In this dissertation the focus will be put on the strain measurement resolution.

1. 2. MONITORING OF FRP STRUCTURES

1. 2. 1. Introduction to fibre reinforced plastics

This paragraph gives a short introduction on the constitution of composite materials and more specific FRPs, and highlights some major benefits over the more conventional materials (e.g. metals). Composite materials are engineered materials which consist of two or more constituents. Most composites (e.g. FRPs) have two constituents: a binder or matrix, and reinforcement fibres.

The reinforcement is much stronger and stiffer than the matrix, and gives the composite its good mechanical properties. The matrix holds the reinforcement fibres in an orderly pattern. Because the reinforcements are usually not bonded, the matrix also helps to transfer load among the reinforcements.

Commonly used **reinforcement fibres** are glass, carbon, aramide, etc.. Figure 1-3 gives an overview of the reinforcement fibres used by UK companies. The linear part of the stress strain curve is given for the different fibre types in Figure 1-4. Reinforcement fibres can be unidirectional (fibres uniformly distributed in one direction), they can be randomly spread chopped fibres, or fabrics (knitted, 3D-preforms, etc.) (Figure 1-5).

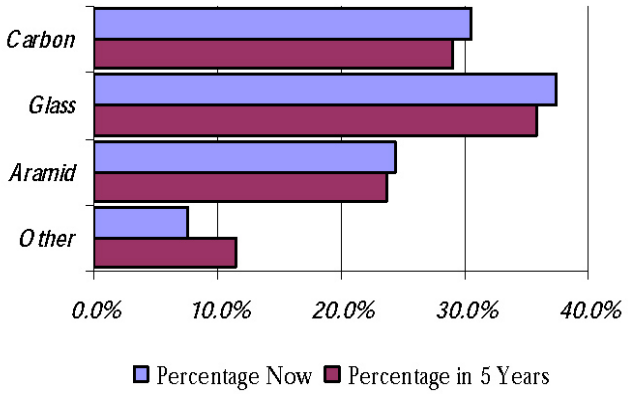

Figure 1-3: Fibres used by UK companies [16].

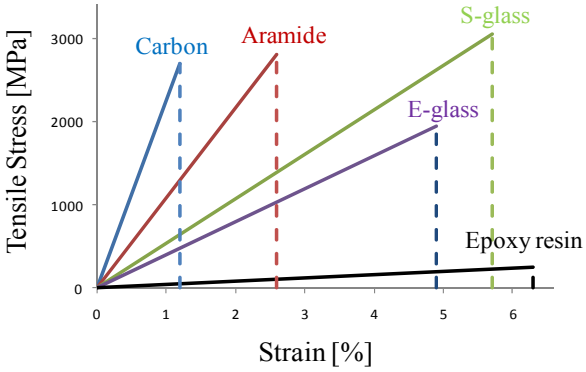

Figure 1-4: Elastic part of the stress-strain relation for different types of reinforcement fibres [16].

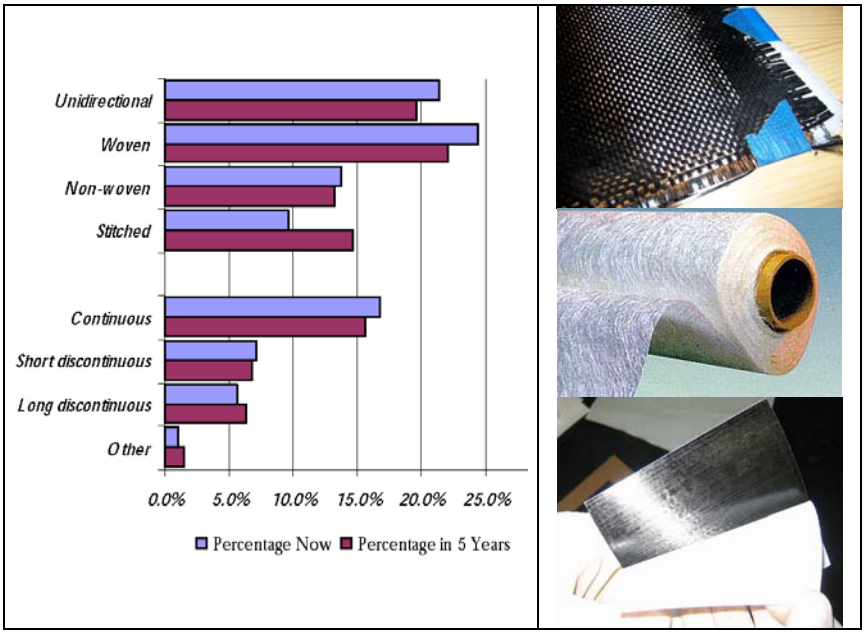

Figure 1-5: Fibre formats used by UK-companies [16]

For **the matrix,** a distinction is made between thermoplastics (PP,PPS,PEI,PEEK,PEKK) and thermoset material (epoxy, polyester). A thermoplastic is a polymer that turns to a viscous liquid when heated and freezes to a very glassy state when cooled sufficiently. Thermoplastic polymers differ from thermosetting polymers because they can, unlike thermosetting polymers, be melted and remoulded [17]. Thermosetting plastics (thermosets) are polymer materials that irreversibly cure form. The cure may be attained through heat (ranging from 70-240°C), a chemical reaction (two-component epoxy, for example), or irradiation such as electron beam processing. Uncontrolled reheating of the material results in reaching the decomposition temperature before the melting point is reached. Therefore, a thermoset material cannot be melted and re-shaped after it has been cured. This implies that thermosets cannot be recycled, except as filler material [17]. Thermoset materials are generally stronger than thermoplastic materials thanks to a dense 3-D network of bonds, and are also more suitable for high-temperature applications.

Several advantages of composite materials for use in structural components are summarized in this paragraph. A first advantage is their high strength for low weight and good stiffness-to-weight ratio. The fibre/resin mix can be customized to meet stiffness, strength and manufacturing requirements. Because of the high specific strength and stiffness, composites can deliver weight savings of 25 to 50 percent over traditional materials. While some applications may require thicker composite

sections to meet strength/stiffness requirements, manufacturers will still benefit from a significant weight reduction. The second advantage is the possible reduction of assemblies and reduced fastener count. Composite material makes it possible to consolidate many parts in one assembly. As a result, the part count along with fasteners, assembly time and weight, is reduced. Also, vulnerable interfaces between joint parts are eliminated. Other benefits of composite materials can be summarized as: good corrosion resistance, good resistance to fatigue damage with good damping characteristics, reduced machining, and low coefficient of thermal expansion. The wide range of fibres and resins available, makes it possible for manufacturers to choose the optimal material combination to meet the specific structural requirements of an application.

The material used in this work is a **carbon fibre reinforced thermoset plastic** material which is space qualified and also known as M55J/M18 pre-impregnated (prepreg) material. The M55J type of high modulus carbon fibre is impregnated with M18 type of epoxy which is partially cured. Storage at -18°C is needed to prohibit further curing of the epoxy matrix. The reinforced plastic prepreg layer can be stacked under different angles to develop a so-called laminate with desired stiffness and strength in different directions dependent on the application and the expected service load. Since one individual layer is a heterogeneous material with anisotropic properties, it is logical that the resulting lamina is also not isotropic. A typical notation of the laminate lay-up is $[0_2,90_2]_{2s}$. This notation should be understood as: the numbers 0 and 90 indicate the angle of the reinforcing fibres with respect to the x-axis, taken positive when oriented from the x-axis to the y-axis; subscript 2 indicates the number of consecutive layers; and subscript s denotes a symmetrical lay-up with respect to the mid-plane (thus a total of 16 layers).

1. 2. 2. Monitoring structures

This dissertation is the continuation of the work done during the PhD of Wim De Waele. In this book [18], a thorough overview of possible fibre optic sensors and their applications, is given. The main body of the work has been mainly focused on embedded as well as surface mounted optical fibre Bragg grating sensors for measuring axial strain. A theoretical model to measure multi-axial strain components, is put forward too. Thus, for a thorough introduction on structural health monitoring of structures using optical fibre sensors, the reader is referred to the work of Wim De Waele. This paragraph gives an overview of the position of the fibre optic sensors and especially the fibre optic stress/strain sensors in the market.

Fibre optic sensors start to become more and more accepted in the sensor market thanks to cost reduction. For example, the cost for an FBG sensor is ~50 €; their read-out systems are already available from ~10 000 € on [19]. Figure 1-6 gives the

present and the future state of the United States' fibre optic sensor market with an expected growth of ~400% in the next 5 years. The potential of fibre optic sensors to measure various perturbations, e.g. axial strain, pressure, temperature, and their advantages over conventional electrical sensors have done the rest. Stress/strain measurement is one of the most important applications of optical fibre sensor technology. Its market potential is given in Figure 1-7. Only 0.2% of the stress strain market was taken by fibre optics in 2006. In 2013 this will be over 4%. In the future, a lot of market potential remains and a steady growth is to be expected.

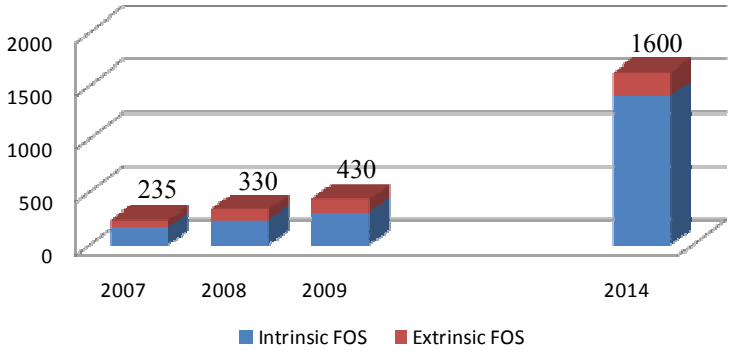

Figure 1-6: Present and future state of the United States' fibre optic sensors market in million dollar [20].

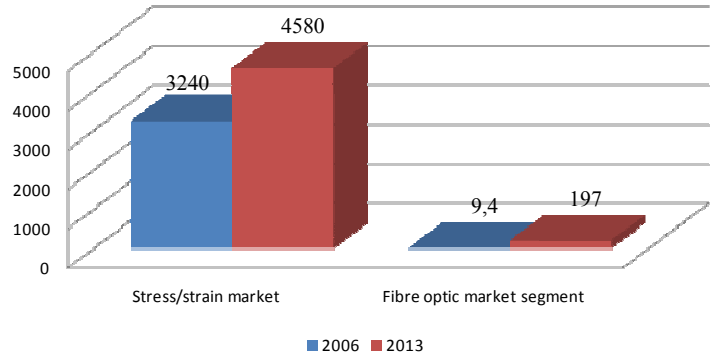

Figure 1-7: Present and future state of the stress/strain sensor market and the part which is, or will be taken, by fibre optic sensors in million dollar [21].

This work will focus on the use of FBGs for strain measurements and especially on the opportunities and pitfalls of embedded FBG strain measurement.

1. 3. STATE OF THE ART – GOAL OF THE RESEARCH

Worldwide, FBGs are mostly mounted on top of structures with or without transduction mechanism. In both cases, the FBGs are only loaded with axial stress. However, to monitor the structural health of composite materials, it is necessary to map all strain components inside the material. Embedded FBGs are well-suited for this task, because of their distinguishing response to axial and transverse strain components whenever subjected to a three-dimensional strain field [22]. In addition, optical fibres can be embedded in composite materials without compromising the structural integrity of the host material [22]. For example, presently, optical fibres have already been integrated in smart patches. This composite patches can be bonded on components of aircrafts which were damaged during service. They are an alternative for conventional aircraft repair techniques which employ bolted or riveted metallic reinforcements which frequently introduce additional stress concentrations caused by the fastener bolts. Research has proven the feasibility of this technique to repair and in the mean time follow up further cracking of an structure [23-27].

The experience in fibre optic sensing in Belgium is mainly located in the field of research. Several universities and research institutions explore the possible applications of fibre optics and especially FBGs. Faculté Polytechnic de Mons is mainly interested in chemical sensing, and strain sensing. Multitel, which started as spin-off of this faculty, has the ability to write FBG gratings in all sorts of optical fibres and develops customized solutions for chemical, physical or biological sensing. They integrated fibre optics in fabrics for health care monitoring and started research activities on embedding FBGs in composite materials. The NDT group at KULeuven-MTM embedded fibre optics in composite material as an alternative for the rather robust piezo-electric transducers used for acoustic emission monitoring. In the AISHA project [28], single mode optical fibre sensors were used in a polarimetric set-up to detect the Lamb wave signals that are generated in composite samples. FOS&S located in Geel (Belgium) is developing fibre optic transducers mainly based on the Bragg grating technology. A strain kit was developed which makes surface mounting as simple or even simpler than the mounting of classical electrical strain gauges [29]. VUB-TONA has expertise in theoretical modelling and characterization of FBGs written in micro-structured optical fibres.
The research group ‘Mechanics of Materials and Structures’ of UGent has a lot of experience in quantitative monitoring of deformation of all sorts of materials (especially composites) with all sorts of sensors. A PhD on structural monitoring of composite elements using optical fibres with Bragg-sensors was successfully finished in academic year 2001-2002 [18]. The main goal of this research was proving the feasibility of strain sensing with FBGs which are surface mounted or

embedded. The author performed his PhD in the framework of a co-funded ESA-project (with acronym MASSFOS and in cooperation with FOS&S and XenIC's) on embedding multi-axial FBGs in fibre reinforced plastics. Related research activity is situated in the domain of high strength gratings fabricated on a draw tower. Several parameters of the fabrication process (dimensions of the fibre and coating properties and placement) are studied into detail. These so-called draw tower gratings are also being embedded in thermoplastic fabric composite materials. It has been discussed that the spectrum is significantly altered during manufacturing of these laminates.

This dissertation is based on the work done during the aforementioned ESA-project. The main goal of the author's research can be described as: ***Multi-axial Strain Monitoring of Fibre Reinforced Thermosetting Plastics Using Embedded Highly Birefringent Optical Fibre Bragg Sensors (HiBi-fibres with FBGs)***.

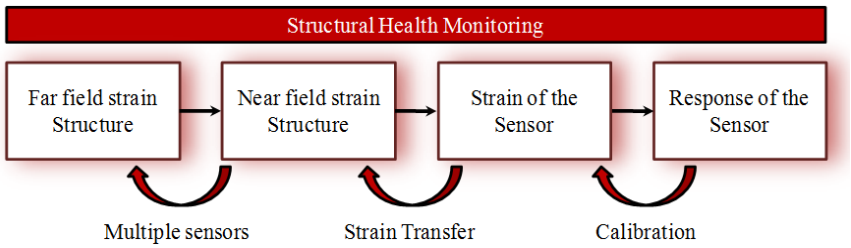

Figure 1-8: Flow chart of the different steps necessary for structural health monitoring using an embedded optical fibre sensor.

Figure 1-8 depicts a flow chart with the different steps necessary for monitoring the health of a structure by using an embedded sensor. The different steps will be evaluated in this dissertation.
Since strain monitoring was aimed for, a basic (theoretical and experimental) know-how on the strain and temperature dependency of FBGs written in HiBi-fibres had to be developed (calibration). As will be proven, a single FBG is not sufficient to measure a multi-axial strain field. Therefore, a sensor configuration had to be developed which has a sufficiently different response for the different strain components. The mechanical interaction between this embedded sensor configuration and its host material should be evaluated (Strain transfer). This also includes the competence of embedding the sensor in fibre reinforced plastics which are generally fabricated in harsh environments (in this work, an autoclave procedure). The orientation, position, and entry point of such a sensor are main topics which need to be studied. A lot of effort has been made in the experimental validation. Therefore, sensors have been embedded in a number of CFRP-samples

which have been subjected to controlled loading conditions. A comparison with more conventional measurement techniques (such as extensometers and surface mounted reference FBGs) and an interpretation of the measurement results are important. Finally, possible representative structural composite applications in which the multi-axial strain sensor configuration is of added value, have been studied.
Recently, a research proposal in cooperation with VUB-TONA and VUB-MECH was submitted to the FWO-institute. The purpose is to overcome the present difficulties which still exist for embedded strain monitoring using FBGs written in classical fibre types. FBGs written in micro-structured fibre technology will be studied. Results of some preliminary work are discussed in this work.

1. 4. OUTLINE OF THE DISSERTATION

Since this dissertation is the continuation of the work done during the PhD of Wim De Waele (promoter of this work), the author first likes to highlight the most important differences with his own work. The main focus of Wim De Waele was on measuring axial strain in composite laminates and structural elements with embedded uni-axial FBGs. These measurements have been compared with reference measurements based on surface mounted FBGs, electrical resistance strain gages and extensometer readings. The strain and temperature dependency (in a small temperature range 10-40°C) of uni-axial FBGs were calibrated experimentally. The embedding method (entry point of the fibre, composite distortion) was evaluated and both static and dynamic experiments have been conducted. In the last chapter of De Waele's work, a theoretical model describing the measurement and calculation of multi-axial strain components was put forward, however without experimental validation.
That last chapter was the starting point of this work. The theoretical model to measure multi-axial strain components is refined, and a complete experimental calibration programme (for transverse strain, for longitudinal strain, and for temperature) is conducted for several types of optical fibres with Bragg grating. The main focus, however, is on multi-axial FBGs. The embedding method, which is more complex as compared to uni-axial FBGs, was evaluated. All aspects of measuring more dimensional strain fields inside composite materials are examined in detail. An overview of the different chapters in this book is given below.

In general, the first two or three chapters of a dissertation are used to give a review of the literature. In this dissertation, the author has chosen to discuss the literature in the related chapters and sections. It is the author's believe that this will comfort the reader when going through this dissertation. This section gives an overview of the different chapters of the dissertation.

1. 4. 1. Chapter 2: Advanced strain sensing using optical fibres with Bragg gratings

In this chapter, a definition of an FBG and its central Bragg wavelength are given. Then, the Bragg wavelength's parameters, which are temperature and strain dependent, are defined. The theoretical response of these parameters for a multi-axial strain field has been evaluated for the case of a non-embedded fibre Bragg grating. The photo-elastic effect and thermo-optic effect were used as starting points. Next, an overview of FBGs written in different types of glass optical fibre is given. The main property to make a distinction between the fibres was their (non) birefringency, with the emphasis on the shape of the corresponding Bragg spectrum. From this point on, the dissertation will focus only on the bow-tie type of HiBi-fibre. This type of fibre has been experimentally characterized for transverse and axial strain, and for thermal loads. A new method for characterization of these fibres is proposed.

1. 4. 2. Chapter 3: Multi-axial strain sensor

Designing a multi-parameter or multi-axial strain sensor (MAxS-sensor) based on optical FBGs should meet several basic requirements, which are discussed in this chapter. The optical fibre sensor should show a high sensitivity for all strain components and should be designed in such a way that it shows a diverse response for the parameters of interest (axial strain, transverse strain, and temperature). First, a literature review on multi-parameter strain sensing is given, followed by the proposition of a new sensor design for measuring the total strain field (axial and two transverse components) with embedded FBGs. In addition, the strain resolution of this sensor and a feasibility study (combined FE modelling and experiments) are discussed.

1. 4. 3. Chapter 4: Embedded fibre Bragg gratings

When embedding an optical fibre in a host material, one should consider several topics. The embedding procedure should be as simple as possible. This means that the in- and egress points, the orientation of the fibre (polarization axes HiBi-fibres), its position, and the necessary embedding time should be examined. A literature review and description of own work on how to design the entry point of an optical fibre sensor is given, followed by a survey on possible orientation procedures, considered during the author's PhD. Next, the mechanical distortion of the composite material due to the presence of an embedded sensor, is briefly discussed. It was shown that the size of the sensor and its orientation with respect to the reinforcement fibres are important. Finally, the strain present in the core of the optical fibre is not equal to that in the host material and will be examined. Finite element simulations show that the relation between both strain fields depends on the

mechanical properties of the host material and the sensor, on the lay-up of the composite material, and on the position of the sensor in a certain layer. Due to the difference in mechanical properties, the resolving power of the sensor is found to be lower than the theoretical resolution of the MAxS-sensor determined in Chapter 3.

1. 4. 4. Chapter 5: Carbon fibre reinforced plastic samples with embedded MAxS-sensor under controlled loading

The chapter begins with an explanation on the manufacturing process of CFRP-samples, using the autoclave technique. Since all samples were made at the UGent autoclave facility, the CFRP sample material properties were defined apart from those given by the manufacturer and other authors. A selection of tests performed during the MASSFOS project on CFRP samples with embedded MAxS-sensor are discussed to prove the working principle of this sensor. The measured strain values are compared with reference measurements (extensometer, displacement, load, surface mounted FBG) and with finite element simulations. In this chapter the calculated strain relation between optical fibre and host material has been experimentally optimized. The feasibility of the MAxS-sensor will be proven.

1. 4. 5. Chapter 6: Perspectives in multi-axial strain sensing with embedded FBGs

In this chapter, some perspectives are given to use this sensor in several real-world applications. The first perspective is following up the existence of residual stresses and strains in composite laminates and structures. This can be done by monitoring the cure cycle during the fabrication process of a composite. A second perspective is the monitoring of a real structure in service. The MAxS-sensor is embedded in a scale model of a T-joint. A new test set-up was designed and fabricated to test this type of structure. A last perspective is the feasibility of Bragg gratings in a micro-structured fibre for measuring transverse strains. It will be proven that FBGs written in such a fibre hold a promising solution for transverse strain measurements without the necessary temperature compensations.

1. 4. 6. Chapter 7: Conclusions

In this concluding chapter, the main achievements in using embedded optical fibres as a multi-axial monitoring technique, are briefly recapitulated. Finally, some recommendations for further research are given, focusing mainly on the further use and design of FBGs written in micro-structured fibres, and on the evaluation of the existing MAxS-sensor under dynamic load.

1. 5. REFERENCES

1. *Courtesy of DLR Braunschweig*.
2. *Courtesy of Boeing inc.*
3. Available from: http://www.airbus.com/en/aircraftfamilies/a350/advanced_materials.html.
4. Available from: http://www.smad.com/42_inch_tank_pressrelease.pdf.
5. Gebremichael, Y.M., Li, W., Boyle, W.J.O., Meggitt, B.T., Grattan, K.T.V., McKinley, B., Fernando, G.F., Kister, G., Winter, D., Canning, L., and Luke, S., *Integration and assessment of fibre Bragg grating sensors in an all-fibre reinforced polymer composite road bridge.* Sensors and Actuators a-Physical, 2005. **118** (1): p. 78-85.
6. Lagace, P.A. and Brewer, J.C. *Studies of delamination growth and final failure under tensile loading*. in *Proceedings of the Sixth international Conference on Composite Materials (ICCM-VI) & Second European Conference on Composite Materials (ECCM-II)*. 1987: Elsevier.
7. Verpoest, I., *Nieuwe ontwikkelingen in de vezelversterkte kunststoffen*, in *Part I: Flanders Technology international*. 1985, VVTI and TI: Gent.
8. Chan, W.S., *Fracture and damage mechanisms in laminated composites*, in *Composites engineering handbook*, P.K. Mallick, Editor. 1997, Marcel Dekker inc.: New York. p. 309-370.
9. Degrieck, J., De Waele, W., and Verleysen, P., *Monitoring of fibre reinforced composites with embedded optical fibre Bragg sensors, with application to filament wound pressure vessels.* NDT & E International, 2001. **34** (4): p. 289-296.
10. De Baere, I., Voet, E., Van Paepegem, W., Vlekken, J., Cnudde, V., Masschaele, B., and Degrieck, J., *Strain monitoring in thermoplastic composites with optical fiber sensors: Embedding process, visualization with micro-tomography, and fatigue results.* Journal of Thermoplastic Composite Materials, 2007. **20** (5): p. 453-472.
11. Degrieck, J., Van Paepegem, W., Cnudde, V., De Baere, I., De Baets, P., Declercq, N., Luyckx, G., Masschaele, B., Moentjens, A., Quintelier, J., Sol, H., Van Hemelrijck, D., and Vlekken, J. *Monitoring of fatigue, impact and wear in Cetex TPC*. in *Cetex - Thermoplastic composites. From scratch to flight.* in *Proceedings of the first Cetex Conference.* 2006. Delft, THE NETHERLANDS
12. Othonos, A. and Kalli, K., *Fiber Bragg gratings: Fundamentals and Applications in Telecommunications and Sensing*. 1999: Artech House.
13. Luyckx, G., De Waele, W., Degrieck, J., Van Paepegem, W., Vlekken, J., Vandamme, S., and Chah, K., *Three-dimensional strain and temperature monitoring of composite laminates.* Insight, 2007. **49** (1): p. 10-16.

14. Chehura, E., Ye, C.C., Staines, S.E., James, S.W., and Tatam, R.P., *Characterization of the response of fibre Bragg gratings fabricated in stress and geometrically induced high birefringence fibres to temperature and transverse load.* Smart Materials & Structures, 2004. **13** (4): p. 888-895.

15. Vlekken, J., *MASSFOS: Preliminary design report*. 2005: Geel.

16. Available from: http://www.adcom.org.uk/downloads/Composites%20-%20sectors%20&%20competitiveness.pdf.

17. Degrieck, J., *Composieten I*. 2004-2005, Master Course at Ghent University.

18. De Waele, W., *Structural monitoring of composite elements using optical fibres with Bragg-sensors.* 2001-2002, PhD dissertation at Ghent University: Ghent.

19. *personal communications* with FOS&S,.

20. Available from:

http://www.opticalfibersensors.org/news/be-en/155/detail/item/1500/.

21. Available from:
http://www.photonics.com/Content/ReadArticle.aspx?ArticleID=31633.

22. Luyckx, G. and Voet, E., *MASSFOS: Summary report*. 2009: Gent.

23. Corvaglia, P., Largo, A., Caponero, M.A., and Fiori, L. *Development and Characterization of a smart FRP Patch with Embedded FBG Sensor for Strain Monitoring of RC Structures*. in *Proceedings of the 3rd International Conference on Structural Health Monitoring of Intelligent Infrastructure*. 2007. Vancouver, CANADA.

24. Crossley, S., Marioli-Riga, Z., Tsamasphyros, G., Kanderakis, G., Furnarakis, N., Ikiades, A., and Konstantaki, M. *Smart Patches: Self-monitoring composite patches for the repair of aircraft*. in *Proceedings of the Conference on Industrial and Highway Sensors Technology*. 2003. Providence, RI.

25. Fernandez-Lopez, A., Guemes, A., Gonzalez-Requena, I., De Miguel-Giraldo, C., and Menendez, J.M. *Damage Detection in Composite Repair Patches using Embedded Optical Sensors*. in *Proceddings of the 4th European Workshop on Structural Health Monitoring*. 2008. Cracow, POLAND.

26. Khalili, S.M.R., Nooramin, A.S., and Shiravi, M. *Experimental characterization of composite and smart patching repaired edge cracked plate in charpy impact*. in *Proceedings of the 2nd International Conference on Advanced Computational Engineering and Experimenting*. 2008. Barcelona, SPAIN.

27. Kressel, I., Botsev, Y., Leibovich, H., Guedj, P., Ben-Simon, U., Ghilai, G., Gorbatov, N., Gali, S., and Tur, M. *Fiber Bragg grating sensing in smart composite patch repairs for aging aircraft*. in *Proceedings of the 17th International Conference on Optical Fibre Sensors*. 2005. Brugge, BELGIUM.

28. Available from: http://www.ndt.net/article/aisha2007/papers/preface.pdf.

29. Available from: http://www.Fos-s.com.

Chapter 2 : Advanced strain sensing using optical fibres with Bragg gratings

Figure 2-1 repeats the structural health monitoring scheme of Chapter 1. The calibration step, necessary to relate the wavelength response of an optical fibre sensor with the strain field at its core, has been highlighted. In this chapter, the theoretical response to a multi-axial strain field and temperature of an optical fibre with Bragg grating has been evaluated.

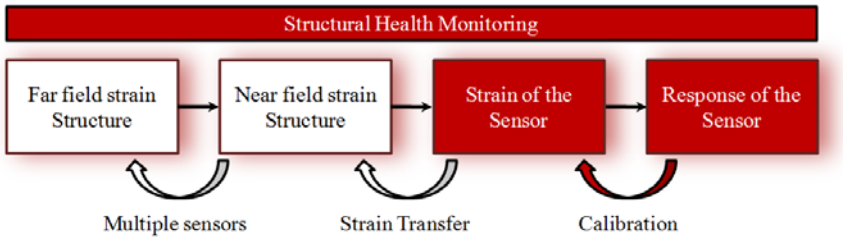

Figure 2-1: Flow chart of the different steps necessary for structural health monitoring using an embedded optical fibre sensor. The calibration step is highlighted.

2. 1. Introduction

A fibre Bragg grating (FBG) is a periodic refractive index variation in the core of a single mode optical fibre, created by appropriately illuminating the fibre sideways with UV-light [1] (Figure 2-2). When a broadband light spectrum is coupled into the fibre in which a Bragg grating is written, only a narrow part of the spectrum will be back reflected (Figure 2-2). The reflected spectrum is centred on the Bragg-wavelength λ_B which is given by

$$\lambda_B = 2n_{eff}\Lambda \qquad \textbf{2-1}$$

in which n_{eff} is the effective refractive index of the fibre at the position of the Bragg-grating, and Λ is the pitch of the Bragg-grating. Both parameters (n_{eff}, Λ) of the grating are strain and temperature dependent. As such the shift of the Bragg wavelength in function of these small perturbations can be written as [2]

$$\Delta\lambda_B = 2\left(n_{eff}\frac{\partial\Lambda}{\partial\varepsilon} + \Lambda\frac{\partial n_{eff}}{\partial\varepsilon}\right)\Delta\varepsilon + 2\left(n_{eff}\frac{\partial\Lambda}{\partial T} + \Lambda\frac{\partial n_{eff}}{\partial T}\right)\Delta T \qquad \textbf{2-2}$$

Ignoring the temperature dependency, FBG-sensors can be considered as the optical counterpart of classical electrical resistance strain gauges. In spite of some disadvantages (e.g. they are fragile, which makes careful handling necessary) this type of sensor has many advantages over classical strain gauges. The strain and temperature information is encoded into a wavelength which is an absolute parameter. Measurement interruption, by accident or intended, does not cause any problem. Long term measurements do not need extra balancing and thus loss of the zero reference, as is most often the case with classical strain gauges due to drift of the components (reference strain gauges, resistance of the wires) of the measuring system. In addition, the result does not depend on the total light level; losses in the connecting fibres or optical couplers, or fluctuations in the power of the broadband light source have therefore no influence. This is an important aspect when considering long-term field measurements. Furthermore, the wavelength-encoded nature of the output facilitates wavelength division multiplexing. It allows the distribution of several gratings over a single optical fibre, by assigning each sensor to a different portion of the available spectrum of the light source. Remark that the measurement of the Bragg-wavelength depends on the stability and reproducibility of the employed interrogators. The measurement algorithm of the interrogator, however, is as important. The determination of the Bragg wavelength using a 'Full Width at Half Maximum' (FWHM) algorithm can differ from a Bragg wavelength determined by a centroid calculation algorithm. This is due to the influence of the grating characteristics (mainly uniformity of the spectral shape, amplitude) and the sampling density of the FBG spectrum, as well as on the uncertainty of the curve fit algorithm for the determination of the Bragg wavelength [3, 4]. In this work, the FWHM algorithm is used.

Thanks to their small size (down to 40 μm cladding diameter [5]), their corrosion resistance, and their insensitivity to electromagnetic interference, optical fibres have become more and more widespread in sensor applications. Strain measurement is one of the most important applications of FBG based sensor technology [6, 7]. For this application FBGs are well known to feature a high axial strain resolution.

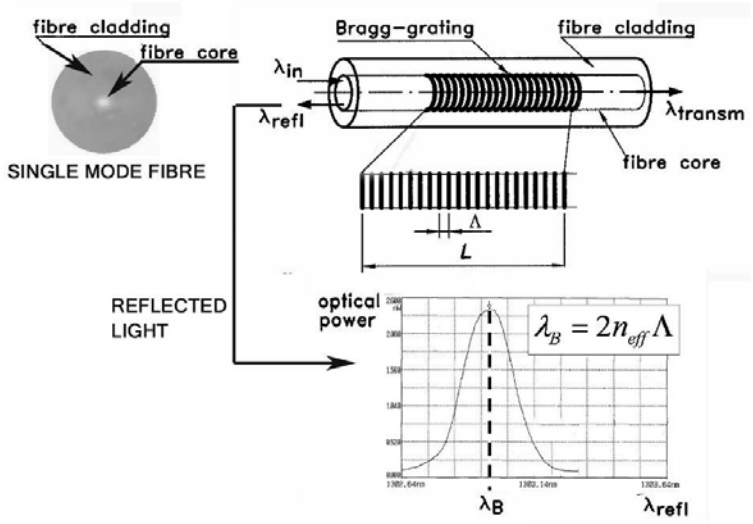

Figure 2-2: Schematic drawing of a Bragg-grating in a conventional single mode optical fibre. Also shown is a typical spectral response of such a grating after in-coupling of broadband light.

Strain measuring FBGs are mostly surface mounted with or without strain transduction mechanism [8, 9] and are assumed to be exposed to axial stress only. However, to monitor the structural health of complex materials such as fibre reinforced plastics, it is necessary to map the complete stress/strain field inside the material, and more particularly the transversal stress/strain components are of high interest because they can cause catastrophic damage such as delamination [10]. It should be noted that for this purpose, optical fibres can be embedded in composite materials without compromising the structural integrity of the host material [11].

In the next section of this chapter the author first determines the theoretical effect of a (multi-axial) strain field on the impermeability tensor of an isotropic optical fibre, which is also called the photo-elastic effect. Following, this photo-elastic effect is used to determine the spectral response of an FBG to a multi-axial strain field. In addition, the temperature response is discussed. In a following section, several commonly used types of optical fibres in which a Bragg grating can be written are discussed. Finally, a proper calibration method, to determine the FBGs axial and transversal strain sensitivity as well as their temperature sensitivity, is discussed.

2. 2. RESPONSE TO STRAIN OF NON-EMBEDDED FBGS

Figure 2-3 shows the orthogonal coordinate system used in this work. The *1'*- and *2'*-axes are in transverse directions while the *3'*-axis is aligned with the axis of the

optical fibre. The ‘ is used to avoid confusion with the coordinate system of a single layer of a composite laminate which will be defined in a forthcoming chapter.

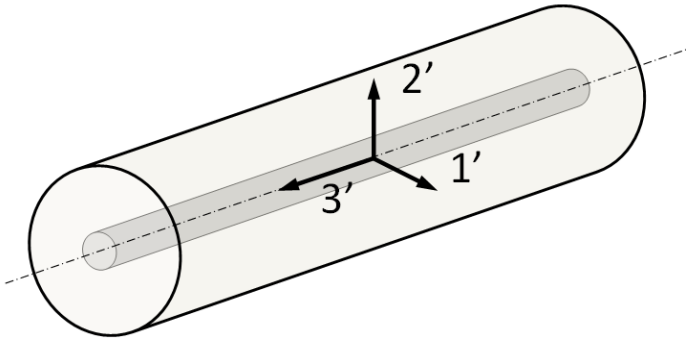

Figure 2-3: The used coordinate system of an optical fibre.

2. 2. 1. The photo-elastic effect of an isotropic optical fibre

The photo-elastic effect can be described as the property of certain materials to become optically anisotropic once mechanical stress/strain is applied to the material [12]. This phenomenon is also referred to as stress birefringence or mechanical birefringence.

An application of the photo-elastic effect, in general, is the visualization of mechanical stresses in photo-elastic materials (like some epoxies, polymethylmetacrylate, …). This method was very popular in the beginning of the twentieth century and was used to visualize plane stress situations. A prototype, a replica or a scale model of the real structure was made of photo-elastic material and subjected to similar anticipated loads as for the finished structure. As such, the maximum stress regions could be observed, which could lead to a redesign of the structure.

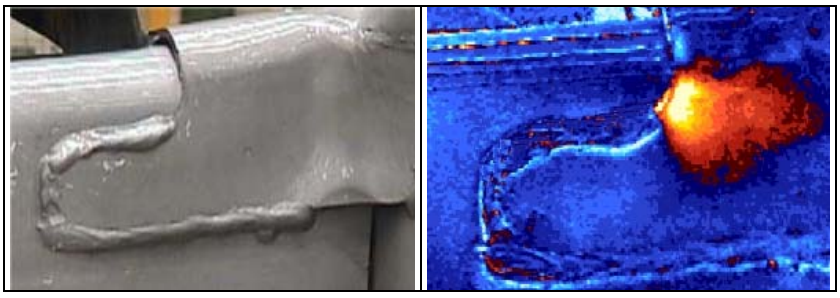

Figure 2-4: A thin photo-elastic coating is put on a weld (left) and analysed using polarized light to visualize the photo-elastic fringes (right) [13].

A quick and simple approach to photo-elastic analysis involves applying a thin epoxy coating onto a metal, glass or plastic component or even a model of a component. When the component is loaded, stresses are transmitted into the coating and when viewed under polarized light, photo-elastic fringes can be observed and analyzed. This method can be used to very quickly identify load paths within a structure as well as determining areas of stress concentration which could lead to a potential fatigue failure. For example in Figure 2-4: a thin photo-elastic coating is put on a weld (left) and analyzed using polarized light to visualize the photo-elastic fringes (right) [13]. For more information on this topic the reader is pointed to the specialized literature (e.g. [14, 15]).

In this work, only strain birefringence of a glass optical fibre is discussed. Once mechanical strain is applied to the optical fibre, the refractive index of the glass fibre will alter. In which form this happens is discussed below.
In general, the change in the optical impermeability tensor ($\Delta\eta_{ij}$) of a material depends on the strain tensor (ε_{kl}) and the so-called strain-optic tensor (p_{ijkl}) [12].

$$\Delta\eta_{ij} = \Delta\left(\frac{1}{n^2}\right)_{ij} = p_{ijkl}\varepsilon_{kl} \qquad \textbf{2-3}$$

$$\eta_{ij} = \eta_{ij}^{(0)} + p_{ijkl}\varepsilon_{kl} \qquad \textbf{2-4}$$

Where $\eta_{ij}^{(0)}$ is the initial impermeability tensor. Since both η_{ij} and ε_{kl} are symmetric tensors, the indices *i* and *j* as well as *k* and *l* can be permuted. As such, the contracted indices can be used in the notation. Equation 2-3 then becomes:

$$\Delta\left(\frac{1}{n^2}\right)_i = p_{ij}\varepsilon_j \quad i,j = 1,2,\ldots,6 \qquad \textbf{2-5}$$

The form of the strain–optic tensor depends on the symmetry of the material. For isotropic materials (e.g. fused silica) this tensor will contain only two independent coefficients (p_{11} and p_{12} in Equation 2-6).

$$\begin{bmatrix} \Delta\left(\frac{1}{n^2}\right)_1 \\ \Delta\left(\frac{1}{n^2}\right)_2 \\ \Delta\left(\frac{1}{n^2}\right)_3 \\ \Delta\left(\frac{1}{n^2}\right)_4 \\ \Delta\left(\frac{1}{n^2}\right)_5 \\ \Delta\left(\frac{1}{n^2}\right)_6 \end{bmatrix} = \begin{bmatrix} p_{11} & p_{12} & p_{12} & 0 & 0 & 0 \\ p_{12} & p_{11} & p_{12} & 0 & 0 & 0 \\ p_{12} & p_{12} & p_{11} & 0 & 0 & 0 \\ 0 & 0 & 0 & \frac{1}{2}(p_{11}-p_{12}) & 0 & 0 \\ 0 & 0 & 0 & 0 & \frac{1}{2}(p_{11}-p_{12}) & 0 \\ 0 & 0 & 0 & 0 & 0 & \frac{1}{2}(p_{11}-p_{12}) \end{bmatrix} \begin{bmatrix} \varepsilon_1 \\ \varepsilon_2 \\ \varepsilon_3 \\ \varepsilon_4 \\ \varepsilon_5 \\ \varepsilon_6 \end{bmatrix} \quad \textbf{2-6}$$

Because the index perturbations due to the photo-elastic effect are small (0.2% change for 1% longitudinal strain) we can use the relationship $dn = -\frac{1}{2}n^3 d(\frac{1}{n^2})$ to rewrite Equation 2-6:

$$\Delta(n)_i = -\frac{n_i^3}{2} p_{ij}\varepsilon_j \quad i,j = 1,2,\ldots,6 \qquad \textbf{2-7}$$

Thus, the perturbation of the refractive index is proportional to the magnitude of the applied strain.

The strain optic coefficients for pure bulk silica were found to be p_{11} = 0.121 and p_{12} = 0.270 [12, 16] (measured at a wavelength of 630 nm). However, due to the presence of dopant elements in the core (usually GeO2) and/or in the cladding of glass fibres, the effective values may differ up to 7%. For example, measurements on single-mode fibres (at the same wavelength as above) yielded values of p_{11} = 0.113 ± 0.005 and p_{12} = 0.252 ± 0.005 [17]. These values were measured based on two photo-elastic experiments, namely the polarimetric measurement of optical activity induced by mechanical twist, and the interferometric measurement of optical path length change induced by static longitudinal strain. In these experiments and calculations the Poisson's ratio was assumed to be $\nu_f = 0.16 \pm 0.01$ and the effective refractive index $n_{eff} = 1.458$. In section 2. 4. 1. c., the coefficients p_{11} and p_{12} were determined experimentally using an FBG written in a single-mode fibre: $p_{11} = 0.111 \pm 0.008$ and $p_{12} = 0.247 \pm 0.017$ [18]. Not only the strain optic coefficients of the optical fibre are known to vary depending on the concentration of GeO_2 expressed in %mol. Other parameters are the refractive index, the thermal expansion coefficient, the thermo-optic coefficient, the Young's modulus, and the

Poisson's ratio of the optical fibre. This should be considered important in terms of advanced modelling of the optical fibre.

It should be noted that the principal axes of birefringence of a material coincide with the principal axes of the strain tensor. In addition, when measuring with optical FBG sensors, it will not be possible to measure shear deformations (ε_4 , ε_5 , and ε_6), as these have no effect on the first two impermeability values and as such on the refractive indices of the fibre. Therefore, a good orientation and positioning of the sensor is necessary (see Chapter 5).

2. 2. 2. Spectral response of an FBG to a multi-axial strain field

As mentioned before in Equation 2-1, the Bragg wavelength depends on the effective index of refraction (n_{eff}) and on the pitch (Λ) of the grating. Both the refractive index and the pitch will be affected by applied mechanical strain as well as by temperature. As such, under the assumption of isothermal condition ($\Delta T = 0$), the Bragg-condition can be written as:

$$\lambda_B\left(\varepsilon\right) = 2n_{eff}\left(\varepsilon\right)\Lambda\left(\varepsilon\right) \qquad \textbf{2-8}$$

where $\varepsilon = \left[\varepsilon_{1'}, \varepsilon_{2'}, \varepsilon_{3'}\right]^T$ are the strain components along the axes of the used coordinate system (Figure 2-3); the strain components $\varepsilon_{4'}$, $\varepsilon_{5'}$ and $\varepsilon_{6'}$ have no influence neither on n_{eff} nor on Λ [19]. Supposing that a change in strain state occurs, following:

$$\varepsilon_i = \varepsilon_{i,0} + \Delta\varepsilon_i \qquad i = 1,2,3 \qquad \textbf{2-9}$$

By substitution of $2n_{eff}\left(\varepsilon_{i,0}\right) = \dfrac{\lambda_B\left(\varepsilon_{i,0}\right)}{\Lambda\left(\varepsilon_{i,0}\right)}$ and $2\Lambda\left(\varepsilon_{i,0}\right) = \dfrac{\lambda_B\left(\varepsilon_{i,0}\right)}{n_{eff}\left(\varepsilon_{i,0}\right)}$, Equation 2-2 can be transformed into:

$$\frac{\Delta\lambda_B\left(\Delta\varepsilon\right)}{\lambda_B\left(\varepsilon_{i,0}\right)} = \left[\frac{\partial\Lambda\left(\Delta\varepsilon\right)}{\Lambda\left(\varepsilon_{i,0}\right)\partial\Delta\varepsilon_i}\Delta\varepsilon_i\right] + \left[\frac{\partial n_{eff}\left(\Delta\varepsilon\right)}{n_{eff}\left(\varepsilon_{i,0}\right)\partial\Delta\varepsilon_i}\Delta\varepsilon_i\right] \qquad \textbf{2-10}$$

The first component of the equation is the change of the pitch due to the deformation of the fibre. The second one is the change of the refractive index. Using Equation 2-6, Equation 2-10 can be rewritten as

$$\frac{\Delta\lambda_{B,1'}}{\lambda_{B,0}} = \varepsilon_{3'} - \frac{1}{2} n_{eff,1'}^2 \left[p_{11}\varepsilon_{1'} + p_{12}\left(\varepsilon_{2'} + \varepsilon_{3'}\right)\right]$$
$$\frac{\Delta\lambda_{B,2'}}{\lambda_{B,0}} = \varepsilon_{3'} - \frac{1}{2} n_{eff,2'}^2 \left[p_{11}\varepsilon_{2'} + p_{12}\left(\varepsilon_{1'} + \varepsilon_{3'}\right)\right] \quad \textbf{2-11}$$

Where $\varepsilon_{1'}$, $\varepsilon_{2'}$, and $\varepsilon_{3'}$ are the principal strains of the fibre according to the coordinate system of Figure 2-3. The wavelength shift of light travelling according to both (*1'* and *2'*) axes will differ due to a different change of the refractive index induced by the strain field present in the core of the optical fibre. This could lead to a spectrum which can become broader than the original one or even split into two distinct peaks (e.g. Figure 2-35).
In the specific case that only axial stress ($\sigma_{3'}$) is applied on the fibre, the transversal strains ($\varepsilon_{1'}$, $\varepsilon_{2'}$) are a fraction of the axial strain ($\varepsilon_{3'}$):

$$\varepsilon_{1'} = \varepsilon_{2'} = -\nu_f \varepsilon_{3'} \quad \textbf{2-12}$$

Filling in the values for the transversal strain components in Equation 2-11 the well known equation for the response of an non-embedded FBG subjected to axial stress is obtained [2]:

$$\frac{\Delta\lambda_{B,1'}}{\lambda_{B,0}} = \frac{\Delta\lambda_{B,2'}}{\lambda_{B,0}} = (1-P)\varepsilon_{3'} \quad \textbf{2-13}$$

In which *P* is the strain optic constant,

$$P = \frac{1}{2} n_{eff}^2 \left[p_{12} - \nu_f \left(p_{11} + p_{12} \right)\right] \quad \textbf{2-14}$$

Substitution of p_{11} = 0.113 ± 0.005 and p_{12} = 0.252 ± 0.005 [17] in Equation 2-13 and 2-14 gives a value of the strain-optic coefficient P = 0.21. As such, the anticipated strain sensitivity for an FBG in the C-band (e.g. 1550 nm) will be 1.2 pm/με.

2. 2. 3. Response to temperature

Under the assumption of a strain free condition ($\varepsilon_i = 0$), Equation 2-2 becomes

$$\Delta\lambda_B = 2\left(n_{eff} \frac{\partial\Lambda}{\partial T} + \Lambda \frac{\partial n_{eff}}{\partial T} \right)\Delta T \quad \textbf{2-15}$$

Equation 2-14 represents the effects of temperature on the Bragg wavelength. A temperature increase causes a thermal expansion of the fibre with Bragg grating (and

thus a change of its pitch) and also a change in the refractive index. This fractional wavelength shift for a small temperature change ΔT may be written as:[2]

$$\begin{aligned}\Delta\lambda_B &= \lambda_B\left(\alpha_f + \alpha_n\right)\Delta T \\ &= \lambda_B \beta \Delta T\end{aligned} \qquad \textbf{2-16}$$

where $\alpha_f = \frac{1}{\Lambda}\frac{\partial\Lambda}{\partial T}$ is the thermal expansion coefficient of the optical fibre (approximately 0.55 x 10^{-6} 1/K for silica [20]). The quantity $\alpha_n = \frac{1}{n_{eff}}\frac{\partial n_{eff}}{\partial T}$ represents the so-called **thermo-optic coefficient**, which is dependent on the type of dopant(s) and the concentration of dopant(s). Values between 3.0 x 10^{-6} [21] and 8.6 x 10^{-6} 1/K for a germania-doped, silica-core fibre have been reported [22]. The coefficients α_f and α_n can be combined in the so-called **temperature coefficient** β. Clearly the index change is by far the dominant effect. From Equation 2-16 it can be calculated that the temperature sensitivity of an FBG with a thermo-optic coefficient of 5.9 x 10^{-6} 1/K [23] in the C-band (e.g. 1550 nm) is ~10 pm/K.

It now becomes apparent that any change in wavelength, associated with the action of an external perturbation to the grating, is the sum of mechanical deformation and temperature terms. Therefore, in sensing applications where only one perturbation is of interest, the deconvolution of temperature and strain becomes necessary!

2. 3. TYPES OF GLASS OPTICAL FIBRES USED FOR FBG SENSORS

2. 3. 1. Low birefringent fibres

The first type of fibre is a standard telecom single mode optical fibre. Such a fibre typically consists of a core of a few micrometers surrounded by a cladding with an external diameter of 80 to 125 µm. In Figure 2-5 an 80 µm draw tower fibre (highly Ge-doped) is depicted with the reflection spectrum of an FBG written in the core of this fibre. Draw tower fibre Bragg gratings are written directly during the drawing process of the optical fibre, using one single laser pulse with a special FBG inscription set-up, which is mounted onto the fibre draw tower.

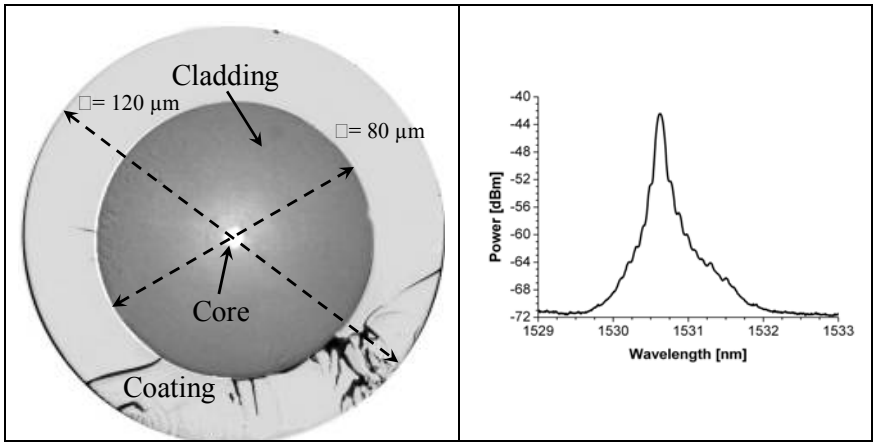

Figure 2-5: Left, typical cross section of a low birefringent fibre. Right, the spectral response of an FBG written in its core.

2. 3. 2. High birefringent fibres

As shown in Figure 2-8 and Figure 2-11, an FBG in a high birefringent (HiBi) fibre returns two distinct Bragg peaks, each of which corresponds to one of the two propagating orthogonally polarized modes. Both modes fulfil the Bragg condition for a different effective refractive index, leading to two Bragg wavelengths.

$$\lambda_{B,fast} = 2\left(n_{eff} - \frac{B}{2} \right)\Lambda$$
$$\lambda_{B,slow} = 2\left(n_{eff} + \frac{B}{2} \right)\Lambda \qquad \textbf{2-17}$$

The subscripts slow and fast denote the two orthogonally polarized modes propagating in the birefringent fibre, $\lambda_{B,slow}$ and $\lambda_{B,fast}$ are their corresponding Bragg peak wavelengths, B the phase modal birefringence at $\lambda_{B,mean} = \frac{\left(\lambda_{B,slow} + \lambda_{B,fast}\right)}{2}$ and n_{eff} is the mean effective refractive index of both polarization modes in the grating zone at the same wavelength. Clearly the Bragg peak separation depends on the phase modal birefringence (Equation 2-17). The high birefringent fibre can be subdivided in two main groups i.e. the stress and shape induced birefringent fibres, and the micro-structured fibres.

2. 3. 2. a. Stress and shape induced birefringence

For this type of fibres, the internal birefringence of the glass fibre is produced either by a geometric effect of the core (shape induced birefringence) or by a stress effect

around the core [24, 25]. In the first case birefringence is induced whenever the circular shape of the core is modified (e.g. elliptical core [26], Figure 2-6). In the second case, birefringence is generated through the use of stress applying parts (SAPs) introduced in the cladding of the optical fibre. Due to the differences in thermal expansion coefficients between the (in most cases with Boron) doped SAP regions and the cladding, a residual stress field occurs in the core during the cooling phase of the fibre's pulling process. This residual stress induces the birefringence of the glass fibre core via the elasto-optic effect. The difference in Bragg wavelength for both polarization modes (Equation 2-11) can be written as:

$$\Delta\lambda_{B,2'} - \Delta\lambda_{B,1'} = \frac{n_{eff}^2}{2}\left(p_{12} - p_{11}\right)\left(\varepsilon_{2'} - \varepsilon_{1'}\right)\lambda_{B,0} \qquad \textbf{2-18}$$

Based on Equation 2-18, we can determine the (net) residual strains necessary to obtain a certain peak split of the spectrum.

$$\varepsilon_{2'} - \varepsilon_{1'} = \varepsilon_{R,0} = \frac{4}{n_0^2}\frac{\lambda_{B,2'} - \lambda_{B,1'}}{\left(\lambda_{B,1'} + \lambda_{B,2'}\right)\left(p_{12} - p_{11}\right)} \qquad \textbf{2-19}$$

In which

$$\begin{aligned} \lambda_{B,1'} &= \lambda_{B,0} + \Delta\lambda_{B,1'} \\ \lambda_{B,2'} &= \lambda_{B,0} + \Delta\lambda_{B,2'} \end{aligned} \qquad \textbf{2-20}$$

The birefringence is literally frozen in the core of the optical fibre. Elliptical cladding fibres, Panda fibres, and bow-tie fibres are examples of such stress induced high birefringent fibres. Figure 2-6 gives an overview of common stress and shape induced high birefringent fibres [27]. For each type of fibre both polarization axes (slow and fast) are shown.

Since in this dissertation only FBGs written in bow-tie fibre were used, the author will focus on this type. Figure 2-7 shows the coordinate system of the used HiBi fibre. The slow axis is the 1'-axis while the fast axis equals the 2' axis in this figure. A cross section of a 80 µm birefringent bow-tie fibre with FBG from Fibercore inc.([20]) together with its Bragg spectrum is shown in Figure 2-8. The birefringence in this fibre is induced by moon shaped SAPs of boron-doped silica present in the fibre cladding. The temperature expansion coefficient of these 10 mol% boron-doped parts differs significantly from the temperature expansion coefficient of the fibre core and cladding (Table 2-1). This results in temperature induced stress during the cooling phase of the manufacturing process which in turn induces material birefringence in and around the core. At a wavelength of 1550 nm, the phase modal birefringence in this bow-tie fibre is 3×10^{-4}.

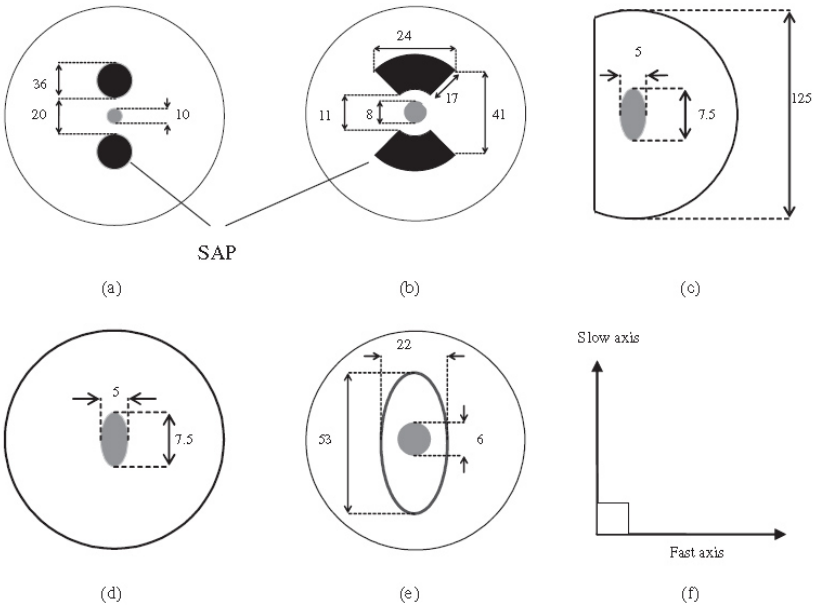

Figure 2-6: HiBi fibre cross-sectional geometry: (a) Panda and true Phase fibres, (b) bow-tie fibre, (c) D cladding and elliptical core fibre, (d) elliptical core fibre, (e) elliptical cladding and (f) polarization axes configuration.[27]

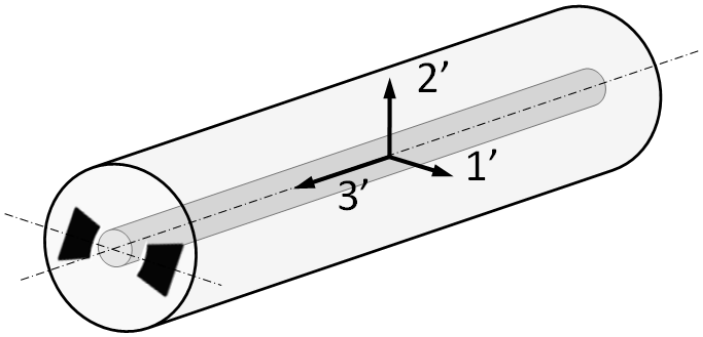

Figure 2-7: The used coordinate system of a bow-tie high birefringent fibre.

Table 2-1: Mechanical properties of the bow-tie fibres used in this dissertation [28]

	Young's modulus E (GPa)	Poisson's ratio ν (-)	Coefficient of thermal expansion α (1/°C)
Silica	70	0.17	$5.5*10^{-7}$
Borosilicate	51	0.21	$14*10^{-7}$

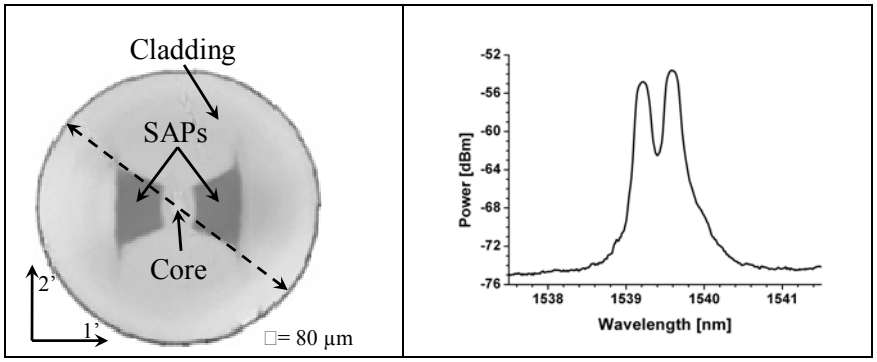

Figure 2-8: Typical cross section of a high birefringent bow-tie fibre, with the spectral response of an FBG written in its core.

According to Okamoto [29] finite element methods have the most potential for modeling the complicated stress distributions for any kind of HiBi optical fibres. Therefore, using the mechanical properties of the bow-tie fibre listed in Table 2-1, a linear elastic finite element simulation model was built to estimate the effect of geometrical parameters of the SAPs on the residual strain field in the core of the fibre and as such on the birefringence (Figure 2-9). The FE model exists of ~10300 linear triangular elements (CPE3T). In the simulations, the mechanical properties were kept constant because of their unknown thermal variation. A temperature drop is chosen in such a manner that the simulated residual strains agree with the actual ones which can be calculated using the wavelengths of the fast and the slow axes (Equation 2-18). When cooling the fibre, stresses will be created due to the difference in the thermal expansion of the silica fibre and the SAPs. Only changing the distance of the SAPs with regard to the core already leads to a significantly different strain field (Figure 2-9) and thus stress induced birefringence (Figure 2-10). By diametrically loading the model in ABAQUS^{TM}, a calibration curve (wavelength shift as function of applied load) is obtained (see section 2. 4. 1. c.).

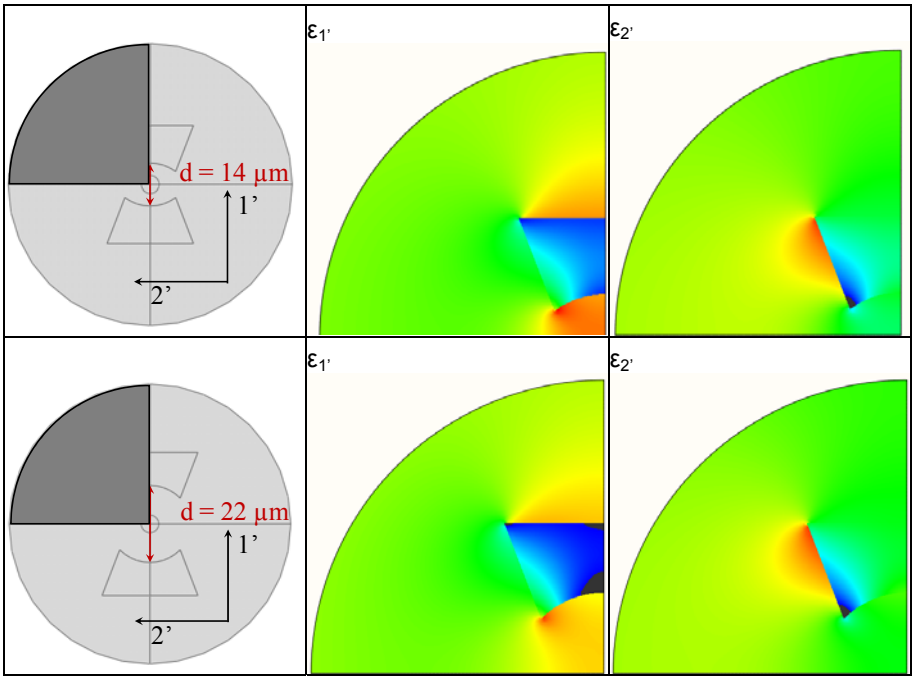

Figure 2-9: Two configurations of a 2D FE model of an 80 µm bow-tie fibre. In the lower case the distance between the SAPs and the core of the fibre is significantly different, which leads to a different induced strain field in the core of the optical fibre.

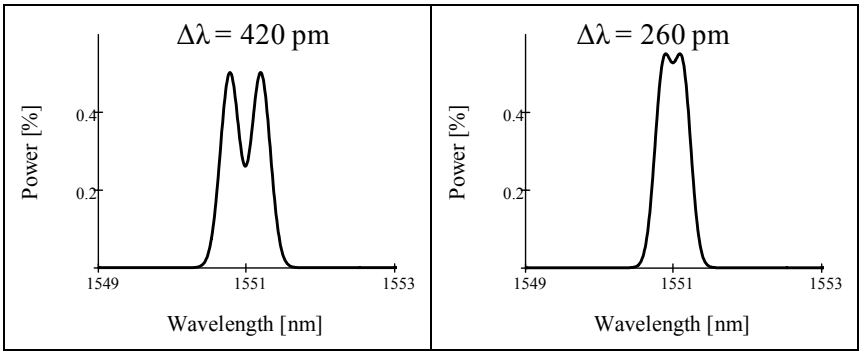

Figure 2-10: Resulting spectra of an FBG in two different types of bow-tie fibre.

2. 3. 2. b. Micro-structured fibre

A completely different type of fibre in which FBGs can be shot, is a micro-structured optical fibre (MOF FBG). In contrast to conventional (step-index) fibres, light in these fibres is confined to the centre of the fibre by a (periodic) pattern of air holes around the core. The position, the shape and the size of these air holes can be

tailored with an unprecedented freedom of design [30]. This makes it possible to achieve dedicated properties for the light that is guided in the fibre core [31, 32], e.g. the phase modal birefringence in the MOF studied here was measured to be 8×10^{-4} at a wavelength of 1550 nm. The microstructure of the MOF shown in Figure 2-11 was described in [33]. The fabrication of FBGs in micro-structured fibres is not always straightforward, because the numerous air-silica interfaces compromise the ability to form an interference pattern in the core with transversal laser inscription beams. Nevertheless, the compatibility of this particular type of micro-structured fibres with conventional UV FBG inscription set-ups was demonstrated in [34]. More information on this fibre can be found in Chapter 6.

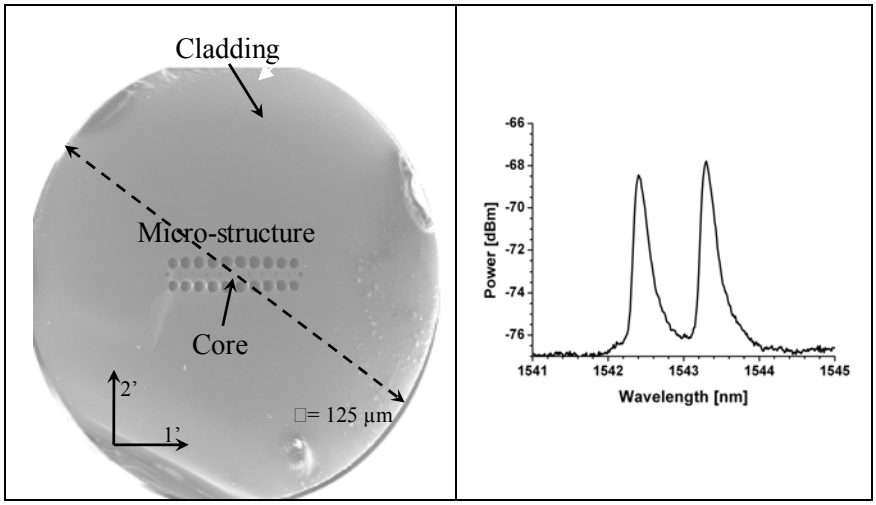

Figure 2-11: Typical cross section of a high birefringent micro-structured fibre, with the spectral response of an FBG written in its core.

2. 3. 3. Bandwidth of the Bragg peak

Different types of fibres with typical Bragg spectra were discussed in the previous paragraphs. These spectra are significantly different from each other with regard to the Bragg peak separation of the FBG. Another aspect that defines the shape of the spectrum is the bandwidth of the Bragg peaks. The bandwidth of the peaks is mainly defined by the length of the inscribed grating. Figure 2-12 represents a simulated reflection spectrum of an FBG of 3 mm length inscribed in a fibre with a $3.2\ 10^{-4}$ birefringence [35]. The obtained separation between the two peaks is 0.3 nm. Because of the short length of the grating, the peaks are wide and thus they overlap slightly. To show the influence of the grating length on the separation peaks three FBGs with different lengths (2.5 mm, 3 mm, 8 mm) were simulated in a HiBi fibre with the same birefringence ($3.2\ 10^{-4}$) [36]. Since the reflectivity of the FBG spectra

depends on the length of the grating and the index modulation (δn), the author adjusted the δn of the gratings so as to have the same reflectivity of the FBG. We can see clearly that for the 2.5 mm grating length the peaks overlap and to make a distinction between the peaks one should use polarized light oriented parallel to each axis. In the case of the 3 mm grating the peaks are still overlapping but the two peaks are already distinguishable. For the 8 mm grating the two peaks are well separated, even with a birefringence of 3.2 10^{-4}. An even longer FBG length will give a better peak separation, however, the grating becomes too large and cannot longer be considered as a point sensor.

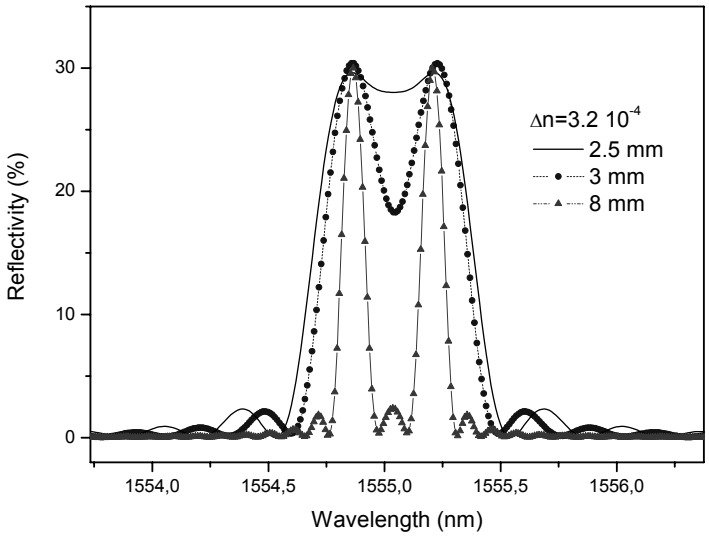

Figure 2-12: Simulated reflectivity spectra of three FBGs in HiBi fibre of 3.2 10^{-4} birefringence and different grating lengths: 2.5 mm (straight line), 3 mm (circle) and 8 mm (triangles). [36]

2. 4. STRAIN CALIBRATION OF FIBRE BRAGG GRATINGS

Whenever FBGs are used as a sensor to determine one or several components of the strain present in a material, the strain sensitivities (pm/με) of the sensor need to be determined. According to Equation 2-20 which was found in section 2. 2. 2. we have to determine the strain optic coefficients (p_{11} and p_{12}) to completely define the strain dependency of a fibre Bragg grating.

$$\frac{\Delta\lambda_{B,1'}}{\lambda_{B,0}} = \varepsilon_{3'} - \frac{1}{2} n_{eff,1'}^2 \left[p_{11}\varepsilon_{1'} + p_{12}\left(\varepsilon_{2'} + \varepsilon_{3'}\right)\right]$$
$$\frac{\Delta\lambda_{B,2'}}{\lambda_{B,0}} = \varepsilon_{3'} - \frac{1}{2} n_{eff,2'}^2 \left[p_{11}\varepsilon_{2'} + p_{12}\left(\varepsilon_{1'} + \varepsilon_{3'}\right)\right] \quad \textbf{2-21}$$

Several calibration methods are discussed in the upcoming paragraphs, starting with the transverse strain calibration. Such a calibration method induces the most simple strain state in the core of the fibre (only two transverse strain components). A longitudinal calibration method (paragraph 2.4.2) induces a three-axial strain field.

2. 4. 1. Transverse strain calibration

2. 4. 1. a. Strain in the core of an SM optical fibre due to a pure diametrical compression.

When a single mode optical fibre (isotropic) is diametrically brought into contact with a pressure plate they initially touch along a line. Under the action of the slightest load they deform in the vicinity of their point of first contact so that they touch over an area which is finite though small compared with the dimensions of the two bodies (Figure 2-13). A theory of contact is required to predict the shape of this contact region and how it grows in size with increasing load [37]. With this theory, components of deformation and stress in the optical fibre can be calculated in the vicinity of the contact region.

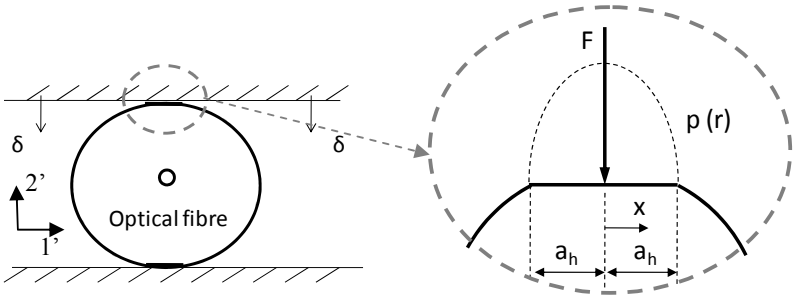

Figure 2-13: A cylindrical optical fibre is loaded in compression (F) by a rigid body. As a result, a certain stress distribution p(r) is created at the contact interface.

The compressive load per unit axial length (F) gives rise to a Hertzian distribution of pressure.

$$p = \sqrt{\frac{2F}{\pi a_h}\left(1 - x^2 \Big/ a_h^2\right)} \qquad \textbf{2-22}$$

in which the semi-contact-width is defined by

$$a_h = \sqrt{2FD_f \Big/ \pi E_f} \qquad \textbf{2-23}$$

Where E_f is the composite modulus of the optical fibre and the contacting body and D_f the diameter of the optical fibre. With this pressure distribution, the stress distribution in the centre of the optical fibre due to diametrically opposed concentrated loads can be calculated [38]. It comprises the superposition of the stress fields due to two concentrated forces F (Figure 2-13) acting on the plane boundaries of two half spaces tangential to the cylinder.

$$\sigma_{1'} = 2\frac{F}{\pi D_f} \qquad \sigma_{2'} = -6\frac{F}{\pi D_f} \qquad \textbf{2-24}$$

Once the stress is known, the values of the strain state can be found from Hooke's law for plane strain [39].

$$\varepsilon_{2'} = \left(\frac{1-\upsilon_f^2}{E_f}\right)\left(\sigma_{2'} - \frac{\sigma_{1'}\upsilon_f}{1-\upsilon_f}\right) \qquad \varepsilon_{1'} = \left(\frac{1-\upsilon_f^2}{E_f}\right)\left(\sigma_{1'} - \frac{\sigma_{2'}\upsilon_f}{1-\upsilon_f}\right) \qquad \textbf{2-25}$$

If a theoretical load of $F = 1N \Big/ mm$ is applied on the optical fibre which has a Young's modulus of $E_f = 70GPa$ and a Poisson's ratio of $\upsilon_f = 0.17$ one can determine the strains induced in the core of the optical fibre.

Table 2-2: The strain induced in the core of a 125 µm or 80 µm fibre due to a diametrically applied load

	$\sigma_{1'}$ [MPa]	$\sigma_{2'}$ [MPa]	$\varepsilon_{1'}$ [$\mu\varepsilon$]	$\varepsilon_{2'}$ [$\mu\varepsilon$]
$D_f = 125\mu m$	4.71	-14.14	105.6	-209.6
$D_f = 80\mu m$	7.95	-23.86	178.2	-353.7

By applying a diametric load on an axi-symmetric fibre, a state of plane strain ($\varepsilon_{3'} = 0$) is produced. Thus, during calibration both wavelengths (Equation 2-21) are only influenced by the transversal strains and can be reduced to

$$\frac{\Delta\lambda_{B,1'}}{\lambda_{B,1'}} = -\frac{1}{2} n_{eff,1'}^2 \left[p_{11}\varepsilon_{1'} + p_{12}\varepsilon_{2'} \right]$$
$$\frac{\Delta\lambda_{B,2'}}{\lambda_{B,2'}} = -\frac{1}{2} n_{eff,2'}^2 \left[p_{11}\varepsilon_{2'} + p_{12}\varepsilon_{1'} \right] \qquad \textbf{2-26}$$

By diametrically loading the optical fibre and simultaneously measuring the wavelength shifts ($\Delta\lambda_{B,1'}, \Delta\lambda_{B,2'}$), the strain optic coefficients (p_{11} and p_{12}) can be determined or, vice versa, the theoretical wavelength shifts when using the experimentally determined strain optic coefficients (p_{11} = 0.113 and p_{12} = 0.252) of Bertholds and Dändliker [17]. Using these values and knowing that the refractive index equals $n_{eff} = 1.456$ and $\lambda_{B,1'} = \lambda_{B,2'} = 1550nm$, the wavelength shifts become:

Table 2-3: The wavelength shifts of a 125µm or 80µm fibre due to a diametrically applied load

	$\frac{\Delta\lambda_{B,1'}}{F}$ $\left[\frac{nm}{(N/mm)}\right]$	$\frac{\Delta\lambda_{B,2'}}{F}$ $\left[\frac{nm}{(N/mm)}\right]$
$D_f = 125\mu m$	0.067	-0.0048
$D_f = 80\mu m$	0.113	-0.0081

If one aims at determining the strain optic coefficients in a precise way, one should take care of the following points:

- The small loads applied during the calibration experiment should be measured with a load cell with high accuracy.
- The loading stamp should lead to a good transfer of the load onto the optical fibre.
- A well known relation between applied load and induced strain in the core of the fibre is necessary. To calculate this relation accurate mechanical properties for the glass fibre are needed.

In the following paragraphs a literature overview is given of several calibration devices used to transversally calibrate an optical fibre with Bragg grating. Afterwards the authors' proposal is presented.

2. 4. 1. b. Diametrical compression test set-up

In what follows, the used coordinate system and notation of the cited authors have been adjusted to the orthogonal coordinate system of an optical fibre defined in

Figure 2-7. This was done in order to compare more easily the different cited solutions.

In literature, several designs for transverse strain calibrations are proposed; they can be subdivided into two main groups. The first group of authors uses a leverage arm to load the fibre, the other group is directly pressing the fibre. Both groups, however, designed an apparatus which produces a state of plane strain (axial strain is zero, $\varepsilon_{3'} = 0$) to simplify the strain state of the optical fibre core. This is necessary to be able to simply determine the strain optic coefficients out of Equation 2-26.

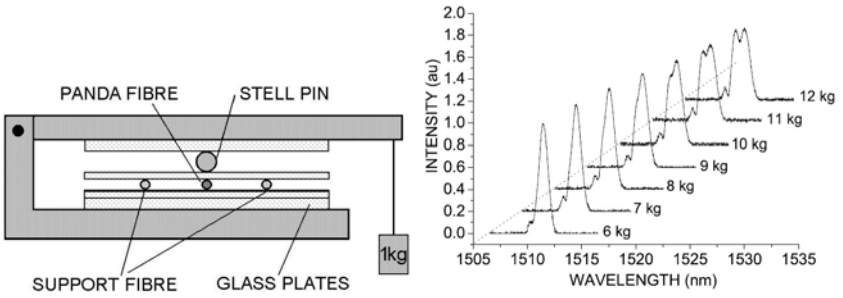

Figure 2-14: Left, calibration device designed by Abe et al. [40-43] using a leverage arm to load the fibre Bragg grating and two support fibres. Right, the first results of Abe et al. [43] when transversely loading the fibre up to 12kg.

Abe et al. [43] used a leverage arm to calibrate a Panda FBG (length = 1 mm) (Figure 2-14). Weights of different masses (1 to 12 kg) were suspended in the pivoted arm of the apparatus. The contact length between the optical fibre and the glass plates was 10 mm. Two support fibres and one Panda fibre have been used. A stell pin on a plate was used to transfer the load of the pivot arm onto the top of the fibre. If the stell pin was positioned exactly above the Panda fibre and both support fibres are at an equal distance of the stell pin, the load transferred to the fibre is the load transferred to the stell pin through the leverage arm divided by three. One can imagine the big errors which can be made using this set-up due to the indirect loading of the fibre. Additionally, support fibres as well as Panda fibre should have exactly the same diameter to avoid errors. Abe reported that the optical spectrum without load showed a single reflection peak with 1nm bandwidth and the spectra of the gratings began to change at 6kg of load. This is due to the length of the FBG (1mm) which reflects only a single peak of 1nm width (Figure 2-14).

In 2006 **Abe et al. [41],** repeated their experiments for an 80 µm bow-tie fibre, a standard 125 µm internal elliptical cladding (IEC) fibre, and a chemically etched 82 µm IEC fibre. It should be noted that the transverse strain is defined here as the

difference in strain along both polarization axis. The maximum and minimum strain sensitivity is given for each polarization mode.

Table 2-3: Comparing the strain sensitivities of FGBs written in an etched IEC fibre with FBGs written in commercially available HiBi-fibres [41]

		Spectral sensitivities	
		$\frac{\Delta\lambda_{B,slow}}{\Delta\varepsilon}$	$\frac{\Delta\lambda_{B,fast}}{\Delta\varepsilon}$
Fibre type (cladding diameter)	Load direction [Parallel to]	$\left[pm/\mu\varepsilon \right]$	$\left[pm/\mu\varepsilon \right]$
Etched IEC (82 µm)	Slow	-0.70	2.23
	Fast	3.40	-0.10
Bow-tie (80 µm)	Slow	-0.02	1.16
	Fast	1.20	0.3.
Standard IEC (125 µm)	Slow	-0.29	1.55
	Fast	7.02	1.02

In 1996 **Wagreich** et al. [38] used another set-up slightly different from that of Abe et al. [43] by eliminating one of the support fibres. As such, one is certain that both fibres will have contact with the pressure plate. A stainless steel rod is attached to an optical bench at the pivot point and the load is applied to the opposite end. This rod comes into point contact with a copper pin perpendicularly oriented to the steel rod. The copper pin is attached to an aluminum compression plate which is placed on top of two more copper pins and another polished aluminum plate to reduce the influence of bending moments on the load applied to the grating and to reduce the effects of micro-bending. The test fibre and a support fibre of equal diameter are situated on top of a glass plate and are stressed by the aluminum plate above them. The support fibre is added to keep the polished aluminum plate parallel to the glass plate, thereby producing diametrically opposed applied loads on the fibre. Both support fibre and test fibre have a length of 25 mm on which diametric load is applied.

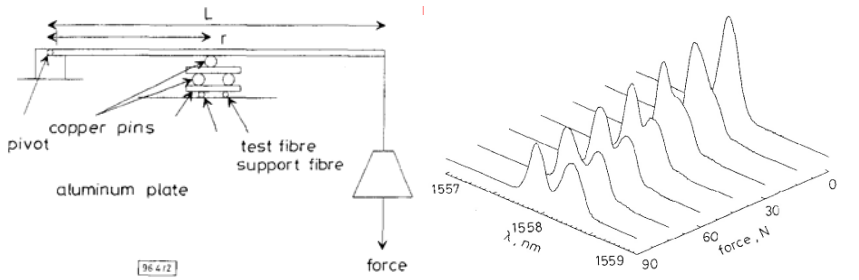

Figure 2-15: Left: the calibration device designed by Wagreich et al. using a leverage arm to load the fibre Bragg grating and one support fibre. Right: the results obtained by diametrically loading the fibre up to 90N. [38]

Wagreich et al. [38] recorded the spectra reflected by the grating for various applied loads. The resulting waterfall plot of the normalized reflected light intensity from the grating against wavelength and applied load is shown in Figure 2-15. Without load applied, the reflected spectrum has a single peak centered around the nominal Bragg wavelength. As the load is increased a broadening of the reflected spectrum could be observed until the split of the reflected intensity peaks becomes actually distinguishable at an applied load of 40 N. At that point, the intensity of light is split evenly between the two wavelength peaks, and integration of the total reflected power shows negligible loss even under very high loads. The load sensitivity was found to be:

$$\frac{\Delta\lambda_{B,1'}}{F} = 0.163\frac{nm}{(N/mm)}, \quad \frac{\Delta\lambda_{B,2'}}{F} = -0.0255\frac{nm}{(N/mm)} \qquad \textbf{2-27}$$

These values are higher than the theoretical obtained load sensitivity reported in the previous paragraph ($\frac{\Delta\lambda_{B,1'}}{F} = 0.067\frac{nm}{(N/mm)}$, $\frac{\Delta\lambda_{B,2'}}{F} = -0.0048\frac{nm}{(N/mm)}$). In the opinion of the author, this could be caused by differences in transferred load between the test and support fibre, due to misaligned copper pins.

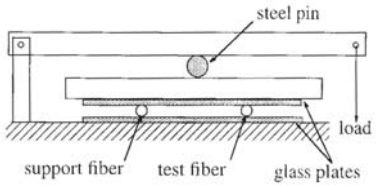

Figure 2-16: Calibration device designed by Lawrence et al. using a leverage arm to load the fibre Bragg grating and one support fibre.[44]

Several authors [40, 44-47] used a similar test set-up as Wagreich et al.[38]; however, they eliminated the copper pins to avoid extra errors (Figure 2-16). Lawrence et al. [44] calibrated HiBi optical fibres existing of an inner cladding, an elliptical stress applying region and an outer cladding. A schematic of the fibre and the measured peak response when the load is oriented $\theta = 75\,\text{deg}$ with respect to the 1'-axis is illustrated in Figure 2-17. The response for different orientations of the load $\theta = 0\ldots180\,\text{deg}$ is depicted in Figure 2-18.

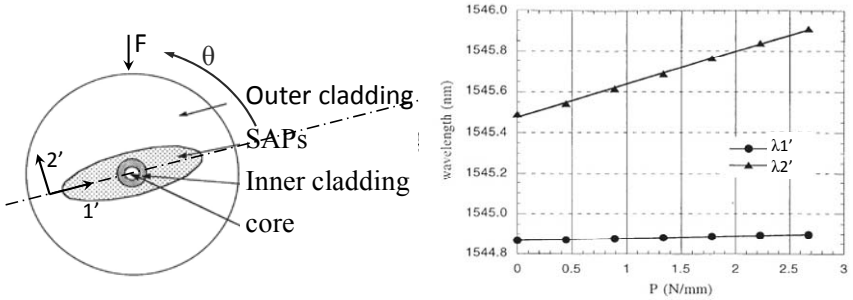

Figure 2-17: Left, schematic of an elliptical cladding HiBi optical fibre. Right, the diametrical compressive load response for this type of fibre when the load is oriented θ = 75° with respect to the 1'-axis. [44]

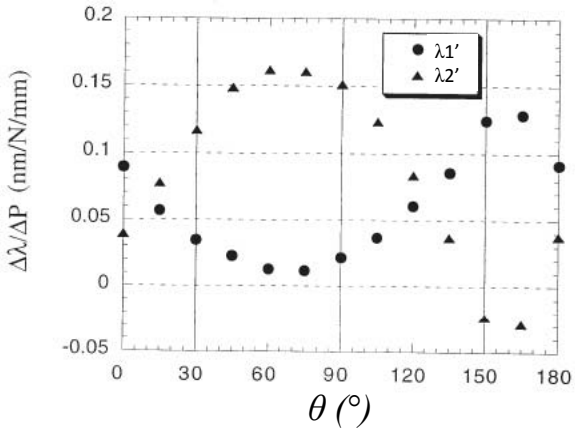

Figure 2-18: Sensor response of an elliptical cladding HiBi optical fibre as a function of angle (θ) of applied load. [44]

For some of the applied angles of rotation of the optical fibre, Lawrence et al. noticed a certain non-linearity in the peak response vs. the applied load. The possible explanation of rotation of the polarization axes due to the applied load has been proposed. For an unloaded elliptical cladding fibre, the orientation of the

principal optical axes is determined by the intrinsic birefringence generated by the elliptical stress applying region. Superimposed transverse loading will generate an additional extrinsic birefringence that may rotate the orientation of the principal optical axes.

In order to estimate the magnitude of the transverse strains applied to the fibre during these experiments, a finite element model was used to compute the average strain in the core of the optical fibre as a function of applied transverse load. A plane strain assumption was chosen because of the long contact length between the clamp and the fibre (25.4mm) relative to the fibre diameter (125 µm). Lo et al. [48] indicated that this plane strain assumption is valid because the length of the fibre is greater than a few centimeter.

Lawrence et al. [44] used the curves in Figure 2-18 to define a *K*-matrix which contains the strain sensitivities determined during the upper described calibration procedure.

$$\begin{bmatrix} \Delta\lambda_{B,2'} \\ \Delta\lambda_{B,1'} \end{bmatrix} = K \begin{bmatrix} \varepsilon_{2'} \\ \varepsilon_{1'} \end{bmatrix} \qquad \textbf{2-28}$$

In which $K = \begin{bmatrix} -370 & -742 \\ -963 & -587 \end{bmatrix} 10^{-6} \frac{nm}{\mu\varepsilon}$.

Compared to the theoretical values (section 2. 4. 1. a.) determined for a single mode fibre, these parameters are almost doubled (Equation 2-29).

$$K = \lambda_B \begin{bmatrix} -\frac{1}{2} n_0^2 p_{11} & -\frac{1}{2} n_0^2 p_{12} \\ -\frac{1}{2} n_0^2 p_{12} & -\frac{1}{2} n_0^2 p_{11} \end{bmatrix} = \begin{bmatrix} -185 & -412 \\ -412 & -185 \end{bmatrix} 10^{-6} \frac{nm}{\mu\varepsilon} \qquad \textbf{2-29}$$

in which $\lambda_B = \lambda_{B,1'} = \lambda_{B,2'}$.

A possible explanation is the misalignment of the force which can be overcome by using two test fibres instead of one combined with a dummy fibre and taking the mean response of both sensors.

Bosia et al. [45] used the same set-up to calibrate a bow-tie fibre and numerically checked the influence of the SAPs on the shape of the calibration curve. Figure 2-19 (a) shows that for a diametrical compression under a certain angle with the principal axis the wavelength shift is not linearly related to the diametrical compressive force. If a linear fitting is used on the wavelength shift vs. applied load big deformation of the calibration curve can be observed.(Figure 2-19 (b))

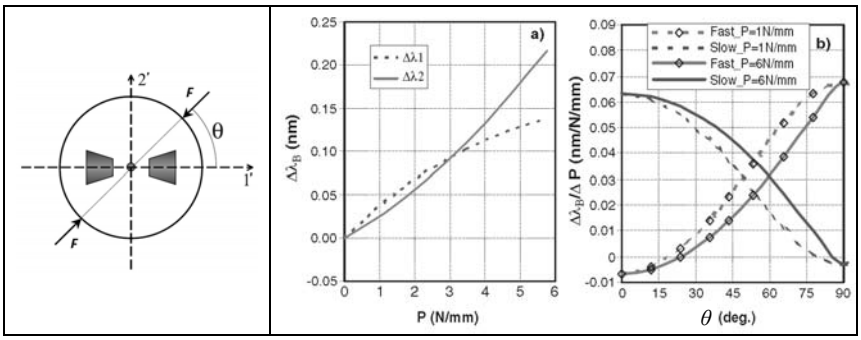

Figure 2-19: Left: schematic of a PM fibre subjected to diametrical compression. Right:(a) Numerically calculated Bragg wavelength shifts as a function of applied load for θ = 54 deg; (b) numerically calculated angular sensitivities of the PM-fibre sensor in diametrical compression, for F= 1 and 6 N mm^{-1}.

Experiments were executed and showed good similarity for the load sensitivity of the slow axis; the experimental load sensitivity for the fast axis is half of the one obtained via simulations. Assumed causes were investigated by changing the values of the Young's modulus of the Borosilicate bow-ties, however no satisfying results were found (Figure 2-20). Other possible explanations for the observed discrepancy are formulated as an oversimplified model of the loading configuration, or a displacement of the grating location in the core with respect to the geometrical centre of the fibre.

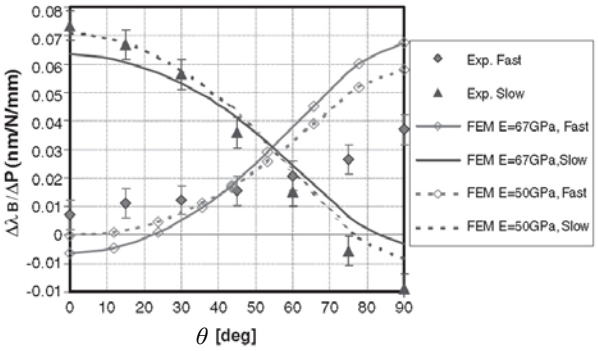

Figure 2-20: Comparison between the experimentally measured and numerically calculated angular sensitivities of the fast and slow axes of a bow-tie fibre sensor for a maximum diametrical compression of (P= 1N mm^{-1})

Mawatari et al. [49] altered the set-up of Lawrence et al. [44]. Their fixture employs two cantilever arms to magnify the forces generated by an offset cam driven by a

computer controlled stepper motor (Figure 2-21). A support (dummy) fibre and a test fibre containing a HiBi FBG were placed between two plates resting on a load cell. Guide pins (which can cause additional friction) were added to the loading block to prevent horizontal displacement of the plates. Transverse loading tests were conducted at different angles and over a range of loads up to 10 Nmm^{-1}. Data at an angle of 0 deg and 135 deg were used to determine a similar *K*-matrix as defined by Lawrence:

$$K = \begin{bmatrix} -294.4 & -377.7 \\ -275.8 & -277.7 \end{bmatrix} 10^{-6} \frac{nm}{\mu\varepsilon} \qquad \textbf{2-30}$$

However, bad results were obtained when using the gauge factors to determine the transverse strains (discrepancies from 10% to over 100% in cases where the magnitude of ε_1, and ε_2, was small). Mawatari et al. believed that the primary cause of these unacceptably large errors in predicting the strains from the wavelength shifts is the inadequacy of a linear model of $\Delta\lambda$ versus the transverse load at lower load levels.

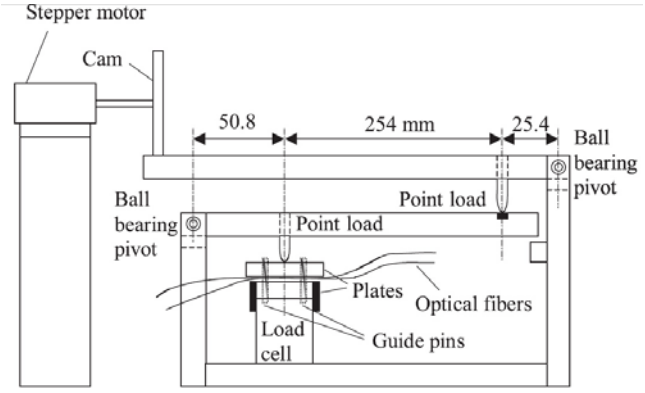

Figure 2-21: Calibration device designed by Mawatari et al. using a leverage arm to load the fibre Bragg grating and one support fibre. [49]

Ye et al. [50] and Chehura et al. [27] used a completely different calibration set-up without a leverage arm to transfer the load onto the optical fibre. The fixture is designed to minimize fibre rotation while applying load to the fibres. The load applied to the fibres (through a rotating screw) was measured using a FUTEK miniature load button with a capacity of 222 N. As in previous cases, two fibres were used. The test fibre can be positioned using two fibre rotators in order to assess the influence of the fibre orientation relative to the load direction.

Ye et al. [50] used the set-up to calibrate a bow-tie fibre (Figure 2-22). The measured load sensitivities and their standard deviations are plotted against the fibre

orientation in Figure 2-23. The transverse load sensitivities varied between -0.028 and 0.122 nm/(N/mm^{-1}) for the slow-axis mode. For the fast axis mode they varied between 0.016 and 0.056 nm/(N/mm). The amplitude of the load sensitivity variation with the fibre orientation for the slow-axis mode seems approximately two to three times higher than that for the fast-axis mode.

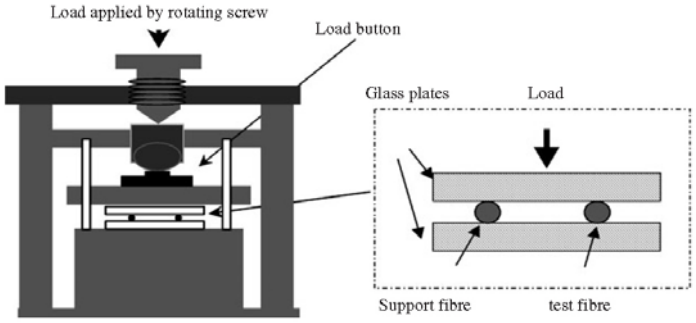

Figure 2-22: Calibration device designed by Ye et al. using a load stamp to load the fibre Bragg grating and one support fibre. [50]

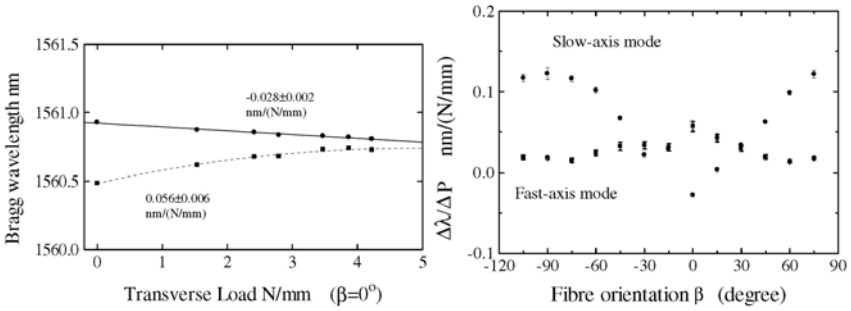

Figure 2-23: Left: the Bragg wavelength versus transverse loading for the PM FBG with a fibre orientation of 0 deg. Right: the transverse load sensitivities as a function of fibre orientation for the slow and fast-axis modes for the PM FBG. [50]

An extensive study was done by Chehura et al. [27] with the same set-up as Ye et al. [50]. They compared the sensitivities of different HiBi fibres (Figure 2-6) and tried to determine the most sensitive fibre type (Table 2-4). In this research only the load response of the different types of HiBi fibres were compared, as such it is difficult to compare the strain sensitivities of these fibres with the theoretically found values in 2. 4. 1. a..

Table 2-4: Maximum and minimum transverse load sensitivities of different HiBi FBG sensors for (a) slow and (b) fast axis [27].

(a)	Slow axis sensitivity (nm/(N/mm))	
Fibre type	Minimum	Maximum
D-clad	-0.030 ± 0.008	0.18 ± 0.02
Elliptical core	-0.011 ± 0.008	0.12 ± 0.01
TruePhase	-0.038 ± 0.009	0.15 ± 0.02
Panda	-0.035 ± 0.008	0.14 ± 0.01
Bow-tie	-0.063 ± 0.008	0.18 ± 0.02
Elliptical clad	-0.092 ± 0.008	0.23 ± 0.02
(b)	Fast axis sensitivity (nm/(N/mm))	
D-clad	0.061 ± 0.009	0.12 ± 0.03
Elliptical core	-0.020 ± 0.008	0.12 ± 0.01
TruePhase	0.030 ± 0.009	0.082 ± 0.009
Panda	0.014 ± 0.007	0.14 ± 0.01
Bow-tie	0.020 ± 0.008	0.098 ± 0.008
Elliptical clad	0.011 ± 0.008	0.17 ± 0.01

Fernandez et al. [51] modified the set-up of Ye et al. [50] to a fully PC-controlled calibration set-up. The set-up is able to apply axial and transverse forces, rotate the fibre sensor and control the temperature next to the fibre.

Guemes et al. [52] altered the set-up of Ye et al. and Chehura et al. [27, 50]. The guiding pins were removed to avoid all friction components. Two parallel LoBi fibres with Bragg gratings were used instead of one test fibre with dummy fibre. As such, averaging possible asymmetries due to misalignments in the applied loads can be done. No quantitative results were reported in this paper. The test set-up was also used by Suo et al. [53] to calibrate excessively tilted gratings (81 deg). The results, however, are of no importance to this work and are, therefore, not mentioned.

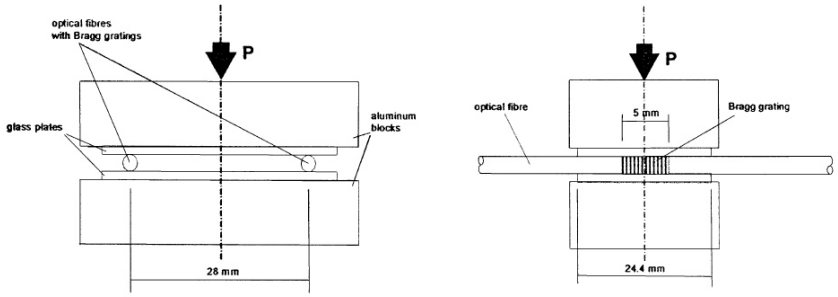

Figure 2-24: Calibration device designed by Guemes using a load stamp to simultaneously load two fibre Bragg gratings. [52]

A similar set-up is used in this dissertation (Figure 2-25). A steel support base plate is used, on which a glass plate (30 mm x 80 mm) is attached. Two FBGs are positioned in the middle of the glass plate with 70 mm of distance in between both FBGs (Figure 2-25, A). A polished load stamp (25 mm x 80 mm) made of stainless steel is used to transfer the load onto the fibres. A ball joint is used to overcome bending moments during calibration; only diametrically applied load is transferred (Figure 2-25, B). Four manual rotation stages (with an accuracy of 2 deg to 3 deg) are used (two for each fibre), to rotate the fibre (Figure 2-25, C). As will be discussed in the following paragraphs, after each calibration step the fibres will be rotated over 15 deg in 13 steps (from 0 deg to 180 deg). In between each calibration step the load stamp is lifted with a load release mechanism consisting of four pins. A sliding mechanism forces a simultaneous lift of all four pins (Figure 2-25, D). Experimental results of the load responses and determination of the strain optic coefficients (p_{11} and p_{12}) and thus the strain sensitivities will be discussed in the following section.

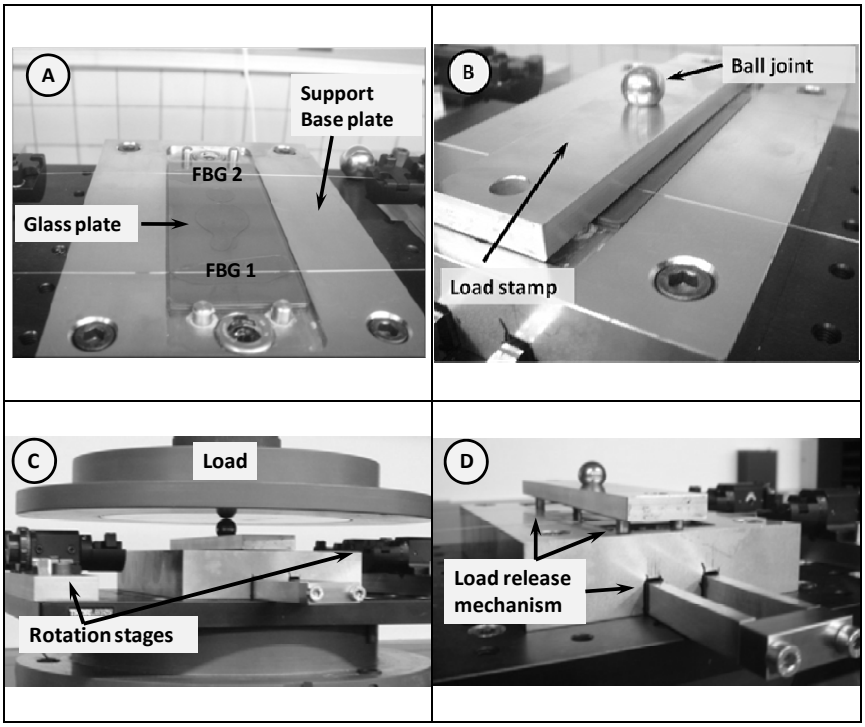

Figure 2-25 (A, B, C, D): Different parts of the calibration device designed by Luyckx et al. using a load stamp to simultaneously load two fibre Bragg gratings. [54]

2. 4. 1. c. Experiments and simulations

Several 80 µm HiBi bow-tie fibres with Bragg grating (bow-tie FBG) from Fibrecore inc. ([20], Figure 2-8) were calibrated in the course of this dissertation. After several improvements to the design of the test set-up, an optimized calibration procedure consisting of three steps is suggested.

In the first step (Figure 2-26) the optical fibres are positioned with random (unknown) orientation inside the calibration device. Due to this random positioning, both fibres will most probably not have the same orientation. A first calibration is performed in which the transverse load response of both FBGs (for each 15 degrees of orientation, θ in Figure 2-26) is measured and plotted. This transverse load response is measured for both slow and fast axis. The orientation of slow and fast axes can be determined from these first calibration curves. We determine the zeros of the slow axis calibration curve, sum the corresponding orientation angles, and divide this sum by two. (Figure 2-26)

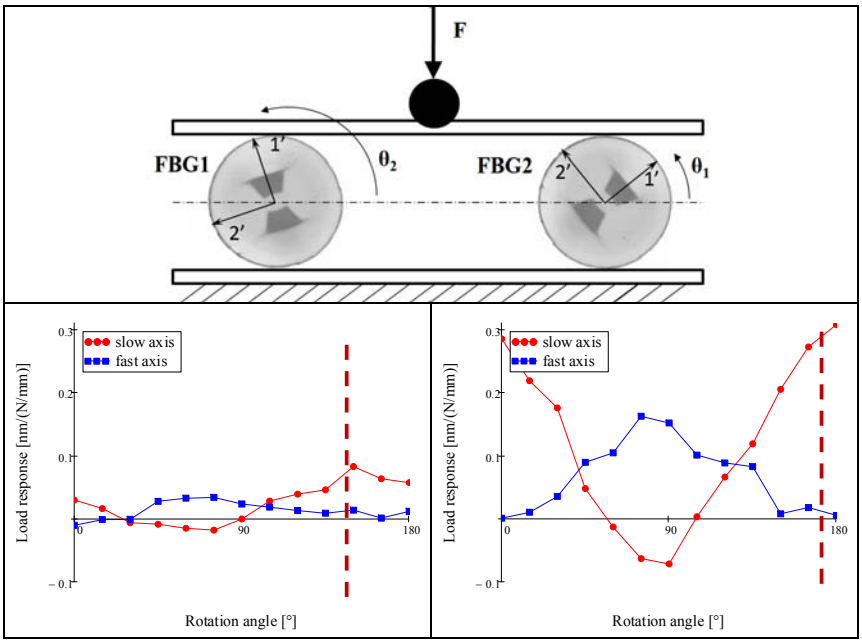

Figure 2-26: Top: first step in the calibration method, the fibres are placed in the set-up with a random (unknown) orientation. Bottom: their transverse load response is determined for both fibre eigenaxes; the dashed line is the orientation of one of the eigenaxis.

In the second step of calibration procedure, both FBGs are oriented along the same axis and a new transverse calibration step can be executed (Figure 2-27). From the

obtained calibration (load response) curves, one can see that the orientation of both FBGs is the same. Though, the load response of both FBGs differ significantly due to the misalignment of the load (FBG 2 experiences more load than FBG 1). Since both FBGs are written in the same batch of bow-tie optical fibre, the response should normally be almost equal. By taking the mean of the load response curves of both FBGs, one can overcome the misalignment of the load during the calibration procedure.

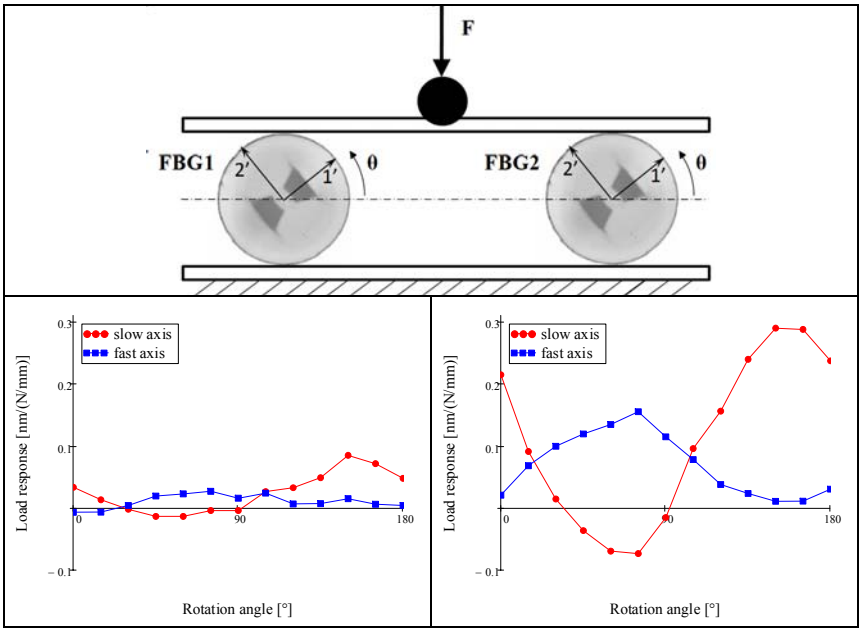

Figure 2-27: Second step in the calibration method. Fibres are placed with identical orientation and a transverse load calibration is performed.

The mean calibration curve is depicted in Figure 2-28. These measurements indicate less sensitivity to transverse compressive load for the fast axis, which was also observed by other authors in similar experiments [44, 45]. Probably this is caused by the SAPs introduced in the cladding of the bow-tie optical fibre. Several authors [45, 55, 56] have done FE-simulations using considerably different material properties of the borosilicate doped regions (Young's modulus and Poisson's ratio) to explain the differences in the calibration curves.

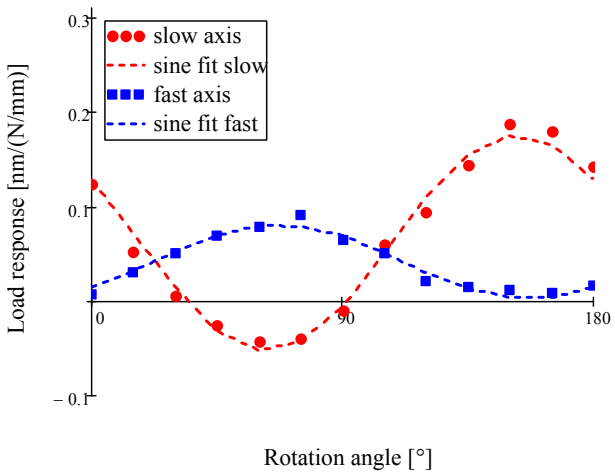

Figure 2-28: The mean diametrically applied load response for the polarization modes of both FBGs. A sine fit of the calibration curves is determined (dashed line).

The last step is fitting a sine through the mean experimental curves, to use this for determining the strain optic coefficients (p_{11} , p_{12}) of the calibrated optical fibre. The values of the load response curves of the slow and/or fast calibration curve at $\theta = 0\,\text{deg}$ and $\theta = 90\,\text{deg}$ are substituted in Equation 2-31 (both should give the same result).

$$\begin{bmatrix} p_{11} \\ p_{12} \end{bmatrix} = -\frac{2}{n_{eff}^2} \begin{bmatrix} \varepsilon_{1'}/_{F}(0°) & \varepsilon_{2'}/_{F}(0°) \\ \varepsilon_{1'}/_{F}(90°) & \varepsilon_{2'}/_{F}(90°) \end{bmatrix}^{-1} \begin{bmatrix} \dfrac{\Delta\lambda_{B,1'}/_{F}(0°)}{\lambda_{B,1'}} \\ \dfrac{\Delta\lambda_{B,1'}/_{F}(90°)}{\lambda_{B,1'}} \end{bmatrix} \qquad \textbf{2-31}$$

In Table 2-5 the different FBGs for which this optimized transverse strain calibration set-up was used, are summarized. Each FBG was calibrated in pairs (1 and 2, 3 and 4).

Table 2-5: Overview of the bow-tie fibres calibrated for transverse strains

	FBG length	$\lambda_{B,\,fast}$ [nm]	$\lambda_{B,\,slow}$ [nm]
1	8 mm	1539.145	1539.542
2	8 mm	1538.820	1539.203
3	8 mm	1540.073	1540.465
4	8 mm	1539.335	1539.736

The mean load response of the four FBGs for diametrically applied load is shown in Figure 2-29. Fitting a sine through the obtained data points gives $\left(0.043\sin(\theta)+0.044\right)\left(nm/N/mm\right)$ for the fit of the load response of the fast axis and $\left(0.109\sin(\theta)+0.062\right)\left(nm/N/mm\right)$ for the load response of the slow axis.

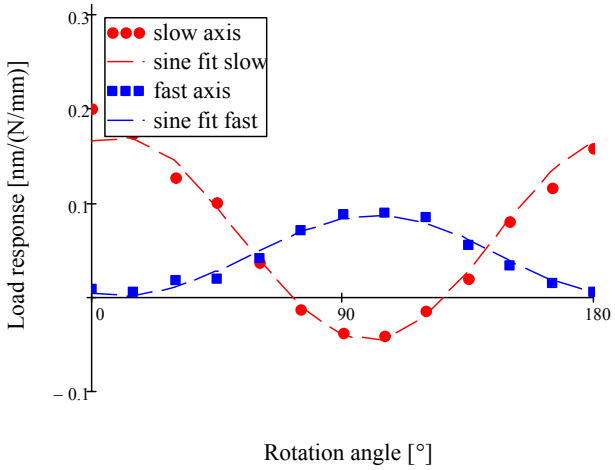

Figure 2-29: The mean curves of both polarization modes of the transversally calibrated FBGs. The dashed line is the sine fit for both curves.

Since the mechanical properties of the SAPs and the core/cladding of the bow-tie fibre are significantly different (Table 2-1), it should be remarked that the strain field induced by a compressive load along the fast axis is not equal to the strain field induced by a compressive load along the slow axis (Figure 2-30). The FE-model of Figure 2-9 can be used to determine the strains in the core of the optical bow-tie fibre (Table 2-6).

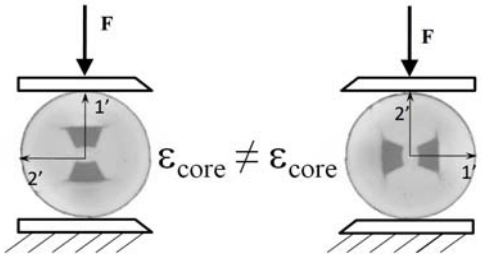

Figure 2-30: The strain field induced in the core of the bow-tie optical fibre by the compressive load is different when the load is parallel to one of the two axes. (θ = 0 deg and θ = 90 deg)

Table 2-6: The strain field induced in the core of the bow-tie optical fibre by a compressive load.

Load direction parallel with	slow axis	fast axis
$\varepsilon_{1'}$ [με]	218.3	170.7
$\varepsilon_{2'}$ [με]	-327.6	-417.9

By substituting the values of Table 2-6 into Equation 2-31, the strain optic coefficients (p_{11} , p_{12}) are found. By using one time the slow and then the fast load response curve, we should find the same resulting coefficients, which is not the case (Table 2-7). A difference of ~31% is found for the p_{12} and ~15% for the p_{11}.

Table 2-7: The strain optic coefficients found using the calibration curves of both polarization modes.

Load response	Slow axis	Fast axis
p_{11}	0.108	0.092
p_{12}	0.292	0.223

When using Equation 2-31 one should know the exact strain field ($\varepsilon_{1'}$ and $\varepsilon_{2'}$) induced in the fibre core by the compressive load (F). Though, due to the unknown mechanical properties of the SAPs used in the cladding of the optical fibres, it is extremely difficult to determine the right strain optic coefficients.

A second disadvantage is the significant rotation of the optical eigenaxes of the HiBi optical fibre for a certain relative angle (e.g. θ = 30 deg in Figure 2-31) for high diametrically applied loads.

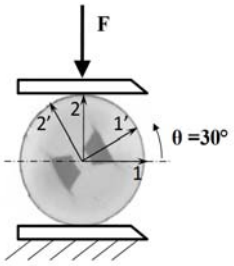

Figure 2-31: A diametrically compressed fibre leads to induced strain components along the 1' ($\varepsilon_{1'}$) and 2'-axis ($\varepsilon_{2'}$). These strains can cause a rotation of the optical eigen-axes of the fibre which are defined by the residual strains ($\varepsilon_{R,1'}$ and $\varepsilon_{R,2'}$) already present in the core of the HiBi-fibre.

As discussed before, stress induced HiBi optical fibres have a certain residual strain field ($[\varepsilon_R]$) present in the core of the optical fibre (2. 3. 2. a.). When diametrically loading the fibre, a second strain field is induced in the core ($[\varepsilon_F]$). By using superposition of both strain fields ($[\varepsilon_R]$ and $[\varepsilon_F]$), the total strain field $[\varepsilon_{tot}]$ according to the 1- and the 2-axis in Figure 2-31 is found to be:

$$[\varepsilon_{tot}] = [\varepsilon_F] + [a][\varepsilon_R][a]^T \quad \textbf{2-32}$$

In which $[a]$ is dependent of the angle θ in Figure 2-31 and can be defined for a plane strain assumption as:

$$[a] = \begin{bmatrix} \cos(\theta) & \sin(\theta) & 0 \\ -\sin(\theta) & \cos(\theta) & 0 \\ 0 & 0 & 1 \end{bmatrix} \quad \textbf{2-33}$$

From the total strain field ($[\varepsilon_{tot}]$) in which a shear component is present, the new principal direction (90 deg - θ') of the slow axis relative to the diametrically applied load can be found. For high diametrically applied loads this will significantly differ from the original one (90 deg - θ, Figure 2-32).

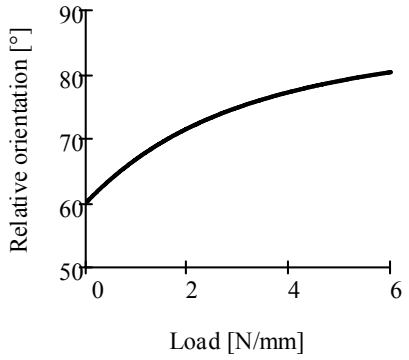

Figure 2-32: Change of the relative orientation of the diametrically applied load and the slow axis

Using the principal strains of the total induced strain field $[\varepsilon_{tot}]$, one can define the theoretical response for a diametrically loaded fibre when the load is oriented (90 deg – θ *deg)* with respect to the slow axis. A clear non-linear response can as such be calculated which is also visible in the experimental results (Figure 2-33).

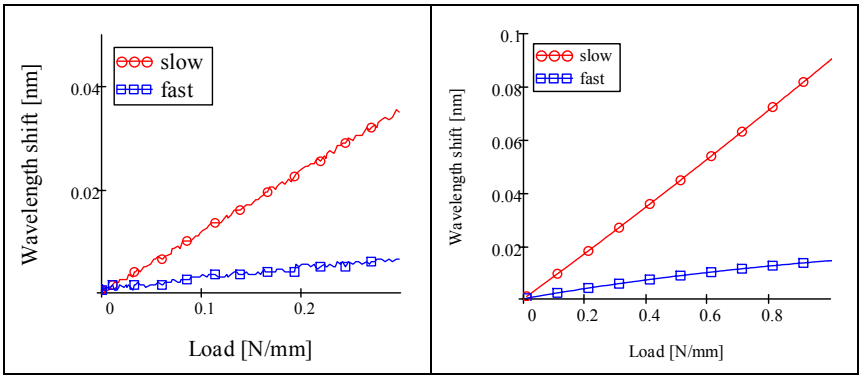

Figure 2-33: Left: experimental response when load is diametrically applied under an angle of 30 deg with the 1'-axis. Right: theoretically determined response when load is diametrically applied under an angle of 30 deg with the 1'-axis.

When linearly fitting the curves of Figure 2-33 and determining the load response, big errors can be observed for high diametrically applied loads. In Figure 2-34 the theoretical load response curves are given when diametrically loading the fibre from 0 to 0.1 N/mm, from 0 to 1.5 N/mm, and from 0 to 3 N/mm. By increasing the maximum diametrically applied load, the load response curves differ more and more from a perfect sine.

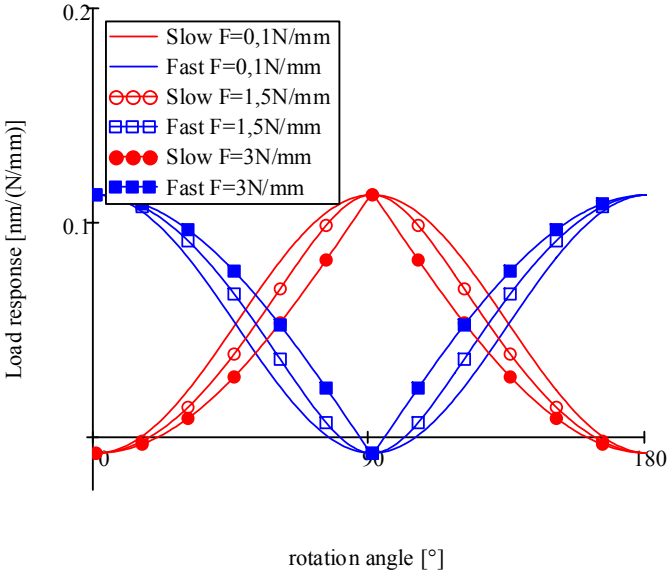

Figure 2-34: theoretically determined calibration curves for small to high diametrically applied loads F = 0.1 to 3 N/mm

Based on the difficulties in calibrating HiBi optical fibres, the author suggests to use the presented calibration procedure and calibrate uni-axial FBGs (shot in a low-birefringent SMF) with exactly the same fibre core (mechanical and optical) material properties as for the HiBi optical fibre. As such, the asymmetric straining effect caused by the SAPs of the optical fibre is eliminated. For LoBi fibres (i.e. isotropic fibres) one can easily relate the diametrically applied load with the strain state inside the optical fibre core (Section 2. 4. 1. a.). As this is a uni-axial FBG, only one Bragg peak is back reflected (black spectrum in Figure 2-35). A certain preload is necessary to induce enough differential transverse strain to split up the spectrum (from red to green, and finally to the blue spectrum in Figure 2-35). From this moment on both Bragg peaks become distinguishable and the transverse load response can be determined.

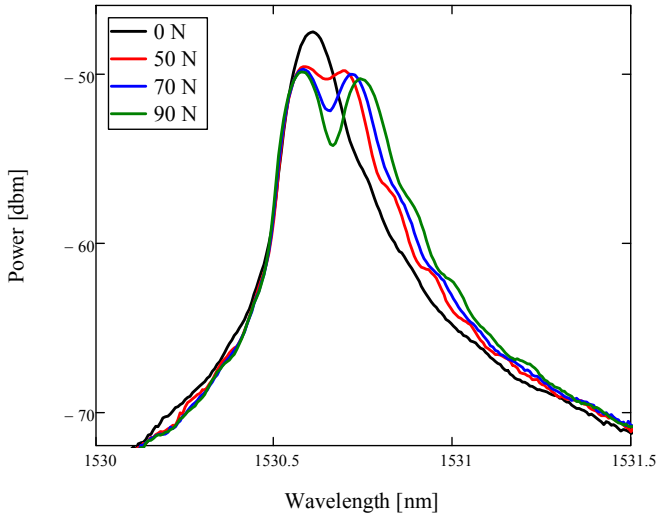

Figure 2-35: Spectra of a diametrically loaded uni-axial LoBi fibre. Initially one Bragg peak is visible (black curve), after a certain diametrically applied preload both polarization modes reflect part of the light resulting in two Bragg peaks.

Relating these experimental results with the expected induced strain state in the core of the SMF, one can determine the strain optic coefficients of the optical fibre using the following equation.

$$\begin{bmatrix} p_{11} \\ p_{12} \end{bmatrix} = -\frac{2}{n_{eff}^2} \begin{bmatrix} \varepsilon_{1'}/F & \varepsilon_{2'}/F \\ \varepsilon_{2'}/F & \varepsilon_{1'}/F \end{bmatrix}^{-1} \begin{bmatrix} \dfrac{\Delta\lambda_{B,1'}/F}{\lambda_{B,1'}} \\ \dfrac{\Delta\lambda_{B,2'}/F}{\lambda_{B,2'}} \end{bmatrix} \qquad \textbf{2-34}$$

Measurements were done for four different orientations of the fibre (every $\theta = 90$ deg). Good results are obtained for the experimentally determined coefficients p_{11} and p_{12} (Table 2-8, [18]) as compared with Bertholds and Dändliker [17].

Table 2-8: Experimentally determined result obtained by diametrically calibrating a uni-axial FBG.

Orientation	0°	90°	180°	270°	Mean
p_{11} [-]	0.120	0.116	0.110	0.099	0.111±0.008
p_{12} [-]	0.270	0.255	0.237	0.226	0.247±0.017

2. 4. 2. Axial strain calibration

2. 4. 2. a. Strain components in the core of a LoBi optical fibre.

In an axial calibration, a situation of pure axial stress is created (Figure 2-36).

$$\sigma_{2'} = \sigma_{1'} = 0$$
$$\sigma_{3'} \neq 0 \qquad \textbf{2-35}$$

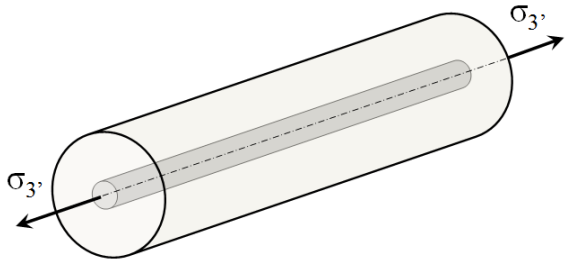

Figure 2-36: Optical fibre loaded with pure axial stress

As a result, a constant strain state is created in the core of the optical fibre, which exists of the following strain components

$$\varepsilon_{3'} = \frac{\sigma_{3'}}{E_f}$$
$$\varepsilon_{1'} = \varepsilon_{2'} = -\nu_f \varepsilon_{3'} \qquad \textbf{2-36}$$

By substituting the transverse strain components in Equation 2-21, one finds the axial strain dependency defined in Equation 2-13.

$$\frac{\Delta\lambda_{B,1'}}{\lambda_{B,0}} = \frac{\Delta\lambda_{B,2'}}{\lambda_{B,0}} = (1-P)\varepsilon_{3'}$$
$$P = \frac{1}{2} n_{eff}^2 \left[p_{12} - \nu_f \left(p_{11} + p_{12} \right) \right] \qquad \textbf{2-37}$$

In section 2.4.2.c., an experimentally determined axial strain gauge factor P will be compared with the one calculated using the strain optic coefficients p_{11} and p_{12} determined in the transverse strain calibration (2.4.1.).

2. 4. 2. b. Axial calibration test set-up

According to Window and Holister [57], a classical electrical resistance strain gauge sensor is often calibrated using the cantilever beam method. In this method, the sensor to be calibrated is bonded to a host beam with accurately known geometrical and material parameters. Depending on the material properties of the test sensor, bonding the test sensor onto the host structure will likely make it unusable after calibration. This is because reusing the sensor would require de-bonding it from the host structure, and in this process, it is likely to get damaged. Non-reuse of the test sensor may not be a problem for sensors that are made in batches with a given tolerance. However, for one-of-a-kind sensors, and for sensors for which precise calibration values are necessary, it would be highly desirable to be able to reuse the sensor following calibration.

In this work we are more interested in calibration methods for sensors based on optical fibre Bragg grating technology. Several authors have done such calibrations, only a very short overview is given. Abe et al. [58] fixed the fibre between two displacement stages, where a known deformation can be applied by a calibrated micrometer. The longitudinal strain sensitivity of an internal elliptical cladding fibre was found to be 1.30 pm/με and 1.39 pm/με for the fast-axis for both sensors (1535 nm and 1547 nm) and respectively 1.39 pm/με and 1.36 pm/με for the slow axis. It seems rather odd that for one grating the strain sensitivity of the fast axis is higher than the strain sensitivity for the slow axis. No measurement errors were given, which makes it difficult to conclude. Secondly, rather high sensitivities were observed, which can be caused by the influence of the coating during the calibration test. The calibration of a coated fibre, a partially coated fibre, or a non-coated fibre will give totally different results.

The same set-up was used by Zhang et al. [59]. The authors described the experimental measurements of the temperature and strain sensitivities of three common types of commercially available HiBi fibres (bow-tie, Panda, elliptical core) without Bragg grating inscribed by using a polarimetric method [60]. A 67 cm long optical fibre was attached to two height adjustable rods by means of an epoxy glue. One rod was positioned on an aluminum base plate and another on a translation stage driven by a stepper motor, which was also positioned on the same base plate. Each step elongates the fibre 2,5 μm. The results of this research cannot be used to compare our own results since no FBG was written in the HiBi FBGs.
Abdi et al. [61] created a fibre optic Fabry-Perot interferometer strain gauge calibration set-up to characterize the displacement, linearity and hysteresis of a mono-morphic piezoelectric actuator (Figure 2-37). The strain gauge factor of an electrical resistance strain gauge was determined too.

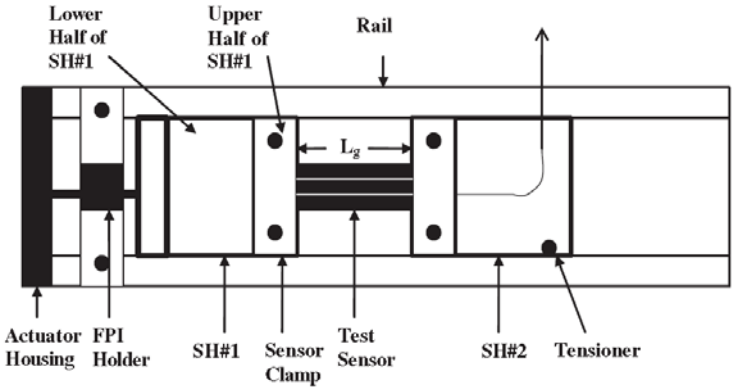

Figure 2-37: The physical layout of the Fabry-Perot interferometric strain gauge calibration system. The system is composed of two sensor holders (SH#1 and SH#2) positioned on a groove. SH#2 is kept fixed using an adjustable side screw (tensioner). The test sensor is held by SH#1 and SH#2.[61]

The reported results show that the measured strain gauge factor is within 2% of the manufacturer's value, with a standard deviation of ±1.6%. The proposed set-up is not as accurate compared to interferometric strain/displacement gauge or batch electrical resistance strain gauge measurements, typically given to be within ±0.5%. However, the set-up is reasonably accurate, as shown above, particularly for cases of one-of-a-kind sensors and/or for cases when the strain gauge factors are not available or given.

The author of this work chose to use a method of fixing the optical fibre at one side on a stationary base plate and on the other side to a displacement stage controlled by a micrometer (with an accuracy of 5 µm). During calibration the FBG is covered to avoid temperature swings. The initial length of the fibre is ~500 mm. (Figure 2-38)

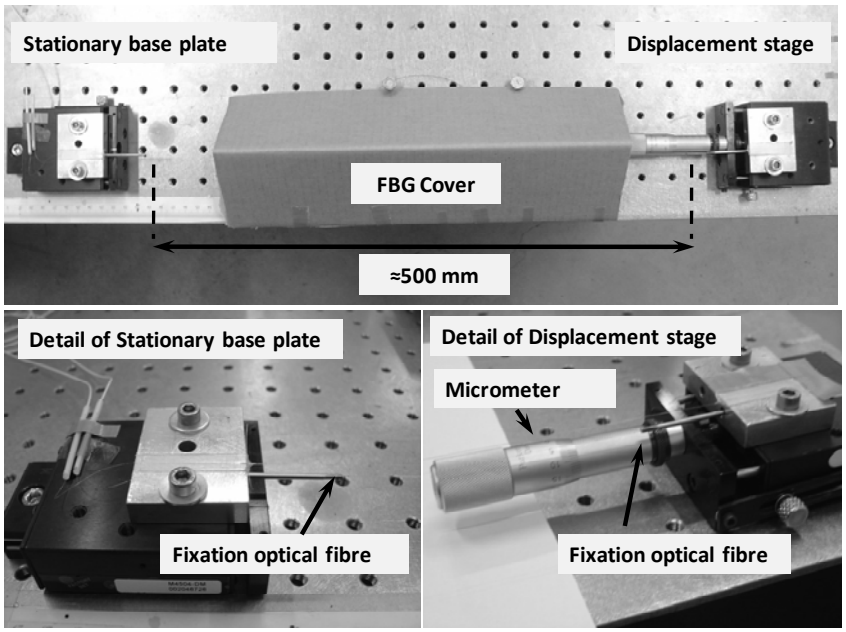

Figure 2-38: Pure axial calibration set-up. At one side the optical fibre is fixed to a stationary base plate and on the other side to a displacement stage controlled by a micrometer.

2. 4. 2. c. Axial calibration experiments and simulations

Experiments were done on several bow-tie FBGs with different wavelengths. An overview of the calibrated fibres is given in Table 2-9.

Table 2-9: Overview of the axial calibration of stripped fibres[62]

			Sensor 1		Sensor 2	
	FBG length	no. of FBGs	$\lambda_{B,\,fast}$ [nm]	$\lambda_{B,\,slow}$ [nm]	$\lambda_{B,\,fast}$ [nm]	$\lambda_{B,\,slow}$ [nm]
1	8 mm	1	1544.072	1544.432		
2	8 mm	1	1544.008	1544.367		
3	8 mm	1	1544.192	1544.552		
4	8 mm	2	1540.184	1540.544	1560.000	1560.368
5	8 mm	2	1540.344	1540.704	1559.992	1560.360
6	8 mm	2	1540.320	1540.688	1560.080	1560.448

The axial strain sensitivity and the strain gauge factors (1-P) of all these FBGs to a pure axial stress are given in Table 2-10. Little variations are found in the axial calibration results for the different FBG samples. Though, for all samples, the strain sensitivity of the fast polarization mode is 0.01 pm lower than for the slow polarization mode. This difference can be explained by using the obtained strain optic coefficients (p_{11} and p_{12}) found during a transverse strain calibration and calculate the corresponding P. Therefore, a 3D FE-model was built with the same cross section and mechanical material properties as the 2D FE-model of Figure 2-9. The FE-model consists of 818 linear hexahedral elements of type C3D8RT for the sections of the core and SAPs and 77688 linear wedge elements of type C3D6T for the section of the cladding. The model is loaded with a pure axial stress. The results of this via FE-model calculated axial strain sensitivity can be found in Table 2-11. Good similarity is found between the experimentally and theoretically determined sensitivities, which is a validation of the experimentally obtained strain optic coefficients (p_{11} and p_{12}).

Table 2-10: Overview of the results of the calibrated fibres

$\lambda_{B,\,fast}$ [nm]	Strain sensitivity fast axis [nm/με]	$(1\text{-}P)_{fast}$ [-]	$\lambda_{B,\,slow}$ [nm]	Strain sensitivity slow axis [nm/με]	$(1\text{-}P)_{slow}$ [-]
1544.072	1.22	0.790	1544.432	1.23	0.796
1544.008	1.22	0.790	1544.367	1.23	0.796
1544.192	1.22	0.790	1544.552	1.23	0.796
1540.184	1.22	0.792	1540.544	1.23	0.798
1540.344	1.21	0.785	1540.704	1.22	0.792
1540.320	1.21	0.786	1540.688	1.22	0.792
1560.000	1.23	0.788	1560.368	1.24	0.795
1559.992	1.23	0.788	1560.360	1.24	0.795
1560.080	1.23	0.788	1560.448	1.23	0.788
Mean		0.789			0.794
Standard dev.		±0.002			±0.003

Table 2-11: Theoretical result of an axially calibrated bow-tie fibre using a 3D FE-model

$\lambda_{B,\,fast}$ [nm]	Strain sensitivity fast axis [nm/με]	$(1\text{-}P)_{fast}$ [-]	$\lambda_{B,\,slow}$ [nm]	Strain sensitivity slow axis [nm/με]	$(1\text{-}P)_{slow}$ [-]
1550	1.242	0.801	1550.4	1.248	0.805

Remark that big errors can be made in axial strain sensitivity when the fibre is only partially (at the position of the grating, e.g. 3 cm) stripped. To compare with the previous results a bow-tie fibre with an acrylate coating was stripped at the FBG before axial calibration (Table 2-12). The results, which are significantly higher than those of the stripped fibres are shown in Table 2-13.

Table 2-12: Overview of an axial calibration of a partially stripped fibre

	FBG length	no. of FBGs	$\lambda_{B,\,fast}$ [nm]	$\lambda_{B,\,slow}$ [nm]
1	8 mm	1	1544.493	1544.913

Table 2-13: Overview of the results of an axial calibration of a partially stripped fibre

$\lambda_{B,\,fast}$ [nm]	Strain sensitivity fast axis [nm/με]	$(1\text{-}P)_{fast}$ [-]	$\lambda_{B,\,slow}$ [nm]	Strain sensitivity slow axis [nm/με]	$(1\text{-}P)_{slow}$ [-]
1544.493	1.24	0.802	1544.913	1.25	0.809

2. 4. 3. Temperature calibration

2. 4. 3. a. Strain components in the core of a LoBi optical fibre.

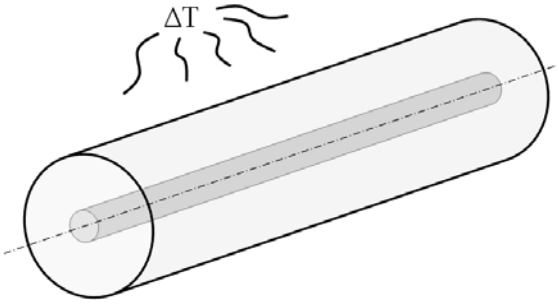

Figure 2-39: Optical fibre under a homogeneous temperature load

In a temperature calibration experiment we want to measure the thermo-optic coefficient α_n of the optical fibre for a known thermal expansion coefficient $\alpha_f = 0.55 \bullet 10^{-6} \frac{1}{K}$ and a certain Bragg peak wavelength. The wavelength shift as function of temperature change is given by the following:

$$\frac{d\lambda_{B,1'}}{\lambda_{B,1'}} = \frac{d\lambda_{B,2'}}{\lambda_{B,2'}} = \left(\alpha_f + \alpha_n\right) dT \qquad \textbf{2-38}$$

In most cases temperature changes are relatively small so that the differentials can be replaced by differences (d into Δ). Equation 2-38 can thus be reorganized in

$$\alpha_n = \left(\frac{\Delta\lambda_B / \Delta T}{\lambda_{B,0}} - \alpha_f \right) \quad \textbf{2-39}$$

From which α_n can easily be calculated when the wavelength shift has been experimentally determined as a function of temperature change. It should be noted, that the expansion coefficient α_f is constant over a high temperature range [63], however, the thermo-optic coefficient α_n is temperature dependent ($\alpha_n = aT + b$, [64]). Therefore, when considering high temperature ranges, a more accurate equation is necessary. By substituting this linear dependency in Equation 2-38, it can be written as:

$$\frac{d\lambda_{B,1'}}{\lambda_{B,1'}} = \frac{d\lambda_{B,2'}}{\lambda_{B,2'}} = \alpha_f dT + (aT + b)dT \quad \textbf{2-40}$$

By integrating Equation 2-40, one find the following equation

$$\ln(\lambda_{B,1'}) = \ln(\lambda_{B,2'}) = \alpha_f T + bT + \frac{a}{2}T^2 + Cte \quad \textbf{2-41}$$

When considering a definite integration of Equation 2-40 between two limits (T_0 and T). Accordingly, Equation 2-41 can be written as

$$\ln\left(\frac{\lambda_{B,1'}(T)}{\lambda_{B,1'}(T_0)}\right) = \ln\left(\frac{\lambda_{B,2'}(T)}{\lambda_{B,2'}(T_0)}\right) = \alpha_f (T - T_0) + b(T - T_0) + \frac{a}{2}(T^2 - T_0^2) \quad \textbf{2-42}$$

Equation 2-42 can be rewritten as

$$\ln\left(\frac{\lambda_{B,1'}(T)}{\lambda_{B,1'_0}(T_0)}\right) = S_2\left(T^2 - T_0^2\right) + S_1\left(T - T_0\right) \quad \textbf{2-43}$$

In which S_1 is the sum of α_f and b and S_2 equals $a/2$.

2. 4. 3. b. Temperature calibration test set-up

Little variation in different set-ups was found in literature since this calibration method is quite straightforward. A sensor free to expand is loaded with a temperature cycle, in several steps the temperature is stabilized and a Bragg peak measurement is done (Figure 2-40).

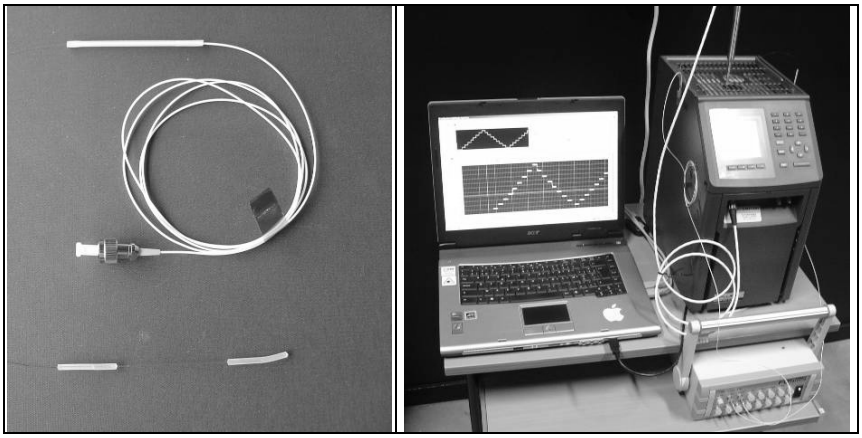

Figure 2-40: Left: fibre Bragg grating prepared to do a temperature calibration cycle. Right: the set-up of the calibration test set-up at FOS&S used in this dissertation. The cycle of the calibration test is shown on the computer screen.

2. 4. 3. c. Temperature experiments and simulations

The temperature calibration results are summarized in Table 2-14. The results are considered for small temperature changes. A small difference in α_n exists for slow and fast axes. These differences can be due to the use of Equation 2-39 in which a constant α_f is used, while due to the presence of the SAPs in the cladding probably the expansion of the fibre will lead to different strain components for the 1'-axis (slow) and the 2'-axis (fast) (i.e. anisotropic thermal expansion). In theory, the opposite of the phenomena by which birefringence is built up during fibre manufacturing should happen. From these results, it is clear that the response of the fast polarization mode is somewhat higher than for the slow polarization mode due to a release of the residual strains inside the optical fibre.

To determine the wavelength independent temperature sensitivies (S_1 and S_2) of Equation 2-43, an extra temperature cycle was considered in which the temperature is changed from -40 °C up to 140°C. The wavelength shifts for both polarization modes as function of temperature can be found in Figure 2-41. Evaluating this results according to Equation 2-42, the S_1 and S_2 are found (Table 2-15). The results are slightly bigger than for the linearized model. A part of the differences are caused by the influence of thermal expansion of the fibre which is not included in the linearized α_n.

Table 2-14: Overview of the results of the calibrated fibres

$\lambda_{B,\ fast}$ [nm]	Temperature response fast [pm/°C]	$\alpha_{n,\ fast}$ [-]	$\lambda_{B,\ slow}$ [nm]	Temperature response slow [pm/°C]	$\alpha_{n,slow}$ [-]
1544.072	10.61	6.32E-06	1544.432	10.25	6.09E-06
1544.192	10.50	6.24E-06	1544.552	10.15	6.02E-06
1540.184	10.51	6.27E-06	1540.544	10.15	6.04E-06
1540.344	10.46	6.24E-06	1540.704	10.11	6.01E-06
1540.320	10.53	6.28E-06	1540.688	10.17	6.05E-06
1560.000	10.59	6.24E-06	1560.368	10.17	5.97E-06
1559.992	10.57	6.23E-06	1560.360	10.20	5.99E-06
1560.080	10.62	6.26E-06	1560.448	10.23	6.01E-06
Mean		6.26E-06			6.02E-06
Standard dev.		±3.1E-8			±3.7E-8

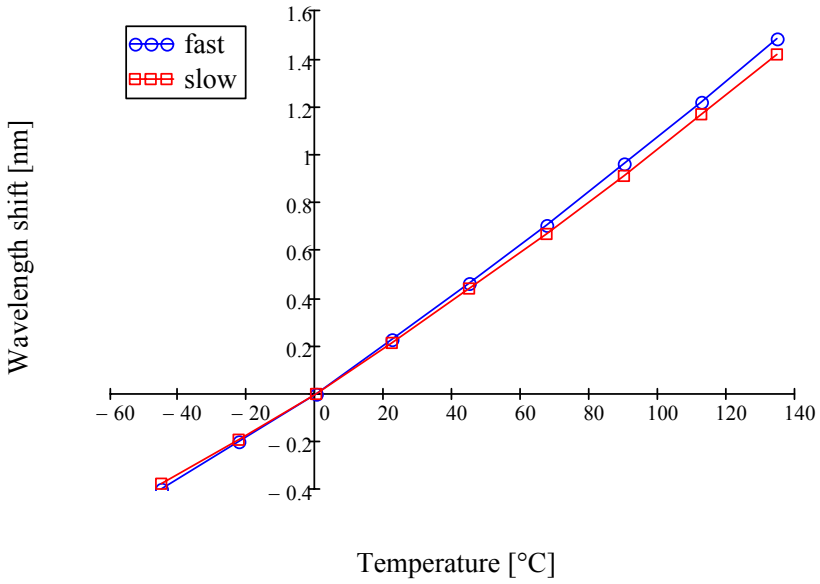

Figure 2-41 Wavelength shifts of a temperature calibration of a bow-tie optical fibre with Bragg grating.

Table 2-15 The wavelength independent temperature sensitivities for both polarization modes of an optical bow-tie fibre with Bragg grating

	S_1 [10^{-6}]	S_2 [10^{-9}]
Fast axis	6.528	6.167
Slow axis	6.167	6.482

2. 5. CONCLUSIONS

FBGs can be seen as the optical counterpart of electrical resistance strain gauges with a lot of advantages in favor of the optical alternative. They are used in a similar way as electrical resistance strain gauges, though, they are sensitive to all strain components acting on the Bragg grating. The spectral response of an FBG exposed to a multi-axial strain field load was theoretically determined using the photo-elastic effect. For a LoBi fibre, axial strain and thermal loading cause the Bragg peak wavelength to homogenously shift to higher wavelengths, transverse strains cause a broadening of the Bragg peak response, which will eventually split in two separate Bragg peaks. Thus, the LoBi fibre is becoming highly birefringent. The theoretical discussion of the photo-elastic effect identified that measuring shear deformation will be impossible.

A distinction is made between LoBi fibre with FBG (which have a single Bragg peak response) and HiBi fibre with FBG (which have a double Bragg peak response, one for each polarization mode of the light). FE-simulations have proven that for the stress induced hiBi fibres, the shape, the dimensions, and the position of the SAPs have an influence on this birefringence. Since both Bragg peaks of the HiBi fibres with FBG act differently for a strain field in the core of the optical fibre, these sensors can be used for multi-axial strain measurements.

It is clear that these FBGs need calibration prior to usage as strain and/or temperature sensor. To fully characterize the (transverse and axial) strain response of an FBG, one needs to determine the strain optic coefficients (p_{11} and p_{12}). Therefore a transverse strain calibration is already sufficient, though, an axial calibration can be used as validation. After a literature review of several authors who designed a transverse calibration set-up and considering the advantages and disadvantages of each set-up, the author designed his own set-up and calibration procedure. The set-up is made of a base plate on which a flat glass surface is glued. A stamp without friction is placed on top of two FBGs to diametrically load the fibre with only 0.3 N/mm to avoid big errors because of the rotation of the optical eigen axes of the HiBi fibre. Next, one should also be aware of the errors that can be made using a single test fibre. To omit the influence of the possible misalignment of the line load, one should use two test fibres and take the mean of both measurements.

Three steps were considered in the calibration procedure; a first step in which both HiBi fibres have a random orientation and in which the orientation of both HiBi fibres is determined; a second step in which both gratings are given the same orientation and the load responses are measured and averaged (to overcome errors due to a misaligned diametrical load); and a third and final step in which the load response curves are sine fitted. Calibration of several bow-tie fibres with FBG proved the feasibility of the transverse strain calibration set-up. However, poor results were obtained when the strain optic coefficients were determined using the load response curves. This was caused by the unknown mechanical properties of the SAPs in the bow-tie fibre. To overcome this problem, the same procedure was proposed using a LoBi fibre with FBG which has the exact same mechanical as well as optical properties as the HiBi fibre. The resulting strain optic coefficients of this single axial FBGs showed good similarities with previously found results of Bertholds and Dändliker.

These strain optic coefficients were validated in an axial strain calibration method. The set-up used for these calibrations consists of a stationary base plate and a displacement stage which is controlled by a micrometer. The author remarked that the fibre with FBG needs to be completely stripped, otherwise the axial strain sensitivity turns out to be too high (~3% for an acrylate coated fibre, with an initial length of ~500 mm and 30 mm stripped FBG).

The temperature calibration set-up was straightforward and did not need to be discussed in detail. The temperature sensitivity was found to be slightly higher for the slow axis than for the fast axis. It should be remarked that temperature compensation is necessary whenever the strain components are measured with FBGs.

This type of sensor (FBG inscribed in a HiBi-fibre) enables the measurement of two Bragg-wavelengths and hence yields the potential of determining two strain components. However, to determine the 3D-strain components which exist along the main axes of the fibre, at least 2 sensors of this type are required. Two FBG sensors would yield 4 measurable wavelengths which theoretically allow the determination of a fourth parameter (e.g. temperature) as well. In the next chapter several configurations using two gratings will be discussed.

2. 6. REFERENCES

1. Meltz, G., Morey, W.W., and Glenn, W.H., *Formation of Bragg gratings in optical fibers by a transverse holographic method.* Optics Letters, 1989. **14** (15): p. 823-825.
2. Butter, C.D. and Hocker, G.B., *Fiber optics strain gauge.* Applied optics, 1978. **17** (18): p. 2867-2869.
3. Dyer, S.D., Williams, P.A., Espejo, R.J., Kofler, J.D., and Etzel, S.M., *Key metrology considerations for riber Bragg grating sensors*, in *Smart Structures and Materials 2004: Smart Sensor Technology and Measurement Systems*, E. Udd and D. Inaudi, Editors. 2004. p. 181-189.
4. Fernandez, A.F., Gusarov, A., Berghmans, F., Kalli, K., Polo, V., Limberger, H., Beukema, M., and Nellen, P., *Round-robin for fibre Bragg grating metrology during COST270 action*, in *Reliability of Optical Fiber Components, Devices, Systems, and Networks Ii*, H.G. Limberger and M.J. Matthewson, Editors. 2004. p. 210-216.
5. Takeda, N., Okabe, Y., Kuwahara, J., Kojima, S., and Ogisu, T., *Development of smart composite structures with small-diameter fiber Bragg grating sensors for damage detection: Quantitative evaluation of delamination length in CFRP laminates using Lamb wave sensing.* Composites Science and Technology, 2005. **65** (15-16): p. 2575-2587.
6. De Waele, W., Degrieck, J., Baets, R., Moerman, W., and Taerwe, L. *Load and deformation monitoring of composite pressure vessels by means of optical fibre sensors*. in *Proceedings of the International Conference on Condition Montoring*. 2001. Oxford, UK.
7. Degrieck, J., De Waele, W., and Verleysen, P., *Monitoring of fibre reinforced composites with embedded optical fibre Bragg sensors, with application to filament wound pressure vessels.* NDT & E International, 2001. **34** (4): p. 289-296.
8. Moerman, W., De Waele, W., Coppens, C., Taerwe, L., Degrieck, J., Baets, R., and Callens, M., *Bragg grating strain measurements during the construction of a prestressed concrete girder bridge.* Insight, 2001. **43** (7): p. 467-469.
9. Moerman, W., Taerwe, L., De Waele, W., DeGrieck, J., and Baets, R. *Remote monitoring of concrete elements by means of Bragg gratings*. in *Proceedings of the 2nd International Workshop on Structural Health Monitoring*. 1999. Stanford, CALIFORNIA (USA).
10. O'Brien, T.K., *Characterization of delamination onset and growth in a composite laminate*, in *Damage in composite materials. ASTM STP 775*, K.L. Reifsnider, Editor. 1982, American Society for testing and materials. p. 140-167.
11. Paolozzi, A., Ivagnes, M., and Lecci, U. *Qualification tests of aerospace composite materials with embedded optical fibers under compression*. in

Proceedings of 2nd Int. Workshop on Structural Health Monitoring. 1999. Stanford, CALIFORNIA (USA).

12. Yariv, A. and Yeh, P., *Optical waves in Crystals*. 1984: J. Wiley & Sons.
13. Available from: www.viseng.com.
14. Calvert, G., Lesniak, J., and Honlet, M., *Applications of modern automated photoelasticity to industrial problems.* Insight, 2002. **44** (4): p. 224-227.
15. Chen, T.Y. and Chen, T.F., *Whole-field digital measurements of isochromatics and isoclinics in photoelastic coatings.* Optics and Lasers in Engineering, 1999. **31** (5): p. 325-338.
16. Pinnow, D., *Elastooptical Materials*, in *Handbook of Lasers*, R.J. Pressley, Editor. 1971: Cleveland (OH).
17. Bertholds, A. and Dandliker, R., *Determination of the individual strain-optic coefficients in single mode optical fibers.* Journal of Lightwave Technology, 1988. **6** (1): p. 17-20.
18. Luyckx, G., Voet, E., De Waele, W., Van Paepegem, W., Degrieck, J., and Vlekken, J. *Strain monitoring of FRP elements using an embedded fibre optic sensor*. in *Advances in Science and Techology*. 2008.
19. De Waele, W., *Structural monitoring of composite elements using optical fibres with Bragg-sensors.*, in *Department of mechanical construction and production*. 2001-2002, PhD dissertation of Ghent University, Ghent, BELGIUM.
20. http://www.fibercore.com.
21. Sugden, K., Zhang, L., Williams, J.A.R., Fallon, R.W., Everall, L.A., Chisholm, K.E., and Bennion, I., *Fabrication and characterization of bandpass filters based on concatenated chirped fiber gratings.* Journal of Lightwave Technology, 1997. **15** (8): p. 1424-1432.
22. Othonos, A. and Kalli, K., *Fiber Bragg gratings: Fundamentals and Applications in Telecommunications and Sensing*. 1999: Artech House.
23. Hagemann, V.J., *Untersuchungen zum dynamischen Einzelpuls-Einschreiben von Faser-Bragg-Gittern un zu deren Anwendung*. 2001, PhD dissertation of the Friedrich-Schiller University: Jena, GERMANY.
24. Noda, J., Okamoto, K., and Sasaki, Y., *Polarization-maintaining fibers and their applications.* Journal of Lightwave Technology, 1986. **4** (8): p. 1071-1089.
25. Rashleigh, S.C., *Origins and control of polarization effects in single-mode fibers.* Journal of the Optical Society of America, 1982. **72** (12): p. 1808-1808.
26. Dyott, R.B., Cozens, J.R., and Morris, D.G., *Preservation of polarization in optical-fibre waveguides with elliptical cores.* Electronics Letters, 1979. **15** (13): p. 380-382.

27. Chehura, E., Ye, C.C., Staines, S.E., James, S.W., and Tatam, R.P., *Characterization of the response of fibre Bragg gratings fabricated in stress and geometrically induced high birefringence fibres to temperature and transverse load.* Smart Materials & Structures, 2004. **13** (4): p. 888-895.

28. Fibercore, *Factnote 4.1.2: The Physical properties of Silica and UV Cure Axrylate Coating Packages*. 2004: Chilworth, UK.

29. Okamoto, K., Varnham, M.P., and Payne, D.N., *Polarization-maintaining optical fibers with low dispersion over a wide spectral range.* Applied optics, 1983. **22** (15): p. 2370-2373.

30. Russell, P.S.J., *Photonic-crystal fibers.* Journal of Lightwave Technology, 2006. **24** (12): p. 4729-4749.

31. Nasilowski, T., Martynkien, T., Statkiewicz, G., Szpulak, M., Olszewski, J., Golojuch, G., Urbanczyk, W., Wojcik, J., Mergo, P., Makara, M., Berghmans, F., and Thienpont, H., *Temperature and pressure sensitivities of the highly birefringent photonic crystal fiber with core asymmetry.* Applied Physics B-Lasers and Optics, 2005. **81** (2-3): p. 325-331.

32. Urbanczyk, W., Martynkien, T., Szpulak, M., Statkiewicz, G., Olszewski, J., Golojuch, G., Wojcik, J., Mergo, P., Makara, M., Nasilowski, T., Berghmans, F., and Thienpont, H. *Photonic crystal fibers: new opportunities for sensing - art. no. 66190G*. in *Proceedings of the 3rd European Workshop on Optical Fibre Sensors*. 2007. Naples, ITALY.

33. Geernaert, T., Luyckx, G., Voet, E., Nasilowski, T., Chah, K., Becker, M., Bartelt, H., Urbanczyk, W., Wojcik, J., De Waele, W., Dearieck, J., Terryn, H., Berghmans, F., and Thienpont, H., *Transversal Load Sensing With Fiber Bragg Gratings in Microstructured Optical Fibers.* Ieee Photonics Technology Letters, 2009. **21** (1-4): p. 6-8.

34. Geernaert, T., Nasilowski, T., Chah, K., Szpulak, M., Szewski, J., Statkiewicz, G., Wojcik, J., Poturaj, K., Urbanczyk, W., Becker, M., Rothhardt, M., Bartelt, H., Berghmans, F., and Thienpont, H., *Fiber Bragg gratings in germanium-doped highly birefringent microstructured optical fibers.* Ieee Photonics Technology Letters, 2008. **20** (5-8): p. 554-556.

35. Caucheteur, C., Lhomme, F., Chah, K., Blondel, M., and Megret, P. *Novel technique for the simultaneous measurement of strain and temperature using polarization maintaining fiber Bragg gratings*. in *Proceedings of 17th International Conference on Optical Fibre Sensors*. 2005. Brugge, BELGIUM.

36. Vlekken, J., *MASSFOS: Preliminary design report*. 2005: Geel, BELGIUM.

37. Johnson, K.L., *Contact Mechanics*. 1987, Cambridge: Cambridge University Press.

38. Wagreich, R.B., Atia, W.A., Singh, H., and Sirkis, J.S., *Effects of diametric load on fibre Bragg gratings fabricated in low birefringent fibre.* Electronics Letters, 1996. **32** (13): p. 1223-1224.

39. Beitz, W. and Küttner, K.-H., *Dubbel: Handbook of mechanical engineering*. 1994: Springer-Verlag.

40. Abe, I., de Goes, R.E., Fabris, J.L., Kalinowski, H.J., Muller, M., Fugihara, M.C., Falate, R., Diesel, B.W., Kamikawachi, R.C., and Barbosa, C.L., *Production and characterization of refractive index gratings in high-birefringence fibre optics.* Optics and Lasers in Engineering, 2003. **39** (5-6): p. 537-548.

41. Abe, I., Frazao, O., Schiller, M.W., Nogueira, R.N., Kalinowski, H.J., and Piinto, J.L., *Bragg gratings in normal and reduced diameter high birefringence fibre optics.* Measurement Science & Technology, 2006. **17** (6): p. 1477-1484.

42. Abe, I., Fugihara, M.C., Diesel, B.W., Kamikawachi, R.C., Fabris, J.L., Kalinowski, H.J., and Barbosa, C.L. *Modeling and production of high birefringence FOBG sensors*. in *Proceedings of 4th Iberoamerican Meeting on Optics and 7th Latin American Meeting on Optics, Lasers, and Their Applications*. 2001. Tandil, ARGENTINIA.

43. Abe, I. *Modeling and production of High birefringence FOBG sensors*. Available from: http://www.cpgei.cefetpr.br/~hypolito/artigos/optl-89.pdf.

44. Lawrence, C.M., Nelson, D.V., Udd, E., and Bennett, T., *A fiber optic sensor for transverse strain measurement.* Experimental Mechanics, 1999. **39** (3): p. 202-209.

45. Bosia, F., Giaccari, P., Botsis, J., Facchini, M., Limberger, H.G., and Salathe, R.P., *Characterization of the response of fibre Bragg grating sensors subjected to a two-dimensional strain field.* Smart Materials & Structures, 2003. **12** (6): p. 925-934.

46. Lawrence, C.M., Nelson, D.V., Bennett, T.E., and Spingarn, J.R. *Determination of process-induced residual stress in composite materials using embedded fiber optic sensors*. in *Proceedings of the Conference on Smart Sensing, Processing, and Instrumentation - Smart Structures and Materials 1997*. 1997. San Diego, CALIFORNIA (USA).

47. Udd, E., Schulz, W.L., and Seim, J.M. *Measurement of multidimensional strain fields using fiber grating sensors for structural monitoring*. in *Proceedings of the SPIE Conference on Fiber Optic Sensor Technology and Applications*. 1999. Boston, MASSACHUSSETS (USA).

48. Lo, Y.L., Sirkis, J.S., and Ritchie, K.T., *A study of the optomechanical response of a diametrically loaded high-birefringent optical fiber.* Smart Materials & Structures, 1995. **4**: p. 327-333.

49. Mawatari, T. and Nelson, D., *A multi-parameter Bragg grating fiber optic sensor and triaxial strain measurement.* Smart Materials & Structures, 2008. **17** (3).

50. Ye, C.C., Staines, S.E., James, S.W., and Tatam, R.P., *A polarization-maintaining fibre Bragg grating interrogation system for multi-axis strain sensing.* Measurement Science & Technology, 2002. **13** (9): p. 1446-1449.

51. Fernandez, A.F., Ottevaere, H., Van Ierschot, C., Panajatov, K., Berghmans, F., and Thienpont, H. *Multi-parameter force sensing with fiber Bragg grating sensors*. in *Proceedings of Symposium IEEE/LEOS Benelux Chapter*. 2002. Amsterdam, THE NETHERLANDS.

52. Guemes, J.A. and Menendez, J.M., *Response of Bragg grating fiber-optic sensors when embedded in composite laminates.* Composites Science and Technology, 2002. **62** (7-8): p. 959-966.

53. Suo, R., Chen, X.F., Zhou, K.M., Zhang, L., and Bennion, I. *In-fibre directional transverse loading sensor based on excessively tilted fibre Bragg gratings*. in *Proceedings of 19th International Conference on Optical Fibre Sensors*. 2008. Perth, AUSTRALIA.

54. Luyckx, G. and Voet, E., *MASSFOS: Detailed sensor configuration*. 2009: Gent.

55. Lawrence, C.M., Nelson, D.V., and Udd, E. *Measurement of transverse strains with fiber Bragg gratings*. in *Proceedings of the Conference on Smart Sensing, Processing, and Instrumentation - Smart Structures and Materials 1997*. 1997. San Diego, CALIFORNIA (USA).

56. Lo, Y.L., Sirkis, J.S., and Ritchie, K.T., *A study of the optomechanical response of a diametrically loaded high-birefringent optical fiber.* Smart Materials & Structures, 1995. **4** (4): p. 327-333.

57. Window, A.L. and Holister, G.S., *Strain Gauge Technology*. 1982, London: Applied Science Publishers LTD.

58. Abe, I., Kalinowski, H.J., Frazao, O., Santos, J.L., Nogueira, R.N., and Pinto, J.L. *Superimposed Bragg gratings in high-birefringence fibre optics: three-parameter simultaneous measurements*. in *Proceedings of 16th International Conference on Optical Fibre Sensor (OFS-16)*. 2003. Nara City, JAPAN.

59. Zhang, F. and Lit, J.W.Y., *Temperature and strain sensitivity measurements of high-birefringent polarization-maintaining fibers.* Applied optics, 1993. **32** (13).

60. Papp, A. and Harms, H., *Polarization optics of index-gradient optical-waveguide fibers.* Applied optics, 1975. **14** (10): p. 2406-2411.

61. Abdi, A.M. and Kost, A.R., *A fiber optic, Fabry-Perot strain gauge calibrator.* Smart Materials & Structures, 2007. **16** (5): p. 1931-1935.

62. Chah, K. and Van Roosbroeck, J., *MASSFOS: Critical design report*. 2006, FOS&S, Ghent University: Geel and Gent, BELGIUM.

63. Kühn, B. and Schadrack, R., *Thermal expansion of synthetic fused silica as a function of OH content and fictive temperature.* Journal of Non-Crystalline Solids, 2009. **355** (4-5): p. 323-326.

64. Leviton, D.B. and Frey, B.J. *Temperature-dependent absolute refractive index measurements of synthetic fused silica*. 2007; Available from: http://ntrs.nasa.gov/archive/nasa/casi.ntrs.nasa.gov/20070018851_2007019043.pdf.

Chapter 3 : MULTI-AXIAL STRAIN SENSOR

In Figure 3-1 the structural health monitoring scheme of Chapter 1 is repeated, and the multi-axial strain sensor is highlighted. In this chapter, the need for such a sensor is evaluated. Afterwards, a multi-parameter or multi-axial strain sensor based on optical FBGs is designed. A diverse response for the parameters of interest (axial strain, transverse strain, and temperature) is aimed for.

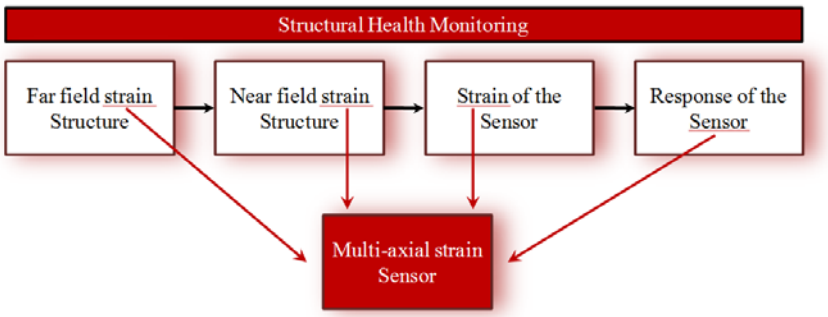

Figure 3-1: Flow chart of the different steps necessary for structural health monitoring using an embedded optical fibre sensor. The necessary multi-axial strain sensor is highlighted.

3. 1. INTRODUCTION

Fibre optic Bragg grating sensors are mostly used for longitudinal strain measurements and are, as such, well documented in literature [1-7]. They have found increased use in surface monitoring of mechanical components as well as civil structures. However, by embedding these sensors in e.g. composite structures it is feasible to obtain strain data from the inside of the material, which has two important advantages compared to surface mounted sensors. The first is the protection of the sensor from environmental effects, excluding the need for a protective coating. Secondly, the measurement is taken inside the material which is favorable for structural health monitoring and detecting damage of e.g. composite structures.

Embedded sensors are exposed to the total strain field present inside the structure which makes interpretation of the sensor response not straightforward. Since transverse strain components can and will be present in the material (Figure 3-2), their influence on the Bragg peak response should be estimated which is impossible using the direct reflected spectrum of uni-axial FBGs. Transverse strain and force

measurements with uni-axial FBGs are, however, possible, based on the identification of the differential group delay and polarization dependent loss [8, 9]. Though, these methods are very intricate to implement in practical structural health monitoring schemes. Therefore this chapter focuses only on the use of HiBi fibres with Bragg grating.

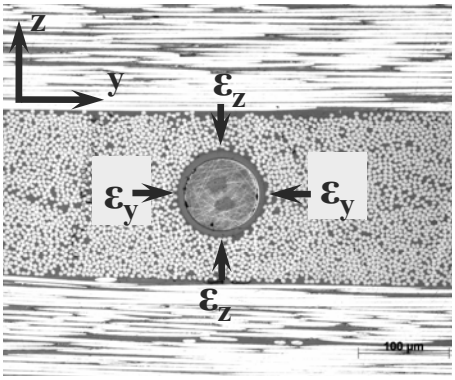

Figure 3-2: The influence of the transverse strain components onto the embedded optical fibre sensor.

Transverse strains are likely to occur in thick-walled composite specimens subjected to out-of-plane loading. As an example, a curved composite beam subjected to torque loading introduces a complex stress field inside the material (Figure 3-3).

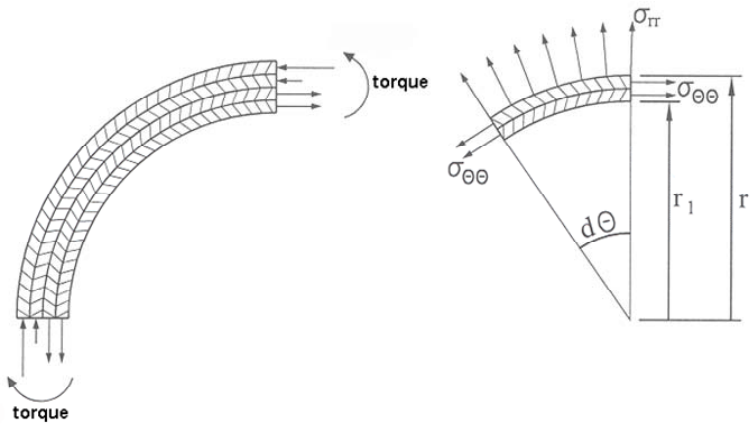

Figure 3-3: Curved composite structure subjected to torque loading , which introduce a complex stress field inside the material.

An example of critical areas in a composite structure are the stiffener-to-skin joints of a fuselage. A complex strain pattern exists due to load transfer in these joints (Figure 3-4)

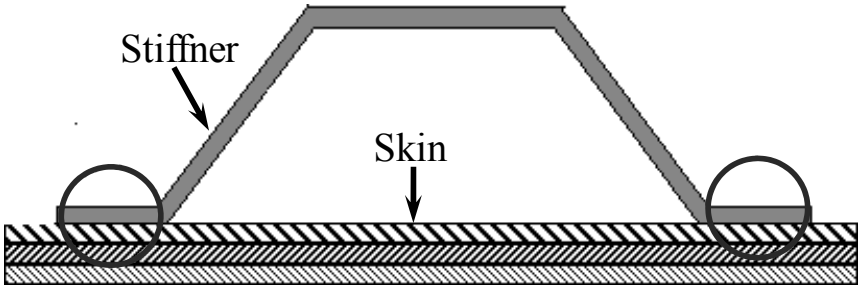

Figure 3-4: Schematic of an omega shaped stiffener, highlighting the regions of interest for measuring the total strain field during flight [10].

Complex strain monitoring of an in-service structure would greatly enhance the insight and confidence in the (long-term) behaviour of high performance composite structures. The feedback from recorded loads, deformations and temperatures of (parts of) existing structures in real conditions (i.e. structural health monitoring), can lead to very valuable information for design conditions.

Designing a multi-parameter or multi-axial strain sensor based on optical FBGs should meet several basic requirements:[11]

- The optical fibre sensor should show a high sensitivity for all the strain components. The sensitivity of an FBG sensor for various strain components was already discussed in Chapter 2.
- The optical fibre sensor should be designed such that it shows a diverse response for the parameters of interest (axial strain, transverse strain, and temperature). This resolving power should be high enough to make possible distinction between the different strain components and if needed also temperature.
- The optical fibre sensor should reduce the composite distortion as much as possible. This topic will be discussed in Chapter 4.
- The coating of the optical fibre sensor should be able to provide a good longitudinal strain transfer between the composite structure and the glass fibre itself. This topic will be discussed in Chapter 4.
- It is of vital importance that the optical fibre sensor survives the composite manufacturing process (high temperature and pressure loading during curing in a autoclave process). The response of the sensor during curing will be discussed in Chapter 6.

- The optical fibre should be resistant to the loading conditions of the composite structure, since it is impossible to repair a broken optical fibre inside a structure. The optical fibre sensor should remain functional for the life of the structure. The failure strain of an optical fibre reaches up to 5% [12-15] which is more than high enough in normal operating conditions.

In this chapter, first, a literature overview on multi-parameter strain sensing is given. Secondly, a new sensor design for measuring the total strain field (axial and two transverse components) with embedded FBGs is proposed. In addition the strain resolution of this sensor and a feasibility study (combined FE modeling and experiments) are discussed.

3. 2. MAPPING MULTI-COMPONENT STRAIN FIELDS: A LITERATURE REVIEW

In this section a literature review on how different authors measure multi-parameter strain or load components is given. The different approaches can be subdivided in configurations in which multiple LoBi fibres with FBG are used and designs based on HiBi-fibres with FBGs. Whenever possible, the notation of the cited authors is altered to the one used in this work to simplify comparison between the different presented configurations.

Similar to conventional electrical resistance strain gauges, FBGs can be applied in a rosette configuration (Figure 3-5) [16-18]. A rosette consists of three sensors and is designed to determine the direction and magnitude of the principal in-plane strains. The advantage of using the optical counterpart of this rosette is the reduction of wiring and size of such an ‘electrical’ rosette. An electrical strain gauge rosette needs at least 6 electrical wires per sensor while the optical one needs only one optical fibre. The minimum dimensions are restricted by the minimum bend radii of the fibre needed to avoid too many bending losses.

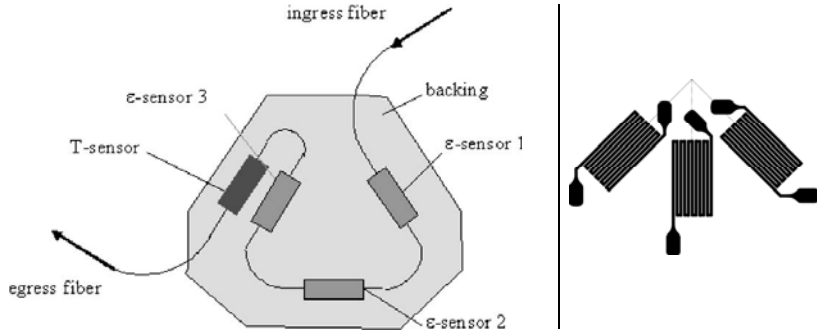

Figure 3-5: Left, FBG rosette (Δ-configuration) with temperature compensation.[16]. At the right, a classical electrical strain gauge rosette (W-configuration).

Fernandez et al [19] used and calibrated 8 multiplexed uni-axial FBGs mounted on an elastic transducing body to work as a compact multi-component force sensor (measuring longitudinal force and torque). The design is based on a Maltese-cross-shaped elastic transducer (Figure 3-6).

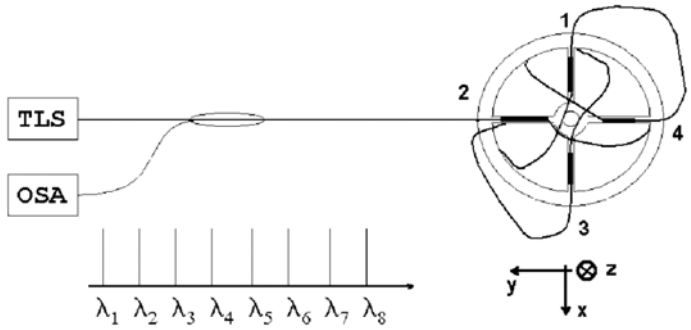

Figure 3-6: Up, schematic view of a multi-component force sensor (Force and torque) based on eight multiplexed FBG strain sensors [19].

Both designs (strain rosette and Maltese-cross) can be attached to the surface of a structure and respond to the in-plane strain components present at the surface. However, to measure the internal strain field of the structure, embedded sensors are needed.

Matrat et al. and Levin and Matrat [20, 21] tried to determine the in-plane strains of a composite specimen by embedding four optical fibres with Bragg grating parallel to the reinforcing fibres in the 0 deg, +45 deg and 90 deg plies of a quasi-isotropic graphite–epoxy laminate. This sensor configuration has only numerically been demonstrated to be viable for point-like measurements of in-plane strains and temperature change. The largest error in the determined in-plane strain components

was in all cases less than 3%. However, to determine the temperature change, one of the four sensors must have a significantly different response to temperature. When the fibres are embedded with a distance of at least two plies in between, no significantly disturbing effect from one sensor to the others was observed.

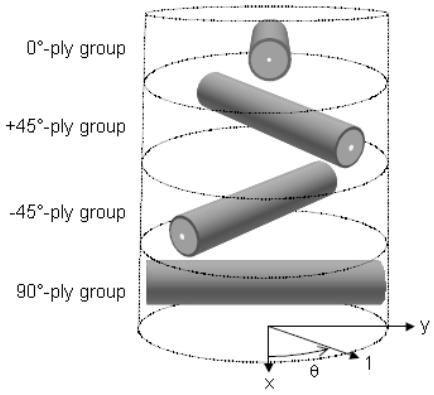

Figure 3-7: Three dimensional scheme close-up of a sensor configuration for measuring in-plane strain and temperature in a composite laminate [20].

The previous discussed sensor configuration is not able to measure the out-of-plane transverse strains, though they are claimed to give a good estimate of the in-plane strains at a certain location. To measure the transverse out-of-plane strains uni-axial FBGs are not sufficient and should be replaced by multi-axial strain FBGs. Not all of the reviewed configurations reported in the following paragraphs have the intention to measure one or more strain components. However, they will be discussed since they were considered for the new designed sensor configuration.

Suo et al. [22] fabricated highly tilted (81 deg) fibre Bragg gratings (Figure 3-8). These tilted fibre Bragg gratings (TFBGs) have a periodic refractive index change which is no longer perpendicular (0 deg) with respect to the optical fibre. Suo et al. experimentally observed a pronounced polarization mode splitting effect caused by the grating. They further investigated the polarization property of such gratings under transverse load and found that TFBGs with excessively tilted structures exhibit distinctive directional polarization mode coupling behaviour under transverse load (Figure 3-9). When load is applied to the equivalent slow axis of the TFBG, the light coupling to the two polarization modes is changing accordingly with the load, thus providing a mechanism to measure the amplitude of transverse load. However, when load is applied to the grating's equivalent fast axis, no light coupling change is observed. As the load induces the transmission loss change, it is possible to measure a load change as small as 1.6×10^{-5} kg. By employing multiple TFBGs with their slow axes pointing to different angles, an optical fibre load sensor

system could be developed with the capability of not just measuring the amplitude but also recognizing the direction of the applied load. However, the disadvantage of such a sensor is the dependency of the FBG response to the light power. Bending losses or changes in the source power could, as such, give rise to big errors in the measurement results! An additional difficulty is related to mass fabrication of such gratings.

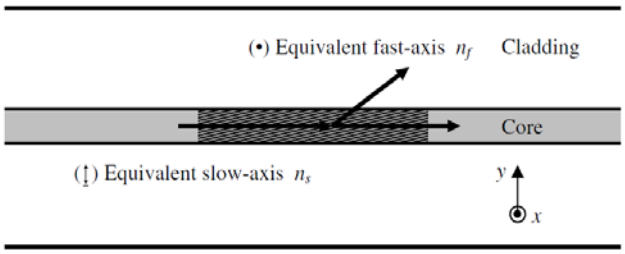

Figure 3-8: Schematic diagram of an 81◦ TFBG with its two orthogonal polarization axes [22].

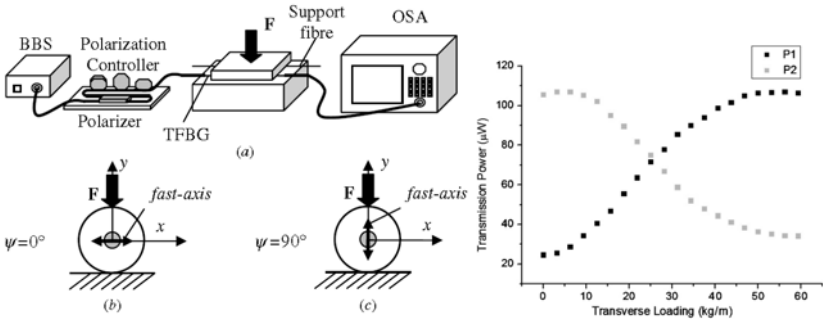

Figure 3-9: (a) Schematic overview of the transverse loading experiment system. The cross section of the TFBG with transverse load applied along slow (b) and fast (c) axes. Transmitted light power for the two orthogonal polarization modes measured using a tunable laser and power meter with the load applied along the equivalent slow axis.[22]

Chen et al. [23] produced a fibre Bragg grating in a novel HiBi-fibre (quasi-rectangle bow-tie fibre depicted in Figure 3-10) and demonstrated its feasibility towards measurement of temperature and gas pressure (which can be seen as a homogenous transverse load onto the fibre). The grating has two Bragg wavelengths and the difference between them is 0.77 nm at room temperature. The two Bragg wavelengths of the grating have different temperature sensitivities and almost the same hydrostatical pressure sensitivity which indicates that the grating can be used to measure temperature and hydrostatical pressure simultaneously. The

measurements of temperature and pressure deviated less than 1°C and 0.5 MPa from the set values.

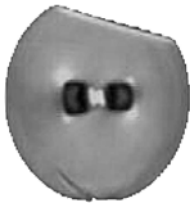

Figure 3-10: Cross-section of the ''quasi-rectangle'' Hi-Bi fibre. The two dark spots are the SAPs. [23]

Silva et al. [24] configured a sensing head based on two fibres with Bragg grating arranged in a twisted configuration to measure three parameters simultaneously, namely temperature, strain, and transverse load (Figure 3-11). One of the gratings is written in a HiBi-fibre and provides two distinct spectral signatures, which together with the signature of the second grating and the geometric characteristics of the sensing head dispose of the degrees of freedom required to achieve the simultaneous measurement functionality. The resolutions achieved with this configuration for the measurement of temperature, strain and transverse load are ±3.1 °C, ±46 με and ±0.01 N/mm, respectively. The biggest disadvantage in embedding this sensor type, is the unknown interaction between both gratings.

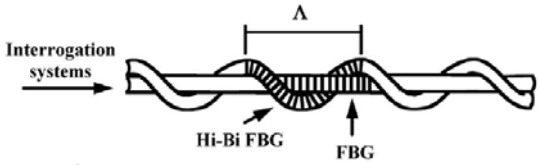

Figure 3-11: Multi-parameter sensor based on two twisted fibres with Bragg grating [24].

Sirkis and Lo [25] designed a surface-mounted optical fibre sensor to simultaneously measure axial and transverse strains. The design is based on the combined use of Michelson and polarimetric fibre optic sensors. These sensors can separate the effects of axial strain from transverse strain in the specific case that the transverse strain components are equal ($\varepsilon_{1'} = \varepsilon_{2'}$). This condition limits the feasibility as an embedded sensor. Singh and Sirkis [26] described an optical fibre sensor that uses an intrinsic Fabry-Perot interferometer and an in-line fibre etalon sensor to simultaneously measure two parameters: either axial and transverse strain (once more the necessary condition is that $\varepsilon_{1'} = \varepsilon_{2'}$) or axial strain and temperature. Jin et al. [27] embedded a similar sensor (Figure 3-12) consisting of a Bragg grating

with an adjacent in-line fibre etalon in a transversely isotropic, unidirectional specimen and loaded the specimen with uni-axial stress. The sensor, which was embedded parallel to the reinforcing fibres, enabled determination of the longitudinal and transverse strain in the sensor and surrounding host material, for the specific case of equal transverse strains in both directions ($\varepsilon_{1'} = \varepsilon_{2'}$).

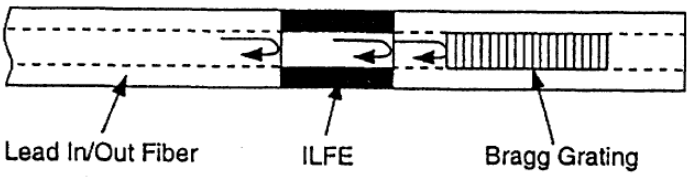

Figure 3-12: Multi-parameter sensor configuration consisting of a Bragg grating with an adjacent in-line fibre etalon [27].

Black et al. and Udd et al.[28-30] embedded a multi-axial strain sensor (FBG in HiBi-fibre) in a biaxial-woven composite and demonstrated that big strain gradients occur during curing. No quantitative analysis was performed for this research. Wang [31] did the same as Black et al. [28], though developed a theoretical model to predict the differences in sensor response to transverse loadings applied uniformly and non-uniformly along the length of the sensor. A study of the spectral response of a FBG fabricated in a high birefringence fibre subjected to transverse stress gradients has been presented with a theoretical model and numerical simulations. At this point it should be noted that in this dissertation, only homogenously transverse strains and thus no strain gradients will be taken into account. Abe et al. [32] used a pair of fibre Bragg gratings written in a HiBi-fibre to measure simultaneously longitudinal and transverse strain and temperature. The FBGs were superimposed as to have a point like sensor. The first FBG had a central wavelength of 1535 nm and the second one 1547 nm. The birefringence of the internal elliptical cladding fibre used in this study was 5.7×10^{-4} , which was derived from the polarization splitting of the reflection spectra of each grating (about 0.8nm). Next, Abe et al. discussed the difficulty to accurately determine both peaks of one Bragg peak spectrum when these come closer to each other. Both sensors were calibrated for longitudinal load and temperature and for a transverse load along the fibre's fast axis. Pressing the fibre on the cladding parallel to its fast axis, gives rise to a differential transverse strain state ($\varepsilon_{1'} - \varepsilon_{2'}$) inside the core of the optical fibre (section 2. 4. 1) which is further called $\Delta\varepsilon_F$. The strain and temperature sensitivities are determined using a set of equations that can be written as

$$\begin{bmatrix} \Delta T \\ \Delta \varepsilon_F \\ \Delta \varepsilon_{3'} \end{bmatrix} = K^{-1} \begin{bmatrix} \Delta \lambda_{B1,1'} \\ \Delta \lambda_{B1,2'} \\ \Delta \lambda_{B2,2'} \end{bmatrix} \quad \textbf{3-1}$$

The sensor was not embedded in a composite material, but tested with a calibration device as discussed in section 2.4.1.b. First a longitudinal tensile force was applied with the micrometer set-up, afterwards a transverse load can be applied over the fibre and the temperature is set by a cooling-heating system. By recording the wavelength shifts and using the recorded *K*-matrix of equation 3-1, the temperature and the strain components were calculated. Reported errors were large; up to 12°C for temperature measurements between 15°C and 45°C, 11 με for differential transverse strain measurements in the range of 12 to 32 με and 74 με for longitudinal measurements in the range of 167 to 251 με. This is due to the bad conditioning of the *K*-matrix of equation 3-1 (condition number = ~113 according to the author's calculations). The condition number will be discussed more in detail in Section 3. 3.1. b. . Abe et al. [33] repeated their experiments for measuring only temperature and differential transverse strain ($\Delta\varepsilon_F$) using a chemically etched IEC HiBi-fibre. During the experiments the longitudinal strain was kept constant. One should be aware that this is not at all representative for realistic strain fields encountered by embedded FBGs. Equation 3-1 is thus reduced to:

$$\begin{bmatrix} \Delta T \\ \Delta \varepsilon_F \end{bmatrix} = K \begin{bmatrix} \Delta \lambda_{B,1'} \\ \Delta \lambda_{B,2'} \end{bmatrix} \quad \textbf{3-2}$$

where the non-singular *K*-matrix representing the FBG spectral sensitivities is given by

$$K = \begin{bmatrix} \dfrac{\delta \lambda_{B,1'}}{\delta T} & \dfrac{\delta \lambda_{B,1'}}{\delta (\varepsilon_{2'} - \varepsilon_{1'})} \\ \dfrac{\delta \lambda_{B,2'}}{\delta T} & \dfrac{\delta \lambda_{B,2'}}{\delta (\varepsilon_{2'} - \varepsilon_{1'})} \end{bmatrix} \quad \textbf{3-3}$$

Experiments were performed using a transverse loading set-up. For the etched IEC fibre sensor, differential transverse strain has been evaluated with an error of ±16 με for set values in the interval between 33 and 94 με, whilst the error on temperature has been estimated to be ±3°C for set values ranging from 16 to 56°C. These values were compared to results obtained for a normal diameter IEC sensor that has strain values evaluated with an error of ±15 με for set values in the interval between 61 and 91 με and this had an error on temperature estimated to be ±4°C for set values ranging from 12 to 46°C [34].

Lawrence et al. [35] created a fibre optic sensor capable of measuring two independent components of transverse strain when temperature and axial strain are kept zero or constant. The sensor consists of a single Bragg grating written into a HiBi optical fibre (IEC type according to Figure 3-13) with a central wavelength of 1550 nm. Assuming an error in the measurement of wavelength shift of 10 pm the transverse strain error becomes ±27 με (condition number of *K*-matrix = ±4). This seems acceptable for many applications, however this estimate does not include errors in the elements of *K* that may arise from non-linearities, cross-sensitivity, experimental error and uncertainties in the strain predicted by the finite element model.

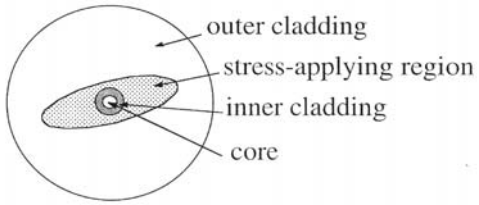

Figure 3-13: Schematic cross-section of a IEC type HiBi optical fibre used by Lawrence et al. [35].

Evidently, significant limitation of the sensor described in their work is that axial strain and temperature changes will affect the measurement of transverse strains. This limits the use of the sensor to isothermal applications and applications where plane strain or plane stress assumptions can be used to relate the axial strain to the transverse strain components. Lawrence et al suggested to expand the capability of the sensor by using a second grating written at a sufficiently different wavelength at exact the same spot. The set of equations relating wavelength shifts to strain components and temperature, can then generally be written as:

$$\begin{bmatrix} \Delta\lambda_{B1,1'} \\ \Delta\lambda_{B1,2'} \\ \Delta\lambda_{B2,1'} \\ \Delta\lambda_{B2,2'} \end{bmatrix} = K \begin{bmatrix} \Delta\varepsilon_{1'} \\ \Delta\varepsilon_{2'} \\ \Delta\varepsilon_{3'} \\ \Delta T \end{bmatrix} \qquad \textbf{3-4}$$

In the next section, the theoretical resolution and condition number of the *K*-matrix of such a sensor will be discussed.

The multi-parameter sensor described in Mawatari et al. [36], is theoretically capable of simultaneously measuring three strain components and temperature changes. The sensor design was first described by Udd et al. and Lawrence et al. [35, 37]. It consists of a HiBi optical fibre with Bragg gratings having two different

wavelengths, one around 1300 nm and the other around 1550 nm. First, a linearized 3 × 3 *K*-matrix was used to calculate the tri-axial strain components, from three measured peak wavelength shifts.

$$\begin{bmatrix} \Delta\lambda_{B1,1'} \\ \Delta\lambda_{B2,1'} \\ \Delta\lambda_{B2,2'} \end{bmatrix} = K \begin{bmatrix} \Delta\varepsilon_{1'} \\ \Delta\varepsilon_{2'} \\ \Delta\varepsilon_{3'} \end{bmatrix} \quad \textbf{3-5}$$

Predictions of the longitudinal strain were relatively good (errors of 1 to 10%), but very bad for transverse strains (errors of 10 to 100%). The condition number of the *K*-matrix in Equation 3-5 was found to be ~31. A generalized non-linear model was then developed to express the wavelength shifts as a function of the loads applied during a sensor calibration tests. It is based on a 4 × 4 *K*-matrix with constant coefficients in the first and fourth column to reflect the observed linearity in wavelength shifts versus longitudinal load and temperature change. The second and third columns contained variable coefficients to reflect the observed non-linearity in wavelength shifts versus transverse load.

An overview of the higher discussed different configurations (principle, measure parameters, condition number calculated by the author of this dissertation, error, and various remarks) is given in Table 3-1.

Table 3-1: Overview of different multi-parameter sensor designs described in literature

Reference	Principle	Measured physical quantities	Condition number	Reported error	Remarks
Betz et al. [16] and Haran et al. [18]	Strain gauge rosette based on uni-axial FBGs	In-plane strain components at the surface	-	-	Out-of-plane strains cannot be measured. The sensor cannot be embedded.
Matrat and Levin [20, 21]	Embedded strain gauge rosette based on uni-axial FBGs	In-plane strain components interior to the structure	-	-	Out-of-plane strains cannot be measured
Suo et al. [38]	Highly tilted (81deg) uni-axial FBG	Magnitude and direction of the transverse load	-	-	Measurement depends on the optical power which can be affected by light source variations due to bending losses. Longitudinal strains cannot be simultaneously evaluated with the transverse strain components.
Chen et al. [23]	Novel HiBi (quasi-rectangle bow-tie fibre)	Pressure and temperature	-	ΔT =1°C ΔP =0.5MPa =±5bar	Transverse load should be hydrostatic. With only one grating the longitudinal effect is not measurable

Reference	Principle	Measured physical quantities	Condition number	Reported error	Remarks
Silva et al. [24]	Combination of a uni-axial FBG twisted around a HiBi-FBG	Transverse line load, longitudinal strain and temperature	-	ΔT=3.1°C $\Delta\varepsilon$=±46 με ΔF=±0.01 N/mm	When embedding this configuration the interction between both fibres becomes uncertain
Singh and Sirkis [26] Jin et al. [39]	Combination of a in-line fibre etalon with an intrinsic Fabry perot interferometer and an FBG respectively.	Axial and transverse strain or axial strain and temperature	-	-	Both transverse strain components have to be equal, which is generally not the case for embedded sensors
Black et al. [28] Udd et al. [30]	FBG in HiBi-fibre	Transverse strain gradients	-	-	No quantitative results were presented. Impossible to measure all the strain components with only one FBG.
Abe et al. [32]	Two FBGsin HiBi-fibre	Longitudinal strain, temperature and differential transverse strain	~113	ΔT=15°C $\Delta\varepsilon_F$ =±11 με $\Delta\varepsilon_3$ =± 74 με	The identification of both transverse strain components was not considered which is necessary for an embedded sensor

Reference	Principle	Physical quantity	Condition number	Printed error	Remarks
Abe et al. [33]	Two FBGs in chemically etched HiBi-fibre		~5	ΔT=3°C $\Delta\varepsilon_F$ =±16 με	The identification of both transverse strain components was not considered which is necessary for an embedded sensor. Longitudinal strain was not taken into account.
Lawrence et al. [35]	One FBG in HiBi-fibre	Transverse strain components	~4	$\Delta\varepsilon_{1'}$ =±27 με $\Delta\varepsilon_2$ =± 27 με	Error results were calculated considering an interrogator with a wavelength shift resolution of 10pm. Longitudinal strain and temperature were not considered.
Mawatari et al. [36]	Two FBGs in HiBi-fibre	Tri-axial strain components	~31	$\Delta\varepsilon_{1'}$ =10-100% $\Delta\varepsilon_2$ =10-100% $\Delta\varepsilon_3$ =1-10%	Reported errors are unacceptably high. Good for embedding purposes. A model was developed to determine the strain components when a fibre is loaded under a certain angle with respect to its optical eigenaxis.

3. 3. STUDIED SENSOR CONFIGURATIONS

3. 3. 1. Measuring principle

The multi-axial sensor configurations described in this section are based on a combination of two FBGs at different wavelengths in commercially available HiBi-fibre (Panda, bow-tie, elliptical cladding, etc.). Chehura et al [40] gave a good overview of the different types of commercially available HiBi-fibres. As described before, due to the difference in refractive index of the two polarization axes, both polarization modes will satisfy the Bragg condition at different wavelengths. Therefore, gratings written in such a fibre will reflect two distinct peaks, one for each polarization axis. As described in Chapter 2, the separation of the two peaks is directly proportional to the birefringence of the fibre. A change in axial strain or temperature will not affect the birefringence of the fibre, but will cause an overall shift of the refractive indices towards higher or lower values. This results in a similar shift in Bragg wavelength for the peaks from both polarization axes, as shown in Figure 3-14. If on the other hand a change in transverse strain is applied, a change of the birefringence of the fibre will occur which results in a change of the peak separation, shown in Figure 3-14. Depending on the direction of the applied transverse strain with respect to the polarization axes of the fibre, the wavelength shift will increase or decrease.

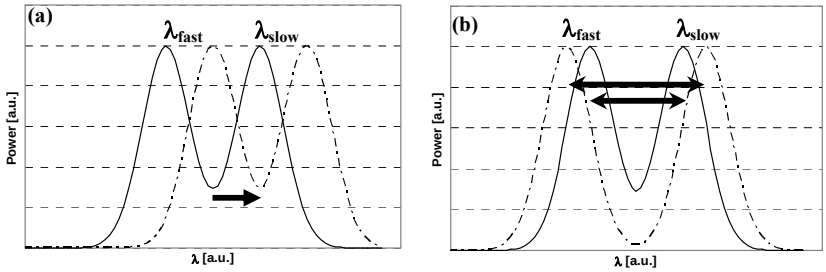

Figure 3-14: Effect on the spectral response of a HiBi-FBG due to (a) axial stress or uniform temperature change and (b) transverse stress. Original spectrum in full line and resulting spectrum due to the applied load in dashed line.

By adding an extra FBG, 4 different wavelengths are obtained. If these two gratings respond differently on external perturbations like axial and transverse strain components one can build a multi-axial strain sensor. The relation between wavelength shifts ($\Delta\lambda_B$) and change in strain components ($\Delta\varepsilon$) can be written in the following general form:

$$\begin{bmatrix} \Delta\lambda_{B1,1'} \\ \Delta\lambda_{B1,2'} \\ \Delta\lambda_{B2,1'} \\ \Delta\lambda_{B2,2'} \end{bmatrix} = K \begin{bmatrix} \Delta\varepsilon_{1'} \\ \Delta\varepsilon_{2'} \\ \Delta\varepsilon_{3'} \end{bmatrix} \quad \textbf{3-6}$$

herein the *K*-matrix equals:

$$K = \begin{bmatrix} K_{11} & K_{12} & K_{13} \\ K_{21} & K_{22} & K_{23} \\ K_{31} & K_{32} & K_{33} \\ K_{41} & K_{42} & K_{43} \end{bmatrix} \quad \textbf{3-7}$$

The coefficients K_{ij} are dependent on the used sensor configuration. By inverting this matrix one can calculate the total strain field interior to a composite structure based on the measured wavelength shifts. However, to invert this matrix, it should be square. Since the set of equations of equation 3-6 has four equations and only three independent unknowns, one of the equations can be omitted. Equation 3-6 then becomes:

$$\begin{bmatrix} \Delta\lambda_{B1,1'} \\ \Delta\lambda_{B1,2'} \\ \Delta\lambda_{B2,2'} \end{bmatrix} = K \begin{bmatrix} \Delta\varepsilon_{1'} \\ \Delta\varepsilon_{2'} \\ \Delta\varepsilon_{3'} \end{bmatrix} \quad \textbf{3-8}$$

in which *K* equals:

$$K = \begin{bmatrix} K_{11} & K_{12} & K_{13} \\ K_{21} & K_{22} & K_{23} \\ K_{31} & K_{32} & K_{33} \end{bmatrix} \quad \textbf{3-9}$$

The strain components can be calculated, by inverting the *K*-matrix and multiplying this with the wavelength shifts. Equation 3-8 becomes:

$$\begin{bmatrix} \Delta\varepsilon_{1'} \\ \Delta\varepsilon_{2'} \\ \Delta\varepsilon_{3'} \end{bmatrix} = K^{-1} \begin{bmatrix} \Delta\lambda_{B1,1'} \\ \Delta\lambda_{B1,2'} \\ \Delta\lambda_{B2,2'} \end{bmatrix} \quad \textbf{3-10}$$

3. 3. 2. Error analysis

For each configuration, the condition number of the *K*-matrix (or its inverse) can be calculated. The condition number of a matrix provides an indication of the numerical stability of the system of equations. A large condition number for the *K*-matrix indicates that small errors in the measurement of a wavelength shift or in the determination of the matrix coefficients can result in large errors in the

calculation of the strains. This condition number will be calculated for the different proposed sensor configurations. The condition number is used to provide a qualitative estimate of the sensor behavior, with the best sensor designs achieving the lowest condition number. However, this approach is of limited real value since it allows only a loose estimate of the maximum error bound to be calculated. To evaluate the effects of small errors in measured wavelength shifts on the measurement of strain, an error analysis of the type described by Jin et al. [41] can be performed.

The assessment of the strain components is influenced by different errors that include the precision with which the wavelength shifts can be determined and any error present in the estimation of the elements of the *K*-matrix which is determined from calibration experiments. In matrix formulation equation 3-8 can be written as:

$$\left[\Delta\lambda\right] = K\left[\Delta\varepsilon\right] \qquad \textbf{3-11}$$

In which $\left[\Delta\lambda\right] = \begin{bmatrix} \Delta\lambda_{B1,1'} \\ \Delta\lambda_{B1,2'} \\ \Delta\lambda_{B2,2'} \end{bmatrix}$ and $\left[\Delta\varepsilon\right] = \begin{bmatrix} \Delta\varepsilon_{1'} \\ \Delta\varepsilon_{2'} \\ \Delta\varepsilon_{3'} \end{bmatrix}$.

Assuming that both wavelength shift determination and *K*-matrix have errors, we can say that:

$$\begin{aligned} \left[\Delta\lambda\right] &= \left[\Delta\lambda\right]_0 + \delta\left[\Delta\lambda\right] \\ K &= K_0 + \delta K \end{aligned} \qquad \textbf{3-12}$$

Where $\left[\Delta\lambda\right]_0$ and K_0 represent respectively the true values of $\left[\Delta\lambda\right]$ and K; $\delta\left[\Delta\lambda\right]$ and δK represent the errors on the components of equation 3-11. In this chapter δK has been neglected since it depends less on the configuration of the sensor and more on the calibration of the gauge factors. The error on the wavelength determination $\delta\left[\Delta\lambda\right]$ can be written as

$$\delta\left[\Delta\lambda\right] = \begin{bmatrix} \delta\Delta\lambda_{B1,1'} \\ \delta\Delta\lambda_{B1,2'} \\ \delta\Delta\lambda_{B2,2'} \end{bmatrix} \qquad \textbf{3-13}$$

The error in recovering the different strain components $\delta\varepsilon_i = \varepsilon_i - \varepsilon_{0,i}$ ($i = 1, 2, 3$) may be calculated as:

$$\delta\left[\varepsilon\right] = K_0^{-1}\delta\left[\Delta\lambda\right] \qquad \textbf{3-14}$$

The parameters $\delta\Delta\lambda_{Bi,j'}$ represent the resolution of the used interrogator. Since all wavelengths are measured with the same interrogator (FBG-scan 608 from FOS&S [42]) they are all equal:

$$\delta\Delta\lambda_B = \delta\Delta\lambda_{B1,1'} = \delta\Delta\lambda_{B1,2'} = \delta\Delta\lambda_{B2,2'} = \sim 1pm \qquad \textbf{3-15}$$

This resolution can be used instead of the uncertainty in the interrogator which is typically one to a few tens of pm, since, in this dissertation, the measurements are differentially encoded in the wavelength separation between two peaks in a very small wavelength window and do not require an absolute wavelength measurement.
The different errors for the strain components can then be found as

$$\begin{aligned}
\delta\varepsilon_1 &\le \frac{(|K_{22}K_{33} - K_{23}K_{32}| + |K_{13}K_{32} - K_{12}K_{33}| + |K_{12}K_{23} - K_{13}K_{22}|)}{\Delta}\delta\Delta\lambda_B \\
\delta\varepsilon_2 &\le \frac{(|K_{31}K_{23} - K_{21}K_{33}| + |K_{11}K_{33} - K_{13}K_{31}| + |K_{21}K_{13} - K_{11}K_{23}|)}{\Delta}\delta\Delta\lambda_B \\
\delta\varepsilon_3 &\le \frac{(|K_{21}K_{32} - K_{22}K_{31}| + |K_{12}K_{31} - K_{11}K_{32}| + |K_{11}K_{22} - K_{12}K_{21}|)}{\Delta}\delta\Delta\lambda_B
\end{aligned} \qquad \textbf{3-16}$$

in which Δ is the determinant of the *K*-matrix.
The method of Jin et al. [41] gives an overestimation of the error because it assumes a worst case scenario in which the errors will be accumulative. This is not the case in a realistic situation because of the opposite wavelength sensitivity of the transverse strain components ($-\frac{1}{2}n_{eff,1'}^2 p_{11}$, and $-\frac{1}{2}n_{eff,1'}^2 p_{12}$ which are negative) and the longitudinal strain component ($1-\frac{1}{2}n_{eff,1'}^2 p_{12}$ which is positive). Therefore, one can switch to simple statistics and calculate the variance ($Var([\varepsilon])$) and the standard deviation σ_ε, on the calculated strain ($[\varepsilon]$) if a certain variance exists on the wavelength shifts($Var([\Delta\lambda])$).

$$Var(\varepsilon_i) = \left(\left(K_{i,1}^{-1}\right)^2 + \left(K_{i,2}^{-1}\right)^2 + \left(K_{i,3}^{-1}\right)^2\right) Var([\Delta\lambda]) \qquad \textbf{3-17}$$

The standard deviation on the calculated strain ($[\varepsilon]$) then becomes:

$$\sigma_{\varepsilon,i} = \sqrt{Var(\varepsilon_i)} \qquad \textbf{3-18}$$

The error $\delta\varepsilon$ and standard deviation σ_ε on the calculated strains $[\varepsilon]$ will be discussed in the next sections for different sensor configurations.

3. 3. 3. Resolution of the different configurations

In order to define the optimal monitoring system, numerical analyses have been performed on three different sensor configurations [43]. In Table 3-2 the fibre material properties, needed to calculate the sensor resolution for each configuration are summarized. By comparing the condition numbers of the *K*-matrices, one can conclude which configuration will lead to the best discrimination potential. In addition an error analysis as in the previous section has been performed. For the estimation of the error, we use the strain optic coefficients and thus gauge factors of FBGs written in HiBi-fibre determined in 2. 4. 1 c..

Table 3-2: Properties used to determine the gauge factors, condition numbers and strain resolution of each sensor configuration.[44]

Young's Modulus	Poisson coefficient	Strain-optic coefficients	Refractive index	Birefringence
E = 70 GPa	$\nu = 0.17$	$p_{11} = 0.111$ $p_{12} = 0.247$	n = 1.458	$\Delta n = 3.3*10^{-4}$

The following assumptions were made:

- For the analyses, a bow-Tie fibre was considered. However, the final results and conclusions are also indicative for other fibre types.
- For each sensor we assume that the temperature is a known parameter (determined by an independent measurement with e.g. a thermocouple) and that only the unknown tri-axial strain state needs to be calculated.
- The strain errors and standard deviations are calculated by assuming that the interrogation equipment has a resolution of 1 pm.
- The results are calculated for a non-embedded fibre. One should be aware that embedding the fibre will have a less good resolving power. This is dependent on the host material (e.g. difference in mechanical properties of glass- and carbon-reinforced epoxy) in which the fibre is embedded. Therefore, the conditioning of the *K*-matrix should be as low as possible. The embedding method and additional strain error will be discussed in Chapter 4.
- The resolution of each configuration is determined using only the strain dependency of the fibre core. The strain transfer, of a randomly applied load on the fibre cladding to the fibre core is neglected. For example the strain field induced by a line load oriented parallel with the slow axis of the fibre is different from the case that the load is oriented parallel with the fast axis. In the determination of a good configuration we neglect the fact that

the HiBi-fibres are non isotropic. Thus, SAPs only play part in the initial birefringence and have no mechanical influence. In Chapter 4 we will consider this anisotropy for the chosen sensor configuration.

The first configuration is called the parallel configuration and is illustrated on Figure 3-15. Two FBGs with a different central wavelength (around 1300 nm and 1550 nm) are inscribed in two bow-tie fibres. Both fibres are spliced together with one fibre rotated 90deg compared to the other. As such, the fast axis of the first fibre is aligned with the slow axis of the second fibre and vice versa. Since the splice makes this configuration extremely vulnerable one can choose to embed two parallel fibres (Figure 3-15, inset). The *K*-matrix of equation 3-8 for this configurations becomes:

$$K = \begin{bmatrix} \lambda_{B1,1'} & 0 & 0 \\ 0 & \lambda_{B1,2'} & 0 \\ 0 & 0 & \lambda_{B2,2'} \end{bmatrix} \begin{bmatrix} -\frac{n_{eff}^2}{2} p_{11} & -\frac{n_{eff}^2}{2} p_{12} & 1-\frac{n_{eff}^2}{2} p_{12} \\ -\frac{n_{eff}^2}{2} p_{12} & -\frac{n_{eff}^2}{2} p_{11} & 1-\frac{n_{eff}^2}{2} p_{12} \\ -\frac{n_{eff}^2}{2} p_{12} & -\frac{n_{eff}^2}{2} p_{11} & 1-\frac{n_{eff}^2}{2} p_{12} \end{bmatrix} \quad \textbf{3-19}$$

In equation 3-18 the second and the third line of the matrix are highly dependent and are even the same if the different (distant) wavelengths of both FBGs are not taken into account. No good conditioning will be obtained. The conditioning is dependent on the different wavelengths of both gratings and these should, as such, been taking as distant as possible. 1300 and 1550 nm wavelengths are commonly used in optical fibre telecommunications and thus all fibre optic devices and instrumentation are available for them. Table 3-3 shows the calculations (condition number and strain resolution) for the first configuration under the assumption that the interrogator's resolution is 1 pm. An extremely high condition number is obtained, meaning that the strain resolution will be very poor.

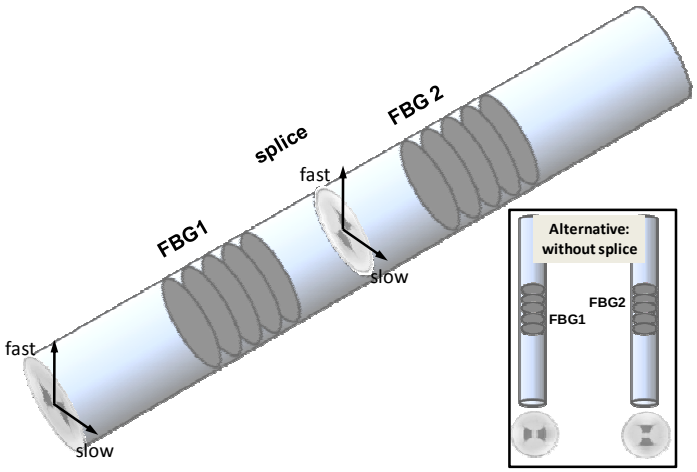

Figure 3-15: The first configuration consists of two HiBi-fibres spliced together with one fibre rotated over 90 deg. Its fast axis is aligned with the slow axis of the other fibre. Two separated fibres can be used as alternative. (see inset)

Table 3-3: Sensitivity analysis for the parallel configuration [45]

Condition number = ~12*10^3		
	Error analysis.	Standard deviation
$\delta\varepsilon_1$, [με]	>4.2 10^3	±4.2 10^3
$\delta\varepsilon_2$, [με]	>4.2 10^3	±4.2 10^3
$\delta\varepsilon_3$, [με]	>2.2 10^3	±2.2 10^3

The second configuration is called the bent configuration and is illustrated in Figure 3-16. Two FBGs with a different central wavelength (around 1300 nm and 1550 nm) are inscribed in one bow-tie fibre which is bend in the material. The FBGs are hereby oriented perpendicular to each other. As such, the slow axes of the FBGs will experience a different in-plane strain condition. However, one has to be careful when embedding such a sensor between two adjacent plies with the same direction of the reinforcement fibres. The reinforcement fibres of the composite will homogeneously surround the first FBG, but, for the second FBG a resin eye can occur which may disturb the strain field and the host structure [44]. These resin eyes can become a starting point of damage inside the material [46, 47]. A possibility to avoid such resin eyes is placing the sensor in between two layers with perpendicularly oriented reinforcing fibres (0 deg and 90 deg). Another possibility is using two separate fibres which are embedded in different layers with different orientations (inset of Figure 3-16). In the last solution strain component calculations

are more complex since both FBGs will experience the strain field of another composite ply.

For this configuration, the *K*-matrix is given by:

$$K = \begin{bmatrix} \lambda_{B1,1'} & 0 & 0 \\ 0 & \lambda_{B1,2'} & 0 \\ 0 & 0 & \lambda_{B2,2'} \end{bmatrix} \begin{bmatrix} -\frac{n_{eff}^2}{2} p_{11} & -\frac{n_{eff}^2}{2} p_{12} & 1-\frac{n_{eff}^2}{2} p_{12} \\ -\frac{n_{eff}^2}{2} p_{12} & -\frac{n_{eff}^2}{2} p_{11} & 1-\frac{n_{eff}^2}{2} p_{12} \\ 1-\frac{n_{eff}^2}{2} p_{12} & -\frac{n_{eff}^2}{2} p_{12} & -\frac{n_{eff}^2}{2} p_{11} \end{bmatrix} \quad \textbf{3-20}$$

Table 3-4 shows the condition number and strain resolution for the bent configuration. Without considering the difficult embedding procedure into mind this is a viable solution. A good condition number and strain resolution is obtained. One can even choose to use 2 FBGs in the range of the 1550 nm wavelengths and thus work with cheaper readout systems which are commercially available on the market.

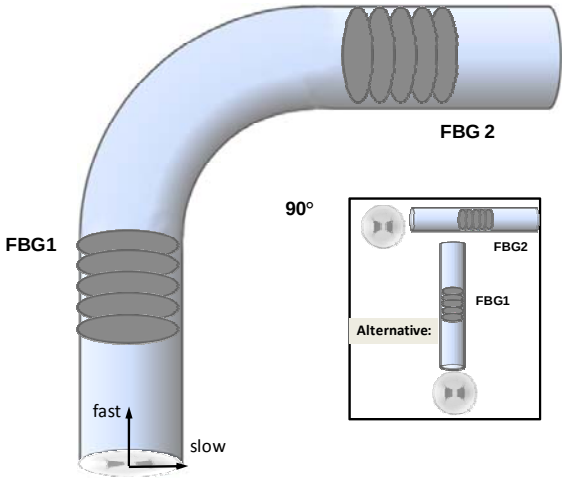

Figure 3-16: The second configuration consists of one HiBi-fibre which is bent over 90deg. As such, the slow axes of the FBGs fibre experience other inplane strain conditions. The fast axes experience the same through-the-thickness strain. As an alternative two separate fibres can be used in the same configuration (see inset).

Table 3-4: Sensitivity analysis for the bent configuration [45]

Condition number = ~19		
	Error analysis	Standard deviation
$\delta\varepsilon_{1'}$ [με]	>5.6	±3.3
$\delta\varepsilon_{2'}$ [με]	>16.0	±10.4
$\delta\varepsilon_{3'}$ [με]	>5.7	±3.7

In the following configuration (Figure 3-18) an optical fibre is shown in which two gratings are inscribed (both with a central wavelength around 1500-1550 nm). From the previous configurations we learned that it is necessary that both gratings have a diverse response on external loading. In this concept we try to reach this goal by decreasing the sensitivity to transverse stress of the second grating. The first grating stays exposed to longitudinal stress as well as transverse stress and the second one is shielded from transverse stress by covering the second grating with a capillary. The optical fibre is an 80 µm cladding diameter bow-tie fibre which has a 37.5 µm thick polyimide coating, thus a total outer diameter of 155 µm. The capillary is a silica tubing coated with polyimide; the inner diameter of this tube is 180 µm while the outer diameter is 340 µm. The capillary is slid over the second grating and sealed at its two ends with epoxy to prevent resin flow into the tube during the composite manufacturing process. Guo [48] and Haran et al. [49] also used such a capillary to isolate one of the gratings completely from every stress/strain influence. As such the only parameter which has an influence on the grating is temperature (Figure 3-17).

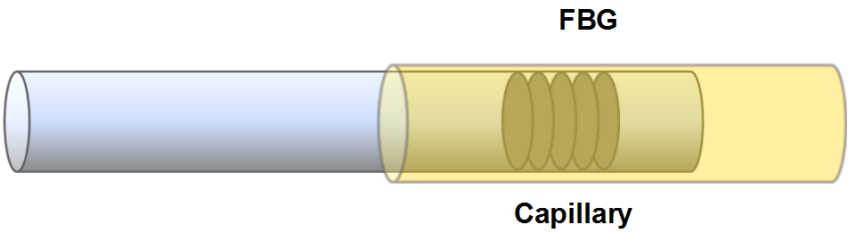

Figure 3-17: Schematic of an optical fibre Bragg grating embedded in a capillary to exclude all external stress/strain components. This sensor can be used as temperature compensation sensor [48],[49].

Fernando et al. [50] created an EFPI sensor by merging two cleaved optical fibres in a precision bore capillary tube (128 µm inner diameter, 300 µm outer diameter). The tube is sealed by fusion (spliced) or by epoxy depending on the application. As such, a cure sensor (strain plus temperature sensor) and a moisture sensor and vibration sensor have been created.

In equation 3-21 one can notice that in this configuration the second grating is not sensitive to transverse strain because the third row of the *K*-matrix has some zero components. Both FBGs are mutually independent and should therefore lead to a very good condition number and strain resolutions (Table 3-5). The axial strain resolution is in this case equal to that of a uni-axial non embedded FBG. The obtained transverse strain resolutions are very good.

$$K = \begin{bmatrix} \lambda_{B1,1'} & 0 & 0 \\ 0 & \lambda_{B1,2'} & 0 \\ 0 & 0 & \lambda_{B2,2'} \end{bmatrix} \begin{bmatrix} -\frac{n_{eff}^2}{2} p_{11} & -\frac{n_{eff}^2}{2} p_{12} & 1-\frac{n_{eff}^2}{2} p_{12} \\ -\frac{n_{eff}^2}{2} p_{12} & -\frac{n_{eff}^2}{2} p_{11} & 1-\frac{n_{eff}^2}{2} p_{12} \\ 0 & 0 & (1-\frac{n_{eff}^2}{2} p_{12}) + \upsilon \frac{n_{eff}^2}{2} (p_{11} + p_{12}) \end{bmatrix} \quad \textbf{3-21}$$

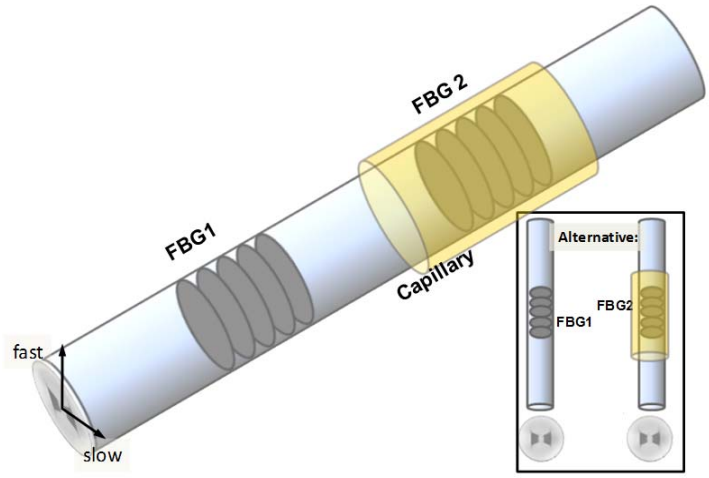

Figure 3-18: The third configuration (capillary configuration) consists of one fibre with two FBGs of which one grating is isolated from transverse stress through the use of a glass capillary.

Table 3-5: Sensitivity analysis for the capillary configuration

Condition number = ~10		
	Error analysis	Standard deviation
$\delta\varepsilon_{1'}$ [με]	>6.9	±4.3
$\delta\varepsilon_{2'}$ [με]	>6.9	±4.3
$\delta\varepsilon_{3'}$ [με]	>0.9	±0.9

Instead of covering one of the gratings with a capillary which would possibly distort the composite structure, a certain amount of isolation can be obtained by recoating one of the gratings. By tailoring the properties of the coating (Young's modulus, Poisson's coefficient, thickness, …) one can design an FBG sensor which is partially isolated from transverse stress. This option was not further experimentally explored in this dissertation.

A transverse stress isolation of x% means that only x% of the transverse stress in the host structure will be transferred to the fibre core. The expected strain resolutions for 25% to 100% of transverse stress isolation is displayed in Table 3-6. It should be remarked that the 1'-axis in the following chapters is taken parallel to the surface of the samples in which they are embedded. For 100% isolation, the strain resolution is evidently optimal, for a lower percentage of isolation the sensitivities become worse. However, depending on the used configuration, they could still meet the requirements. In the MASSFOS project the requirements were ± 5 με for the longitudinal and transverse strain components [51]. Thus a 75% isolation of transverse stress still satisfy the requirements.

Table 3-6: Sensitivity analysis of a sensor with two gratings of which one has obtained a certain percentage of isolation from transverse stress.

Isolation	Condition number		Standard deviation
25%	~26	$\delta\varepsilon_1$, [με]	±8.3
		$\delta\varepsilon_2$, [με]	±11.3
		$\delta\varepsilon_3$, [με]	±4.5
50%	~13	$\delta\varepsilon_1$, [με]	±4.8
		$\delta\varepsilon_2$, [με]	±6.5
		$\delta\varepsilon_3$, [με]	±1.9
75%	~10	$\delta\varepsilon_1$, [με]	±4.3
		$\delta\varepsilon_2$, [με]	±4.7
		$\delta\varepsilon_3$, [με]	±1.2
100% (capillary)	~10	$\delta\varepsilon_1$, [με]	±4.3
		$\delta\varepsilon_2$, [με]	±4.3
		$\delta\varepsilon_3$, [με]	±0.9

Table 3-7: Summary of the different proposed sensor configurations with their strain resolutions. advantages and disadvantages

Principle	Strain resolution [με]	Advantages	Disadvantages
Parallel configuration	$\delta\varepsilon_{1'}$ $\pm 4.2*10^3$ $\delta\varepsilon_{2'}$ $\pm 4.2*10^3$ $\delta\varepsilon_{3'}$ $\pm 2.2*10^3$	Easy to embed Minor composite distortion	Vulnerable splice Bad conditioning
Bent configuration	$\delta\varepsilon_{1'}$ ±3.3 $\delta\varepsilon_{2'}$ ±10.4 $\delta\varepsilon_{3'}$ ±3.7	Low condition number Good strain resolution	Important composite distortion Difficult embedding procedure
Capillary configuration	$\delta\varepsilon_{1'}$ ±4.3 $\delta\varepsilon_{2'}$ ±4.3 $\delta\varepsilon_{3'}$ ±0.9	Low condition number Good strain resolution	Intermediate to low-composite distortion depending on capillary diameter

From Table 3-7, taking all advantages and disadvantages into account, it can be concluded that the best configuration for embedded measurements of more-dimensional strain fields is the one with the capillary design. Each parameter can be calculated within a reasonable precision. This configuration will further be referred to as the 'Multi Axial Strain'-sensor or MAxS-sensor.

3. 4. FEASIBILITY STUDY

To obtain the resolution of the MAxS-sensor as described in Table 3-5, some implied assumptions were made:

- The FBG encapsulated in the capillary should be isolated (100%) from the transverse stresses existing inside the composite structure.
- A 100% longitudinal strain transfer from host structure to fibre core should exist for both FBGs

To this end, the mechanical behavior of the encapsulated FBG embedded in a carbon reinforced plastic (CFRP) lamina has been investigated by means of finite element simulations using the FE-software package ABAQUS^{TM} (version 6.8). Because of symmetry reasons only 1/8 of the elements were modeled (Figure 3-19). The composite model (length = 15 mm, thickness = 0.8 mm, width = 30 mm) exists of 25100 linear hexahedral elements of type C3D8R [52] and 62200 linear wedge elements of type C3D6 [52] in the vicinity of the capillary and the fibre. The material properties of the composite material (M18/M55J by Hexcell) are given in Table 3-8. The capillary ($\square_o$ = 300 µm, $\square_i$ = 184 µm x length = 7.5 mm) was modeled using 7520 linear hexahedral elements of type C3D8R and the fibre ($\square_o$ = 80 µm x length = 30 mm) with 16200 linear hexahedral elements of type C3D8R. The material of the capillary and the optical fibre are fused silica for which the properties were given inTable 3-2. Next to the simulations, an encapsulated FBG and non-encapsulated FBG was embedded in a real composite laminate with a uni-directional lay-up $[0]_{24}$ (Figure 3-20). The sample had a thickness of 2.57 mm, a width of 48.50 mm and a length of 300 mm. The production of such a CFRP-sample and embedding procedure for the MAxS-sensor will be discussed in Chapter 4. For the FE-model and the experiment both higher described assumptions were checked by performing a transverse compression test and a longitudinal strain test (Figure 3-21 and Figure 3-24). The experimentally measured wavelength shifts of both FBGs can be mutually compared. However, they should not be related with the existing strain field inside the composite sample because of their unknown orientations.

Table 3-8: Elastic material properties for the M55J/M18 carbon/epoxy material

E_{11}	$E_{22} = E_{33}$	$G_{12}=G_{13}$	G_{23}	$\nu_{12}=\nu_{13}$	$\nu_{23}=\nu_{32}$	$\nu_{21}=\nu_{31}$
[GPa]	[Gpa]	[Gpa]	[Gpa]	[-]	[-]	[-]
300	6.30	4.30	2.28	0.32	0.38	0.0017

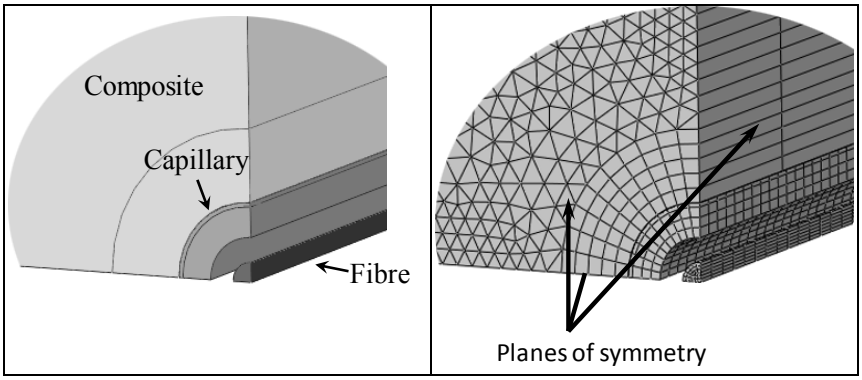

Figure 3-19: Detailed view of the geometrical model at the left, and an overview of the finite element mesh in the vicinity of fibre and capillary at the right.

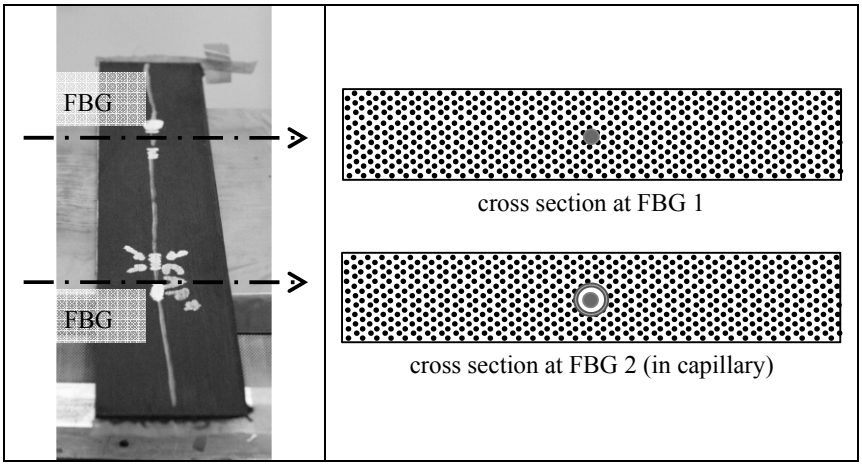

Figure 3-20: A photograph of the produced CFRP-test sample with an embedded MAxS-sensor, together with schematics of the cross sections for both FBG locations

3. 4. 1. Isolation from transverse stress

In Figure 3-21 a schematic of the transverse compressive load experiment is drawn; the load is applied over 15 mm in width on both sensor regions. Both sections will

experience the same compressive load (40 MPa). However, as the second FBG is encapsulated it should not react to the applied load which is nearly the compressive strength (50 MPa) of the composite material in the through-the-thickness direction. The capillary acts as a buffer for the transverse stresses, and the air space between fibre and capillary remains intact. As illustrated in Figure 3-22 the deformation of the capillary in the FE-simulation is limited to about a micrometer.

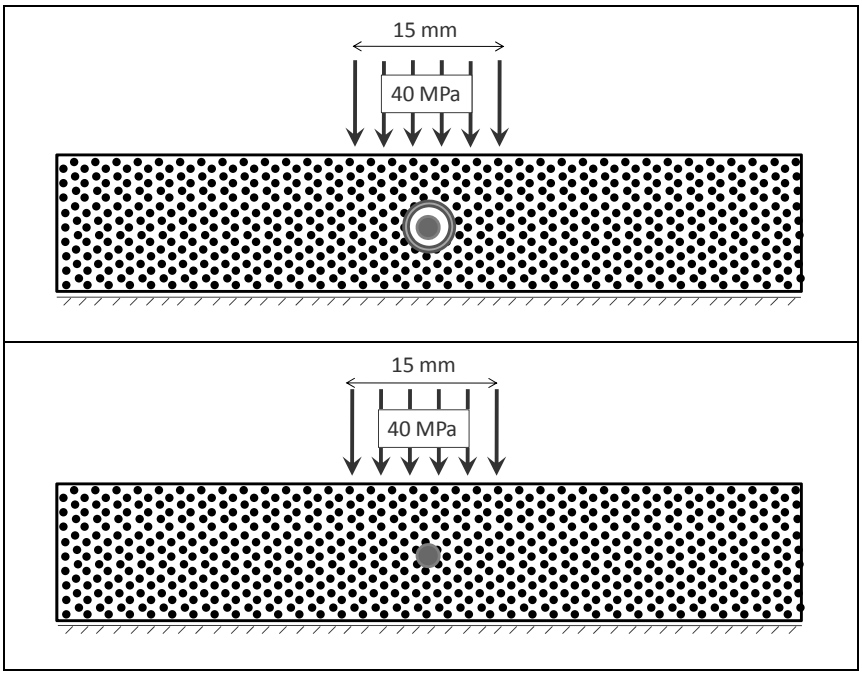

Figure 3-21: Transverse compressive load applied at the location of the FBGs.

In Table 3-9, results of the transverse compression experiment are summarized. The FBG in the capillary shows almost no Bragg peak wavelength shift while the other exhibits a shift of ~10 pm/(N/mm²). The small shift of the FBG in the capillary is due to a small longitudinal strain caused by the Poisson's effect.

Table 3-9: Sensitivity to transverse compressive stress for the different FBGs of the MAxS-sensor

$\left[{}^{pm}/_{(MPa)} \right]$	**FBG 1** (λ_B = 1559.5 nm)	**FBG 2 (cap)** (λ_B = 1539.6 nm)
$\Delta\lambda_{B,1'}$	10.36	0.51
$\Delta\lambda_{B,2'}$	9.36	0.44

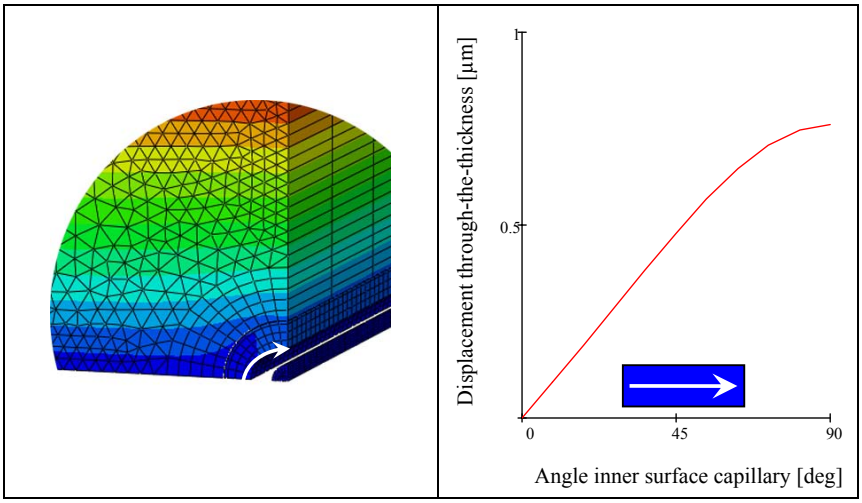

Figure 3-22: Left, the nodal displacement of the FE-model in the through-the-thickness direction. Right, the nodal displacement of the inner circle of the capillary.

Note that if the capillary is not completely sealed, epoxy resin can flow inside during the manufacturing process. This leads to an FBG which is not completely isolated from the transverse stresses that exist inside the material. Experimental evidence is given in Figure 3-23. For two equal samples $[90]_{20}$ a peak split occurs during transverse compression experiments for the sample in which epoxy resin has entered the capillary during manufacturing.

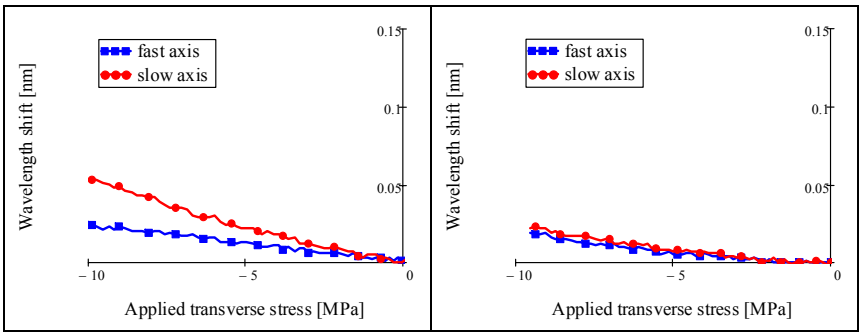

Figure 3-23: Response of FBGs encapsulated in a capillary during transverse compression experiments. Left, epoxy resin has entered the capillary and thus a clear Bragg peak splitting is observed. Right, for a well-sealed capillary no Bragg peak splitting is noticeable indicating that the sensor is isolated from transverse stress.

3. 4. 2. Transfer of longitudinal strain

Figure 3-24 shows a schematic of the tensile test performed on the CFRP-sample with the embedded MAxS-sensor. During the test, both FBGs are subjected to the same longitudinal stress, and thus, should show similar wavelength shifts.

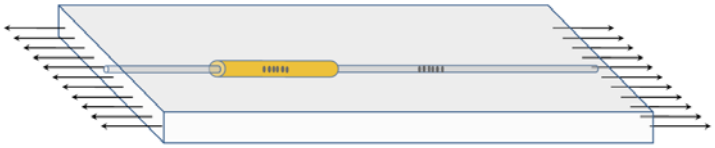

Figure 3-24: Schematic of the tensile test performed on the CFRP sample with an embedded MAxS-sensor.

The FE simulation shows a ratio of $\varepsilon_{3',FBG2} / \varepsilon_{3',FBG1} = 1.0065$ for the longitudinal strain measured with FBG 2 (inside the capillary) and the longitudinal strain measured with FBG 1. The strain in the capillary is less than 1% higher than for FBG 1 outside the capillary. This difference can be neglected. In Table 3-10 the results of the tensile experiment are displayed. Both FBGs exhibit similar wavelength shifts. FBG 1 shows a slightly higher sensitivity as compared to FBG 2 in the capillary. However, taking the different initial Bragg wavelengths into account, both FBGs have almost the same sensitivity which is according to the higher discussed assumption.

Table 3-10: Sensitivity to longitudinal stress for the different FBGs of the MAxS-sensor

$\left[pm/MPa \right]$	**FBG 1 (λ_B = 1559.5 nm)**	**FBG 2 (in capillary) (λ_B = 1539.6 nm)**
$\Delta\lambda_{B,1'}$	4.81	4.66
$\Delta\lambda_{B,2'}$	4.79	4.58

3. 4. 3. Temperature sensitivity

The temperature sensitivity of a MAxS-sensor is much more complicated than described here. In this section, the author only wants to state what is necessary when the total strain field as well as the temperature should be measured simultaneously. The *K*-matrix of Equation 3-9 can be extended with an extra row and column. As such, the following set of equations can be obtained

$$\begin{bmatrix} \Delta\lambda_{B1,1'} \\ \Delta\lambda_{B1,2'} \\ \Delta\lambda_{B2,1'} \\ \Delta\lambda_{B2,2'} \end{bmatrix} = K \begin{bmatrix} \Delta\varepsilon_{1'} \\ \Delta\varepsilon_{2'} \\ \Delta\varepsilon_{3'} \\ \Delta T \end{bmatrix} \quad \textbf{3-22}$$

In which K is

$$K = \begin{bmatrix} \lambda_{B1,1'} & 0 & 0 & 0 \\ 0 & \lambda_{B1,2'} & 0 & 0 \\ 0 & 0 & \lambda_{B2,1'} & 0 \\ 0 & 0 & 0 & \lambda_{B2,2'} \end{bmatrix} \begin{bmatrix} -\frac{n_{eff}^2}{2} p_{11} & -\frac{n_{eff}^2}{2} p_{12} & 1-\frac{n_{eff}^2}{2} p_{12} & \alpha_{n,1'} \\ -\frac{n_{eff}^2}{2} p_{12} & -\frac{n_{eff}^2}{2} p_{11} & 1-\frac{n_{eff}^2}{2} p_{12} & \alpha_{n,2'} \\ 0 & 0 & (1-\frac{n_{eff}^2}{2} p_{12})+\upsilon\frac{n_{eff}^2}{2}(p_{11}+p_{12}) & \alpha_{n,1'} \\ 0 & 0 & (1-\frac{n_{eff}^2}{2} p_{12})+\upsilon\frac{n_{eff}^2}{2}(p_{11}+p_{12}) & \alpha_{n,2'} \end{bmatrix} \quad \textbf{3-23}$$

Out of equation 3-21 and 3-22 it is clear that if one theoretically wants to measure temperature simultaneously with the strain components the thermo-optic coefficients of both polarization axes should be sufficiently different.

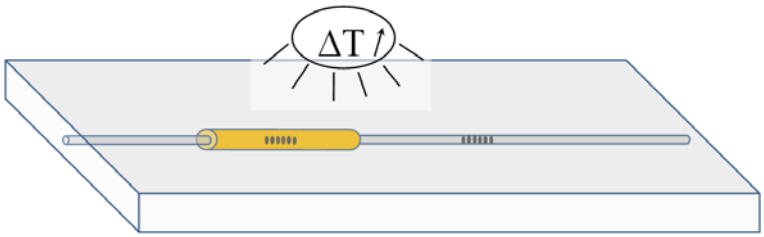

Figure 3-25: Schematic of the temperature test performed on the CFRP sample with an embedded MAxS-sensor.

In Table 3-11 the sensitivity to temperature for the different FBGS of a MAxS-sensor is given. The temperature sensitivity of FBG 2 is slightly higher than for FBG 1. Remark that the temperature sensitivity, here, is the sum of the induced strain through different expansion coefficients of optical fibre and composite material, in which the fibre is embedded, and the thermo-optic effect (change of the refractive index). The sensitivity of the fast and slow axes are, however, not sufficiently different. Thus, it can be concluded that temperature should be separately measured with an external sensor like a thermocouple or an independent Bragg grating temperature sensor as shown in Figure 3-17.

Table 3-11: Sensitivity to temperature for the different FBGs of the MAxS-sensor

$\left[pm/^{\circ}C \right]$	**FBG 1** (λ_B = 1559.5 nm)	**FBG 2 (cap)** (λ_B = 1539.6 nm)
$\Delta\lambda_{B,1'}$	10.53	10.09
$\Delta\lambda_{B,2'}$	10.90	10.44

3. 5. CONCLUSIONS

In this chapter the author reported on a literature review regarding the mapping of multi-component strain fields. Internationally a lot of research has been performed in trying to design such a sensor. Though, no proper solution was found in this matter. As described in the previous chapter, both polarization modes of a HiBi-fibre will satisfy the Bragg condition at different wavelengths. Therefore, gratings written in such a fibre will reflect two distinct peaks, one for each polarization axis. By adding an extra FBG, 4 different wavelengths can be measured. If these two gratings respond differently to external perturbations like axial and transverse strain components, one can build a multi-axial strain sensor.

In a second part of this chapter the author has proposed and studied several sensor configurations consisting of two FBGs in a bow-tie fibre. The first configuration was a derivative of a sensor proposed by several authors (two FBGs in-line with two distant centre wavelengths). However, the author has theoretically proven that such a sensor exhibits a poor strain resolution which is in spite of its embedding simplicity. The second configuration (bent fibre) had a better strain resolution, but missed a certain embedding simplicity. Important composite distortion (e.g. resin eye) can be expected, since one of the FBGs is oriented perpendicular to the reinforcement fibres. In the last configuration the transverse stress sensitivity of the second grating has been decreased placing it inside a capillary. As such, the first grating remains sensitive to longitudinal stress as well as transverse stress. The strain resolution of this configuration was good and the composite distortion was kept as low as possible by choosing a very small capillary (outer diameter: 340 μm). The feasibility of this configuration (MAxS-sensor) was proven by preliminary FE-simulations and experiments. The implied necessary assumptions (isolation of transverse stress and 100% transfer of longitudinal strain) to obtain the desired strain resolution of the MAxS-sensor were checked. If the temperature sensitivity of both gratings is sufficiently different one can think of a MAxS-sensor without temperature compensation.

In this chapter the author tried to design a sensor (MAxS-sensor) to simultaneously measure three strain components and theoretically determined the strain resolution of this sensor. However, another important point when using embedded sensors is the interaction of the sensor and its host material. Because of the different properties of both materials (sensor and host material) the resolving power of the sensor will be

significantly lower than its resolution. In the next chapter the author tries to define this interaction (analytically as well as by FE-simulations).

3. 6. REFERENCES

1. Butter, C.D. and Hocker, G.B., *Fiber optics strain gauge.* Applied optics, 1978. **17** (18): p. 2867-2869.
2. Culshaw, B., *Fiber optics in sensing and measurement.* IEEE Journal of Selected Topics in Quantum Electronics, 2000. **6** (6): p. 1014-1021.
3. Culshaw, B. *Optical fiber sensor technologies: Opportunities and-perhaps-pitfalls*. in *Proceedings of IEEE/OSA Optical Fiber Communications Conference (OFC)*. 2004. Atlanta, Ga (USA).
4. Culshaw, B. *The Smart Bridge of the Future*. in *Proceedings of the 3rd International Conference on Smart Materials, Structures and Systems*. 2008. Acireale, ITALY.
5. Culshaw, B. and Kersey, A., *Fiber-optic sensing: A historical perspective.* Journal of Lightwave Technology, 2008. **26** (9-12): p. 1064-1078.
6. Kersey, A.D., Davis, M.A., Patrick, H.J., LeBlanc, M., Koo, K.P., Askins, C.G., Putnam, M.A., and Friebele, E.J., *Fiber grating sensors.* Journal of Lightwave Technology, 1997. **15** (8): p. 1442-1463.
7. Majumder, M., Gangopadhyay, T.K., Chakraborty, A.K., Dasgupta, K., and Bhattacharya, D.K., *Fibre Bragg gratings in structural health monitoring - Present status and applications.* Sensors and Actuators a-Physical, 2008. **147** (1): p. 150-164.
8. Caucheteur, C., Bette, S., Garcia-Olcina, R., Wuilpart, M., Sales, S., Capmany, J., and Megret, P., *Transverse strain measurements using the birefringence effect in fiber Bragg gratings.* Ieee Photonics Technology Letters, 2007. **19** (13-16): p. 966-968.
9. Caucheteur, C., Bette, S., Garcia-Olcina, R., Wuilpart, M., Sales, S., Capmany, J., and Megret, P., *Transverse force sensor exploiting the birefringence effect in uniform fibre Bragg gratings*, in *OPTICAL SENSING TECHNOLOGY AND APPLICATIONS*, F. Baldini, et al., Editors. 2007. p. U94-U105.
10. Johnson, E. and Rastogi, N. *Load transfer in the stiffener-to-skin joints of a pressurized fuselage*. 1995;
Available from: http://adsabs.harvard.edu/abs/1995STIN...9527865J.
11. Vlekken, J., Vermeiren, J., and De Waele, W., *MASSFOS: Critical design report*. 2006: Geel, Leuven, Gent, BELGIUM.
12. Bouten, P.C.P. and Broer, D.J. *Coating composition and fiber lifetime*. in *Proceedings of the Conference on Fiber Optics Reliability and Testing: Benign and Adverse Environments*. 1993. Boston, Ma (USA).

13. Skontorp, A. *Strength and failure mechanisms of polyimide-coated optical fibers*. in *Proceedings of the Smart Structures and Materials 2000 Conference*. 2000. Newport Beach, Ca (USA).

14. Skontorp, A. and Cammas, J. *Static fatigue life of silica optical fibers and the significance of fiber coating and handling*. in *Proceedings of the Smart Structures and Materials 2001 Conference*. 2001. Newport Beach, Ca (USA).

15. Voet, E.J., Luyckx, G., De Baere, I., Degrieck, J., Vlekken, J., Jacobs, E., and Bartelt, H. *High Strain monitoring during Fatigue Loading of Thermoplastic Composites using imbedded Draw Tower Fibre Bragg Grating Sensors*. in *Proceedings of the 3rd International Conference on Smart Materials, Structures and Systems*. 2008. Acireale, ITALY.

16. Betz, D.C., Thursby, G., Culshaw, B., and Staszewski, W.J., *Advanced layout of a fiber Bragg grating strain gauge rosette.* Journal of Lightwave Technology, 2006. **24** (2): p. 1019-1026.

17. Betz, D.C., Thursby, G., Culshaw, B., and Staszewski, W.J., *Structural damage location with fiber Bragg grating rosettes and Lamb waves.* Structural Health Monitoring-an International Journal, 2007. **6** (4): p. 299-308.

18. Haran, F.M., Rew, J.K., and Foote, P.D. *A fibre Bragg grating strain gauge rosette with temperature compensation*. in *Proceedings of SPIE Conference on Sensory Phenomena and Measurement Instrumentation for Smart Structures and Materials*. 1998. San Diego, Ca (USA).

19. Fernandez, A.F., Berghmans, F., Brichard, B., Megret, P., Decreton, M., Blondel, M., and Delchambre, A. *Multi-component force sensor based on multiplexed fibre Bragg grating strain sensors*. in *Proceedings of 14th International Conference on Optical Fiber Sensors*. 2000. Venice, ITALY.

20. Matrat, J., Levin, K., and Jarlas, R. *Implementation of a Bragg grating strain rosette embedded in composites*. in *Proceedings of the Smart Structures and Materials Conference 2001*. 2001. Newport Beach, Ca (USA).

21. Levin, K. and Matrat, J. *Strain measurements using an interferometrically interrogated embedded fibre optic rosette - art. no. 661945*. in *Proceedings of the 3rd European Workshop on Optical Fibre Sensors*. 2007. Naples, ITALY.

22. Suo, R., Chen, X.F., Zhou, K.M., Zhang, L., and Bennion, I. *In-fibre directional transverse loading sensor based on excessively tilted fibre Bragg gratings*. in *Proceedings of the 19th International Conference on Optical Fibre Sensors*. 2008. Perth, AUSTRALIA.

23. Chen, G.H., Liu, L.Y., Jia, H.Z., Yu, J.M., Xu, L., and Wang, W.C., *Simultaneous pressure and temperature measurement using Hi-Bi fiber Bragg gratings.* Optics Communications, 2003. **228** (1-3): p. 99-105.

24. Silva, S.F.O., Frazao, O., Santos, J.L., Araujo, F.M., and Ferreira, L.A., *Discrimination of temperature, strain, and transverse load by using fiber Bragg gratings in a twisted configuration.* Ieee Sensors Journal, 2006. **6** (6): p. 1609-1613.

25. Sirkis, J.S. and Lo, Y.L., *Simultaneous measurement of 2 strain components using 3x3 and 2x2 coupler-based passive demodulation of Optical-Fiber Sensors.* Journal of Lightwave Technology, 1994. **12** (12): p. 2153-2161.

26. Singh, H., Sirkis, J.S., Andrews, J., and Pulfrey, R., *Evaluation of integrated-optic modulator-based detection schemes for in-line fiber etalon sensors.* Journal of Lightwave Technology, 1995. **13** (8): p. 1772-1779.

27. Jin, X.D., Sirkis, J.S., Chung, J.K., and Venkat, V.S., *Simultaneous measurement of two strain components in composite structures using embedded fiber sensor.* Journal of Composite Materials, 1999. **33** (15): p. 1376-1389.

28. Black, K., Udd, E., Schulz, W., Kreger, S., Kunzler, M., Taylor, T., and Lumsden, R. *Using Multi-Axis Fiber Grating Strain Sensors to Measure Transverse Strain and Transverse Strain Gradients In Composite Materials with Complex Weave Structures*. in *Proceedings of SPIE*. 2002.

29. Udd, E., Black, K., Schulz, W., Kreger, S., Kunzler, M., Heider, D., and Ieee, I. *In-situ evaluation of composite structural performance in presence of high stress/strain gradients using multi-axis fiber grating strain sensors*. in *Proceedings of 15th Optical Fiber Sensors Conference*. 2002. Portland, Or (USA).

30. Udd, E., Schulz, W.L., and Seim, J.M. *Measurement of multidimensional strain fields using fiber grating sensors for structural monitoring*. in *Proceedings of the SPIE Conference on Fiber Optic Sensor Technology and Applications*. 1999. Boston, Ma (USA).

31. Wang, Y.P., Yun, B.F., Chen, N., and Cui, T.P., *Characterization of a high birefringence fibre Bragg grating sensor subjected to non-homogeneous transverse strain fields.* Measurement Science & Technology, 2006. **17** (4): p. 939-942.

32. Abe, I., Kalinowski, H.J., Frazao, O., Santos, J.L., Nogueira, R.N., and Pinto, J.L. *Superimposed Bragg gratings in high-birefringence fibre optics: three-parameter simultaneous measurements*. in *Proceedings of 16th International Conference on Optical Fibre Sensor (OFS-16)*. 2003. Nara City, JAPAN.

33. Abe, I., Frazao, O., Schiller, M.W., Nogueira, R.N., Kalinowski, H.J., and Piinto, J.L., *Bragg gratings in normal and reduced diameter high birefringence fibre optics.* Measurement Science & Technology, 2006. **17** (6): p. 1477-1484.

34. Abe, I., de Goes, R.E., Fabris, J.L., Kalinowski, H.J., Muller, M., Fugihara, M.C., Falate, R., Diesel, B.W., Kamikawachi, R.C., and Barbosa, C.L., *Production and characterization of refractive index gratings in high-birefringence fibre optics.* Optics and Lasers in Engineering, 2003. **39** (5-6): p. 537-548.

35. Lawrence, C.M., Nelson, D.V., Udd, E., and Bennett, T., *A fiber optic sensor for transverse strain measurement.* Experimental Mechanics, 1999. **39** (3): p. 202-209.

36. Mawatari, T. and Nelson, D., *A multi-parameter Bragg grating fiber optic sensor and triaxial strain measurement.* Smart Materials & Structures, 2008. **17** (3).

37. Udd, E., Nelson, D., and Lawrence, C. *Three axis strain and temperature fiber optic grating sensor*. in *Proceedings of the Conference on Smart Sensing, Processing, and Instrumentation - Smart Structures and Materials 1996*. 1996. San Diego, Ca.

38. Suo, R., Chen, X.F., Zhou, K.M., Zhang, L., and Bennion, I. *In-fibre directional transverse loading sensor based on excessively tilted fibre Bragg gratings*. in *Proceedings of 19th International Conference on Optical Fibre Sensors*. 2008. Perth, AUSTRALIA.

39. Jin, X.D., Sirkis, J.S., Chung, J.K., and Venkat, V.S., *Embedded in-line fiber etalon/Bragg grating hybrid sensor to measure strain and temperature in a composite beam.* Journal of Intelligent Material Systems and Structures, 1998. **9** (3): p. 171-181.

40. Chehura, E., Ye, C.C., Staines, S.E., James, S.W., and Tatam, R.P., *Characterization of the response of fibre Bragg gratings fabricated in stress and geometrically induced high birefringence fibres to temperature and transverse load.* Smart Materials & Structures, 2004. **13** (4): p. 888-895.

41. Jin, W., Michie, W.C., Thursby, G., Konstantaki, M., and Culshaw, B., *Simultaneous measurement of strain and temperature: Error analysis.* Optical Engineering, 1997. **36** (2): p. 598-609.

42. Available from: http://www.Fos-s.com.

43. Luyckx, G., Degrieck, J., De Waele, W., Van Paepegem, W., Vlekken, J., and Chah, K. *Multi-axial fiber Bragg sensors for monitoring purposes*. in *Proceedings of the European Conference on Composite Materials*. 2006. Biaritz, FRANCE

44. De Waele, W., *Structural monitoring of composite elements using optical fibres with Bragg-sensors.*, in *Department of mechanical construction and production*. 2001-2002, PhD dissertation of Ghent University: Ghent, BELGIUM.

45. Chah, K. and Van Roosbroeck, J., *MASSFOS: Critical design report*. 2006, FOS&S, Ghent University: Geel, BELGIUM.

46. Mall, S., Dosedel, S.B., and Holl, M.W., *The performance of graphite-epoxy composite with embedded optical fibers under compression.* Smart Materials & Structures, 1996. **5** (2): p. 209-215.

47. Matrat, J., Levin, K., and Jarlas, R. *Effect of debonding on strain measurement of embedded Bragg grating sensors*. in *Proceedings of the 2nd International Workshop on Structural Health Monitoring*. 1999. Stanford, Ca (USA).

48. Guo, Z.-S., *Strain and temperature monitoring of asymmetric Composite Laminate using FBG hybrid sensors.* Structural Health Monitoring-an International Journal, 2007. **6** (3): p. 191-197.

49. Haran, F.M., Rew, J.K., and Foote, P.D., *A strain-isolated fibre Bragg grating sensor for temperature compensation of fibre Bragg grating strain sensors.* Measurement Science & Technology, 1998. **9** (8): p. 1163-1166.

50. Fernando, G.F., Liu, T., Crosby, P., Doyle, C., Martin, A., Brooks, D., Ralph, B., and Badcock, R., *A multi-purpose optical fibre sensor design for fibre reinforced composite materials.* Measurement Science & Technology, 1997. **8** (10): p. 1065-1079.

51. Vlekken, J., *MASSFOS: full proposal GSTP3-project*. 2005: Geel, BELGIUM.

52. ABAQUS, *User's Manual*. 2002, New York: Hibbit, Karlsson & Sörensen inc.

Chapter 4 : EMBEDDED FIBRE BRAGG GRATINGS

Figure 4-1 repeats the structural health monitoring scheme of Chapter 1. The strain transfer from measured sensor strain to structural strain is highlighted. In this chapter, several aspects of the embedding procedure for optical fibres in composite structures are evaluated. The emphasis, at the end of the chapter, lays on determining the interaction between the strain at the core of the optical fibre and the strain in the composite structure close to the optical fibre sensor.

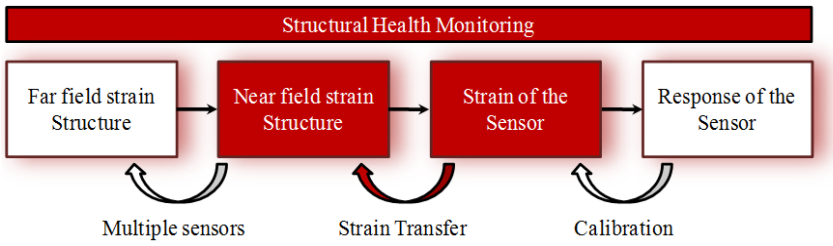

Figure 4-1: Flow chart of the different steps necessary for structural health monitoring using an embedded optical fibre sensor. The calibration step is highlighted.

4. 1. INTRODUCTION

When embedding an optical fibre in a host material, one should consider several topics. Firstly, the embedding procedure should be as simple as possible. In this the in-and egress points, the orientation of the fibre (polarization axes HiBi-fibres), its position, and the embedding time should be considered. When laminating is done by hand, the optical fibre sensor can be manually positioned in between two prepreg layers. When fabrics are used, one can think of co braiding the optical fibre sensor during the production of the fabrics. For example, Jung et al. [1] enforced the optical fibre (250 µm) by embedding it in a nylon wire (350 µm) which could then be co braided in the fabric. Secondly, the mechanical distortion of the composite material due to the presence of an embedded sensor, should be minimized. The size of the sensor and its orientation with respect to the reinforcement fibres are important. Finally, the strain present in the core of the optical fibre is not equal to that in the host material. The relation between both strain fields depends on the mechanical properties of the host material and the sensor, on the lay-up of the composite material, and on the position of the sensor in a certain layer. Due to the difference in mechanical properties, the resolving power of the sensor will be lower than the theoretical resolution of the MAxS-sensor.

4. 2. EMBEDDING PROCEDURE

4. 2. 1. Entry point

The robust entry point of optical fibre leads in a composite component is needed for the successful cost-effective development of embedded sensor technology [2]. The sudden transition of the fibre surrounded by the in most cases stiff host material to the freely bendable fibre gives rise to in- and egress points which are prone to breaking. Accidentally touching this fragile point, or clamping the fibre while moving a structure, can already lead to fibre breakage. Coating the fibres or covering them with additional elements can initiate damage in the material. As such, the protection or interconnection of the in- and outcome of an embedded optical fibre sensing system should be defined as follows [3, 4].

It should be robust, since production processes as well as operating environments of such qualitatively high level structures can be very aggressive in terms of temperature (up to 200°C), pressure (up to 15 bar) and handling, especially at the edges of the structure. Connecting and disconnecting the sensor should remain simple and easy to handle, and have a certain flexibility in this matter. During manufacturing, the optical losses in terms of power should be kept as low as possible (e.g. by avoiding microbending of the fibre). A critical issue is distortion of the material; the distorted region should be small in dimension and should not influence the strength of the material or be a starting point of damage (e.g. delamination) in the structure. At last, compatibility with standard connector systems from telecommunications industry is preferred, to enable standard interfacing with continuously developing instrumentation technology.

In literature, in- and outcome of the optical fibres can be divided into three major categories: the **bare fibre** with or without treatment after production, **the connectors** (edge or surface mounted), and **the protected fibre** (edge or surface outcome).

4. 2. 1. a. Bare fibres

A fibre can be embedded in composite material without any precaution. This method is only applicable for laboratory purposes and is very vulnerable to breakage during production as well as during handling of the test samples (Figure 4-2). The only protection is the primary coating (acrylate, polyimide or Ormocer®) of the optical fibre. Therefore, several authors searched for methods to cover the bare fibre after production of the composite structure to make the in- and egress points more robust.

Figure 4-2: Entry point of an optical fibre embedded in a composite material without any protection.

De Waele[5] protected the entry point of the optical fibres with some flexible silicones after manufacturing of the composite panel (Figure 4-3).

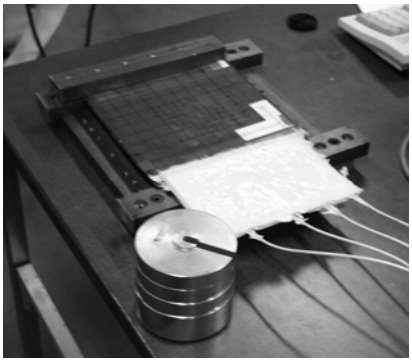

Figure 4-3: In- and egress points of optical fibres embedded in a composite panel protected with flexible silicones.[5]

In fibre reinforced epoxy composites, the viscosity of the matrix drops to very low values during manufacturing. As a result, a certain amount of resin flows at the edges of the laminate (Figure 4-4). This can adhere to the optical fibres, causing an embrittlement of their entry points. This embrittlement makes demoulding of a composite laminate without breaking the optical fibre very difficult. Additionally, in most applications edge trimming is needed after fabrication, which is not possible whenever an optical fibre is present.

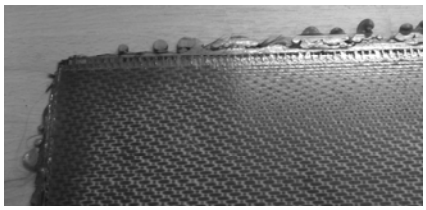

Figure 4-4: Edges of a composite plate after production; excess of resin should be cut away.

This method was immediately dropped for any application whatsoever because it lacks robustness during production [6].

4. 2. 1. b. Connectors

Green et al. [3] led the fibre out from the surface of the host material, and mounted a connector to the surface (Figure 4-5). Surface mounted connectors as well as fibre throughputs at the surface have the disadvantage that the local curvature of the optical fibre can cause high optical losses. Maintenance and attainability of the connectors inside aircraft wings or structures can be difficult.

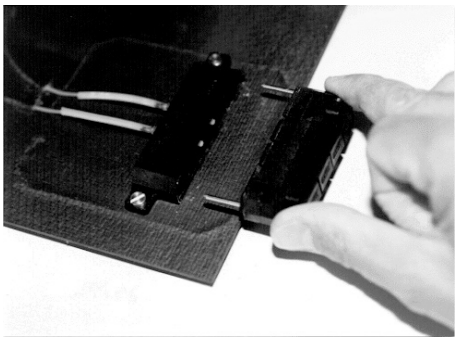

Figure 4-5: Surface mounted fibre optic backplane connector[3]

Therefore, several authors tried to embed a connector at the edge of the structure [6-8] (Figure 4-6 and Figure 4-7). Great advantage of this method is that the optical fibre is connected to the measuring device, only during measurements, which reduces the risk of fibre failure during operation and fabrication (demoulding). The largest disadvantage is that the composite plate is heavily distorted at the position of the entry point. De Waele [5] embedded an OptoClipII-type connector, which is a very robust but not commonly used connector for telecom applications. It is embedded in a silicone form prior to embedment in the composite plate. The shape of the silicone was designed to have a smooth transition from the thickness of the connector to the thickness of the laminate, since a sharp transition would make the composite very prone to delaminations.

Figure 4-6 [6] shows a precision ceramic ferrule, that has been embedded into composite laminates. These ferrules are the critical components of standard optical fibre connectors. They have an outer diameter of 2,5 mm and the ferrule end is polished together with the fibre to provide the required smooth contact surface for low-loss and low reflection optical signal transmission.

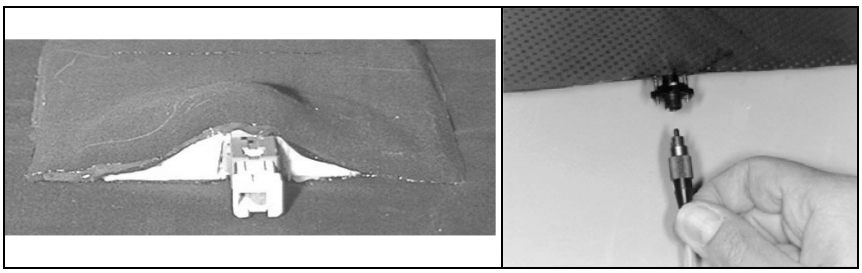

Figure 4-6: Composite plate with embedded optical fibre and fibre connector, fabricated using the autoclave process [5, 6]

Figure 4-6 shows two practical examples of composite specimens with an embedded connector. Only partial edge trimming of the composite remains possible. Therefore Sjôgren et al. [8, 9] developed a similar method as Green et al. [6], however, now only the ferrules are embedded at the edges of the composite laminate, which allows edge trimming. During manufacturing, the ferrules are covered with PTFE dummies. An example of such an embedded connector is shown in Figure 4-7. Several connectors were evaluated and tested for the remaining strength of the composite laminate. It was shown that the failure tensile stress and strain were approximately 50% lower for the specimens with embedded ferrules, compared to the specimens without. The compressive strength was 75% lower than for the specimens without embedded ferrules. It should be noted that these drawbacks could be reduced when the shape of the PTFE dummy had already been cut out the prepreg layers. In that way, distortion of the structure could be minimized. These data show that this solution should only be used at positions of the structure which have no load-bearing function. However, the disadvantage of having created a prone point sensitive to delaminations, exists.

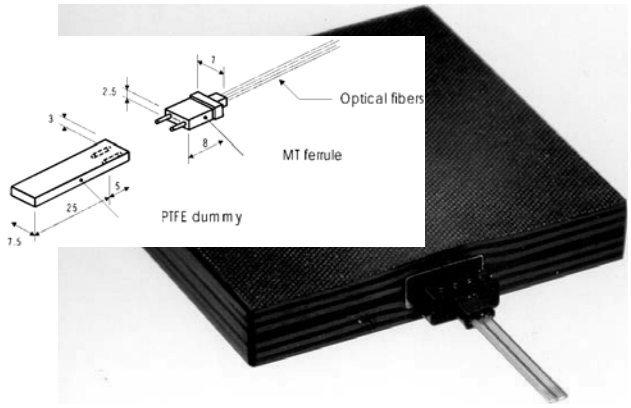

Figure 4-7: The embedded fibre-optic connection. Twenty-two prepreg plies were cut to accommodate the embedded ferrule [8]

4. 2. 1. c. Sleeve protection

Due to the possible damage initiation and large distortion of the host material caused by edge connectors, other solutions were needed. By locally adding a sleeve locally at the in- and outcome of the fibre, better protection is reached than for a bare fibre and the embedding procedure is more simple. De Waele [5] embedded a piece of the protective coating of the optical fibre into the material and realized a smooth transition of the brittle fibre into the stiff composite material (Figure 4-8).

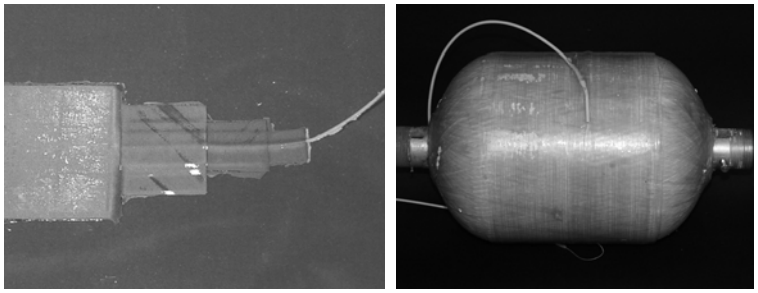

Figure 4-8: In- and egress points of an optical fibre embedded in a composite material protected by embedding a part of the protective coating of the optical fibre [5].

In [2, 10-13], the authors solved the problem related to the necessary composite edge trimming by leading the fibre out through the surface of the structure. In [2, 13], the optical fibre is prepared for embedding by sleeving it with two polyimide and two Teflon tubes of increasing diameter (Figure 4-9). As such, a certain strain relief and thus robustness is created at the egress of the optical fibre. Guemes et al. [11] and Kang et al. [12] lead the fibre out at the surface by extracting it through holes and slits created in the layers of the laminate (Figure 4-10 and Figure 4-11). This point can then eventually be reinforced with a strain relieving structure to avoid damage initiation [12].

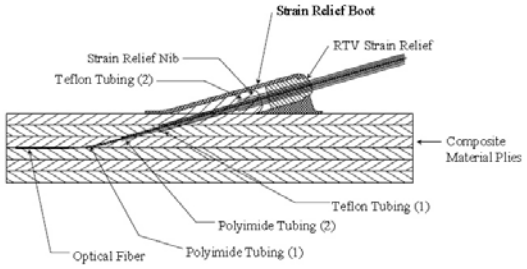

Figure 4-9: Cross section diagram of optical fibre egress from a composite part showing the stepped protective tubing and the silicone strain relief. [2]

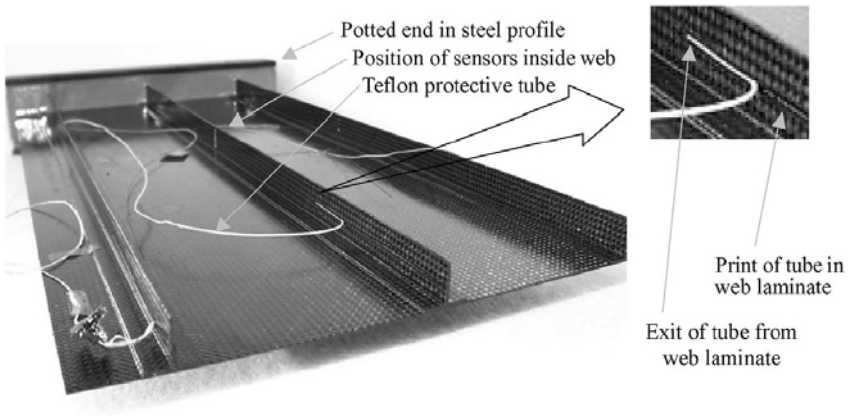

Figure 4-10: Blade-stiffened panels with embedded optical fibre sensors, in- and egress is covered by teflon tubing [11].

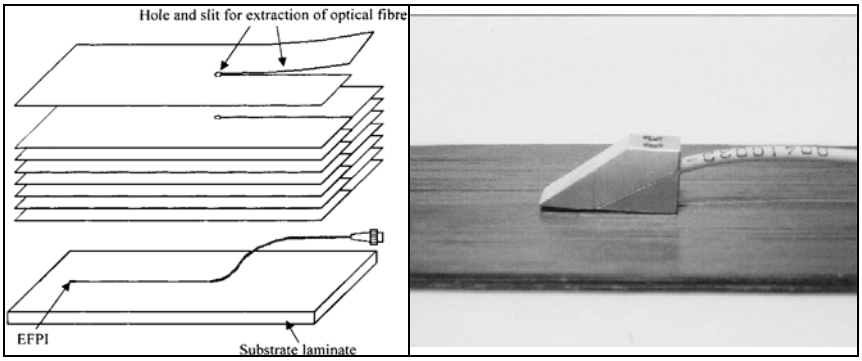

Figure 4-11: Extraction of an optical fibre through holes and slits (left), application of an optical fibre protector (right) [12].

During the MASSFOS project [4], researchers used extra Kapton® foil to protect the fibre outcome. In order to make customised Kapton® foil flex circuits, the fibre is sandwiched between two Kapton® layers (type 100 HN, temperature range: -273°C-400°C [14]) (Figure 4-12). One part of the flex circuit with the FBGs will be embedded in the composite structure, whereas the other part will exit the structure, offering a good protection to the fibres. Figure 4-12 shows a model of a customised Kapton® foil.

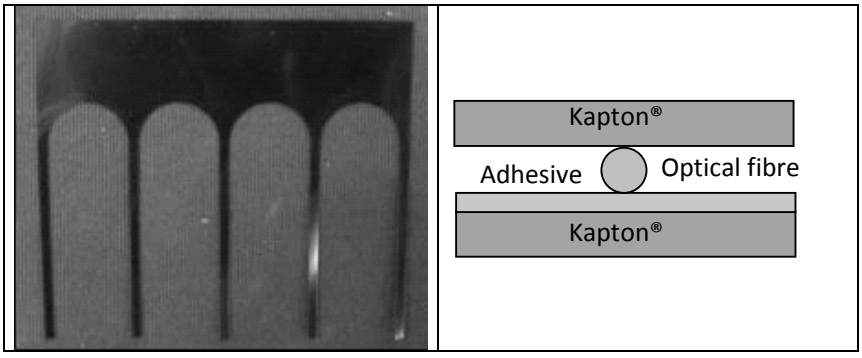

Figure 4-12: Model of customized Kapton® foil (left). In- and egress configuration of an optical fibre covered with Kapton foil [4]

Guemes et al. [11] and the author of this work covered the fibre outcome with a Teflon tubing (PTFE-tubing, 900 µm outer diameter Figure 4-10 and Figure 4-13). The Teflon tubing is very flexible, which creates the opportunity to gently remove excessive resin flow at the edges of the laminate [15]. Great advantage of the Teflon tubing over the Kapton® foil is that the whole fibre (entry point as well as non-embedded tail) is covered and thus protected. In addition, the Teflon tubing gives more strength to the optical fibre when handling the test specimens, which is favourable in clamping the specimens during the executed experiments.

Figure 4-13: The ingress point of the optical fibre is protected using a Teflon tubing [15].

Kapton® foil or flexible Teflon tubing as reinforcement have proven to work in a lab environment. These are robust methods which can withstand high temperatures and pressures. Though, for real-life applications, a fibre supported or not supported on top of the structure or at the edges is not an option. The solution for all these problems could possibly be found in the research on free space optical data communication. In this, an optical fibre is embedded in a host material and the light is spacelessly transmitted to and from the fibre sensor [16-18] (e.g. Figure 4-14). One can, however, have questions on practicality, complexity and cost of such a technology for in-flight monitoring purposes.

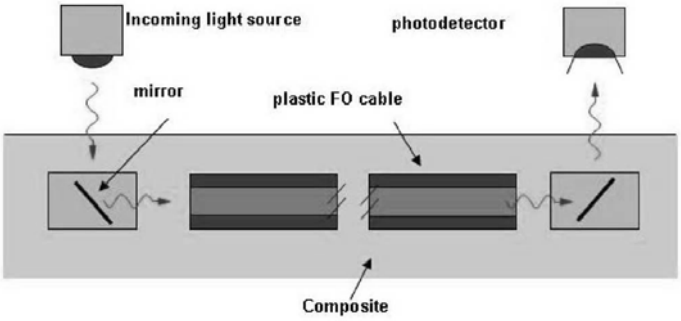

Figure 4-14: Free-space optical porting technique using a self-powered, semiconductor based electronically active transceiver.

4. 2. 2. Fibre orientation procedure

Using HiBi-fibres (Section 2. 3. 2), it is necessary to realize the correct orientation of the fibre when being embedded in a host material. Bad orientation of the fibre (illustrated by angle □ in Figure 4-15) could lead to large errors in the interpretation of measured values of strain.

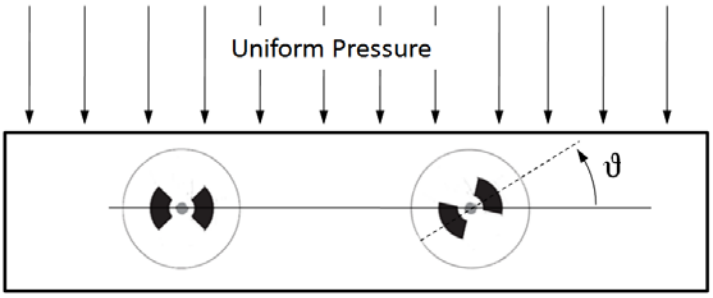

Figure 4-15: Example of two embedded PM optical fibres, one well-oriented and the other □ degrees misaligned.

Two samples were made, one with an embedded fibre misaligned over 13 deg with respect to the surface of the host material, and another misaligned over 60 deg (Figure 4-16). By putting a uniform stress on top of the structure (Figure 4-15), one can see that the Bragg peak shift is clearly different for both sensors. (Figure 4-17) which could lead to an underestimation of the present strain field in the composite material.

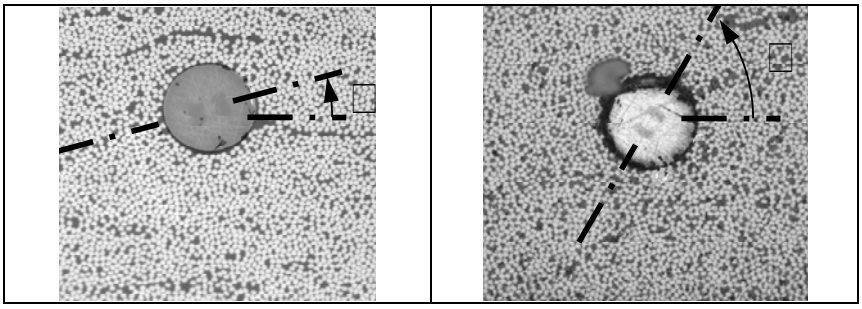

Figure 4-16: Orientation of two embedded fibres, one with a misalignment of 13 deg, the other with a misalignment of 60 deg

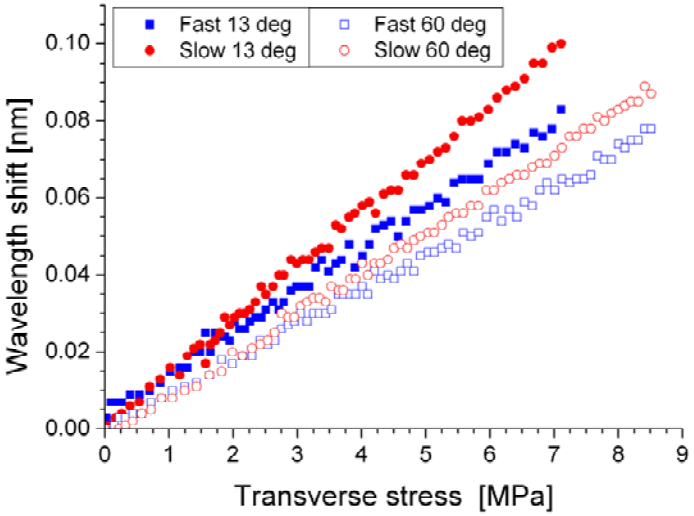

Figure 4-17: Normalized Bragg peak shift vs. applied pressure for the FBG bow-tie in sample 1 (left) and sample 2 (right). □=60 deg and □=13 deg respectively

One can theoretically estimate the error on the calculated strain components due to a badly oriented sensor. As an example, a uniform pressure of 1 MPa is put on top of two unidirectional carbon fibre epoxy laminates. The induced strains along the optical and thus mechanical eigenaxes of the HiBi-fibre can be calculated as function of the angle of misalignment and compared with the strains in a correctly oriented fibre. Table 4-1 shows that large errors can be made in spite of small orientation errors. We should note that in this theoretical example only small strains have been taken into account for which the optical eigenaxes do not rotate significantly. Of course this last effect, which has already been discussed in

section 2. 4. 2. c., will also influence the measurements. It should be noted that the error has been determined using the theoretically calculated transfer coefficient matrix (section 4. 5. 2. a.). These results highlight the importance of a good orientation procedure. In the next sections some procedures will be discussed.

Table 4-1: Measurement error on the transverse strain components when a transverse pressure of 1MPa (σ_{zz}) is put on top of the host structure.

□	ε_{yy} [με/MPa]	Fault on ε_{yy} [με/MPa]	ε_{zz} [με/MPa]	Fault on ε_{zz} [με/MPa]
15 deg	50.0	-14.5	-166.7	14.5
30 deg	50.0	-54.2	-166.7	54.2
45 deg	50.0	-108.3	-166.7	108.3
60 deg	50.0	-162.5	-166.7	162.5

It should be noted that if it is possible to inspect the fibre's orientation in a non-destructive way after production of the structure, the measurement error can be considered for the ultimate result. Micro-tomography (high-resolution 3D X-ray micro-tomography or micro-CT scanning) commonly used to visualize damage or structural changes inside fibre reinforced plastics can be considered [19] as a promising solution for this matter. In this work, however, we rely on polished intersections of samples in post mortem analyses to compare several orientation procedures.

4. 2. 2. a. Backscattering Technique

This method for monitoring the orientation of the principal birefringent axes involves side illumination with a HeNe laser to generate a backscattered interference pattern determined by the fibre cross section [20] (Figure 4-18). By rotating the fibre, the backscattered interference will alter which allows the determination of the right orientation of the HiBi-fibre.

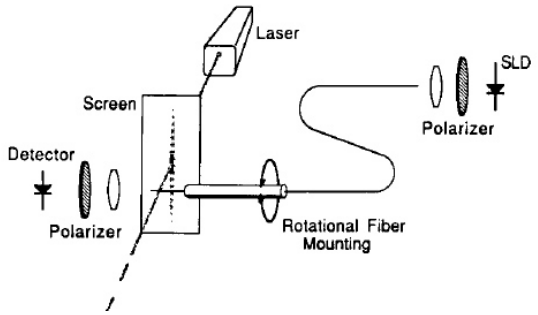

Figure 4-18: A schematic of the backscatter technique for alignment of the principle axes showing the laser, the rotational fibre mounting, and screen [20].

The reliability of such a method was not checked since the necessary optical components were not available.

4. 2. 2. b. Marked ferrules

In this procedure, the orientation of the bow-tie at both ends of the fibre is marked by placing a ferrule with a thin red line (Figure 4-19). Alignment of these ferrules was realized by first cleaving and orienting the fibre under a microscope and finally fixing the ferrules. The author had minimum control on this procedure, since the ferrule placement was done at the company that inscribed the FBGs in the HiBi-fibre. The embedding procedure can be summarized as follows: firstly (Figure 4-20 A), the fibre is oriented by aligning the ferrules, pretensioning and positioning the fibre above the CFRP-sample. Then, the sample is lifted until the optical sensor touches the prepreg layers (Figure 4-20 B). Finally, the remaining prepreg layers can be placed on top of the structure (Figure 4-20 C).

Figure 4-19: Picture of a standard ferrule for optical fibres. The orientation of the fibre is marked with a thin red line (not visible in this picture).

This method, however, has a couple of drawbacks. The alignment is performed over a relatively large distance compared to the dimensions of the sensor (fibre length = ~ 1 m and sensor length = ~1 cm). As such, it is difficult to sustain the correct orientation of the optical fibre at the position of the sensor, because it tends to rotate on the reinforcement fibres in steps (B) and (C) of the embedding procedure (Figure 4-20). In addition, an insecurity exists on the amount of torsion the bow-tie threads get during production (fibre drawing and coating placement) [20]. This leads to an unknown orientation during step (A) of the embedding procedure at the sensor spot.

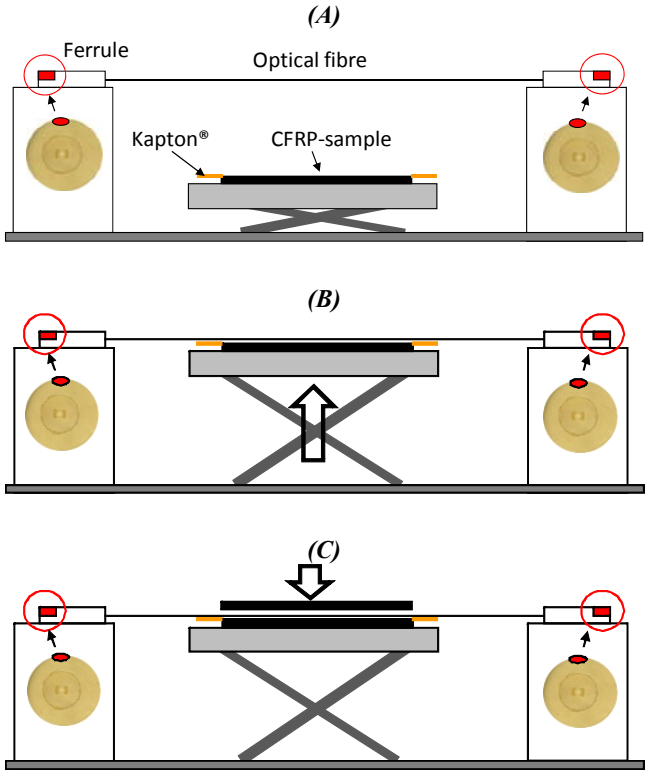

Figure 4-20: The orientation method using marked ferrules at the end of the fibre. (A) The fibre is oriented according to the ferrules, pretensioned and positioned above the CFRP-sample. (B) The sample is lifted until the optical sensor touches the prepreg layers. (C) The rest of the CFRP-sample can be placed on top of the structure.

Figure 4-21 (A) shows the origin of draw induced internal rotation of the birefringent axes due to the rather small misalignment of the fibre draw traction surfaces. It was experimentally found that when freely hanging the optical fibre (with ferrules), the red dots on both ferrules are no longer in line. The fibre had undergone a torsion of approximately 90 deg (Figure 4-21 (B)).

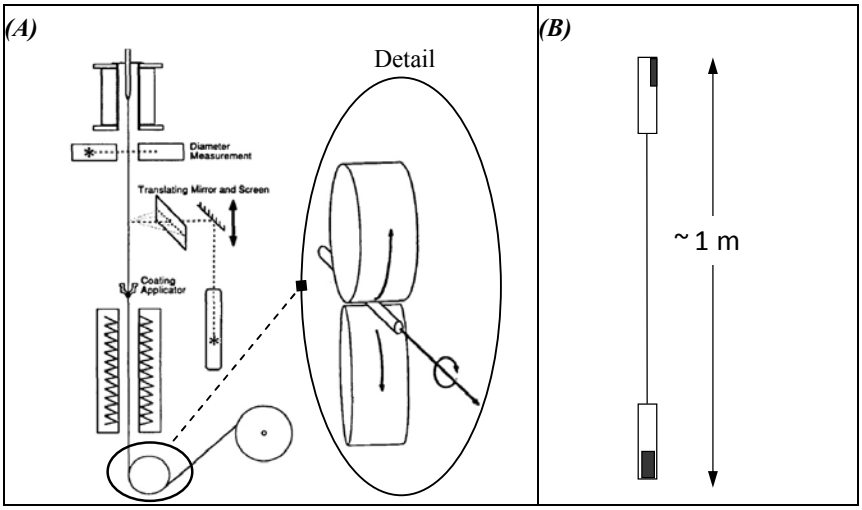

Figure 4-21: (A) Schematic illustration of the fibre drawing process. Misalignment of the fibre draw traction surfaces cause internal rotation of the birefringent axes [20]. (B) Observed torsion of the HiBi-fibre.

Table 4-2 Misalignment observed using the orientation procedure based on marked ferrules.

CFRP Lay-up	Sample 1 [deg]	Sample 2 [deg]
$[0]_{16}$	10	**80**
$[0_2,90_2]_{2s}$	**69**	**62**
$[90]_{16}$	15	15
$[+45_2,-45_2]_{2s}$	**54**	**57**
$[0_2,90_2]_{6s}$	**39**	**25**

In Table 4-2, the orientation errors made for 10 samples, using this method are shown. The results in bold are not acceptable in terms of measurement errors (Table 4-1). As discussed before, the angles were measured by taking a cross section of the CFRP-sample at the sensor location, polishing it and determining the angle between the slow axis and the surface of the sample (horizontal line in Figure 4-22).

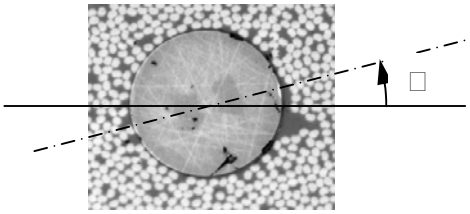

Figure 4-22: Detail of a cross section taken at the location of the sensor to determine the orientation of the optical fibre (bow -tie fibre).

4. 2. 2. c. Microscopic inspection

The orientation is determined by taking a microscopic picture from the side of the fibre (Figure 4-23). This method is derived from the splicing procedure for uncoated HiBi-fibres. During this process, the orientation is controlled using a visual inspection of the stress bars in the cladding.

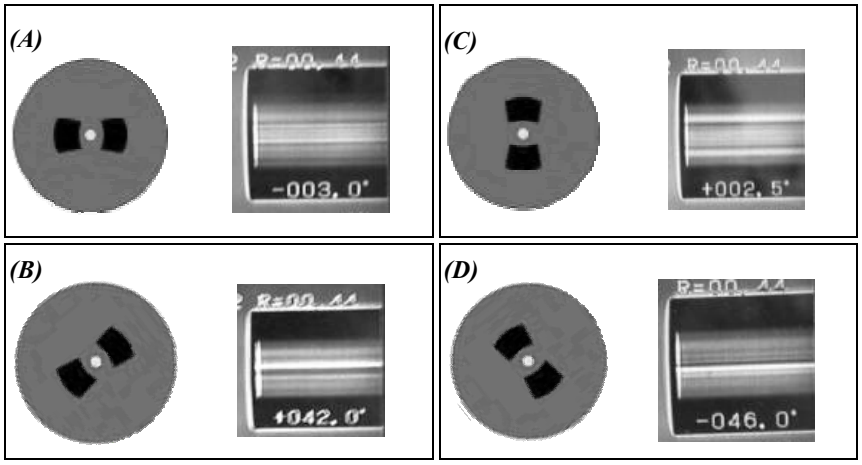

Figure 4-23: The orientation method using a microscope to orient the HiBi-fibre; θ equal to (A) 0 deg , (B) +45 deg, (C) 90 deg, (D) 135 deg

Most fusion splicers view the fibre from the side, focusing on the core with a fairly narrow depth of field. Since the stress members extend in both directions well beyond the plane of the core, they remain substantially out of focus. For this reason, the fibre provides a distinct pattern of two dark lines (90 deg), transitioning to a single dark line (0 deg). In practice, the internal structures of both fibres appear as the series of lighter and darker lines that may be seen in Figure 4-23 (magnification x 200, Sumitomo 35SE Rotary Fusion Splicer). In these images, the main structures that relate to the stress members are the pair of distinct, parallel, 'shadowed' lines. As the fibre rotates, one line grows stronger and the other fades as they move in and

out of the focal plane, during their orbit around the core. This method has not been used in practice because our rotation stages were not aligned accurately enough, which leads to defocusing of the total fibre during its rotation.

4. 2. 2. d. Calibration procedure

By determining the maximum sensitivity of the bow-tie FBG during a qualitative calibration (section 2. 4. 2. c.), one can determine the angle of the mechanical eigenaxes (fast/slow) of the fibre (Figure 4-24). Once these axes are found, the orientation of the HiBi-fibre is fixed with small epoxy drops resulting in a sensor as depicted in Figure 4-25. The biggest advantage compared to the ferrule method is that only the sensor part is oriented, and, as such, extra rotation of the HiBi-fibre during production is omitted. The tabs prevent extra rotation during sensor placement because of the settling of the sensor in between the reinforcement fibres.

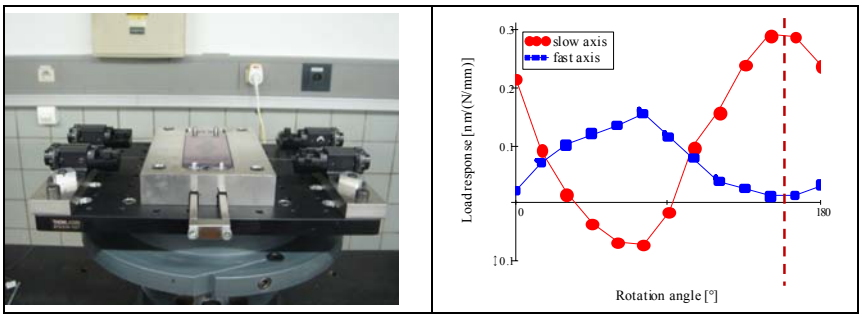

Figure 4-24: Defining the maximum and minimum sensitivity (dashed vertical line) for respectively the fast and the slow axis of the Bow-tie FBG for θ ϵ 0…π using the calibration method described in Chapter 2.

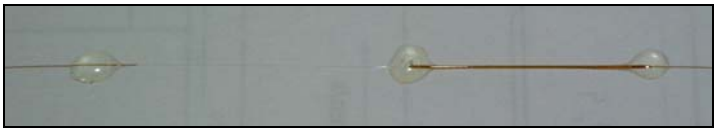

Figure 4-25: Fixing the orientation of the sensor using epoxy tabs right behind the FBGs

Table 4-3: Results of the orientation procedure using a qualitative calibration method for several lay-ups of the CFRP-samples

CFRP Lay-up	Sample 1 [deg]	Sample 2 [deg]
$[0]_{48}$	14	8
$[0_2,90_2]_{6s}$	0	**32**
$[+45_4,-45_4]_{3s}$	**45**	**32**

In Table 4-3, the experimental results for this method are listed for several lay-ups of CFRP-samples. Better results were obtained than when using the method of the marked ferrules. The largest drawback of this method is distortion of the host material during embedding of the epoxy tabs (Figure 4-26), which could lead to damage initiation in the laminate. Therefore, the epoxy tabs need to be kept as small as possible, especially in the case of thin laminates. A second drawback is the embrittlement of the fibre due to rigid tabs, which could lead to breakage of the fibre during the embedding process.

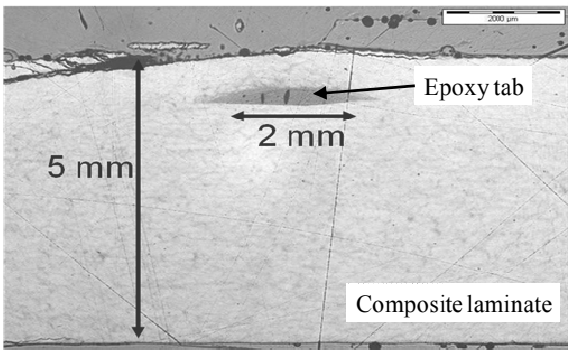

Figure 4-26: Distortion of the laminate due to an embedded epoxy tab.

In order to solve these drawbacks, the epoxy tabs could be replaced by prepreg tabs (Figure 4-27). Since these prepreg tabs have the same material properties as the base material, no distortion is to be expected. Coupons with a $[0_2,90_2]_{6s}$ and a $[\pm45,0_2,90_2,\pm45]_s$ lay-up were fabricated in this way. At the surface of the laminate, no visual external distortion could be noticed even for a thin laminate.

Figure 4-27: Fixing the orientation of the sensor by using prepreg tabs

Remark that using this calibration procedure for orienting the fibre along a certain axis is quite straightforward. However, since this procedure is only performed for one of the two FBGs of the MAxS-sensor (3cm separated from each other), the second FBG could have a slightly different orientation because of intrinsic bow-tie rotation during production (section 4. 2. 2. b.). In addition, it is possible that during handling, i.e. fixation of the fibre using epoxy or prepreg tabs, or even during curing of the laminate, the orientation differs from the one obtained during the calibration process.

It can be stated that yet an optimal solution which is simple, low in cost, not labour intensive, and particularly very accurate was not found. However, the best results were obtained using the calibration procedure. Therefore, this procedure will be used in the rest of this dissertation.

4. 3. COATING OF THE EMBEDDED OPTICAL FIBRE

The coating is the interface between the optical fibre and the host material, and can have a definite impact on the transfer of stresses and strains from the matrix to the fibre. By choosing the right coating, this transfer can be improved in certain principal directions. For example, it is possible to choose a coating for which stress concentrations around the fibre can be avoided and composite distortion minimized [21, 22].

The first studied coating is commonly used in telecommunications, namely **acrylate**. For these applications, the coating serves as a protective layer against moisture and to stop undesirable modes of the light in the cladding [23]. In most cases, the coating consists of a soft (low stiffness) and a hard (high stiffness) coating which makes them easy to strip (the low stiffness of the direct coating is to be avoided in sensor applications in terms of strain transfer). A major requirement is that the coating should survive the production process of the composite specimens. Therefore, acrylate is less suited for sensor applications, since its glass transition temperature is around 100°C [23] (from that point on acrylate becomes viscous), which is a lot lower than the fabrication temperature of autoclave produced composite materials (120°C for glass fibre-epoxy and 180°C for carbon fibre-epoxy).

The second type is **polyimide** coated fibre, which is typically more rugged than the acrylate type. The protective polyimide film is thermally stable for brief periods of time near 600°C and can be used for extended periods at 300°C [23]. Polyimide coatings typically are much thinner (8-20 μm) than acrylate coatings (63 μm) due to processing requirements.

An **Ormocer**® (organic modified ceramic) coating is the last type considered. A lot of properties and applications (except the temperature resistance) of Ormocer® coatings are given in Haas et al. [24]. For more information, the reader is also pointed to the website of the Fraunhofer isc [25].

Two methods are used here to experimentally compare these three different types of coatings (Table 4-4). The first one is the stripping test in which the fibre is clamped at one side between two knives that strip the coating of the fibre. The second one is the pull-out test. Several experiments were executed, and a general judgement was made based on the peak load and the shape of the obtained curves. The experiments were done by the author during the MASSFOS-project [26].

Table 4-4: Dimensions of the different coated optical fibres.

Type	Curing type	Fibre diameter/total diameter [µm]	Remarks
Acrylate	UV	125/245	Dual layer
Polyimide	Thermal	125/155	
Ormocer®	UV	125/195	2 different types

4. 3. 1. Strip force test

The strip force test is widely used in the fibre optic telecommunications industry. This force is connected with the mechanical properties of the coatings, and with the adhesion between the coating and the glass. Figure 4-28 gives an example of a strip force test arrangement [27]. At one end, the fibre is clamped in a stripper, which consists of 2 knifes mounted transversally onto the fibre. On the other end, the fibre is wound on a drum, which is pulled by a universal test machine at constant velocity. While pulling, displacement and applied load are measured. Because polyimide is difficult to strip mechanically this coating will not be evaluated in a strip force test.
When embedded in carbon fibre-epoxy components, the optical fibre will be exposed to high temperatures during the curing cycle, which might influence its own properties and those of its coating. Therefore, a series of fibre strip force tests were done on fibres that had undergone different heat treatments (4 hours in an oven at 125°C or 4 hours at 180°C). Since acrylate is unable to withstand temperatures above 100°C, only the Ormocer® coated fibre was heated.

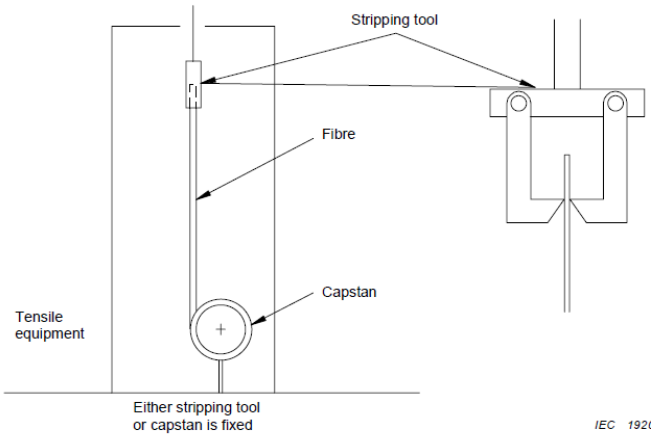

Figure 4-28: Example of a strip force test arrangement [27]

No significant deterioration of the coating properties was observed for the Ormocer® coated fibre after a certain heat treatment [26]. Therefore, the strip force

will be compared only for Ormocer® coated and acrylate coated fibres without heat treatment. The strip force curves of the Ormocer® coated fibre (Figure 4-29, Left) show a saw tooth pattern, which can be interpreted as follows: while pulling the tensile force is increased, since the coating prevents the fibre from moving across the stripper. Due to the increased tensile force, the fibre is strained and thus elongates; this explains the rising of the curves. This process continues until the tensile force is higher than the adhesion force between the coating and the fibre (i.e. the strip force). At that point, the coating-fibre interface breaks at the fibre in the stripper and the tensile force immediately drops down. As such, the maximum strip force for each sample was determined and averaged over 4 samples. The average stripping force is similar to that of the heated fibres (around 4 N).

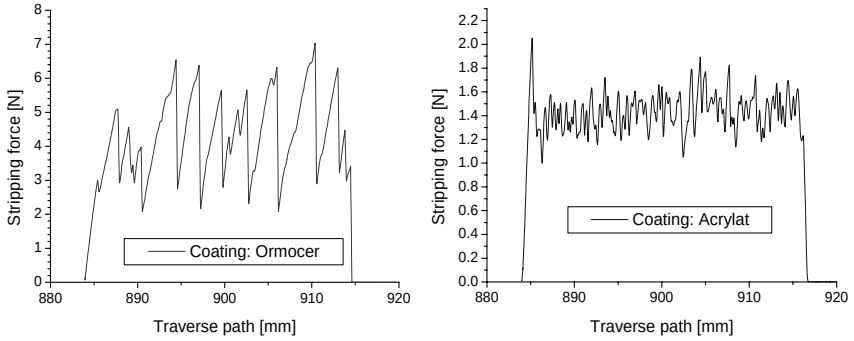

Figure 4-29: Result of a strip force test on Ormocer® coated fibre without heat treatment (left) and standard acrylate coated fibre without heat treatment (right) [26].

In order to compare, the results of a strip force test on standard acrylate coated fibre are also shown in Figure 4-29 at the right (no heat treatment). In the beginning, a threshold force of roughly 2 N is needed to strip the fibre. Once this force is reached, stripping goes very easily and the absence of the saw-tooth pattern indicates a much lower adhesion between coating and fibres compared to the Ormocer® coating.

4. 3. 2. Pull-out test

This type of test is popular in defining the fibre/matrix interface of reinforcement fibres bonded in some kind of epoxy [28, 29]. In this test, a single fibre is pulled out of the surrounding matrix; the corresponding load versus displacement is recorded (Figure 4-30). The same procedure can be used for optical fibres with or without coating to define the fibre/matrix, fibre/coating and coating/matrix properties. The experimental configuration for the pullout tests is depicted in Figure 4-30 (left), in which t is the embedded length of the fibre, P_a is the applied load, l_d is the debonded

length, l_0 is the initial fibre length and δ is the recorded displacement. According to Kerans et al. [30] failure of the fibre/matrix interface will initiate in the region of induced maximum stress, located near the surface (Figure 4-31). After failure, the stress will shift and increase. At this point (point a in Figure 4-30 right), the shear stress needed to drive the debonding crack is the same, however an additional friction stress is causing an increase of the necessary pullout load. Due to friction, the maximum load occurs near the end of the process when the debonding crack has propagated nearly to the fibre end. At that point (point b in Figure 4-30 right), the shear stress at the interface becomes sufficient to break the remaining bonded length catastrophically. The load required for further pullout then drops to the level necessary to slip the debonded fibre against friction.

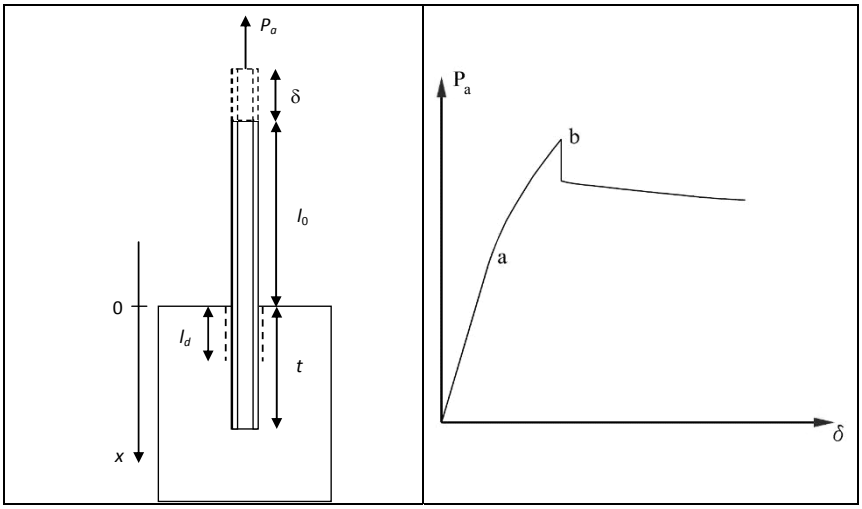

Figure 4-30: The experimental configuration for the pullout tests (left). A theoretical drawing of the load-displacement plot during fibre pullout, debonding initiates at "a" and is complete at "b" (right).

As mentioned before the fibre/matrix interface consists of two interfaces: the fibre/coating interface and the coating/matrix interface. In the following pullout tests, the fibre/coating interface was always the weakest because debonding happened at that interface.

The different types of coated fibres were embedded over 4cm in an epoxy (LY556-HY917-DY070 which is commonly used in aerospace) and cured for 4h at 125°C or for 4h at 180°C. As reference for the acrylate coated fibres, an extra epoxy sample which cured at room temperature was used.

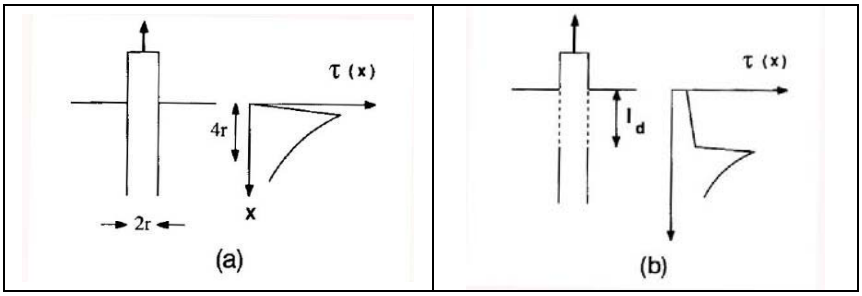

Figure 4-31: Schematic drawing showing the variation of the shear stress along the interface (a) before debonding initiation and (b) after debonding has progressed over a length l_d [30].

Acrylate

The results of the pullout tests performed on the acrylate coated fibre samples are depicted in Figure 4-32. The recorded curves have the expected shape as discussed above, however they show some mutual differences. The epoxy sample cured at room temperature reaches the highest tensile force (over 9 N). The samples cured at higher temperatures (125°C and 180°C) all exhibit a much lower maximum tensile force (< 4 N). Hence, the high temperature curing has reduced the bonding strength of the coating/fibre interface which is caused by the low temperature resistance of acrylate.

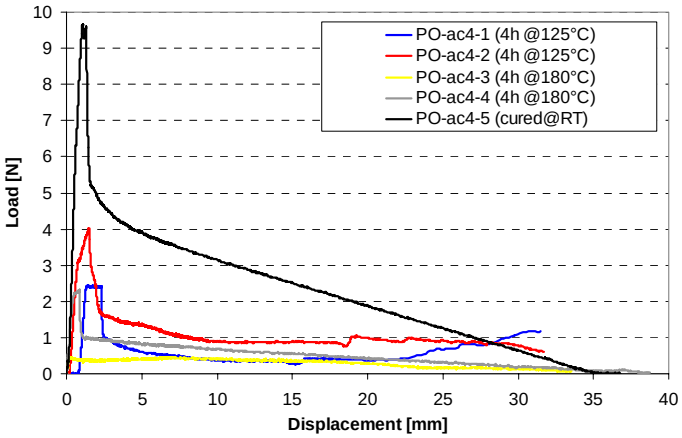

Figure 4-32: Pullout tests of samples with acrylate coated fibre in epoxy cured at different temperatures.

Polyimide

The same tests were done for the polyimide coated fibres. The results are depicted in Figure 4-33. The curves differ slightly from the typical pull-out curve (Figure 4-30) because of the absence of the sharp drop in applied load. This indicates that friction forces are relatively high for this fibre/coating interface. It is indeed generally known that polyimide attaches very well to the glass fibre, which is also the reason why it is difficult to mechanically strip polyimide coated fibres.

The maximum applied load is much higher than for the acrylate coated fibres. Most samples reach their maximum at around 40 to 50 N. Since polyimide is able to withstand high temperatures, no temperature deterioration is observed. Note also the small saw tooth pattern superimposed on most of the curves. This is caused by the so-called stick-slip effect [31]. This effect occurs in mechanical problems where a body is exposed to friction forces. Two types of friction can be observed: static and dynamic friction. Static friction between 2 bodies occurs when both objects are at rest. The friction force is proportional to the external force acting upon the body (here the fibre pulling force) and the proportionality is given by the static coefficient of friction. Dynamic friction occurs when one body moves with respect to the other. Again, there is proportionality but this is given by the dynamic coefficient of friction, which is in general smaller than the static one. Hence, it requires more force to get an object starting to move than to keep it moving, and the coefficient of static friction acts like a threshold for the object to be moved. This threshold is the boundary between 'slipping' and 'sticking', hence stick-slip.

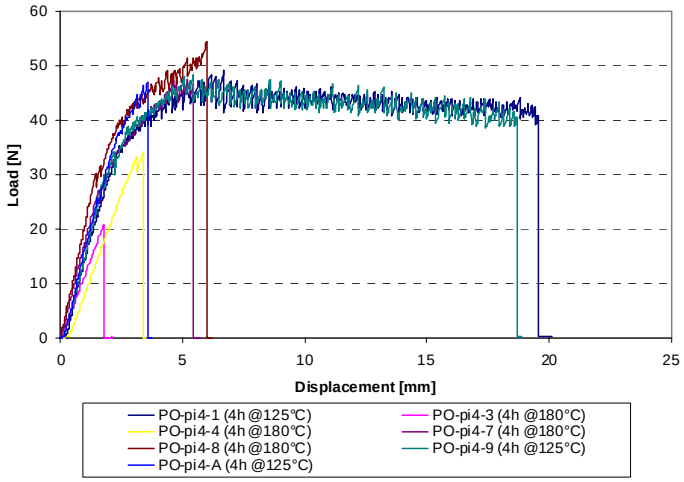

Figure 4-33: Pullout tests of samples with polyimide coated fibre in epoxy cured at different temperatures.

Ormocer®

Two types of Ormocer® with different Young's modulus were tested. The samples named PO-or4-5 and PO-or4-6 are fibres coated with a new type of Ormocer® which has a lower Young's modulus. The results of the pullout tests are presented in Figure 4-34. In all cases, fibre failure occurred before complete pull-out. Final displacements are small, though maximum tensile forces are comparable to those observed for the polyimide samples (between 20 and 50 N).

The curves for the first (PO-or4-1 to PO-or4-3) show a noticeable saw tooth pattern whereas those for the other Ormocer® coated samples show a more moderate saw tooth pattern. In both cases, the presence of the saw tooth has the same origin as in the case of the stripping tests discussed in section 4. 3. 1.. At first, the fibre is linearly strained with increasing load. Shear stress builds up until it becomes larger than the debonding force. At that point, the interface fails and a loud 'tac' sound is audible. Part of the fibre comes loose from its coating and the tensile force is redistributed over the prolonged loose fibre, resulting in a relaxation of the applied load (sharp drop of the saw tooth). Because of the better fibre/coating interface of the first type of Ormocer®, the size of the saw tooth pattern will be larger. Note that early fibre breakage can be related to the sudden release of energy when the built up shear stress has become larger than the debonding force. In addition, no temperature deterioration is observed.

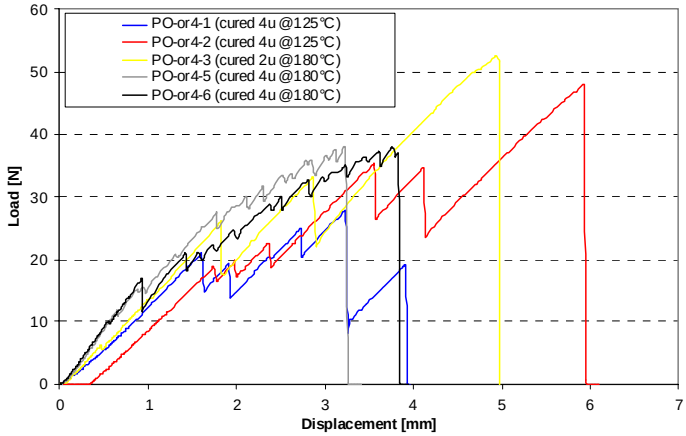

Figure 4-34: Pullout tests of samples with Ormocer® coated fibre in epoxy cured at different temperatures.

Uncoated fibre

For this test, the fibre coating was mechanically removed before being embedded into the epoxy. Figure 4-35 shows the result of one pullout test on a failed sample

that was cured for 1 h at 70°C and 4 h at 180°C. The fibre/matrix interface broke at 20 N, which is worse than Ormocer® and polyimide but a lot better than acrylate. The sudden drop in the curve is not due to fibre breakage but due to a catastrophically failure of the interface. The built up shear stress was high enough to break the complete fibre/epoxy interface.

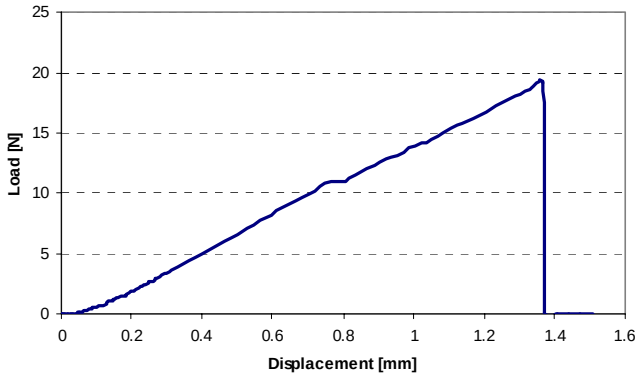

Figure 4-35: Pullout tests of a sample with a non-coated fibre in epoxy

Summary

Different coating types were examined in order to determine the adhesion properties of a fibre embedded in epoxy (pull-out) and the strength of the fibre/coating interface (stripping test). It was found that Ormocer® and polyimide showed excellent adhesion properties in both tests. Even a naked fibre had reasonable adhesion, though friction forces after breakage of the fibre/epoxy interface were very low. Acrylate showed poor adhesion properties. Based on these results, it can be stated that Ormocer® as well as polyimide are acceptable as coating for the optical fibre lead inside the composite structure. However, in this work, no coating was applied at the sensor region to obtain a good transfer of the total strain field in the host material onto the sensor. A secondary coating generally has a much lower Young's modulus than the glass fibre and therefore it can act as a buffer.

4. 3. 3. Evaluation of interface properties with a chirped grating

In this section, a new method is proposed to follow up the interface properties of an embedded recoated fibre during pull-out. During a conventional pull-out test only displacement and applied load is recorded. It will be shown that by embedding a chirped grating written at the fibre end in a pull-out sample, one can measure the debonded length as well. This method was developed in cooperation with Multitel (Mons, Belgium).

In chirped gratings, the period of the grating (Λ) varies along the length of the grating. As such, the Bragg wavelength ($\lambda_B = 2n_{eff}\Lambda$) also changes, resulting in the broad spectrum of Figure 4-36 (right).

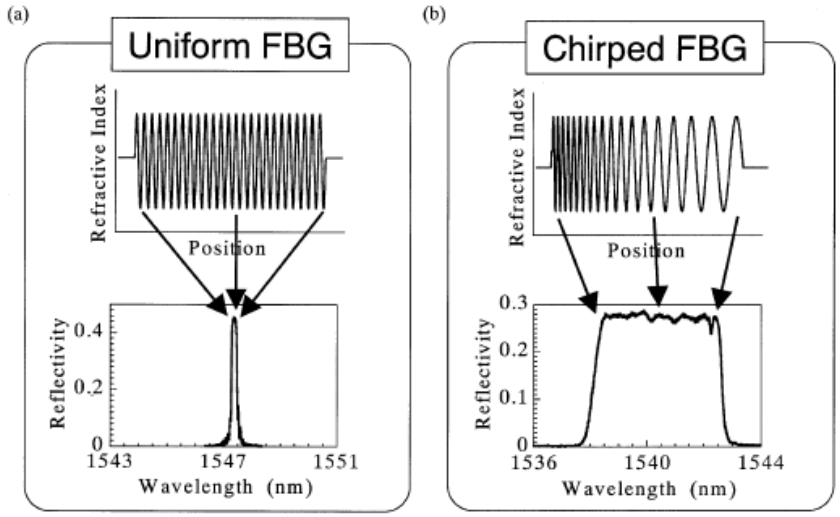

Figure 4-36: Comparison of the reflected wavelengths for a uniform Bragg grating (a) and a chirped Bragg grating (b) [32].

The sensor configuration for this pull-out test is an 11.5 mm long recoated chirped fibre Bragg grating which is embedded in an epoxy sample. The strain outside the sample is measured using a 1mm long uniform fibre Bragg grating. The recoating of the chirped grating is done with acrylate (Figure 4-37).

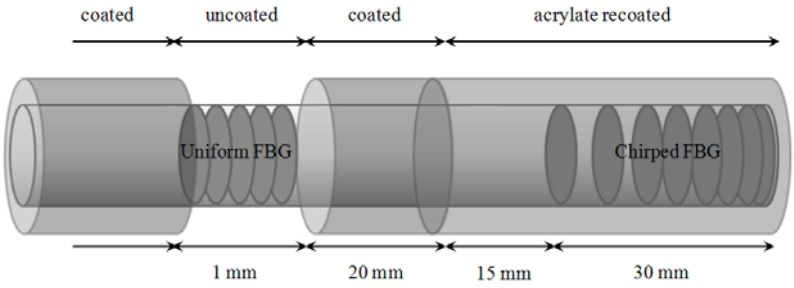

Figure 4-37: FBG sensor configuration used to evaluate the debonded length during a pull-out test

The reflected spectrum of this configuration is given in Figure 4-38, in which the plateau (1530-1545 nm) is caused by the chirped grating and the single peak

(1557 nm) is caused by the uniform grating. During the pull-out test, the reflected spectrum is measured every 4 seconds with a commercially available interrogator (FBG-scan 406 of FOS&S [33])

During a preliminary experiment, the spectrum of the chirped grating will grow in width while the single Bragg peak shifts to the right due to straining of the external part of the fibre (Figure 4-39).

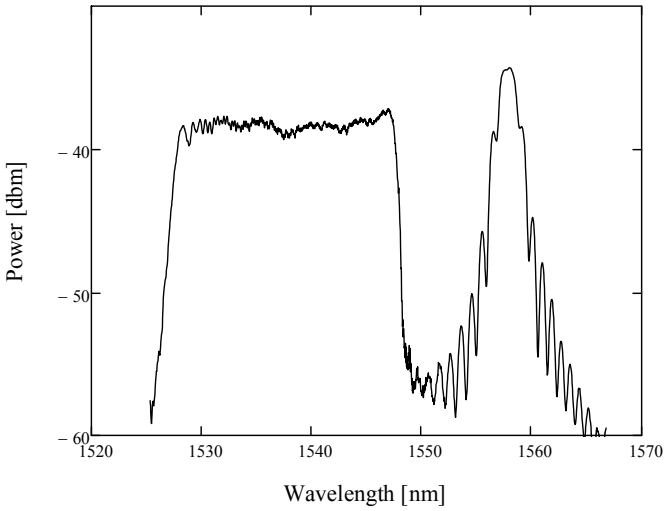

Figure 4-38: Spectrum of the unloaded fibre before pull-out [34]

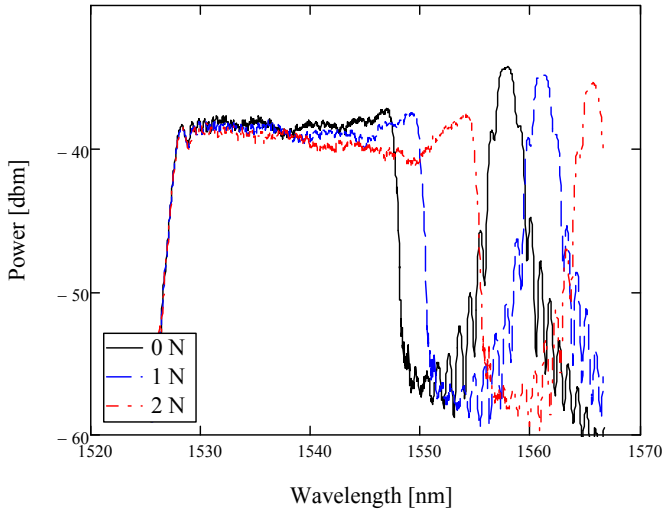

Figure 4-39: Spectrum of the unloaded fibre (full line) and loaded fibre (dashed lines) during pull-out [34]

Whenever debonding occurs somewhere in between the chirped grating, part of this grating will be strained and thus part of the spectrum will shift to higher wavelengths. The spectrum of the unstrained part will remain unaltered. As such, a local minimum of the spectrum will occur at the position of the end of the partially debonded fibre (Figure 4-40).

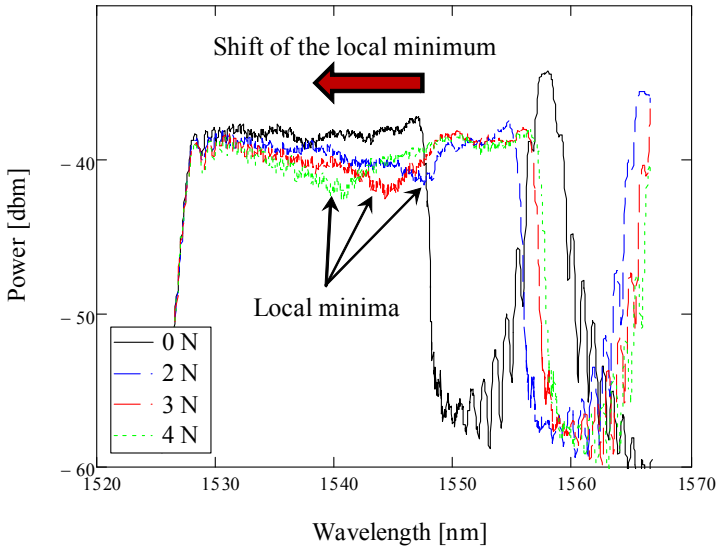

Figure 4-40: Spectra with minima indicating the position of the fibre debonding (spectra smoothed with a running average method) [34]

Calculating the corresponding position in the fibre of each minimum gives the debonded length as function of time (Figure 4-41).
This seems a promising method to determine the interface properties of different coated optical fibres. However, a faster interrogation unit (higher sample frequency) will be necessary for determining the interface properties of for example a polyimide or Ormocer® coated fibre. More research is necessary to optimize the proposed method.

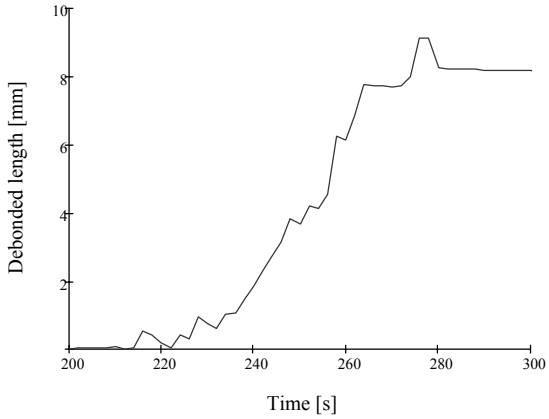

Figure 4-41: Debonded length as function of the time [34]

4. 3. 4. Strength of the optical fibre

The mechanical strength of a coated optical fibre is determined according to the IEC793_1_3 standard. The testing is performed using a Zwick Z010 tensile testing facility. Fibres with and without heat treatment were tested to check possible deterioration of the strength after, for example, the curing process of a thermoset material. The tests were executed by winding the fibre at both ends on a drum-like fixation. The applied load is recorded as a function of time. The results for the tensile test with the pre-heated Ormocer® coated fibre are presented in Figure 4-42. The results for the pre-heated polyimide coated fibres are shown in Figure 4-43.

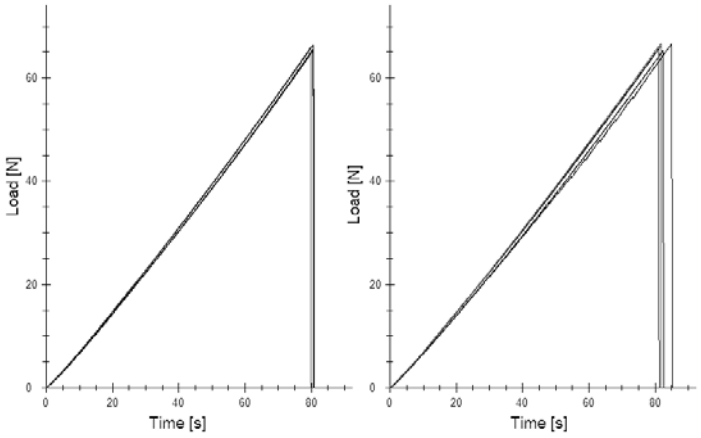

Figure 4-42: Tensile tests on Ormocer® coated fibre aged 4 h at 125°C (left) and at 180°C (right).

For the Ormocer® coated fibres, no difference could be observed between the samples heated up for 4 h at 125°C and those heated up for 4 h at 180°C. Also, no significant difference exists between the pre-heated fibres and the untreated fibre (failure occurs at roughly 64 N [26]). However, for the polyimide coated fibres, a significant difference can be observed for the heat treatments at both temperatures (Figure 4-43). The samples heated up for 4 h at 125°C, already have a lower tensile strength compared to the untreated fibres and for the samples heated up for 4 h at 180°C, the fibres' tensile strength was reduced drastically to breaking forces of ±12 N. Note however, that this effect might be related to oxidation of the polyimide coating, which possibly deteriorates it and makes it weak at higher temperatures. In this case, as the sensor is embedded, the effect will be much lower.

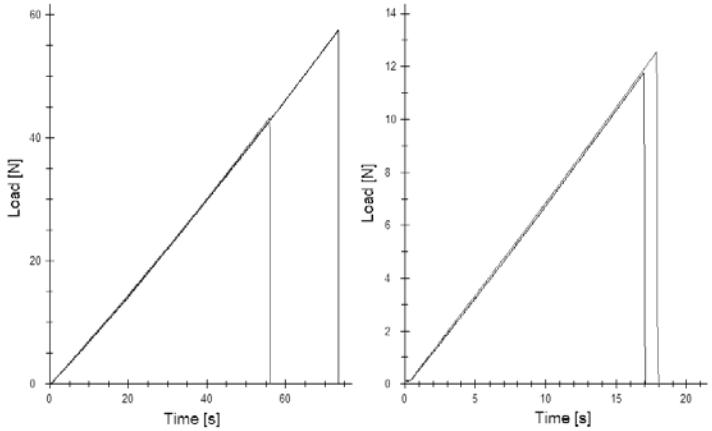

Figure 4-43: Tensile test of polyimide coated fibre aged 4 h at 125°C (left) and at 180°C (right).

Since the fibres in this work will be stripped prior to writing the FBGs and embedding them, it is also worth considering the strength of an uncoated fibre. The strength of an optical fibre tends to drop under 1% whenever the coating is stripped before writing the FBG [35]. This stripping can be done mechanically or chemically. Chemical stripping is preferred (for polyimide this can be done with hot sulphur acid; for acrylate and Ormocer®, dichlorometane (CH_2CL_2) can be used) over mechanically removed coatings [36]. If the possibility exists one should write the grating during the production process of the fibre [37]. This has never been done with HiBi-fibres and, as such, chemical stripping was preferred. It should be noted that the failure strain of the host material (M55J/M18 prepreg material from Hexcel) is around 0.6% [38], which is lower than the intrinsic failure strength of the optical fibre (5%) [39, 40].

4. 4. DISTORTION OF THE COMPOSITE MATERIAL

It is well-known that an embedded optical fibre will cause a distortion of the material in which it is embedded. This distortion depends on the size of the optical fibres, the size of the reinforcement fibres, the type of material used (uni-directional, fabric, …), and the relative orientation of the optical fibre with respect to the reinforcement fibres.

Size matters: the smaller the optical fibres the less distortion of the structure. In literature, the size of the optical fibres is situated in the range of 125 μm [41] (which is a classical telecom fibre) down to 52 μm [42]. Such small diameter optical fibres have both mechanical and optical properties similar to those of conventional optical fibres with 125 μm in cladding diameter, and do not cause any significant reduction in strength of composites when embedded parallel to the reinforcing fibres in laminates [43]. When such a small diameter optical fibre is embedded inside a lamina, resin-rich regions (also called resin eye) are not found around the fibre. To the contrary, this is the case for embedded standard telecom optical fibres [5, 35, 44]. The fibres in this work are bow-tie fibres with a cladding diameter of 80 μm. A comparison between the size of a typical optical fibre and some typical reinforcement fibres is found in Table 4-5.

Table 4-5: Comparison of the size of an optical fibre with the size of typical reinforcement fibres

Type of fibre	Diameter [μm]
Optical fibre:	
non-coated	40 – 125
coated	52-250
Glass fibre	10 (5 – 20)
Carbon fibre	6 (5 – 10)
Kevlar	12

Notwithstanding the absence of a resin eye, embedded optical fibres can still have an effect on the mechanical behaviour of the structure in which they are embedded. Shivakumar and Emanwori [45] embedded optical fibres with a relative orientation to the reinforcement fibres and examined the size of the resin eye. This size was not influenced by the relative orientation (when different from 0 deg). Afterwards, tensile and compression tests were executed. No significant lower tensile strength was observed for all the samples. In compression, however, the strength drops as the relative orientation is larger than 60 deg (fibre almost perpendicularly oriented with respect to the reinforcement fibres). Structural properties were not affected when the fibre was embedded parallel to the reinforcement fibres. In the following work of

this dissertation, the optical fibre sensor has always been embedded parallel to the reinforcement fibres of the material in which it is embedded.

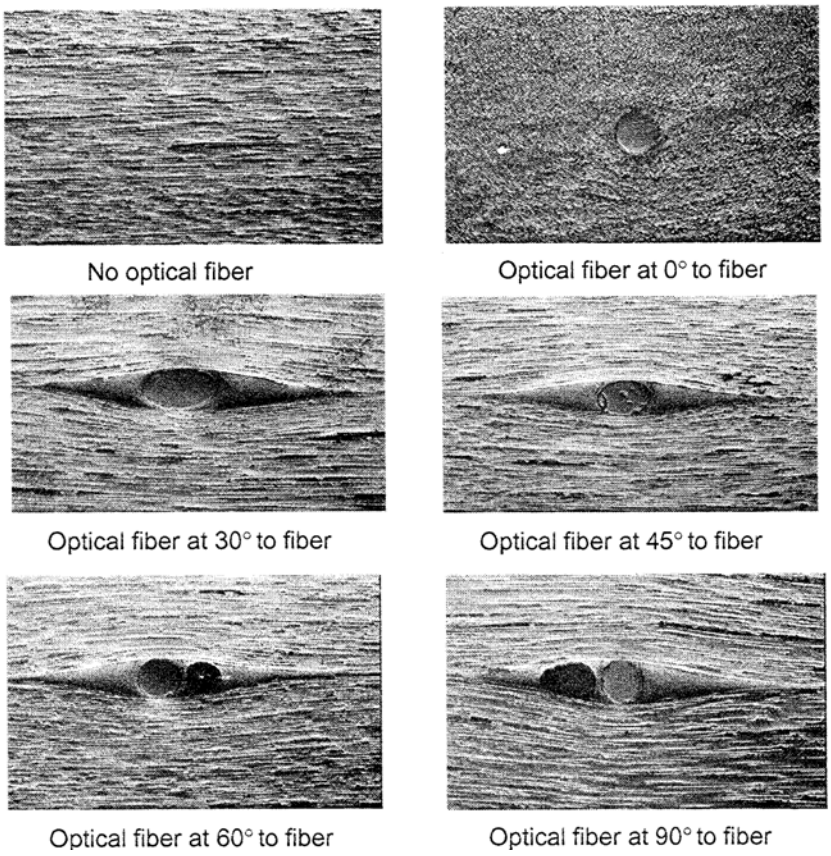

Figure 4-44: Microscopic pictures for different relative orientations of the embedded optical fibre to the reinforcement fibres [45].

This structural strength analysis does not consider the disturbance of the stress/strain field. The strain field around an embedded optical fibre is significantly changed and the interfacial stresses increase [46]. In addition, the stress/strain field present in the composite host material will differ significantly from the one present in the core of the optical fibre, due to the different mechanical properties of both materials. Several researchers have studied this interaction; an overview is given in the next section.

4. 5. STRAIN DISTURBANCE – TRANSFER COEFFICIENT MATRIX

Figure 4-1 illustrates the overview of a structural health monitoring scheme which was given in the beginning of this dissertation. From right to left, the second step in this scheme is the transition of strain in the embedded sensor to the local (near field) strain in the host material. This strain relationship is simple for equal elastic properties of host and sensor, however, in most cases they are substantially different. Thus, one needs to be careful when relating the measured strain with the one existing in the structure [47].

In this work, the embedded sensor is an optical fibre sensor and the host structure is a carbon fibre reinforced epoxy which has different material properties (Table 4-6 and Table 4-7). As such, **a strain transfer coefficient matrix (*TC*-matrix)** needs to be defined that relates the strain of the sensor with the strain inside the structure as if no sensor would be present. This *TC*-matrix depends on the elastic properties of the sensor as well as on those of the host material.

Table 4-6: Elastic material properties for the M55J/M18 carbon/epoxy material

E_{11}	$E_{22} = E_{33}$	$G_{12}=G_{13}$	G_{23}	$\nu_{12}=\nu=$	$\nu_{23}=\nu_{32}$	$\nu_{21}=\nu_{31}$
[GPa]	[GPa]	[GPa]	[GPa]	[-]	[-]	[-]
300	6.3	4.3	2.283	0.32	0.38	0.0017

Table 4-7: Elastic material properties for a fused silica bow-tie optical fibre

E_{fibre}	ν_{fibre}	E_{SAP}	ν_{SAP}
[GPa]	[-]	[GPa]	[-]
70	0.17	51	0.21

Several authors have embedded optical fibre sensors in composite material to measure axial strain. In most cases, the relationship between axial strain of the sensor and host material is given; a coated sensor is used and the influence of transverse strain components is neglected. In this section, the author first briefly describes the method used by other authors to define the axial strain transfer and then switches to a method to define the multi-axial strain transfer.

4. 5. 1. Axial strain transfer

Although in this work only embedded sensors are being examined in detail, the author wants to give some remarks on the strain transfer of surface-mounted FBG strain sensors. These sensors are embedded in a thin layer of adhesive, and bonded to the surface of a structure. The adhesive layer thickness and properties of this layer have a certain influence on the strain transferred from the structure to the bonded

FBG [48]. Li et al. [49] determined the strain transmission rate of an FBG bonded on top of a substrate (Figure 4-45). The strain transmission loss is small when the substrate is thick and stiff compared to the bonding layer and the FBG. However, it becomes large when the substrate is thin and made of low modulus materials. Moreover, bonded on a thin and low-modulus substrate, the FBG changes the original strain on the substrate.

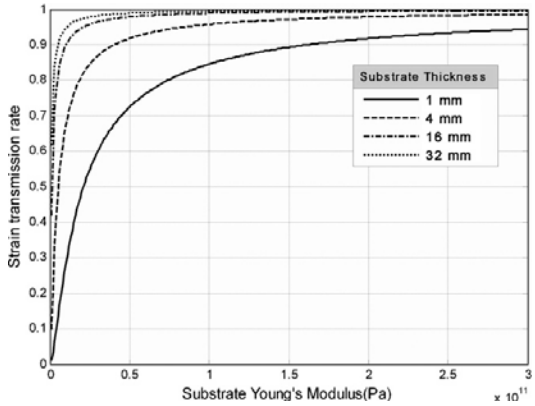

Figure 4-45: The strain transmission rate as function of the Young's modulus of the substrate and substrate thickness [49].

Wan et al. [50] found that for a surface bonded fibre, the strain transfer is dominated by (i) adhesive thickness between the bottom of the fibre and the substrate and (ii) the bond length of the fibre (Figure 4-46). Three different types of fibre were considered; the bare fibre gave the best results both analytically as in FEM simulations.

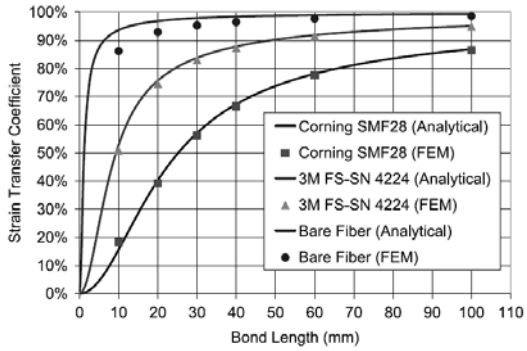

Figure 4-46: Variation of strain transfer coefficient for different fibre types as function of bond length (bottom thickness = 0.1 mm, side width = 2 mm, top thickness = 0.15 mm) [50].

Bond length and thickness are important for mounted optical fibre sensors. However, since embedded fibres are completely surrounded by the host material, one cannot speak of bond thickness and bond length. Chang et al. [51] found that apparent strain gradients only exist over 2 mm starting at the entry point of the embedded fibre, which proves that bond length is not an issue. It should be noted that this length depends on the material properties of both host and embedded optical fibre. A lower Young's modulus of the host material results as such in longer sections of non-uniform axial strain near the ingress and egress sections of the optical fibre.

Cox [52] analytically determined the strain transfer for the case of a finite length cylindrical inclusion embedded into a surrounding material with an axially constant strain field. Chang et al. [51] measured the load acting in a transverse direction by measuring the strains induced by Poisson effects (axial strain) in a direction perpendicular to the load direction. In addition, they compared the model of Cox with a FE-model. Both approaches showed good agreements. Fan et al. [53] experimentally determined the influence of additionally induced radial strain in optical fibres whenever embedded in a host material. Once integrated in the structure, the gauge factor ($\left(1-P\right)$, Section 2. 2. 2.) of a bare fibre cannot be used anymore. The authors tried to quantify this mismatch by producing two $[0_8,90_4]_s$ composite specimens in which two FGBs were embedded; one along the the 0deg direction and one along the 90 deg direction. Errors were found up to 8% when using the bare FBGs gauge factor for axial strain. To correct this factor, the authors suggest to use a coefficient which is dependent on the type of load, tensile or compression (respectively + 3% and -8%).

Former research activities pointed out the need to determine the total strain field response of an embedded FBG in a host material. All strain components, not only axial strain, have to be considered.

4. 5. 2. Multi-axial strain transfer

Bosia et al [54] studied the response of a sensor embedded in an epoxy specimen experiencing biaxial loading. Using finite elements, the difference in strain of the host material and the embedded sensor was shown for transversally applied loads. However, no longitudinal strain and temperature changes were taken into account.

Due to the complex interaction between the host material and the embedded optical fibre sensors, the relationship between the strain present in the core of the sensor and in the host material is difficult to predict and can in general form be written as:

$$\begin{bmatrix} \varepsilon_1^c \\ \varepsilon_2^c \\ \vdots \\ \varepsilon_6^c \\ \Delta T^c \end{bmatrix} = \begin{bmatrix} TC_{11} & TC_{12} & \cdots & TC_{16} & TC_{17} \\ TC_{21} & TC_{22} & \cdots & TC_{26} & TC_{27} \\ \vdots & \vdots & \ddots & \vdots & \vdots \\ TC_{61} & TC_{62} & \cdots & TC_{66} & TC_{67} \\ TC_{71} & TC_{72} & \cdots & TC_{76} & TC_{77} \end{bmatrix} \begin{bmatrix} \varepsilon_1^s \\ \varepsilon_2^s \\ \vdots \\ \varepsilon_6^s \\ \Delta T^s \end{bmatrix} \quad \textbf{4-1}$$

In which ε_i^c ($i = 1,\ldots,6$) is the strain of the composite material as if no optical fibre sensor was present, ε_i^s ($i = 1,\ldots,6$) is the strain field present in the core of the optical fibre sensor. In both cases the subscript $i = 1,\ldots,6$ refers to the components of stresses and strains in contracted notation [55]. The strain relationship is based on 49 independent transfer coefficients (TC_{ij} ($i, j = 1,\ldots,7$)). Considering the dimensions of the optical fibre sensor, one can assume that the temperature of the host material (ΔT^c) equals that of the sensor (ΔT^s). As such, Equation 4-1 can be reduced to the strain components.

$$\begin{bmatrix} \varepsilon_1^c \\ \varepsilon_2^c \\ \vdots \\ \varepsilon_6^c \end{bmatrix} = \begin{bmatrix} TC_{11} & TC_{12} & \cdots & TC_{16} \\ TC_{21} & TC_{22} & \cdots & TC_{26} \\ \vdots & \vdots & \ddots & \vdots \\ TC_{61} & TC_{62} & \cdots & TC_{66} \end{bmatrix} \begin{bmatrix} \varepsilon_1^s \\ \varepsilon_2^s \\ \\ \varepsilon_6^s \end{bmatrix} \quad \textbf{4-2}$$

In the following, an analytical model based on a study by Kollar et al. [56] will be considered. Afterwards, this model will be evaluated using a FEM model for different laminates (layer thickness, lay-up, size of the optical fibre, …).

4. 5. 2. a. Analytical model for transversally isotropic materials

Stresses and strains in a transversely isotropic material

The analytical model considers the optical fibre sensor as a circular inclusion inside the host material which is considered to be homogeneous and orthotropic (Figure 4-47.). To avoid the presence of a resin eye and associated complexity of strain transfer, the sensor is aligned with the reinforcement fibres of the adjacent plies of the host material. Perfect bonding, between the fibre and the host material, is assumed. Deformations are assumed to be small and both materials (sensor and host) are considered to behave in a linear elastic manner.

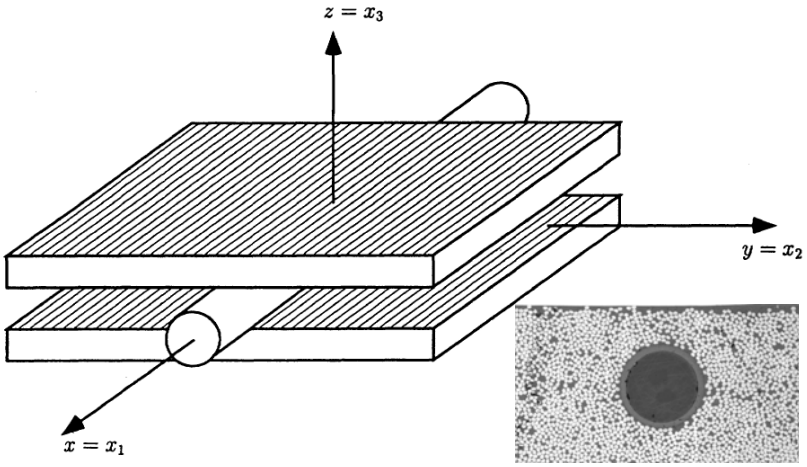

Figure 4-47: A circular isotropic glass fibre embedded inside an orthotropic fibre reinforced composite. The sensor is aligned with the reinforcing fibres in the adjacent plies[56].

For a certain load applied at infinity, the strain and stress in the material at a distance far from the sensor (3 or 4 sensor diameters [57]) approximate the farfield strain and stress (Figure 4-48). Close to the sensor a certain gradient of strain and stress exists [57]. In the analysis, we assume that the stresses and strains are constant in the sensor. Kim et al. [58] have shown analytically that this condition is valid for uncoated sensors embedded in an anisotropic material.

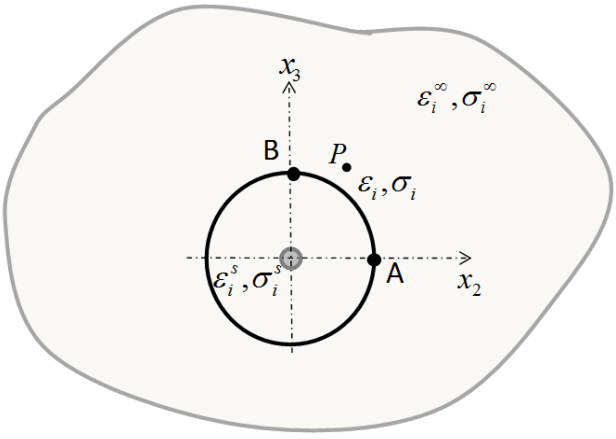

Figure 4-48: A hole or an inclusion alters the stress and strain fields in a material. The strain of the far field (ε_i^∞) differs from the strain near the inclusion ε_i for example at point P.

The strains in any point of the sensor and host material are related with the displacements (u_1, u_2, u_3) at these locations by [59]

$$\begin{aligned} \varepsilon_1 = \varepsilon_{11} = \frac{\partial u_1}{\partial x_1} \quad \varepsilon_4 = \gamma_{23} = \frac{\partial u_3}{\partial x_2} + \frac{\partial u_2}{\partial x_3} \\ \varepsilon_2 = \varepsilon_{22} = \frac{\partial u_2}{\partial x_2} \quad \varepsilon_5 = \gamma_{13} = \frac{\partial u_3}{\partial x_1} + \frac{\partial u_1}{\partial x_3} \\ \varepsilon_3 = \varepsilon_{33} = \frac{\partial u_3}{\partial x_3} \quad \varepsilon_6 = \gamma_{12} = \frac{\partial u_2}{\partial x_1} + \frac{\partial u_1}{\partial x_2} \end{aligned} \qquad \textbf{4-3}$$

And, the stress-strain relation is given by

$$\sigma_i = C_{ij}^c \varepsilon_j \qquad \textbf{4-4}$$

In which C_{ij}^c is the stiffness matrix of an orthotropic material and the inverse of the compliance matrix S_{ij}^c :

$$S_{ij}^s = \begin{bmatrix} \frac{1}{E_1} & \frac{-\upsilon_{12}}{E_1} & \frac{-\upsilon_{13}}{E_1} & 0 & 0 & 0 \\ \frac{-\upsilon_{21}}{E_2} & \frac{1}{E_2} & \frac{-\upsilon_{23}}{E_2} & 0 & 0 & 0 \\ \frac{-\upsilon_{31}}{E_3} & \frac{-\upsilon_{32}}{E_3} & \frac{1}{E_3} & 0 & 0 & 0 \\ 0 & 0 & 0 & \frac{1}{G_{23}} & 0 & 0 \\ 0 & 0 & 0 & 0 & \frac{1}{G_{31}} & 0 \\ 0 & 0 & 0 & 0 & 0 & \frac{1}{G_{12}} \end{bmatrix} \qquad \textbf{4-5}$$

E_i are the Young's moduli according to the principal orthotropic axes. G_i is the shear modulus in the i-j symmetry plane. ν_{ij} is the Poisson's coefficient for the j[th] principal axis when loaded according to the i[th] principal axis. Since the sensor is considered to be isotropic, its compliance matrix can be written as:

$$S_{ij}^{s} = \begin{bmatrix} \frac{1}{E_s} & \frac{-\upsilon_s}{E_s} & \frac{-\upsilon_s}{E_s} & 0 & 0 & 0 \\ \frac{-\upsilon_s}{E_s} & \frac{1}{E_s} & \frac{-\upsilon_s}{E_s} & 0 & 0 & 0 \\ \frac{-\upsilon_s}{E_s} & \frac{-\upsilon_s}{E_s} & \frac{1}{E_s} & 0 & 0 & 0 \\ 0 & 0 & 0 & \frac{1}{G_s} & 0 & 0 \\ 0 & 0 & 0 & 0 & \frac{1}{G_s} & 0 \\ 0 & 0 & 0 & 0 & 0 & \frac{1}{G_s} \end{bmatrix} \quad \textbf{4-6}$$

The far field displacements u_i^{∞} are obtained by integrating the expressions in Equation 4-3. In the absence of rigid body motion, the resulting expressions are

$$\begin{aligned} u_1^{\infty} &= \varepsilon_1^{\infty} x_1 + \varepsilon_6^{\infty} x_2 + \varepsilon_5^{\infty} x_3 \\ u_2^{\infty} &= \varepsilon_2^{\infty} x_2 + \frac{1}{2}\varepsilon_4^{\infty} x_3 \\ u_3^{\infty} &= \frac{1}{2}\varepsilon_4^{\infty} x_2 + \varepsilon_3^{\infty} x_3 \end{aligned} \quad \textbf{4-7}$$

Stresses and strains near a hole or inclusion

A hole or an inclusion alters the stress (σ_i) and strain (ε_i) fields. Stress, strain and displacement at a certain point P in the near field (Figure 4-48) can be expressed as

$$\begin{aligned} \sigma_i &= \sigma_i^{\infty} + \sigma_i^{*} \\ \varepsilon_i &= \varepsilon_i^{\infty} + \varepsilon_i^{*} \\ u_i &= u_i^{\infty} + u_i^{*} \end{aligned} \quad \textbf{4-8}$$

ε_i^{*} is related to σ_i^{*} through the stress-strain relation of Equation 4-4. For circular or elliptical holes, expressions for σ_i^{*}, ε_i^{*} and u_i^{*} have been presented by Lekhnitskii [57].

Continuity conditions at the fibre interface

In order to calculate the applied strains in the optical fibre in relation to the farfield strains and temperature, we must invoke two continuity conditions at the interface between the material and the sensor. It is sufficient to enforce these conditions at only two points on the sensor surface in order to automatically enforce the continuity conditions everywhere on the interface between the sensor and the surrounding material [58]. We select the points A and B in the $x_1 = 0$ plane (Figure 4-48). The displacement continuity condition states that the sensor displacements must equal the displacements of the surrounding material at two points (A and B) on the sensor surface.

$$u_i^s = u_i \quad i = 1,2,3 \tag{4-9}$$

Secondly, the interface traction in the sensor and material must be the same. This stress continuity condition state that certain sensor stress components must equal the corresponding stress components in the surrounding material at two points at the interface between the sensor and the material surrounding the sensor

$$\begin{aligned} &\sigma_2^s = \sigma_2 && \sigma_3^s = \sigma_3 \\ &\sigma_4^s = \sigma_4 \ \textbf{at point A} && \sigma_4^s = \sigma_4 \ \textbf{at point B} \\ &\sigma_6^s = \sigma_6 && \sigma_5^s = \sigma_5 \end{aligned} \tag{4-10}$$

Results obtained for an embedded isotropic optical fibre in a transversely isotropic host material

Since shear stress/strain has no influence on the response of an optical fibre Bragg grating sensor, equation 4-2 can be reduced to

$$\begin{bmatrix} \Delta\varepsilon_1^c \\ \Delta\varepsilon_2^c \\ \Delta\varepsilon_3^c \end{bmatrix} = \begin{bmatrix} TC_{11} & TC_{12} & TC_{13} \\ TC_{21} & TC_{22} & TC_{23} \\ TC_{31} & TC_{32} & TC_{33} \end{bmatrix} \begin{bmatrix} \Delta\varepsilon_1^s \\ \Delta\varepsilon_2^s \\ \Delta\varepsilon_3^s \end{bmatrix} \tag{4-11}$$

The strain components of the sensor $\Delta\varepsilon_i^s$ can be written according to the coordinate system that was defined for an optical fibre(Figure 2-3).

$$\begin{bmatrix} \Delta\varepsilon_1^s \\ \Delta\varepsilon_2^s \\ \Delta\varepsilon_3^s \end{bmatrix} = \begin{bmatrix} \Delta\varepsilon_{3'} \\ \Delta\varepsilon_{1'} \\ \Delta\varepsilon_{2'} \end{bmatrix} \tag{4-12}$$

If the composite structure is loaded at infinity one can find the strain relation (equation 4-11), by using the above described method of Kollar et al. [56]. The properties of an isotropic optical fibre (sensor) and a transversally isotropic composite material (host material) (respectively in the first two columns of Table 4-7 and in Table 4-6) were used to find the *TC*-matrix.
TC_{ij} ($i, j = 1, 2, 3$) is found to be:

$$TC = \begin{bmatrix} 1 & 0 & 0 \\ 1.035 & 7.538 & -0.829 \\ 0.878 & -0.964 & 6.809 \end{bmatrix} \qquad \textbf{4-13}$$

In this matrix, TC_{11} is found to be 1 which means that the longitudinal strain component of the host material equals that of the optical fibre sensor. The other diagonal elements (TC_{22} and TC_{33}) are around seven times higher which indicates the poor transverse strain transfer. It should be noted that this coefficient will play a significant role in the performance of the sensor in terms of strain resolving power (section 4. 6.). The longitudinal strain component has a positive influence on the transverse strain components, while the opposite transverse strain component will have a negative influence of the same magnitude.

4. 5. 2. b. FE-model for a transversally isotropic material

Another method for defining the relationship of the strain field in the core of an optical fibre to the one present in the composite material is by simulations through finite elements, using the FE-software package ABAQUS™. Due to symmetry reasons only 1/8 of an embedded fibre was modelled (Figure 4-49). The composite model (10 mm x 1.2 x 10 mm for a 24 layer laminate) consists of 17600 linear hexahedral elements of type C3D8R [60], in the vicinity of the fibre the mesh is refined. The total amount of elements depends on the lay-up and on the thickness of the laminate (more elements for a thick laminate). The material properties of the composite material (M55J/M18 by Hexcell) are given in Table 4-6. The fibre (□ 80 µm x10 mm) consists of 1700 linear hexahedral elements of type C3D8R. The material of the optical fibre is fused silica and the properties are given in the first two columns of Table 4-7, the properties of the bow-tie SAPs are given in the last two columns of Table 4-7.

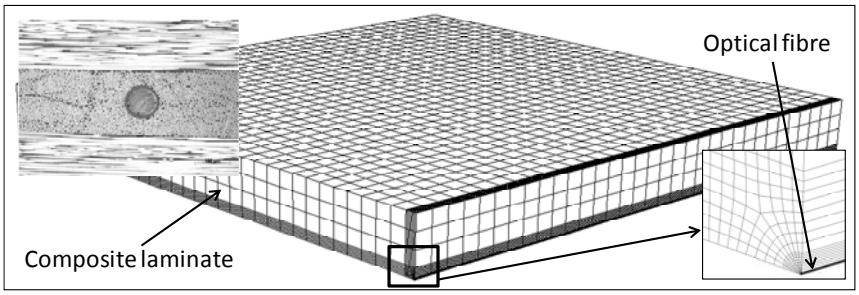

Figure 4-49: Finite element model used for simulation of the strain transfer between embedded optical fibre and CFRP laminate.

The strain transfer coefficients are determined from the simulation by considering the three principal strains in the core of the optical fibre and comparing them with those in the laminate as if the sensor is not present.

$$\begin{bmatrix} \Delta\varepsilon_x \\ \Delta\varepsilon_y \\ \Delta\varepsilon_z \end{bmatrix} = \begin{bmatrix} TC_{11} & TC_{12} & TC_{13} \\ TC_{21} & TC_{22} & TC_{23} \\ TC_{31} & TC_{32} & TC_{33} \end{bmatrix} \begin{bmatrix} \Delta\varepsilon_{3'} \\ \Delta\varepsilon_{1'} \\ \Delta\varepsilon_{2'} \end{bmatrix} \qquad \textbf{4-14}$$

The *TC*-matrix has 9 independent parameters which can be determined from the FE-models subjected to three independent loading conditions (Figure 4-50, Figure 4-51, and Figure 4-52). By substituting the found numerical strains ($\Delta\varepsilon_{1'}, \Delta\varepsilon_{2'}, \Delta\varepsilon_{3'}$) of the optical fibre as well as those of the composite material ($\Delta\varepsilon_{xx}, \Delta\varepsilon_{yy}, \Delta\varepsilon_{zz}$) for the three loading conditions one will obtain 9 equations from which the 9 unknown *TC*-parameters can be determined.

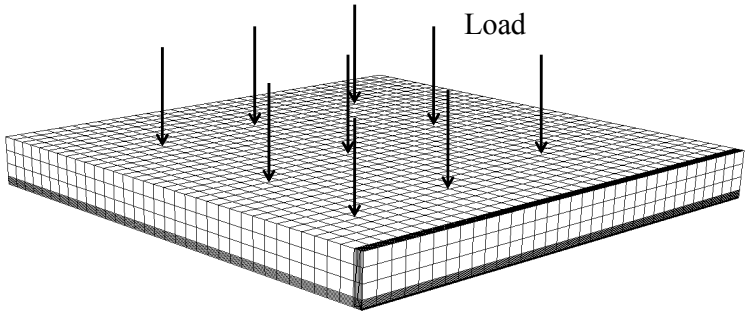

Figure 4-50: Transversally applied load (out-of-plane)

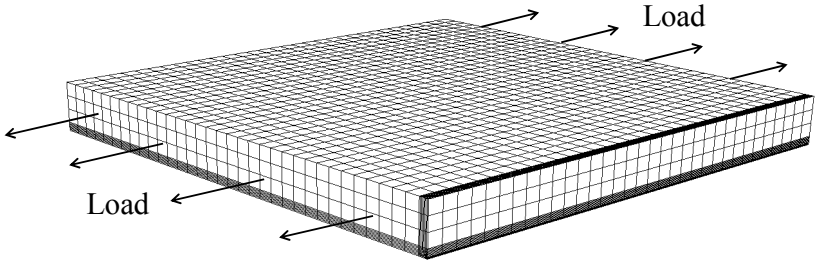

Figure 4-51: Longitudinally applied load

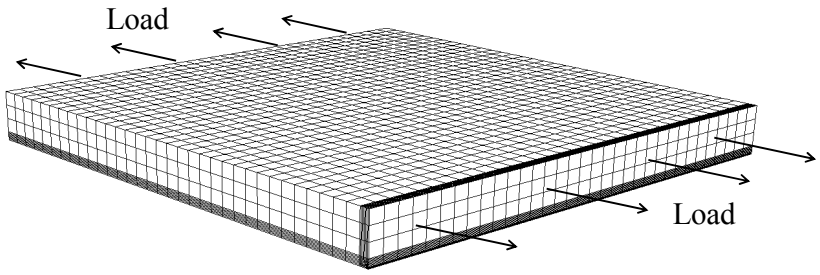

Figure 4-52: Transversally applied load (in-plane)

4. 5. 2. c. Parametric study

Using the above described finite element model, one can, by changing several properties of sensor and/or host, examine their effect on the *TC*-matrix. The study considers the following parameters:

- the mechanical properties of the host material (Young's modulus and Poisson's ratio);
- the lay-up of the composite laminate (layer thickness and stacking sequence);
- the position of the sensor inside a certain layer of the host material (middle or near the boundary);
- the properties of the sensor (dimension and type);

Host material properties

The influence of the mechanical properties (Young's modulus and Poisson's ratio) of the host material, which is considered isotropic, is evaluated in this paragraph.
In Table 4-8, the results can be found for the case of changed ***Poisson's ratio*** values; the Young's modulus of host and sensor material are considered equal ($E_h = E_s = 70$ GPa).

Table 4-8: *TC*-matrices when host and sensor material have equal Young's modulus but different Poisson's ratio.

$E_h = E_s$=70GPa and v_s = 0.17		
v_h =0.17	v_h =0.255	v_h =0.34
$\begin{bmatrix} 1 & 0 & 0 \\ 0 & 1 & 0 \\ 0 & 0 & 1 \end{bmatrix}$	$\begin{bmatrix} 1.000 & 0.000 & 0.000 \\ -0.078 & 0.956 & -0.089 \\ -0.076 & -0.088 & 0.958 \end{bmatrix}$	$\begin{bmatrix} 1.000 & 0.000 & 0.000 \\ -0.182 & 0.878 & -0.208 \\ -0.178 & -0.204 & 0.882 \end{bmatrix}$

Obviously, when the properties of sensor and host material are the same, the unity matrix is found. Therefore, the strain field in the sensor (optical fibre) will equal that of the host material (isotropic). Altering the Poisson's ratio of the host material with 0.085 (υ_h = 0.255), the diagonal elements of the matrix slightly decrease (~4%) and the other elements become slightly negative (~8% difference). Doubling the difference in Poisson's ratio (υ_h = 0.34) leads to a more than proportional change of the *TC-matrix* elements. The diagonal elements differ ~12% with the unity matrix and the other elements ~20%.

In Table 4-9, the results can be found for the case that ***the Young's modulus*** are considered different and the Poisson's coefficient ($\upsilon_h = \upsilon_s$ = 0.17) equal.

Table 4-9: *TC*-matrices when host and sensor material have equal Poisson's ratio but different Young's modulus.

$v_s = v_h$ =0.17 and E_s=70GPa		
E_h =70GPa	E_h = 35GPa	E_h = 6GPa
$\begin{bmatrix} 1 & 0 & 0 \\ 0 & 1 & 0 \\ 0 & 0 & 1 \end{bmatrix}$	$\begin{bmatrix} 1.000 & 0.000 & 0.000 \\ 0.100 & 1.630 & -0.044 \\ 0.097 & -0.053 & 1.622 \end{bmatrix}$	$\begin{bmatrix} 1.000 & 0.000 & 0.000 \\ 1.081 & 8.013 & -0.655 \\ 1.011 & -0.882 & 7.827 \end{bmatrix}$

Altering the Young's modulus of the host material, the diagonal elements of the matrix increase significantly. When the host material is less stiff than the sensor, only part of the strain is transferred to the glass optical fibre sensor when loading the structure in the transverse direction (Figure 4-50 and Figure 4-52). In the *TC*-matrix, this is expressed by an increase of the diagonal elements. Multiply by ~1.6 when the host Young's modulus equals E_h = 35GPa and multiply by ~8 when the modulus equals E_h = 6GPa. Further, for a Young's modulus, which gets near that of the transverse modulus (6.3 GPa)of the M55J/M18 composite material used in this work, the TC_{ij} (i = 1 and j =2,3) elements of the first column are increased. This means that the axial strain component (in most loading cases the highest strain component) has a big influence on the calculation of the transverse strain

components. In the same order of magnitude, the in-plane transverse strain component will have a negative influence on the out-of-plane transverse strain component and vice-versa. In most loading cases, these strain components are relatively small and have, as such, lesser influence than the axial strain component. It should be noted that this depends on the orientation of the sensor in the host material. If the sensor is embedded perpendicular to the major eigenaxis of the host materials, the in-plane transverse strain component will have the most influence.

Lay-up of the composite laminate

Simulations of a glass optical fibre sensor (first two columns of Table 4-7) embedded in a composite laminate composed of several M55J/M18/ prepreg layers (Table 4-6) are discussed hereinafter.

First, the thickness of ***a unidirectional laminate*** $[0]_x$ is changed, which corresponds to changing the amount of layers (x) stacked to manufacture the laminate. The sensor is located at mid-thickness (Figure 4-53).

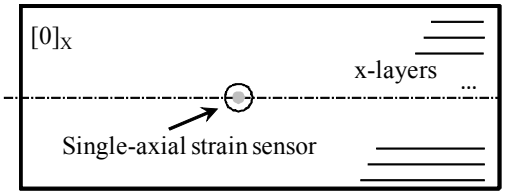

Figure 4-53: Schematic of a single axial optical fibre sensor embedded at the centre of an x-layers thick uni-directional laminate.

In Table 4-10, an example of the simulated ratios of fibre strain to laminate strain ($\varepsilon_i^s / \varepsilon_i^c$) is given for a $[0]_{32}$ laminate for the loading conditions above. For ease of comparing, the coordinate system of a single layer of the laminate (1,2,3) is used. For example, the axial strain component of the sensor equals ε_1^s.

Table 4-10: Strain ratios for three loading conditions applied to a $[0]_{32}$ laminate.

Loading direction	$\varepsilon_1^s / \varepsilon_1^c$	$\varepsilon_2^s / \varepsilon_2^c$	$\varepsilon_3^s / \varepsilon_3^c$
Side	~100%	12.6%	7.4%
Top	~100%	7.4%	12.6%
Along fibre	~100%	55.2%	55.2%

Using Equation 4-11 and Table 4-10, the *TC*-matrix can be calculated. The results in Table 4-11 start with a laminate consisting of only two prepreg layers and end with a

laminate consisting of 100 prepreg layers. The glass optical fibre is embedded in the middle of the laminate.

Table 4-11: *TC*-matrices for a glass optical fibre sensor embedded in the middle of a unidirectional laminate $[0]_n$.

$[0]_2$

$$\begin{bmatrix} 1.000 & 0.000 & 0.001 \\ 1.112 & 8.509 & -0.404 \\ 0.394 & -2.118 & 6.210 \end{bmatrix}$$

$[0]_4$

$$\begin{bmatrix} 1.000 & 0.000 & 0.001 \\ 0.896 & 7.915 & -1.045 \\ 0.705 & -1.509 & 7.315 \end{bmatrix}$$

$[0]_8$

$$\begin{bmatrix} 1.000 & 0.000 & 0.000 \\ 0.838 & 7.732 & -1.193 \\ 0.791 & -1.309 & 7.587 \end{bmatrix}$$

$[0]_{16}$

$$\begin{bmatrix} 1.000 & 0.000 & 0.000 \\ 0.825 & 7.699 & -1.231 \\ 0.811 & -1.262 & 7.647 \end{bmatrix}$$

$[0]_{24}$

$$\begin{bmatrix} 1.000 & 0.000 & 0.000 \\ 0.823 & 7.708 & -1.248 \\ 0.814 & -1.265 & 7.668 \end{bmatrix}$$

$[0]_{32}$

$$\begin{bmatrix} 1.000 & 0.000 & 0.000 \\ 0.822 & 7.702 & -1.25 \\ 0.817 & -1.256 & 7.675 \end{bmatrix}$$

$[0]_{48}$

$$\begin{bmatrix} 1.000 & 0.000 & 0.000 \\ 0.816 & 7.648 & -1.233 \\ 0.821 & -1.23 & 7.679 \end{bmatrix}$$

The results in Table 4-11 show that compared to the *TC*-matrix of an isotropic host material with a Young's modulus of E_h = 6GPa (Table 4-9), the diagonal elements (TC_{ij} with $i = j = 2,3$) are slightly higher. The transverse strain component influence is considerably higher (~50%) for the transversely isotropic laminate. This could be caused by the additional effect of different Poisson's ratio of sensor and host material.

When looking at the influence of the thickness of the laminate, another important observation can be made for the TC_{ij}-elements with $i, j = 2,3$. This partial matrix is symmetric for the thick laminates. However, when reducing the number of layers (see e.g. $[0]_8$), it becomes non-symmetric. The *TC*-matrix of the $[0]_2$ and the $[0]_4$ laminate differs significantly from that of the thicker laminates, with exception of the first row. The cause of this difference can be related to the difference in strain disturbance in the surroundings of the embedded optical fibre sensor. In Figure 4-54 and Figure 4-55, cross sections of a thick ($[0]_{24}$) and a thin ($[0]_4$) laminate are

depicted. The transverse strain components (ε_{22} and ε_{33}) are shown in the surrounding of the embedded fibre. The disturbance fades out for the thick laminate while for the thin laminate, the disturbance extends to the boundaries of the laminate. This leads to a different *TC*-matrix for both lay-ups.

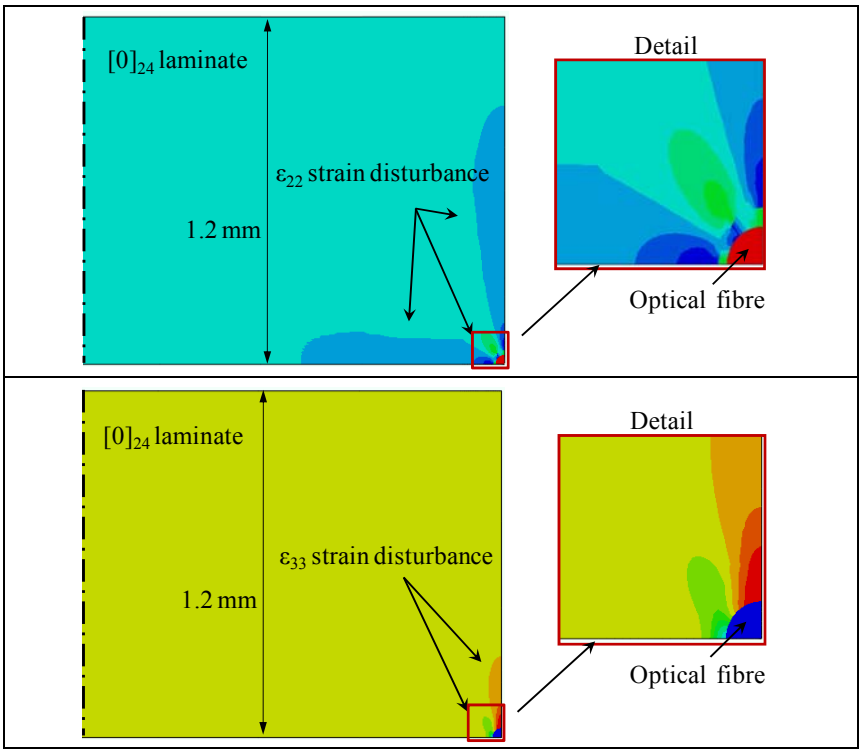

Figure 4-54: Transverse strain disturbance for a thick laminate $[0]_{24}$, when loaded on top. The optical fibre sensor is embedded in the middle of the laminate.

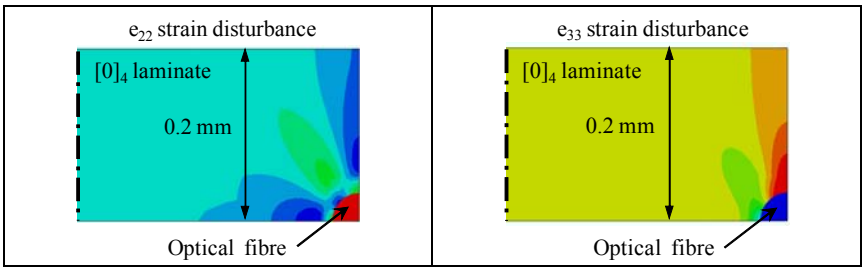

Figure 4-55: Transverse strain disturbance for a thin laminate $[0]_4$, when loaded on top. The optical fibre sensor is embedded in the middle of the laminate.

In a ***cross ply laminate*** ($[0_x,90_x]_{ns}$ or $([90_x,0_x]_{ns}$), the succession of layers with a different stacking direction is rather small (Figure 4-56). Therefore a big disturbance can be expected. In Table 4-12, the ratios of the fibre to laminate strain ($\varepsilon_i^s / \varepsilon_i^c$) are given for three independent loading conditions and a $[90_4,0_4]_{2s}$ laminate. One can observe that the transverse strain transfer is highly dependent on the loading situation. For the in-plane strain component, an opposite sign can be observed when the laminate is loaded on top and a gigantic strain ratio can be observed when the load is oriented parallel to the fibre. However, as will be shown in the following results, when calculating the TC-matrix, no big differences were found between the uni-directional and the cross-ply laminates.

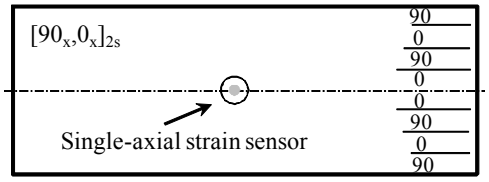

Figure 4-56: Schematic of a single axial optical fibre sensor embedded at the centre of cross-ply laminate ($[90_x,0_x]_{2s}$)

Table 4-12: Strain ratios for three loading conditions applied to a $[90_4,0_4]_{2s}$ laminate.

Loading direction	$\varepsilon_1^s / \varepsilon_1^c$	$\varepsilon_2^s / \varepsilon_2^c$	$\varepsilon_3^s / \varepsilon_3^c$
Side	~100%	12.7%	7.2%
Top	~100%	-104,8%	13.6%
Along fibre	~100%	995.3%	42.5%

In Table 4-13, the calculated *TC*-matrices are given for different cross-ply laminates. The optical fibre is embedded in the middle of the composite laminate, in the direction of the surrounding reinforcing fibres. The thickness of the middle section varies from 1 to 4 layers on each side of the sensor.

Table 4-13: TC-matrices for a glass optical fibre sensor embedded in the middle of a cross-ply laminate $[90_X,0_X]_{2s}$.

$[90,0]_{2s}$	$[90_2,0_2]_{2s}$
$\begin{bmatrix} 1.000 & 0.000 & 0.000 \\ 0.812 & 7.431 & -1.048 \\ 0.780 & -1.115 & 7.311 \end{bmatrix}$	$\begin{bmatrix} 1.000 & 0.000 & 0.000 \\ 0.818 & 7.631 & -1.206 \\ 0.809 & -1.221 & 7.592 \end{bmatrix}$
$[90_3,0_3]_{2s}$	$[90_4,0_4]_{2s}$
$\begin{bmatrix} 1.000 & 0.000 & 0.000 \\ 0.817 & 7.657 & -1.235 \\ 0.816 & -1.239 & 7.652 \end{bmatrix}$	$\begin{bmatrix} 1.000 & 0.000 & 0.000 \\ 0.818 & 7.672 & -1.248 \\ 0.818 & -1.248 & 7.671 \end{bmatrix}$

Little variation in the values of the *TC*-matrix can be observed for the laminate consisting of two, three or four successive layers. Only one layer of prepreg significantly altered the *TC*-matrix. For this single layer lay-up, non-symmetric partial matrix (TC_{ij} with $i, j = 2,3$) is observed. In addition, TC_{31} is different from the value obtained for the other lay-ups. In Figure 4-57 and Figure 4-58, two cross-sections (of a $[90_4,0_4]_{2s}$ and a $[90,0]_{2s}$ laminate) are depicted, showing the transverse strain components in the surrounding of the embedded fibre. The strain-field disturbance is again more pronounced for the thin laminate, which leads to a different *TC*-matrix for both lay-ups.

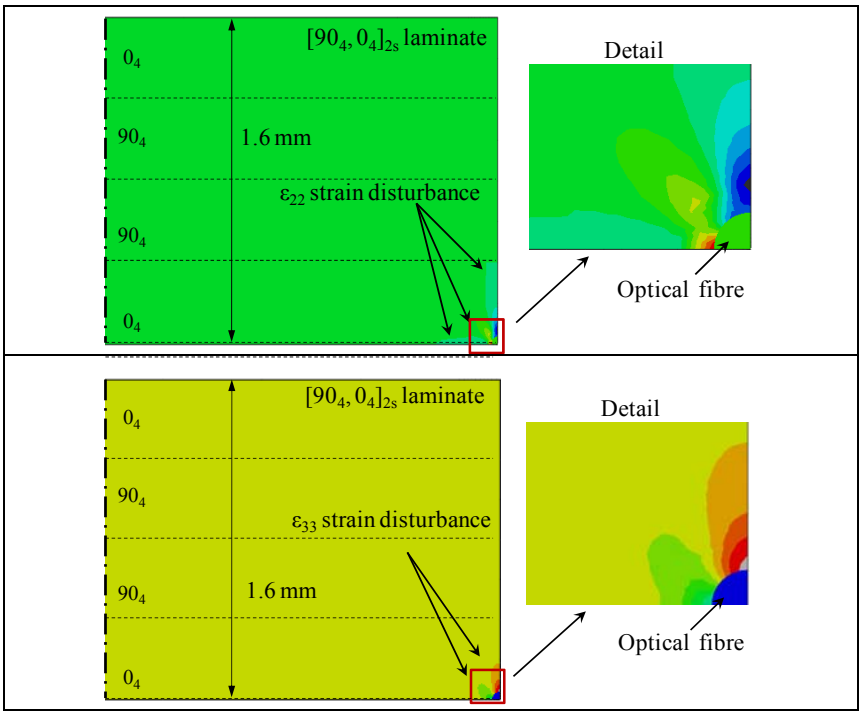

Figure 4-57: Transverse strain-field disturbance for a cross ply laminate with a $[90_4,0_4]_{2s}$ stacking sequence, when loaded on top. The optical fibre sensor is embedded in the middle of the laminate.

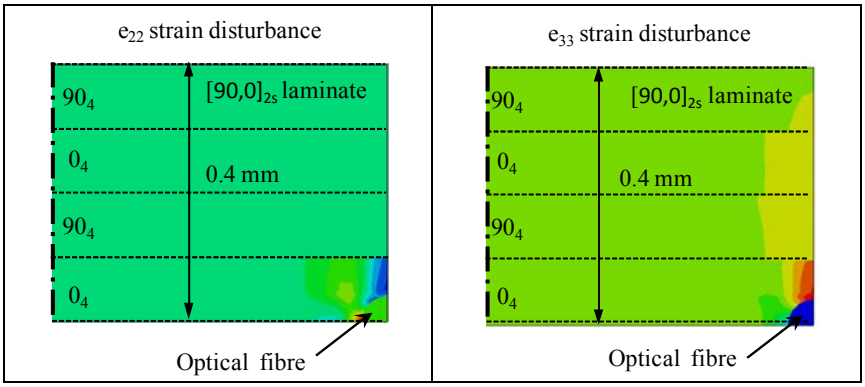

Figure 4-58: Transverse strain-field disturbance for a cross ply laminate with a $[90,0]_{2s}$ stacking sequence, when loaded on top. The optical fibre sensor is embedded in the middle of the laminate.

Position of the sensor in the composite laminate

Since a certain embedding depth error can occur during the embedding and manufacturing process, it is interesting to evaluate its influence on the *TC*-matrix. When the sensor is located near to the surface of the laminate, or near a change of layer direction, the *TC*-matrix will change (Figure 4-59). In Table 4-14, the results are given for an optical fibre sensor which is embedded in a thick composite laminate $[90_4,0_4]_{2s}$. In each configuration, the embedding depth of the sensor is changed (0.1 mm) corresponding to the thickness of one prepreg layer.

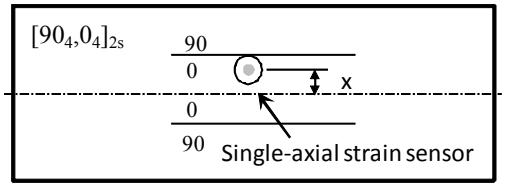

Figure 4-59: Schematic of an optical fibre sensor embedded out of the centre of a cross-ply laminate ($[90_4,0_4]_{2s}$)

Table 4-14: TC-matrices for different positions of the sensor in a cross-ply laminate

$[90_4,0_4]_{2s}$	
$x = 0$	$x = 0.1$
$\begin{bmatrix} 1.000 & 0.000 & 0.000 \\ 0.818 & 7.672 & -1.248 \\ 0.818 & -1.248 & 7.671 \end{bmatrix}$	$\begin{bmatrix} 1.000 & 0.000 & 0.000 \\ 0.814 & 7.642 & -1.242 \\ 0.821 & -1.235 & 7.679 \end{bmatrix}$
$x = 0.2$	$x = 0.3$
$\begin{bmatrix} 1.000 & 0.000 & 0.000 \\ 0.814 & 7.635 & -1.235 \\ 0.819 & -1.232 & 7.661 \end{bmatrix}$	$\begin{bmatrix} 1.000 & 0.000 & 0.000 \\ 0.808 & 7.543 & -1.186 \\ 0.812 & -1.187 & 7.574 \end{bmatrix}$

The mutual influence of the opposite transverse strain components (TC_{23} and TC_{32}) tends to decrease when approaching the 90 degree layers. In the last case, where only one 0 degree layer is left on top of the optical fibre, the diagonal elements are slightly decreased too. This effect is caused by the strain disturbance area which is touching the 90 degree layer (Figure 4-60). One can imagine that the impact on the *TC*-matrix will be large for thin laminates.

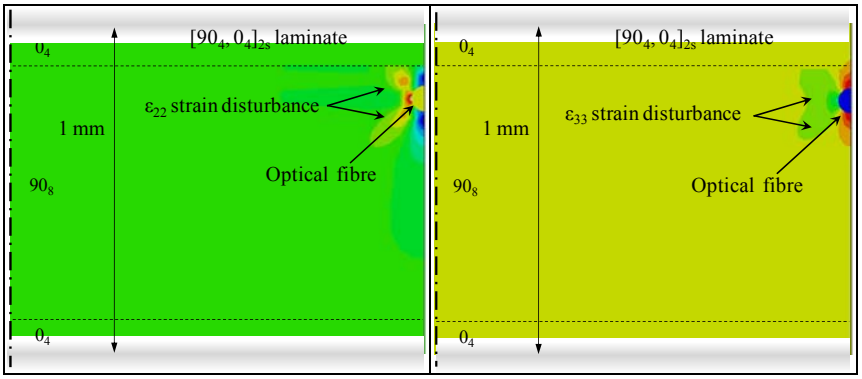

Figure 4-60: Transverse strain disturbance for a cross ply laminate with a $[90_4,0_4]_{2s}$ stacking sequence, when loaded on top. The optical fibre sensor is embedded asymmetrically in between 8 composite layers (1 above and 7 below)

Sensor properties

First, ***the size of the sensor*** is changed from an 80 µm fibre diameter to a 125 µm diameter. In Table 4-15, the calculated *TC*-matrices (for the two different fibre diameters and two laminate thicknesses) are summarized.

Table 4-15: TC-matrices for optical fibre sensor with different diameters

□ = 80 µm	□ = 125 µm
$[0]_{24}$	$[0]_{24}$
$\begin{bmatrix} 1.000 & 0.000 & 0.000 \\ 0.823 & 7.708 & -1.248 \\ 0.814 & -1.265 & 7.665 \end{bmatrix}$	$\begin{bmatrix} 1.000 & 0.000 & 0.000 \\ 0.824 & 7.695 & -1.233 \\ 0.811 & -1.264 & 7.652 \end{bmatrix}$
$[0]_{48}$	$[0]_{48}$
$\begin{bmatrix} 1.000 & 0.000 & 0.000 \\ 0.816 & 7.648 & -1.233 \\ 0.821 & -1.23 & 7.679 \end{bmatrix}$	$\begin{bmatrix} 1.000 & 0.000 & 0.000 \\ 0.819 & 7.669 & -1.235 \\ 0.818 & -1.241 & 7.669 \end{bmatrix}$

An increase of ~50% of the fibre diameter does not lead to significantly different *TC*-matrices. For a thick ($[0]_{48}$) laminate and thinner ($[0]_{24}$) laminate, the matrix remains almost unaltered. Based on previous observations, one can assume that the influence will be much larger for thin laminates with only 16 or less prepreg layers.

Changing ***the sensor type*** from a uni-axial into a ***multi-axial*** optical fibre (bow-tie) sensor leads to the results summarized in Table 4-16. The same model was used for the laminate, though, the mesh of the optical fibre sensor was refined to 8700 linear

wedge elements of type C3D6. The wedge elements were needed to homogenously mesh the multi-axial optical fibre with embedded SAPs.

The following observations can be made, when comparing the strain transfer matrix of an embedded uni-axial strain sensor and an embedded multi-axial strain sensor. The influence of the longitudinal strain component (TC_{ij} i = 1,2,3, j =3) remains almost unaltered for a different type of sensor. More strain transfer (TC_{33} becomes smaller, ~10%) could be noted for the out-of-plane transverse strain component, and less (TC_{22} becomes bigger, ~7%) for the in-plane transverse strain component. The mutual influence of the transverse strain components are smaller (4% up to 19%) for the multi-axial sensor. Only small changes could be observed in the *TC*-matrices of the embedded strain sensor, when changing the lay-up of the laminate.

Table 4-16: TC-matrices for different types of optical fibre sensor

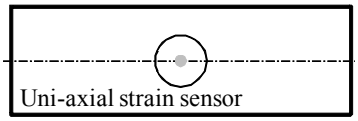 Uni-axial strain sensor	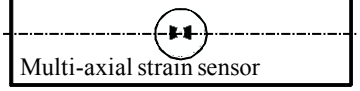 Multi-axial strain sensor
$[0]_{48}$	$[0]_{48}$
$\begin{bmatrix} 1.000 & 0.000 & 0.000 \\ 0.816 & 7.648 & -1.233 \\ 0.821 & -1.23 & 7.679 \end{bmatrix}$	$\begin{bmatrix} 1.000 & 0.000 & 0.000 \\ 0.827 & 8.152 & -1.003 \\ 0.814 & -1.178 & 6.936 \end{bmatrix}$
$[90_2,0_2]_{2s}$	$[90_2,0_2]_{2s}$
$\begin{bmatrix} 1.000 & 0.000 & 0.000 \\ 0.818 & 7.631 & -1.206 \\ 0.809 & -1.221 & 7.592 \end{bmatrix}$	$\begin{bmatrix} 1.000 & 0.000 & 0.000 \\ 0.822 & 8.082 & -0.969 \\ 0.805 & -1.160 & 6.867 \end{bmatrix}$
$[90_4,0_4]_{2s}$	$[90_4,0_4]_{2s}$
$\begin{bmatrix} 1.000 & 0.000 & 0.000 \\ 0.818 & 7.672 & -1.248 \\ 0.818 & -1.248 & 7.671 \end{bmatrix}$	$\begin{bmatrix} 0.998 & -0.008 & -0.005 \\ 0.826 & 8.139 & -1.002 \\ 0.813 & -1.172 & 6.927 \end{bmatrix}$

Changing ***the orientation of the bow-tie*** optical fibre sensor leads to a change of the second and the third row of the *TC*-matrix.

Table 4-17: TC-matrices for a different orientation of a bow-tie optical fibre sensor

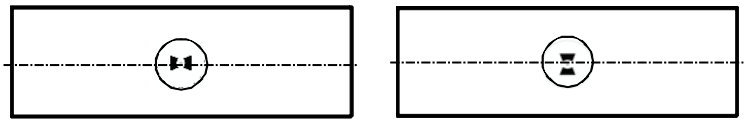

$[0]_{48}$	$[0]_{48}$
$\begin{bmatrix} 1.000 & 0.000 & 0.000 \\ 0.827 & 8.152 & -1.003 \\ 0.814 & -1.178 & 6.936 \end{bmatrix}$	$\begin{bmatrix} 1.000 & 0.000 & 0.000 \\ 0.815 & 6.936 & -1.176 \\ 0.826 & -1.003 & 8.147 \end{bmatrix}$

4. 5. 2. d. Experimental validation

To validate the numerically determined *TC*-matrices, a testing procedure was developed to introduce a well-defined homogeneous strain field inside a host material. Several 1.54 mm thick carbon fibre reinforced epoxy laminates were produced with at the mid-thickness an embedded 80 µm uni-axial FBG (Figure 4-61). The coating of the optical fibre is stripped for a few centimetres at the location of the FBG. The FBG itself has a length of 8 mm. The test specimens (50 x 50 x 1.54 mm) have a balanced and symmetric lay-up ($[90_2,0_2]_{2s}$) with in total 16 layers. This cross-ply laminate provides a maximal in-plane stiffness (x- and y-direction) and the lowest out-of-plane stiffness (z-direction). Two metal blocks (20 x 40 x 20 mm) were attached to the surfaces, using a thin epoxy layer with a uniform thickness. In addition, a ball hinge is used on top of the metal blocks during testing, to ensure a uniform stress distribution on the surface of the sample (Figure 4-62).

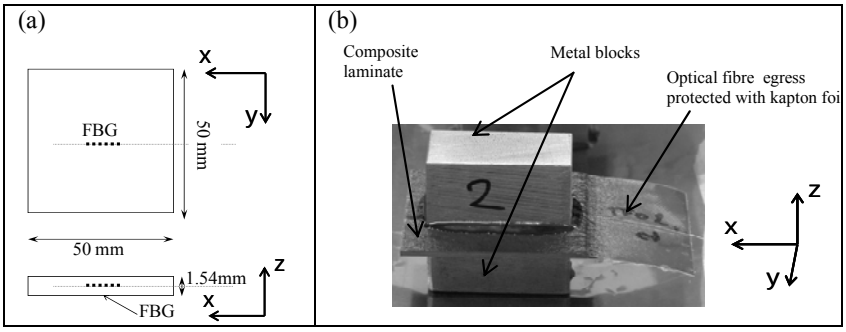

Figure 4-61: (a) Schematic drawing of the composite laminate with optical fibre sensor in the centre. (b) Picture of a composite laminate with metal blocks glued to the surface for transverse testing.

Using the set-up shown in Figure 4-62, the samples were loaded in the z-direction up to a maximum pressure of 92 MPa. The simulated (FEM) transverse strain (through-the-thickness) was used as reference strain measurement.

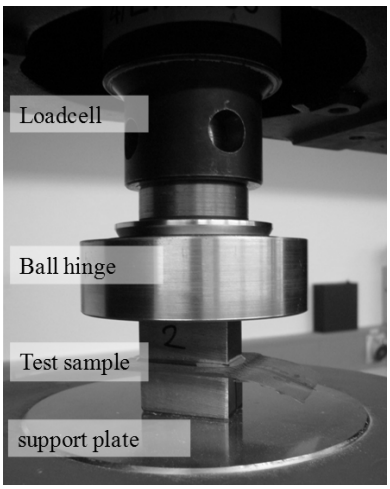

Figure 4-62: Picture of the test-set-up for transverse compression loading.

In Figure 4-63, the wavelength shifts as function of the applied transverse stress are given. Both polarization modes show a linear shift with increasing pressure, with the highest shift for the slow axis. These shifts can be used to define the three principal strains of the laminate by using the following equation

$$\left[\Delta\varepsilon^{c}\right] = TC \cdot K^{-1}\left[\Delta\lambda\right] \qquad \textbf{4-15}$$

Substituting the proper *TC*- and *K*-matrix, Equation 4-15 becomes

$$\begin{bmatrix}\Delta\varepsilon_{xx}\\ \Delta\varepsilon_{yy}\\ \Delta\varepsilon_{zz}\end{bmatrix} = \begin{bmatrix}1.000 & 0.000 & 0.000\\ 0.818 & 7.631 & -1.206\\ 0.809 & -1.221 & 7.592\end{bmatrix} \cdot \begin{bmatrix}1.250 & 0.000 & 0.000\\ 2.392 & -4.727 & 2.123\\ 2.392 & 2.123 & -4.727\end{bmatrix} \begin{bmatrix}\Delta\lambda_{B2,fast}\\ \Delta\lambda_{B1,slow}\\ \Delta\lambda_{B1,fast}\end{bmatrix} \qquad \textbf{4-16}$$

$\Delta\lambda_{B1}$ are the wavelength shifts measured with the embedded optical fibre sensor. $\Delta\lambda_{B2,fast}$ is calculated using the axial strain simulated by subjecting the top of the FE-model with a homogeneous pressure.

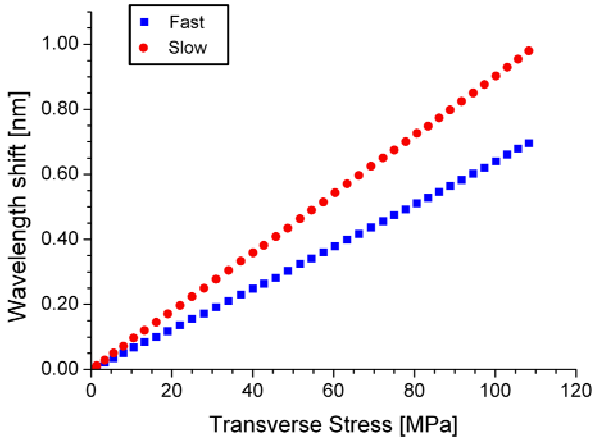

Figure 4-63: Wavelength shift measured during a transverse compression test on a small cross-ply laminate with an embedded single axial FBG.

In Figure 4-64, the three principal measured strains ($\Delta\varepsilon_{xx}$, $\Delta\varepsilon_{yy}$, $\Delta\varepsilon_{zz}$) of the laminate are plotted against the reference strain ($\Delta\varepsilon_{zz\_ref}$). A maximum compressive strain of approximately 1000 με was measured in the z-direction which corresponds well with the reference through-the–thickness strain. Up to 500 με ($\Delta\varepsilon_{zz}$), the measured value of the strain in the y-direction is very similar to the reference strain. At that point, the curve is not linear anymore and is bent away into a negative shift. This can be caused by damage initiation (e.g. optical fibre interface cracking) in the material or a non linear behaviour of the axial strain during the test caused, for example, by friction.

Based on these results, one can state that a valid *TC*-matrix was obtained for a uni-axial FBG using the procedure of the finite elements. In future work, an extra sample with an encapsulated FBG should give knowledge on the magnitude of the axial strain during such a compressive test.

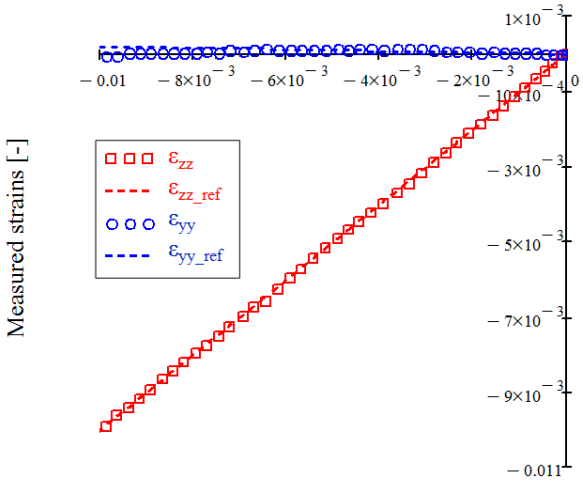

Figure 4-64: The measured principal strain components ($\Delta\varepsilon_{xx}$, $\Delta\varepsilon_{yy}$ and $\Delta\varepsilon_{zz}$) in the composite laminate as a function of the simulated (FEM) reference strain $\Delta\varepsilon_{zz\_ref}$

4. 6. RESOLVING POWER OF AN EMBEDDED MAXS-SENSOR

The resolving power of an embedded sensor can be defined as the ability of this sensor to distinguish 3D-strain components of the material in which it is embedded. The resolution of a non-embedded MAxS-sensor has already been discussed in Chapter 3. The general equation used to calculate the strain field in the core of an optical fibre Bragg sensor is formulated as

$$\left[\Delta\lambda\right] = K\left[\Delta\varepsilon^{s}\right] \qquad \textbf{4-17}$$

in which K is the gauge factor matrix. As discussed in Chapter 3, the resolution of this sensor depends on the condition number of this K-matrix. The obtained results are repeated in Table 4-18.

Table 4-18: Sensitivity analysis for the MAxS-sensor

	Condition number = ~10	
	Error analysis [με]	Standard deviation [με]
$\delta\varepsilon_{1'}$	±6.9	±4.3
$\delta\varepsilon_{2'}$	±6.9	±4.3
$\delta\varepsilon_{3'}$	±0.9	±0.9

By substituting equation 4-11 in equation 4-15, the general equation, to calculate the strain field in the composite material knowing the wavelength shift of an FBG sensor, can be formulated:

$$\left[\Delta\varepsilon^{c}\right] = TC \cdot K^{-1}\left[\Delta\lambda\right] \quad \textbf{4-18}$$

In which K is the gauge factor matrix and TC^{-1} is the inverse of the transfer coefficient matrix. The same method as described in section 3.3.1.b, can be used to calculate the variance ($Var\left(\left[\varepsilon^{c}\right]\right)$) and the standard deviation ($\sigma\left(\left[\varepsilon^{c}\right]\right)$) of the calculated strain ($\left[\varepsilon^{c}\right]$) if a certain variance exists on the wavelength shift ($Var\left(\left[\Delta\lambda\right]\right)$)

$$Var\left(\varepsilon_i^{c}\right) = \left(\left((TC \cdot K^{-1})_{i,1}\right)^2 + \left((TC \cdot K^{-1})_{i,2}\right)^2 + \left((TC \cdot K^{-1})_{i,3}\right)^2\right) Var\left(\left[\Delta\lambda\right]\right) \quad \textbf{4-19}$$

Using the calculated (FEM) *TC*-matrix (section 4. 5. 2. c.) and the calibrated *K*-matrix, one can determine the theoretical resolving power of the MAxS-sensor (Table 4-19). The resolving power of the sensor to measure transverse strain components, is worse than the theoretical resolution of the non-embedded sensor. The longitudinal strain resolving power stays the same, since the FBG in the capillary can be seen as a non-embedded sensor, as it is isolated from transverse stress. Dependent on the application, the resolving power of the transverse strain components can be considered satisfactory. In addition, in Chapter 5, it will be shown experimentally that more strain transfer can be expected than theoretically calculated. As such, a better resolving power of the MAxS-sensor can be assumed. In addition, by improving the resolution of the interrogator, the resolving power of the total strain field can become close to the strain requirements which were put forward in Chapter 1.

Table 4-19: Resolving power of the MAxS-sensor

	Condition number = ~80	
	Error analysis [με]	Standard deviation [με]
$\delta\varepsilon_{yy}$	±46.0	±34.1
$\delta\varepsilon_{zz}$	±43.9	±31.3
$\delta\varepsilon_{xx}$	±0.9	±0.9

4. 7. CONCLUSIONS

An embedded sensor is the best solution for determining the internal strain field of composite elements. Some general but essential issues should, however, be considered before embedding fibre optic sensors in a host material.

- The embedding procedure should be optimized. The in- and egress points of the optical fibre should be as robust as possible. In this work, these

fragile points were protected with a Kapton layer or with Teflon tubing, which both work fine in lab environments. In industrial applications however, new solutions are required. When using a HiBi-fibre as a sensor, the orientation is very important and should be controlled. In this work, all sensors were placed by hand. For industrial applications, an automated procedure is desirable.

- The coating and size of an embedded optical fibre have an impact on the distortion of the surrounding composite. This work compared three different types of fibre coating (acrylate, Ormocer®, and polyimide). Ormocer® and polyimide have superior interface properties compared to the acrylate coating. A naked fibre was also considered, since the sensor used in the following chapters is a stripped optical fibre. Acceptable interface properties were obtained for stripped fibres as well. Another point of attention concerning composite distortion, is the relative orientation of the sensor to the reinforcement fibres. When the sensor is embedded parallel to the reinforcement fibres, no visible distortion could be observed and even the strength properties remained unaltered.
- The strain measured with an embedded sensor is not necessarily equal to the one present in the structure. A certain discrepancy will exist, depending on the material properties of the sensor and the host structure. In this chapter, we determined the specific strain transfer of an optical fibre embedded in a transversally loaded CFRP laminate by using FE-simulations. Afterwards, this strain transfer was validated using a transverse load experiment. A good similarity between measured (FBG-sensor) and calculated strain (FE-model) was observed.
- The theoretical resolving power of the designed MAxS-sensor is worse than the theoretical resolution of the sensor determined in Chapter 3, especially in terms of the transverse strain components. Though, for several applications this should be sufficient.

In the next chapter, the MAxS-sensors are embedded in several composite laminates, which were subjected to standardized experiments. The theoretically determined strain transfer coefficient matrix (*TC*) will be used to determine the principal strains in the composite laminate. It will be shown that the theoretical *TC*-matrix is not sufficient to accurately determine all strain components. Therefore, an experimental approach of determining an optimized *TC*-matrix will be evaluated.

4. 8. REFERENCES

1. Jung, K. and Kang, T.J., *Cure monitoring and internal strain measurement of 3-D hybrid braided composites using fiber Bragg grating sensor.* Journal of Composite Materials, 2007. **41** (12): p. 1499-1519.
2. Friebele, E.J., Askins, C.G., Bosse, A.B., Kersey, A.D., Patrick, H.J., Pogue, W.R., Putnam, M.A., Simon, W.R., Tasker, F.A., Vincent, W.S., and Vohra, S.T., *Optical fiber sensors for spacecraft applications.* Smart Materials & Structures, 1999. **8** (6): p. 813-838.
3. Green, A.K., Zaidman, M., Shafir, E., Tur, M., and Gali, S., *Infrastructure development for incorporating fibre-optic sensors in composite materials.* Smart Materials & Structures, 2000. **9** (3): p. 316-321.
4. Vlekken, J., *Preleminary Design report.* 2005. Geel, BELGIUM.
5. De Waele, W., *Structural monitoring of composite elements using optical fibres with Bragg-sensors.*, in *Department of mechanical construction and production*. 2001-2002, PhD dissertation of Ghent University: Ghent, BELGIUM.
6. Green, A.K. and Shafir, E., *Termination and connection methods for optical fibres embedded in aerospace composite components.* Smart Materials & Structures, 1999. **8** (2): p. 269-273.
7. De Waele, W., *Structural monitoring of composite elements using optical fibres with Bragg-sensors.*, in *Department of mechanical construction and production*. 2001-2002, PhD dissertation of Ghent University: Ghent, BELGIUM.
8. Sjogren, A., *Manufacturing technique for embedding detachable fiber-optic connections in aircraft composite components.* Smart Materials & Structures, 2000. **9** (6): p. 855-858.
9. Sjogren, B.A., *Static strength of CFRP laminates with embedded fiber-optic edge connectors.* Composites Part a-Applied Science and Manufacturing, 2001. **32** (2): p. 189-196.
10. Aldridge, N.B., *Fibre optic connectors and methods*, U.S.P.A. Publication, Editor. 2005: USA.
11. Guemes, J.A., Menendez, J.M., Frovel, M., Fernandez, I., and Pintado, J.M. *Experimental analysis of buckling in aircraft skin panels by fibre optic sensors*. in *Proceedings of the European COST F3 Conference on System Identification and Structural Health Monitoring*. 2000. Madrid, SPAIN.
12. Kang, H.K., Park, J.W., Ryu, C.Y., Hong, C.S., and Kim, C.G., *Development of fibre optic ingress/egress methods for smart composite structures.* Smart Materials & Structures, 2000. **9** (2): p. 149-156.

13. Simon, W.R., *Apparatus for ingress and egress of fibrer optic sensor leads from the surface of composite parts and a method for the manufacture thereof*, U. Patent, Editor. 2001.

14. Available from: http://www2.dupont.com/Kapton/en_US/assets/downloads/pdf/HN_datasheet.pdf

15. Luyckx, G. and Voet, E., *MASSFOS: WP3000 embedding proc-manufacturing proc*. 2009: Gent, BELGIUM.

16. Teitelbaum, M.E., O'Brien, D.J., Wetzel, E.D., and Goossen, K.W. *Passive and active data porting to composite integrated optical fibers via integrated optics - art. no. 69282Q*. in *Conference on Active and Passive Smart Structures and Integrated Systems*. 2008. San Diego, CA (USA).

17. Teitelbaum, M.E., Yarlagadda, S., O'Brien, D.J., Wetzel, E.D., and Goossen, K.W., *Normal incidence free space optical data porting to embedded communication links.* Ieee Transactions on Components and Packaging Technologies, 2008. **31** (1): p. 32-38.

18. Teitelbaum, M.E., O'Brien, D., Wetzel, E.D., and Goossen, K.W., *Mirrored line-of-sight input nodes for embedded optical waveguides.* Optical Engineering, 2008. **47** (11).

19. De Baere, I., Voet, E., Van Paepegem, W., Vlekken, J., Cnudde, V., Masschaele, B., and Degrieck, J., *Strain monitoring in thermoplastic composites with optical fiber sensors: Embedding process, visualization with micro-tomography, and fatigue results.* Journal of Thermoplastic Composite Materials, 2007. **20** (5): p. 453-472.

20. Askins, C.G. and Marrone, M.J., *Technique for controlling the internal-rotation of principal axes in the fabrication of birefringent fibers.* Journal of Lightwave Technology, 1988. **6** (9): p. 1402-1405.

21. Dasgupta, A. and Sirkis, J.S., *Importance of coatings to optical fiber sensors embedded in smart structures.* Aiaa Journal, 1992. **30** (5): p. 1337-1343.

22. Sirkis, J.S. and Dasgupta, A. *Optimal coating for intelligent structure fiber optical sensors*. in *Conf on Fiber Optic Smart Structures and Skins 3*. 1990. San Jose, Ca.

23. Clark, P., Boriniski, J., Gunther, M., Poland, S., Wigent, D., and Watkins, S., *Modern fibre optic sensors.* Smart Materials Bulletin, 2001. **2001** (6): p. 8-11.

24. Haas, K.-H. and Wolter, H., *Synthesis, properties and applications of inorganic-organic copolymers (ORMOCER®s)*. Current Opinion in Solid State and Materials Science, 1999. **4** (6): p. 571-580.

25. Available from: http://www.ormocer.de/EN/.

26. Vlekken, J., Vermeiren, J., and De Waele, W., *MASSFOS: Critical design report*. 2006: Geel, Leuven, Gent, BELGIUM.

27. IEC, *Optical fibres .Part 1-32:Measurement methods and test procedures - Coating strippability*. 2001.

28. DiFrancia, C., Ward, T.C., and Claus, R.O., *The single-fibre pull-out test .1. Review and interpretation.* Composites Part a-Applied Science and Manufacturing, 1996. **27** (8): p. 597-612.

29. Herrerafranco, P.J. and Drzal, L.T., *Comparison of methods for the measurement of fiber matrix adhesion in composites.* Composites, 1992. **23** (1): p. 2-27.

30. Kerans, R.J. and Parthasarathy, T.A., *Theoretical-analysis of the fiber pullout and pushout tests.* Journal of the American Ceramic Society, 1991. **74** (7): p. 1585-1596.

31. Available from: http://en.wikipedia.org/wiki/Stick-slip_phenomenon.

32. Okabe, Y., Tsuji, R., and Takeda, N., *Application of chirped fiber Bragg grating sensors for identification of crack locations in composites.* Composites Part a-Applied Science and Manufacturing, 2004. **35** (1): p. 59-65.

33. Available from: http://www.Fos-s.com.

34. Burgelman, N., *Studie en modellering van pull-out proeven*, in *Mechanical construction and production*. 2006-2007, Master thesis at Ghent university: Gent, BELGIUM.

35. Levin, K., *Durability of embedded Fibre optic sensors in composites*, in *Departement of Aeronautics, Royal institute of technology*. 2001, PhD dissertation of the University of Stockholm: Stockholm, SWEDEN.

36. Ang, J., Li, H.C.H., Herszberg, I., Bannister, M.K., and Mouritz, A.P. *Tensile Fatigue Performance of Surface Mounted Bragg Grating Optical Fibres for Use in Structural Health Monitoring*. in *4th European Workshop on Structural Health Monitoring*. 2008. Cracow, POLAND.

37. Chojetzki, C., Rothhardt, M., Ommer, J., Unger, S., Schuster, K., and Mueller, H.R., *High-reflectivity draw-tower fiber Bragg gratings - arrays and single gratings of type II.* Optical Engineering, 2005. **44** (6).

38. Available from: http://www.toraycfa.com/pdfs/M55JDataSheet.pdf.

39. Skontorp, A. *Strength and failure mechanisms of polyimide-coated optical fibers*. in *Proceedings of the Smart Structures and Materials 2000 Conference*. 2000. Newport Beach, Ca (USA).

40. Skontorp, A. and Cammas, J. *Static fatigue life of silica optical fibers and the significance of fiber coating and handling*. in *Proceedings of the Smart Structures and Materials 2001 Conference*. 2001. Newport Beach, Ca (USA).

41. De Waele, W., Degrieck, J., De Baets, P., Moerman, W., and Taerwe, L., *Feasibility of integrated optical fibre sensors for condition monitoring of composite structures - Part II: Combination of Bragg-sensors and acoustic emission detection.* Insight, 2003. **45** (8): p. 542.

42. Takeda, N., Okabe, Y., Kuwahara, J., Kojima, S., and Ogisu, T., *Development of smart composite structures with small-diameter fiber Bragg grating sensors for damage detection: Quantitative evaluation of delamination length in CFRP laminates using Lamb wave sensing.* Composites Science and Technology, 2005. **65** (15-16): p. 2575-2587.

43. Saton, K., Fukuchi, K., Kurosawa, Y., Hongo, A., and Takeda, N. *Polyimide-coate small-diameter optical fiber sensors for embedding in composite laminate structures*. in *Proceedings of SPIE*. 2001. Newport Beach, CA (USA).

44. Leka, L.G. and Bayo, E., *A close look at the embedment of optical fibers into composite structures.* Journal of Composites Technology & Research, 1989. **11** (3): p. 106-112.

45. Shivakumar, K. and Emmanwori, L., *Mechanics of failure of composite laminates with an embedded fiber optic sensor.* Journal of Composite Materials, 2004. **38** (8): p. 669-680.

46. Jensen, D.W., Pascual, J., and August, J.A. *Finite element analysis of composite laminates containing transversely embedded optical fiber sensors*. in *Proceedings of the First European Conference on Smart structures and Materials, ECCM-1*. 1992. Glasgow, UK.

47. Itoh, T. and Springer, G.S., *Strain measurement with microsensors.* Journal of Composite Materials, 1997. **31** (19): p. 1944-1984.

48. Cheng, C.C., Lo, Y.L., Pun, B.S., Chang, Y.M., and Li, W.Y., *An investigation of bonding-layer characteristics of substrate-bonded fiber Bragg grating.* Journal of Lightwave Technology, 2005. **23** (11): p. 3907-3915.

49. Li, W.Y., Cheng, C.C., and Lo, Y.L., *Investigation of strain transmission of surface-bonded FBGs used as strain sensors.* Sensors and Actuators a-Physical, 2009. **149** (2): p. 201-207.

50. Wan, K.T., Leung, C.K.Y., and Olson, N.G., *Investigation of the strain transfer for surface-attached optical fiber strain sensors.* Smart Materials & Structures, 2008. **17** (3).

51. Chang, C.C., LeBlanc, M., and Vohra, S. *Investigation of transverse stress measurements by using embedded fiber Bragg grating sensors subjected to host Poisson's effect*. in *Smart Structures and Materials 2000 Conference*. 2000. Newport Beach, Ca (USA).

52. Cox, H.L., *The elasticity and strength of paper and other fibrous materials.* British Journal of Applied Physics, 1952. **3** (3): p. 72-79.

53. Fan, Y. and Kahrizi, M., *Characterization of a FBG strain gage array embedded in composite structure.* Sensors and Actuators a-Physical, 2005. **121** (2): p. 297-305.

54. Bosia, F., Giaccari, P., Botsis, J., Facchini, M., Limberger, H.G., and Salathe, R.P., *Characterization of the response of fibre Bragg grating sensors subjected to a two-dimensional strain field.* Smart Materials & Structures, 2003. **12** (6): p. 925-934.

55. Beitz, W. and Küttner, K.-H., *Dubbel: Handbook of mechanical engineering*. 1994: Springer-Verlag.

56. Kollar, L.P. and Van Steenkiste, R.J., *Calculation of the stresses and strains in embedded fiber optic sensors.* Journal of Composite Materials, 1998. **32** (18): p. 1647-1679.

57. Lekhnitskii, S., *Theory of elasticity of an anisotropic body*. 1977, Moscow: MIR Publishers.

58. Kim, K.S., Kollar, L., and Springer, G.S., *A model of embedded fiber optic Fabry-perot temperature and strain sensors.* Journal of Composite Materials, 1993. **27** (17): p. 1618-1662.

59. Herakovitch, C.T., *Mechanics of fibrous composites*. 1998, New York: John Wiley and Sons inc.

60. *ABAQUS: User's Manual*. 2002, New York: Hibbit, Karlsson & Sörensen inc.

Chapter 5 : EXPERIMENTAL VALIDATION OF AN EMBEDDED MAXS-SENSOR

In this chapter, the theoretically calculated relation between optical fibre strain and host material has been experimentally optimized. The feasibility of the MAxS-sensor is extensively evaluated in a test program (Figure 5-1). Extra attention was paid to measuring shear and temperatures as well. This chapter begins with an explanation of the manufacturing process of CFRP-samples, using the autoclave technique.

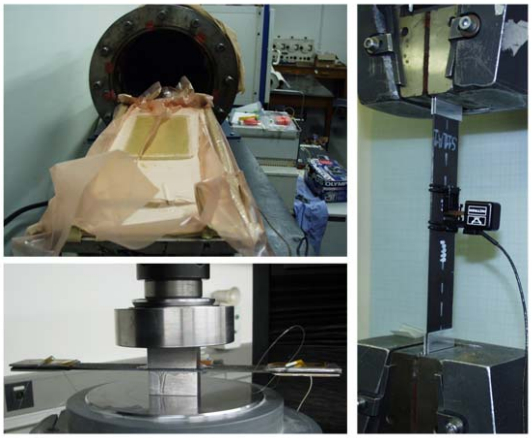

Figure 5-1: Autoclave production facility, a transverse compression test, and an axial tensile test.

5. 1. CFRP LAMINATES

5. 1. 1. Global and local coordinate system of the CFRP-laminates

Generally, two different orthogonal coordinate systems are used to define the strains inside composite laminates. Figure 5-2 shows the orthogonal coordinate system corresponding with an individual lamina. The 1-axis is aligned with the reinforcement fibres while the 2- and 3-axes are in the transverse directions (in-plane and through-the-thickness respectively).

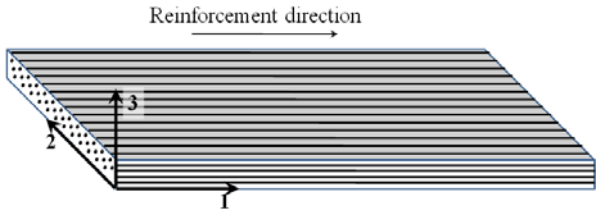

Figure 5-2: The local orthogonal coordinate system on lamina level

Figure 5-3 shows the global orthogonal coordinate system of a laminate. The x-axis is aligned with the major direction (length) of the sample. The z-axis is the direction through-the-thickness of the sample and the y-axis is the remaining in-plane axis (width).

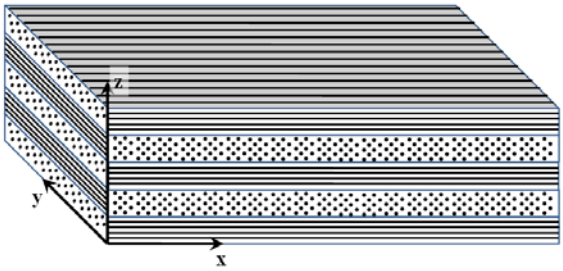

Figure 5-3: The global orthogonal coordinate system on laminate level

During the MASSFOS project [1], a lot of sensors have been embedded in CFRP samples and tested under controlled loading conditions (tensile testing, transverse compression testing, four point bending testing, shear tensile testing, and thermal load testing). In the following paragraphs, a selection of these tests is used to optimize the *TC*-matrix and prove the feasibility of the MAxS-sensor. The measured strain values will be compared with reference measurements like extensometer, displacement, load, or surface attached FBG together with finite element simulations. In this work, the following colour code is used for the graphical representation of strain; black for the x-axis, blue for the y-axis and red for the z-axis. The reference strains will be depicted as dashed lines and the measured strains as full line with diamond, circle or square symbols for the x-, y- and z-axis respectively.

5. 1. 2. Manufacturing process

As discussed before, carbon-epoxy prepreg (M55j/M18) was used as raw material for the manufacturing of the CFRP samples. M55j/M18 is a space qualified uni-directional carbon fibre reinforced epoxy [2]. The reinforcing carbon fibres are “high modulus” fibres with a Young’s modulus of 540 GPa [3]. One layer of prepreg material will have a final layer thickness of 0.1 mm after curing.

To produce the lay-up of the laminates, the author used the following procedure, illustrated in Figure 5-4. (1) The prepreg material is wrapped on a roll (width = 300 mm, length = 75 m) covered with a protective film on each side. (2) Several layers (laminae) with the desired orientation are cut from the roll. (3) One of the protective films is removed and (4) a lamina is stacked in the right sequence. (5) The resulting laminate is pressed together using a roller pin. (6) Finally, the other protective film is removed and the process can be repeated until the complete laminate is produced.

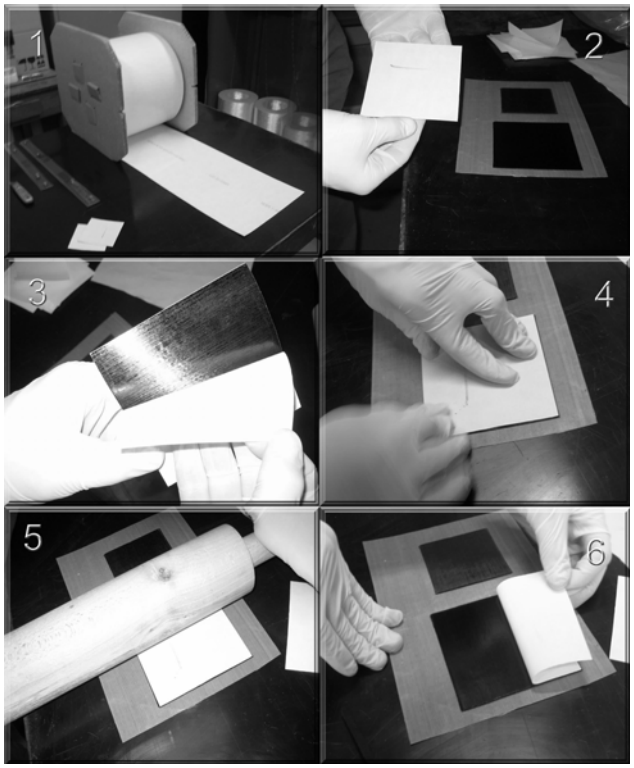

Figure 5-4: Prepreg lay-up procedure

The laminate needs a strict curing cycle, that consists of a combination of temperature, pressure and vacuum. The temperature cycle drives the curing process and controls the autoclave pressure. In order to meet the requirements of the curing cycle, a special oven/pressure vessel is needed: the autoclave (Figure 5-5).

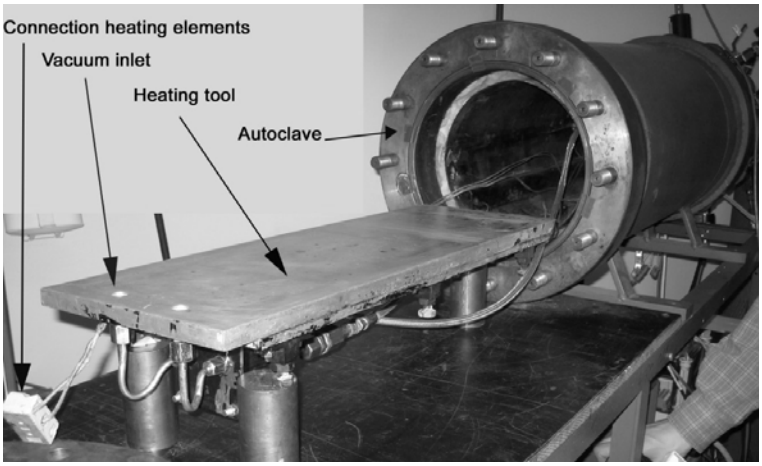

Figure 5-5: The autoclave of Ghent university, department of Materials Sciences and Engineering.

To follow the curing cycle optimally, the uncured laminate is placed in a vacuum bag in between several layers of fabrics and films as shown in Figure 5-6. The lowermost tool serves as a heating device. On this, firstly, a release film is placed which prevents the prepreg laminate from sticking to the tool and which promotes, together with the peel ply, easy removal. The bleeder fabric on top of the peel ply is used to absorb excess resin from the curing laminate. The breather, which is in this case the same material of the bleeder, is needed to transport gasses, generated from the curing resin, out of the autoclave. Thermocouples are placed in the vicinity of the laminate to control the manufacturing process.

Figure 5-7 illustrates the curing cycle used to produce the CFRP samples. The curing cycle starts by building up a vacuum pressure inside the vacuum bag, that covers the entire lay-up. This vacuum is needed for withdrawal of possible air bubbles included during the manual stacking of the lamina. Water from condensation reactions or volatile elements (such as solvents) can be absorbed too during fabrication or handling of the prepreg. When a constant vacuum pressure of -0.7 bar is reached, the temperature is raised up to 120°C at a rate of 3°C/min and subsequently kept constant for 20 min. During this so-called dwell step, the temperature is kept constant at the level of optimal epoxy viscosity [4], allowing the epoxy resin to flow and the layers to stick together. At the end of the dwell step, the autoclave pressure is raised to a level of 7 bar (consolidating pressure). At 7 bar, the temperature is raised to a maximum of 180°C and kept constant for 100 minutes. During this period, actual hardening of the laminate occurs; because of cross-linking, the viscous resin is transformed into a thermal stable, stiff material. After this period, the autoclave cools down by turning of the heating, but keeps the

pressure to prevent deformation of the laminate due to thermal stresses, during cooling. When the temperature reaches 60°C, both vacuum and autoclave pressure are dropped to atmospheric pressure.
The optimal form of the cure cycle was deduced from practical experience obtained during a master thesis at Ghent University [5].

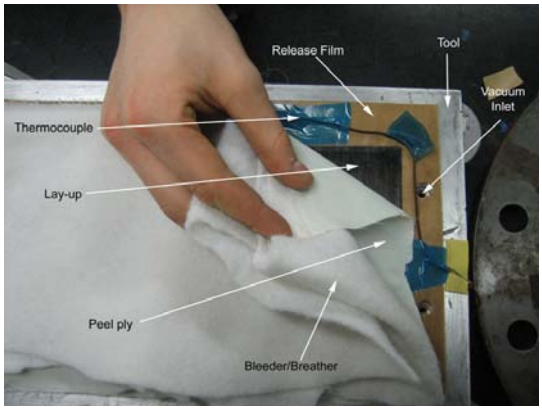

Figure 5-6: Build-up in the autoclave for laminate production using prepreg lamina [5].

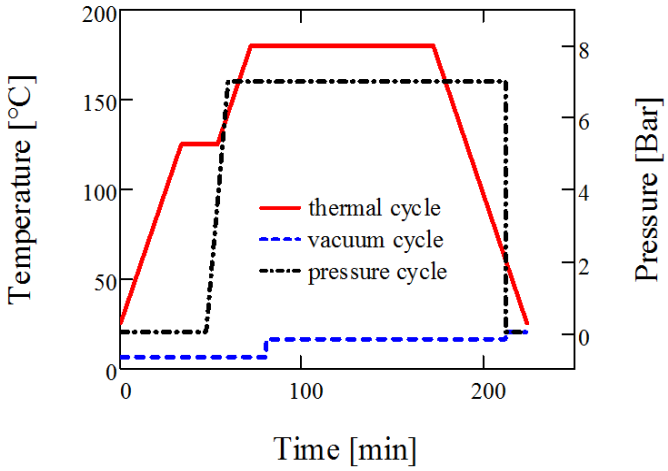

Figure 5-7: Curing cycle used to produce the M55j/M18 CFRP samples

5. 1. 3. Mechanical properties of the CFRP laminates

The manufacturer did provide a datasheet for this material, containing most of the material properties. However, the actual lamina properties depend on the production method and have to be determined. Mechanical properties are determined using tensile experiments performed on standardized test samples [5].

Three sets of samples with different dimensions and/or fibre directions were manufactured (Figure 5-8) and tested according to the D3039 ASTM standard [6]. The autoclave produced laminates were cut to a width of 2 cm, followed by glueing end tabs, needed to mount the test samples in the clamps of the tensile testing facility. The tabs have a specific shape: one end is milled to an angle of 12° in order to prevent stress concentrations by gradually introducing the stress from the end part to the samples. The test samples were instrumented with a strain gauge, mounted perpendicular to the loading direction to measure the contracting strain (Poisson's effect). An extensometer recorded strain in the displacement direction (Figure 5-9). The extensometer is removed from the test sample at one third of the expected ultimate tensile strength, to prevent it from being damaged due to breaking of the sample.

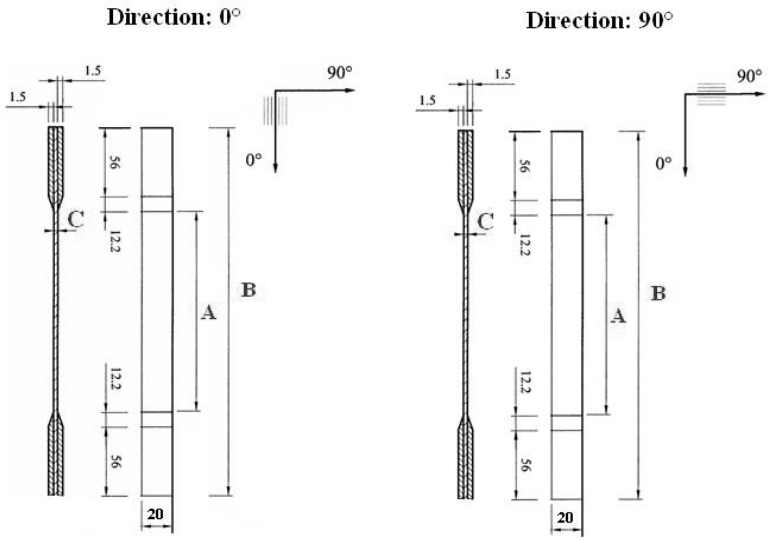

Figure 5-8: Dimensions of the test samples used to determine the mechanical properties of the M55j/M18 prepreg material according to ASTM standard D3039.

Dimensions of the three sets of test samples are given in Table 5-1.

Table 5-1: Dimensions of the 3 sets of test samples (in mm)

	SET 1	SET 2	SET 3
Lay-up	$[0]_{10}$	$[0]_{16}$	$[90]_{20}$
# of samples	4	3	3
A	~124	~144	~147
B	~260	~280	~283

C	1.0	1.5	2.0

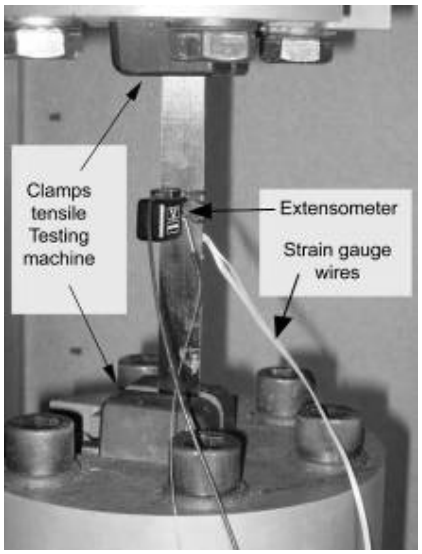

Figure 5-9: Sample mounted in the tensile testing facility

Table 5-2 shows the test results for a fibre direction of 0 deg and 90 deg, and compares them to the values noted in the data sheet of the manufacturer [7], and to data obtained by Jose et al. [8].

Normally, sets 1 and 2 (Table 5-2) should result in similar material properties. However, there is a fairly big difference, which suggests that the composite plates had a different composure. In set 2, more extraction of resin was observed after curing, which resulted in a smaller ply thickness. In [9] is explained that, in the case of carbon-fibres, material properties are highly dependent on the fibre direction. Even the slightest deviation from the 0 deg direction, causes a significant change in material properties (a drop in the E_{11} and longitudinal strength values and a slight raise of the v_{12} value). So we can conclude that the difference in resin content, together with a slight deviation of the reinforcing fibres from the 0 deg direction for set 2, cause the difference in material properties between set 1 and 2. For later use in finite element simulations, the author adopted the material properties noted in Table 5-3. These values approximate the results of sets 1 and 3.

Table 5-2: Summary of the values found for the elastic and strength properties of the M55j/M18 composite materials, compared with those of the manufacturer

			[5]		[7]	[8]
		Set 1	Set 2	Set 3		
Elastic constants	Longitudinal modulus E_{11} [GPa]	298.4	248.9		340.0	329.0
	Transverse modulus E_{22} [GPa]			6.3		6
	Poisson's ratio ν_{12} [-]	0.321	0.327			0.346
	Poisson's ratio ν_{21} [-]			0,0017		
	Poisson's ratio ν_{23} [-]				0.38	
	Shear modulus G_{12} [GPa]					4.4
Strength properties	Longitudinal strength [MPa]	2131	1648		2010	1327
	Transverse strength [MPa]			22	34	22

Table 5-3: Elastic material properties for the M55J/M18 carbon/epoxy material

E_{11}	$E_{22} = E_{33}$	$G_{12}=G_{13}$	G_{23}	$\nu_{12}=\nu_{13}$	$\nu_{23}=\nu_{32}$	$\nu_{21}=\nu_{31}$
[GPa]	[GPa]	[GPa]	[GPa]	[-]	[-]	[-]
300.0	6.3	4.3	2.3	0.320	0.380	0.002

5. 1. 4. Inventory of all tested CFRP laminates with embedded MAxS-sensor

A complete inventory of the tested samples and their dimensions is summarized in Table 5-4. In the second last column, the position of the sensor is indicated (between which two layers it has been embedded) . In most of the samples, the MAxS-sensor is positioned near the surface of the sample to achieve the highest bending response. In each sample the sensor is embedded parallel with the reinforcement fibres, to achieve the least composite distortion. Since the MAxS-sensor is almost 4cm in length (2 FBGS in series), it is impossible to embed it in the $[90]_n$ and $[\pm 45]_n$ samples as a whole. Therefore, in these cases the sensor is split up in two separate fibres (FBGs) of which one is encapsulated in a capillary (Figure 5-39 and Figure 5-58). In the last column of the table, the orientation of the sensor's slow axis with respect to the surface of the sample, is given.

Table 5-4: Complete inventory of the tested samples with embedded sensors.

Lay-up	Length	Width	Thickness	Sensor's position	Sensor's orientation
	[mm]	[mm]	[mm]	Layer (L)	
$[0]_{16}$	250	15.0	1.83	L13 - L14	broken
$[0]_{16}$	250	15.0	1.83	L13 - L14	75 deg
$[0]_{16}$	250	28.4	1.62	L13 - L14	13 deg
$[0]_{16}$	250	30.0	1.60	L13 - L14	broken
$[0]_{48}$	250	32.5	5.70	L40 - L41	9 deg
$[0]_{48}$	250	32.0	5.90	L40 - L41	6 deg
$[90]_{24}$	175	40.0	2.30	L20 - L21	14 deg
$[90]_{24}$	175	40.0	2.30	L20 - L21	15 deg
$[90_2,0_2]_{6s}$	300	24.0	4.95	L3 - L4	0 deg
$[90_2,0_2]_{6s}$	300	25.0	5.05	L3 - L4	32 deg
$[90_2,0_2,90_2,0]_s$	250	25.0	1.34	L11 - L12	69 deg
$[90_4,0_4]_{3s}$	102	30.0	5.50	L24 - L25	45 deg
$[90_4,0_4]_{3s}$	102	29.1	5.00	L24 - L25	22 deg
$[0_2,90_2]_{6s}$	250	25.0	1.34	L8 – L9	66 deg
$[0_2,90_2]_{6s}$	250	25.0	1.34	L8 – L9	90 deg
$[+45_2,-45_2]_{2s}$	250	40.0	1.60	L11 - L12	57 deg
$[+45_2,-45_2]_{2s}$	250	40.0	1.60	L11 - L12	50 deg
$[+45_2,-45_2]_{6s}$	275	40.0	4.90	L3 - L4	48 deg
$[+45_2,-45_2]_{6s}$	275	40.0	5.00	L3 - L4	31 deg

5. 2. TEST METHODS

The following five test methods were selected to induce different homogeneous strain fields in the CFRP-laminate. These methods were used to evaluate the strain response of the MAxS-sensor and eventually optimize the theoretically determined *TC*-matrix of Chapter 4.

5. 2. 1. Axial tensile experiment

The axial tensile experiment is based on the ASTM D3039 standard [6]. This standard is normally used to determine tensile properties of a matrix reinforced with high modulus reinforcement fibres. For this test, a thin flat strip of material having a constant rectangular cross section, is mounted in the grips of a mechanical testing machine and monotonically loaded in tension. In order to be able to clamp the composite sample, aluminium tabs were glued at the ends of the sample (Figure 5-10). These tabs are gripped by mechanical clamps of a universal testing machine. In order to avoid breakage of the optical fibre at the egress points during clamping of the sample, some space (approx. 10mm) was left between the top of the aluminium tabs and the mechanical clamp. As such, the optical fibre could be bent out of the mechanical clamp. An electrical extensometer was mounted to serve as reference measurement of the applied axial strain.

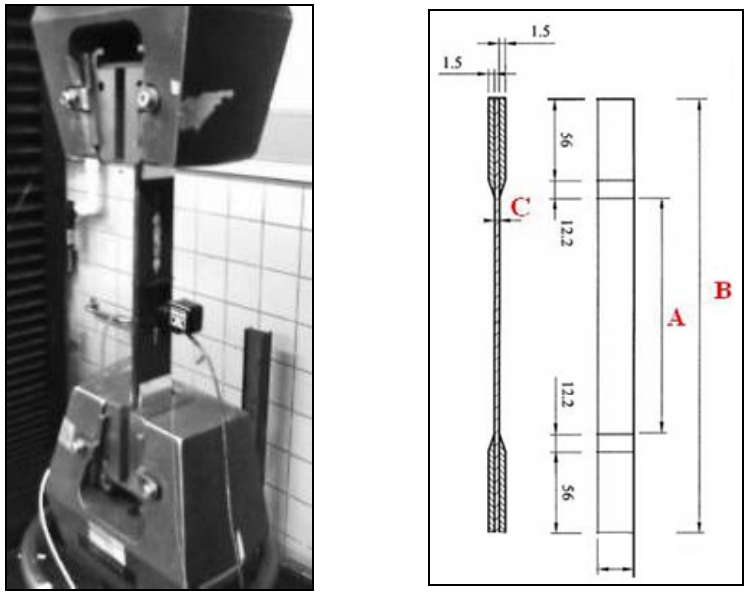

Figure 5-10: Tensile test specimen mounted in a universal testing machine, and using an extensometer as reference measurement (left). An illustration of the dimensions of a test sample (right).

5. 2. 2. Transverse tension and compression experiment

As shown in Section 5. 1. 3. , carbon fibre reinforced epoxy features a high stiffness in the reinforcement direction and can consequently resist high loads in that direction. However, perpendicularly to the carbon fibres, the strength of the composite sample is determined by the lower strength properties of the epoxy matrix. Strain in a plane perpendicular to the carbon fibres can thus pose a threat to the structural integrity of the composite sample. For this reason, structural health monitoring in this type of structures necessitates a transversal strain measurement. Because the composite material is usually only a few millimeters thick, it is not straightforward to assess the strain in this direction. The MAxS-sensor possibly holds a promising solution for this application. **Transverse tension and compression tests** have been executed, to evaluate the transverse performance of the sensor. Three different set-ups were used to perform this type of tests.

In a first set-up, metal T-joints are attached to the surfaces of the sample, applying epoxy glue (Figure 5-11). The T-joints are clamped in the testing machine and introduce compressive and tensile loading (and corresponding strains) in the samples. Load and displacement of the clamps were recorded. By comparing the response of the MAxS-sensor during a compression experiment, to the response during a tension experiment, a possible different response of the sensor to

compressive or tensile load can be evaluated. If no differences are observed, one can easily use the compression test to check the transverse resolving power of the MAxS-sensor.

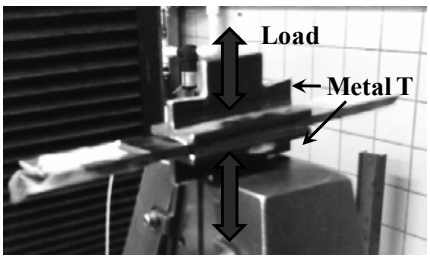

Figure 5-11: Test method for determining the transverse stress sensitivity of the MAxS-sensor, using metal T-joints glued on top of the specimen.

Due to different reasons, no strain values can be calculated using this set-up. One reason is the uncertain load transfer to the sample due to deformation of the metal T-joints during the experiments (Figure 5-12). A second reason is the uncertain position of the sensor with regard to the T-joint.

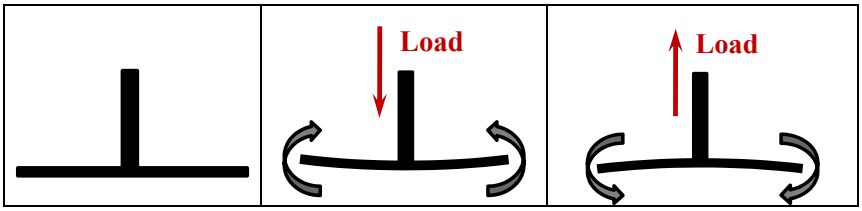

Figure 5-12: Deformation of the metal T-joint during the transverse compression experiment and during the transverse tension experiment.

In the second set-up, a piece of rubber covering the zone of the MAxS sensor at one side of the composite laminate, was used to generate a homogeneous transverse compressive load (Figure 5-13). This method generates bad results (i.e. non-linearity) at low transverse compressive loads. However, when pressing harder, the rubber flattens out and a uniform transverse load is transferred on the sample, generating a good (and linear) strain field measured by the MAxS sensor (Figure 5-13). In the discussion of the results, only that last linear part will be shown.

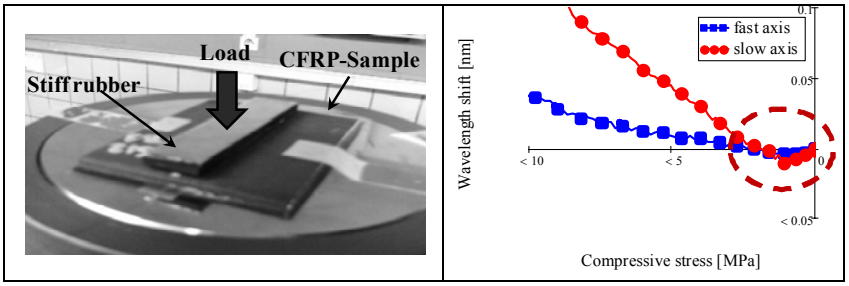

Figure 5-13: The compression test set-up using reinforced rubber

To overcome the non-linearity introduced by the rubber, it was replaced by two metal blocks which were glued to the surfaces of the sample (Figure 5-14, left). For this type of set-up, the response of the sensor is clearly linear during the compressive experiment (Figure 5-14, right).

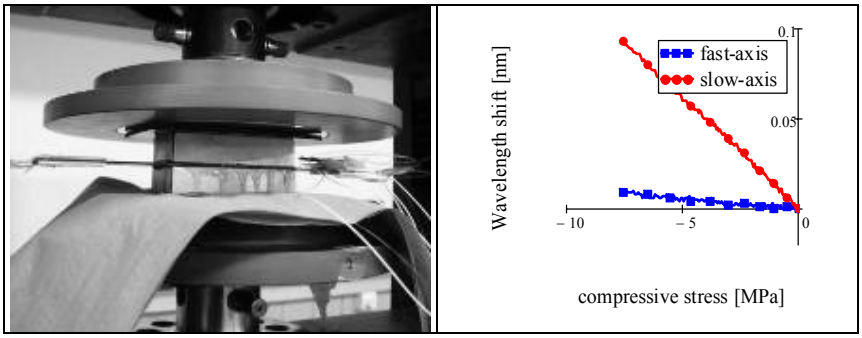

Figure 5-14: Compressive test set-up using polished metal blocks glued with a uniform epoxy layer to the specimen's surfaces (left). The linear response of a sample with embedded MAxS-sensor under compressive load (right).

5. 2. 3. A four point bending experiment

A bending test represents quite well the actual load on a structural component (e.g. loading of airplane wings). Therefore, **a four point bending experiment** was performed based on the ASTM standard D6272 [10]. This standard covers the determination of flexural properties of high-modulus composites. A coupon of rectangular cross section rests on two supports and the load is introduced at two points, each at an equal distance from the adjacent support point (Figure 5-15). The distance between the loading noses (the load span) is one half of the support span. In this test, a constant bending moment is created over the load span and thus a constant strain field over the length of the MAxS sensor is created. Using this set-up, the sensors can be loaded in compression as well as in tension. The applied load, the displacement of the support span and the wavelength shift of a surface mounted FBG (in between the loading noses), were taken as reference measurements.

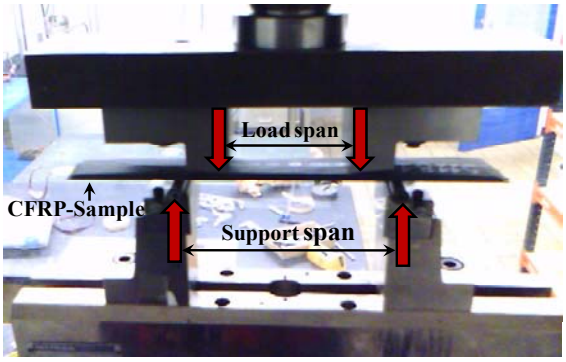

Figure 5-15: Set-up used to perform a four point bending test.

Note that there is a disadvantage in using a fixed test rig instead of a rig connected with the load cell through a hinge-joint. In the fixed rig set-up (like the one used in this dissertation), the lower rig is able to move up and down while the upper rig is fixed to the load cell. The fixed rig cannot overcome alignment errors of both rigs and/or surface roughness of the specimen (Figure 5-16). Therefore, at the beginning of the bending experiment, the specimen is loaded in three point bending instead of four point bending. Thus at the start of the experiment, only the support span and one roll of the load span will be touching the sample.

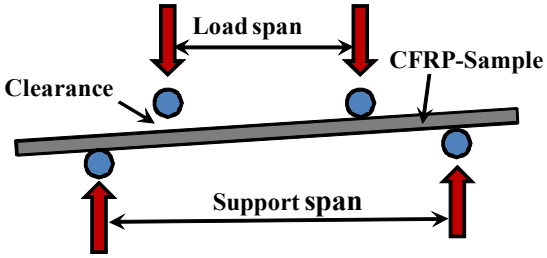

Figure 5-16: Schematic drawing of the problem at the start of a four point bending experiment when using a fixed test rig. Only one roll of the load span is touching the CFRP sample. The sample is thus loaded in three point bending.

5. 2. 4. In-plane shear tensile experiment

In-plane shear tensile experiments are based on the ASTM standard D3518 [11]. The shear response of a composite specimen is determined by performing a tensile test on a ±45° laminate [11] (Figure 5-17). Besides the response of the sensor, load and displacement were captured together with a surface mounted FBG at the centre of the sample and an electrical extensometer mounted at the same position as the reference FBG.

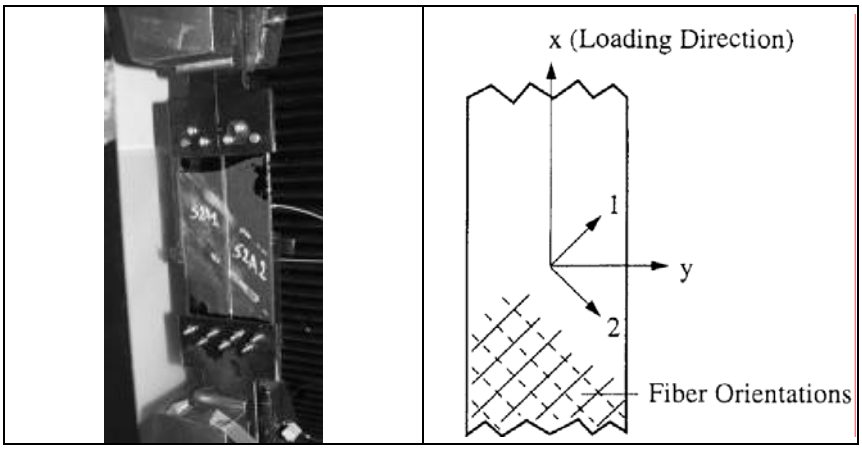

Figure 5-17: Shear tensile experiment set-up (left). Orientation of the reinforcement fibres with respect to the loading direction (right).

5. 2. 5. Thermal cycle experiment

Finally, preliminary **thermal cycle experiments** have been performed (Figure 5-18). The (cured) samples were put inside an autoclave and the temperature was set to 120°C. The Bragg wavelengths of the MAxS-sensor were monitored during heating and cooling of the samples. An unforced cooling cycle creates a slow and homogeneous temperature drop in the oven and sample. A thermocouple was put on top of the composite sample to measure the temperature inside the autoclave.

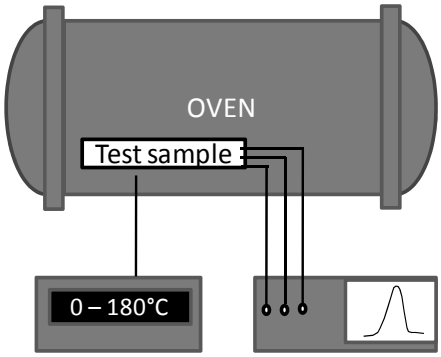

Figure 5-18: The test sample is put in an oven (autoclave) to perform a thermal cycle

5. 2. 6. Optical read-out set-up

In all types of experiments, the repetition rate of the FBG measurements was much higher than the time scale of the loading. As a result, all measurements are

considered to be static. A general overview of the Bragg peak wavelength recording set-up is schematically shown in Figure 5-19.

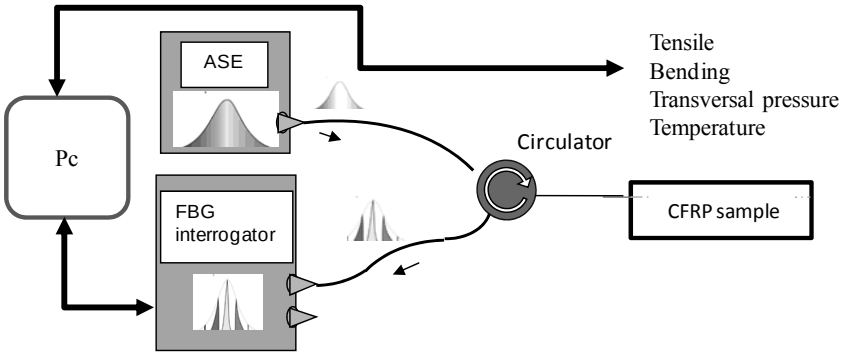

Figure 5-19: Set-up for the optical read-out during static tests

A broadband amplified spontaneous emission (ASE) light source couples light into the optical fibre. The light is backreflected on the Bragg grating and directed via a circulator to an FBG interrogator (FBG-scan commercialised by FOS&S [12]) with a resolution of 1 pm and a frequency of 1 Hz. As the frequency is low, the static testing should be performed at very low loading speed.

5. 3. STRAIN CALCULATION PROCEDURE

During the experiments, controlled loading of the sample causes a certain homogeneous strain field in the sample. The core of the optical fibre sensor that is embedded in the structure, will sense a somewhat different strain field. The relation between the strain field at the core of the MAxS-sensor and that of the sample, is determined by the strain transfer matrix. In its turn, straining the core of the optical fibre causes a wavelength shift. The relation between strains and wavelength shifts is defined by the *K*-matrix, which is closely related to the strain-optic effect discussed in section 2. 2. 1.. Figure 5-20 shows the different calculation steps needed to determine the strain field in the sample, starting from the wavelength response of the MAxS-sensor. In the following paragraphs, these steps are further elaborated. A transverse compressive load is taken as example.

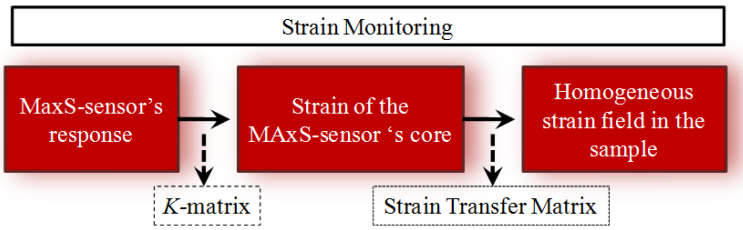

Figure 5-20: Monitoring schedule using a MAxS-sensor to determine the strain field of a CFRP-sample subjected to a homogeneous load.

5. 3. 1. Recording the response of the MAxS-sensor

In Figure 5-21, the response of a MAxS-sensor embedded in a laminate with a unidirectional lay-up ($[0°]_{48}$) is depicted. A high Bragg peak separation can be observed for FBG1 while very small wavelength shifts and no Bragg peak separation can be observed for the encapsulated FBG.

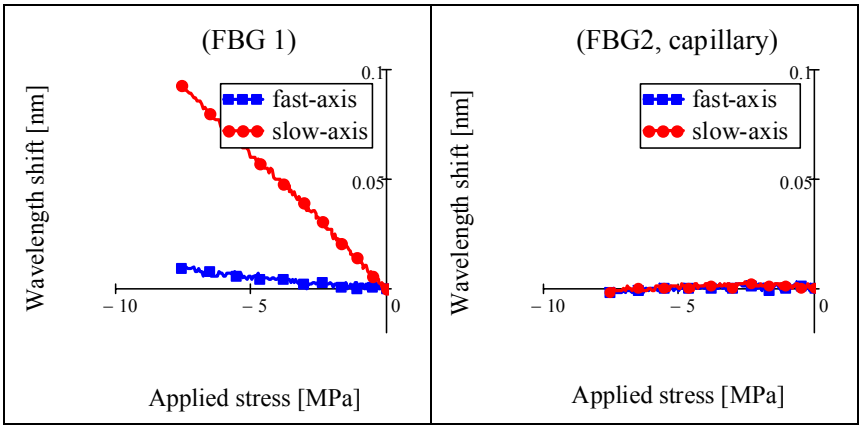

Figure 5-21: The MAxS-sensor's response under transverse compression.

5. 3. 2. Determination of the strain field at the fibre core

Using the *K*-matrix, which form depends on the sensor configuration (Chapter 3) and which content is dependent on the strain-optic coefficients (Chapter 2), one can calculate the strain field present at the core of the optical fibre sensor. This by using the following set of equations:

$$\begin{bmatrix} \Delta\varepsilon_{11'} \\ \Delta\varepsilon_{22'} \\ \Delta\varepsilon_{33'} \end{bmatrix} = K^{-1} \begin{bmatrix} \Delta\lambda_{B1,1'} \\ \Delta\lambda_{B1,2'} \\ \Delta\lambda_{B2,2'} \end{bmatrix} \qquad \textbf{5-1}$$

In which the *K*-matrix is defined as

$$K=\begin{bmatrix}\lambda_{B1,1'} & 0 & 0\\ 0 & \lambda_{B1,2'} & 0\\ 0 & 0 & \lambda_{B2,2'}\end{bmatrix}\begin{bmatrix}-\frac{n_{eff}^2}{2}p_{11} & -\frac{n_{eff}^2}{2}p_{12} & 1-\frac{n_{eff}^2}{2}p_{12}\\ -\frac{n_{eff}^2}{2}p_{12} & -\frac{n_{eff}^2}{2}p_{11} & 1-\frac{n_{eff}^2}{2}p_{12}\\ 0 & 0 & (1-\frac{n_{eff}^2}{2}p_{12})+\upsilon\frac{n_{eff}^2}{2}(p_{11}+p_{12})\end{bmatrix} \quad \textbf{5-2}$$

Substituting the strain-optic coefficients found in section 2. 4. 1 ($p_{11}=0.111$ and $p_{12}=0.247$) and using $\lambda_{B1,1'}=1539.219\,nm$, $\lambda_{B1,2'}=1538.729\,nm$ and $\lambda_{B2,2'}=1553.462\,nm$ the *K*-matrix becomes.

$$K=\begin{bmatrix}-183.167 & -407.893 & 1131.324\\ -407.763 & -183.109 & 1130.966\\ 0 & 0 & 1242.770\end{bmatrix}nm \quad \textbf{5-3}$$

Figure 5-22 represents the calculated strains at the core of the embedded MAxS-sensor during the transverse compression test by substituting Equation 5-3 into Equation 5-1 and using the wavelength shifts shown in Figure 5-21.

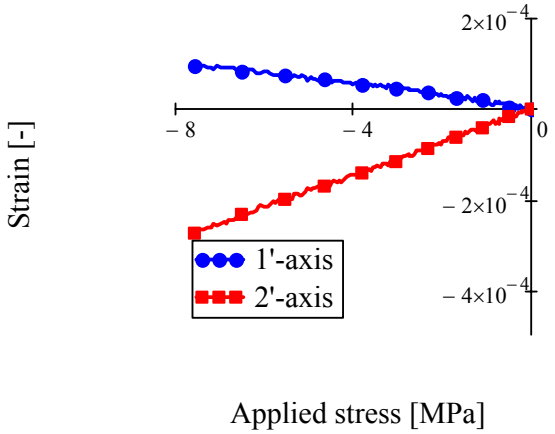

Figure 5-22: The measured strain in the core of the embedded MAxS-sensor during a transverse compressive test

5. 3. 3. Determination of the strain field in the composite structure

Using the transfer matrix, which is dependent on the mechanical properties of the sensor and the host material (Section 4. 5. 2), one can calculate the strain field present in the host material. The following set of equations applies:

$$\begin{bmatrix} \Delta\varepsilon_{xx} \\ \Delta\varepsilon_{yy} \\ \Delta\varepsilon_{zz} \end{bmatrix} = \begin{bmatrix} TC_{11} & TC_{12} & TC_{13} \\ TC_{21} & TC_{22} & TC_{23} \\ TC_{31} & TC_{32} & TC_{33} \end{bmatrix} \begin{bmatrix} \Delta\varepsilon_{3'} \\ \Delta\varepsilon_{1'} \\ \Delta\varepsilon_{2'} \end{bmatrix} \qquad \textbf{5-4}$$

Substituting the theoretically determined *TC*-coefficients for a bow-tie fibre sensor embedded in a $[0]_{48}$-laminate (Section 4. 5. 2. c.) into Equation 5-4:

$$\begin{bmatrix} \Delta\varepsilon_{xx} \\ \Delta\varepsilon_{yy} \\ \Delta\varepsilon_{zz} \end{bmatrix} = \begin{bmatrix} 1.000 & 0.000 & 0.000 \\ 0.827 & 8.152 & -1.003 \\ 0.814 & -1.178 & 6.936 \end{bmatrix} \begin{bmatrix} \Delta\varepsilon_{3'} \\ \Delta\varepsilon_{1'} \\ \Delta\varepsilon_{2'} \end{bmatrix} \qquad \textbf{5-5}$$

The calculated composite strains are presented in Figure 5-23. Based on a comparison with reference strains (determined by FE-simulations), one can conclude that the calculated strains are overestimated. For a small part, this could be caused by a difference in actual mechanical properties and the values used in the FE-model. It is believed that the main cause is an underestimation of the strain that is transferred from the host material to the core of the optical fibre. Therefore, in the next paragraph, several experimental results will be used, to optimize the *TC*-matrix.

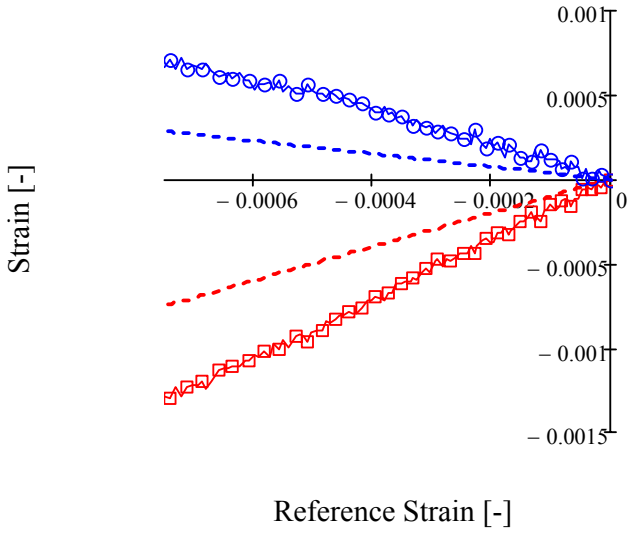

Figure 5-23: The calculated and reference strains inside the host material during a transverse compression test.

5. 4. Optimization of the Strain Transfer Coefficients Matrix

The *TC*-matrix consists of 9 independent components (Equation 5-4), which can be determined by loading a sample according to three independent loading conditions

(see Section 4.5.2. b.). For each loading condition the following set of 3 equations can be developed.

$$\begin{bmatrix} \Delta\varepsilon_{xx} \\ \Delta\varepsilon_{yy} \\ \Delta\varepsilon_{zz} \end{bmatrix} = \begin{bmatrix} TC_{11} & TC_{12} & TC_{13} \\ TC_{21} & TC_{22} & TC_{23} \\ TC_{31} & TC_{32} & TC_{33} \end{bmatrix} \begin{bmatrix} \Delta\varepsilon_{3'} \\ \Delta\varepsilon_{1'} \\ \Delta\varepsilon_{2'} \end{bmatrix} \quad \textbf{5-6}$$

Combining all equations, the *TC*-matrix should equal

$$\begin{bmatrix} TC_{11} & TC_{12} & TC_{13} \\ TC_{21} & TC_{22} & TC_{23} \\ TC_{31} & TC_{32} & TC_{33} \end{bmatrix} = \begin{bmatrix} \Delta\varepsilon_{xx\_1} & \Delta\varepsilon_{xx\_2} & \Delta\varepsilon_{xx\_3} \\ \Delta\varepsilon_{yy\_1} & \Delta\varepsilon_{yy\_2} & \Delta\varepsilon_{yy\_3} \\ \Delta\varepsilon_{zz\_1} & \Delta\varepsilon_{zz\_2} & \Delta\varepsilon_{zz\_3} \end{bmatrix} \begin{bmatrix} \Delta\varepsilon_{33'\_1} & \Delta\varepsilon_{33'\_2} & \Delta\varepsilon_{33'\_3} \\ \Delta\varepsilon_{11'\_1} & \Delta\varepsilon_{11'\_2} & \Delta\varepsilon_{11'\_3} \\ \Delta\varepsilon_{22'\_1} & \Delta\varepsilon_{22'\_2} & \Delta\varepsilon_{22'\_3} \end{bmatrix}^{-1} \quad \textbf{5-7}$$

In which the extra index 1,2,3 is used to group the strain components by their independent loading condition. For each loading condition, 3 equations can be defined which determine the percentage of strain that is transferred at the core of the fibre:

$$\begin{aligned} \Delta\varepsilon_{33'\_i} &= x_{3'i}\%\Delta\varepsilon_{xx\_i} \\ \Delta\varepsilon_{11'\_i} &= x_{1'i}\%\Delta\varepsilon_{yy\_i} \\ \Delta\varepsilon_{22'\_i} &= x_{2'i}\%\Delta\varepsilon_{zz\_i} \end{aligned} \quad \textbf{5-8}$$

i = 1, 2, 3 represent the type of loading (compression on top, tension on the side or longitudinal tension of the composite sample). By substituting the 9 equations of Equation 5-8 into Equation 5-7, the *TC*-matrix can be determined.

The optimization procedure will be executed for two composite laminates with different lay-ups: a unidirectional laminate $[0]_n$ or $[90]_n$, and a cross-ply laminate $[0_x,90_x]_{ns}$. But first, the sensor's response to compressive and tensile loads is investigated.

5. 4. 1. Transverse tension vs. transverse compression

An ideal sensor should show the same absolute response when the structure is loaded in tension or in compression. When this is the case, a general definition of the optimized *TC*-matrix can be given.

The wavelength shifts of the embedded sensor are compared for a sample which is loaded in transverse tension and in transverse compression. In both experiments, the absolute values of the imposed strain components are equal.

$$\begin{aligned} \left|\Delta\varepsilon_{xx\_tension}(>0)\right| &= \left|\Delta\varepsilon_{xx\_compression}(<0)\right| \\ \left|\Delta\varepsilon_{yy\_tension}(<0)\right| &= \left|\Delta\varepsilon_{yy\_compression}(>0)\right| \\ \left|\Delta\varepsilon_{zz\_tension}(<0)\right| &= \left|\Delta\varepsilon_{zz\_compression}(>0)\right| \end{aligned} \quad \textbf{5-9}$$

The results for a sample with a lay-up of $[0°]_{48}$ subjected to tensile and compressive loading are visualized in Figure 5-24.

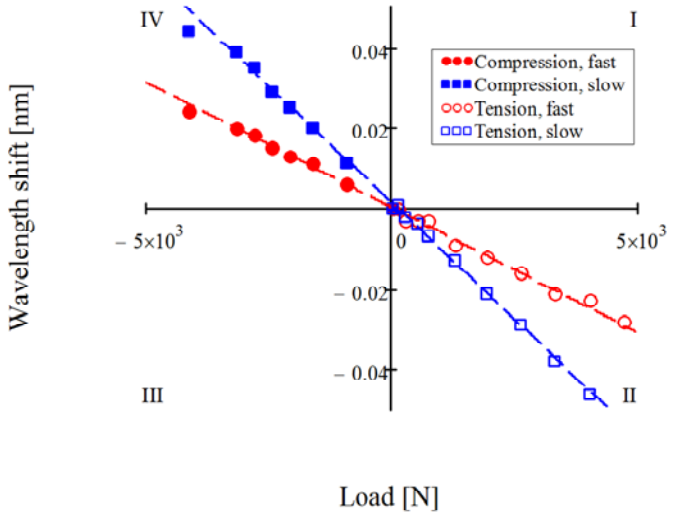

Figure 5-24: Data of a transverse tension experiment (II) and a transverse compression experiment (IV) for a sample with a lay-up of $[0°]_{48}$.

A positive wavelength shift can be noticed for the compression experiment and a negative wavelength shift for the transverse tension experiment. The results of the compressive experiment are presented in the fourth quadrant of Figure 5-24, the results of the tension experiment are presented in the second quadrant. The slope of the wavelength shifts of both polarization modes (fast, slow) versus the load is identical in both experiments.

In Figure 5-25, similar results can be found for a sample with a lay-up of $[0_4,90°_4]_{3s}$.

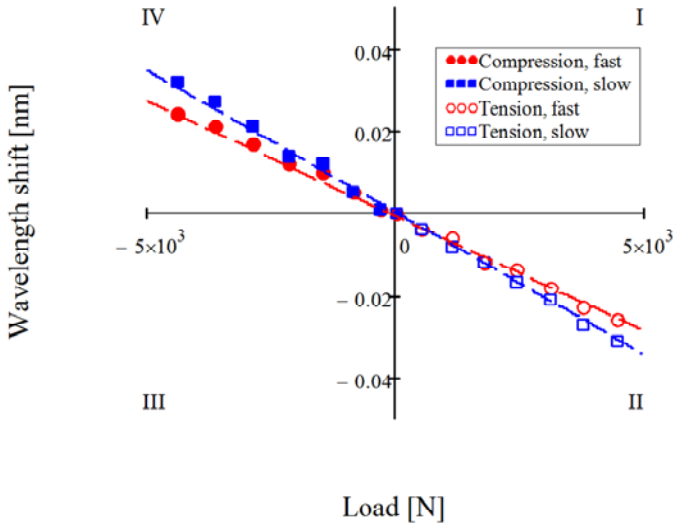

Figure 5-25: Data of a transverse tension experiment (II) and a transverse compression experiment (IV) for a sample with a lay-up of $[0°_4,90°_4]_{3s}$.

5. 4. 2. *TC*-matrix optimization procedure

In the following paragraphs, the optimization procedure will be discussed thoroughly for unidirectional and cross-ply laminates.

In Section 4. 5. 2. c. it was theoretically proven that only small differences exist in the *TC*-matrix for a $[0]_{16}$, a $[0]_{24}$, and a $[0]_{48}$ lay-up. Therefore, no distinction was made for the optimization of the transfer coefficient matrix of a bow-tie optical fibre sensor embedded in a uni-directional laminate. The slow axis (1'-axis) was chosen parallel to the surface of the laminate. This is different for the cross-ply laminates, where the orientation of the fibre's fast axis (2'-axis) was chosen parallel with the surface of the laminate (transverse in-plane direction) (Figure 5-26). For the cross-ply laminates, it should be noted that only a few samples had a (reasonably) good fibre orientation. This limits the accuracy of the optimization procedure, but it has been evaluated to demonstrate the differences to a uni-directional laminate.

It is obvious that the measurement errors will drop significantly when only one lay-up (lay-up of the structure which should be monitored) is considered during the optimization process.

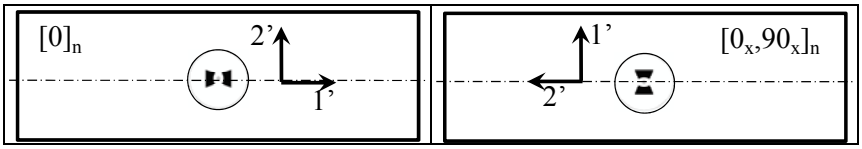

Figure 5-26: The desired orientation of the embedded bow-tie optical fibre embedded in a uni-directional laminate (left) and a cross-ply laminate.

5. 4. 2. a. Transversally applied load – out-of-plane

In the first experiment, the load is put on top of the surface of the specimens, to create a transversally applied load. The fibre is embedded parallel to the reinforcement fibres, in the x-direction (Figure 5-27).

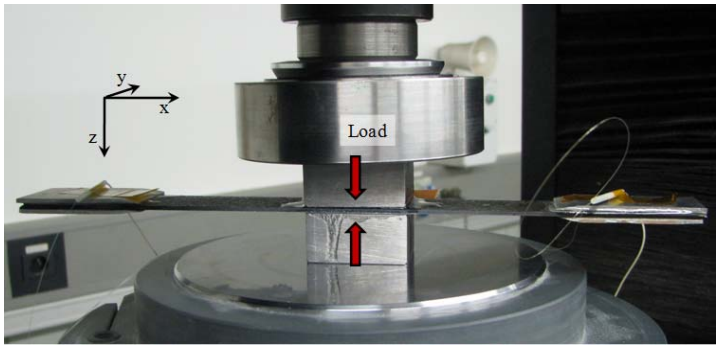

Figure 5-27: The test set-up used to transversally apply load on top of the test specimen (out-of-plane).

Unidirectional laminates

In Figure 5-28, the results of the transverse compression test on a **$[0]_{48}$-specimen** are depicted. The strain field at the core of the optical fibre and the strain components in the composite laminate are plotted against the applied compressive load. The increment of the measured strain components can be compared to the increment of the simulated strains as function of the applied compressive stress. The resulting ratios ($\Delta\varepsilon(\text{MAxS}) / \Delta\varepsilon(\text{Laminate})$) are given in Table 5-5. It should be mentioned that during this test, the longitudinal strain component is low and does not even exceed 1 με, which is smaller than the theoretical longitudinal strain sensitivity of the MAxS-sensor. Due to these small strains, the ratio of the longitudinal sensor and laminate strains could not be obtained but was considered 100%, as was observed in the finite element simulation executed during the parametric study in Section 4. 5. 2. c. Only small differences were observed for the ratios of both $[0]_{48}$-samples.

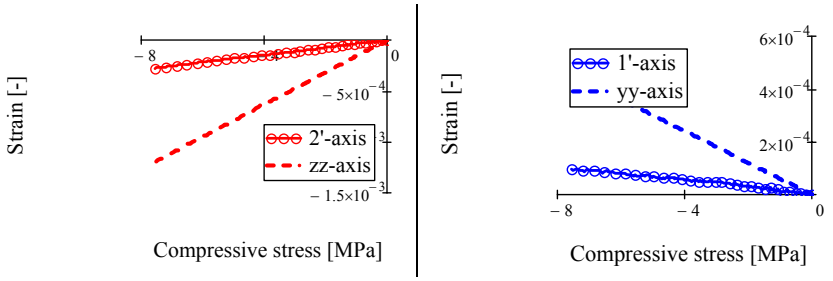

Figure 5-28: Transverse sensor and composite strain increments for a $[0]_{48}$-laminate during a compression test.

The same experiment was repeated for a thin sample **$[0_{16}]$.** The resulting ratios are also given in Table 5-5. More strain is transferred onto the first thin sample as compared to the thick samples. Less strain transfer is observed for the second thin sample. Here it should be mentioned that the orientation of the sample is unknown due to breakage of the sample during testing. Therefore, these results will not be considered in determining the mean in Table 5-5.

Table 5-5: Comparison of the strain field at the core of the optical fibre and the strain field of a $[0]_{48}$ and a $[0]_{16}$-laminate (in%)

	$[0]_{48}$		$[0]_{16}$		
	S 1	S 2	S 1	S 2	MEAN
$\frac{\Delta\varepsilon_{33'}(MAxS)}{\Delta\varepsilon_{yy}(Lam.)}$	100	100	100	(100)	100
$\frac{\Delta\varepsilon_{11'}(MAxS)}{\Delta\varepsilon_{xx}(Lam.)}$	22	24	27	(25)	24.5
$\frac{\Delta\varepsilon_{22'}(MAxS)}{\Delta\varepsilon_{zz}(Lam.)}$	23	25	27	(19)	25

The same comparison can be made for a sample with a $[90]_{24}$-lay-up. The results are depicted separately since the longitudinal strain component (x-axis of the laminate) here, is the in-plane transverse strain component (1'-axis of the optical fibre). However, similar results as for the $[0]_n$ samples should be observed. The results in Table 5-6 show slightly smaller ratios than for the $[0]_n$-samples. This is attributed to a worse orientation of the sensor (Table 5-4).

Table 5-6: Comparison of the strain field at the core of the optical fibre and the strain field of a $[90]_{24}$-laminate (in%)

	$[90]_{24}$		
	Sample 1	Sample 2	MEAN
$\frac{\Delta\varepsilon_{33'}(MAxS)}{\Delta\varepsilon_{yy'}(Lam.)}$	100	100	100
$\frac{\Delta\varepsilon_{11'}(MAxS)}{\Delta\varepsilon_{xx'}(Lam.)}$	19	19	19
$\frac{\Delta\varepsilon_{22'}(MAxS)}{\Delta\varepsilon_{zz'}(Lam.)}$	22	19	20.5

Cross-ply laminates

The same procedure as above can be used to determine the ratios of the strain field at the core of the optical fibre and the strain field in a cross-ply laminate (in this case a $[0_2,90_2]_{2s}$ laminate). In Figure 5-29, the resulting strains are plotted against the applied compressive load. The resulting ratios are given in Table 5-7.

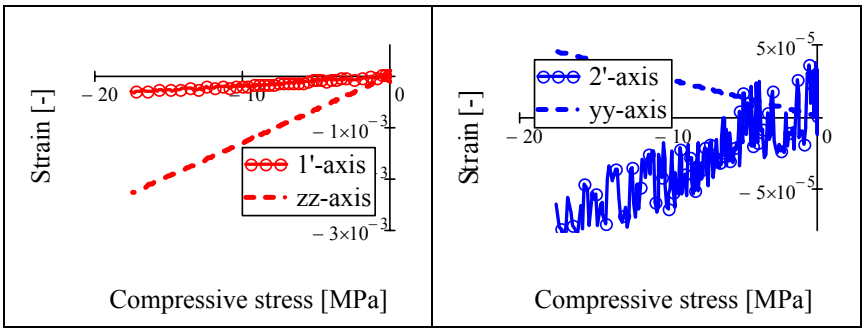

Figure 5-29: Results of the compression tests for the samples $[0_2,90_2]_{2s}$.

The strain along the 1'-direction of the optical fibre is 15% of the strain in the through-the-thickness direction (z-axis) of the laminate. This ratio is driven by the difference in stiffness of both materials (70 GPa for the optical fibre and only 6.3 GPa in the 2'-direction of a prepreg layer). The strain along the 2' direction is only a fraction of the strain along the 1' direction and is near to the resolution of the MAxS-sensor (the leaps in the strain curve). It is also opposite to the strain along the in-plane transverse direction of the laminate (y-direction). This phenomenon was also observed during the finite element simulations of a cross-ply laminate loaded in compression (parametric study of Section 4. 5. 2. c).

Table 5-7: Comparison of the strain field at the core of the optical fibre and the strain field of a $[90_2,0_2]_{ns}$-laminate (in%)

	$[90_2,0_2]_{ns}$	
	Sample 1	Sample 3
$\frac{\Delta\varepsilon_{33'}(MAxS)}{\Delta\varepsilon_{xx}(Lam.)}$	-	100
$\frac{\Delta\varepsilon_{11'}(MAxS)}{\Delta\varepsilon_{zz}(Lam.)}$	-	15
$\frac{\Delta\varepsilon_{22'}(MAxS)}{\Delta\varepsilon_{yy}(Lam.)}$	-	-150

5. 4. 2. b. Transversally applied load – in-plane

In a second test, the load direction is chosen perpendicular to the embedding direction of the fibre (Figure 5-30). The fibre is thus transversally loaded in the plane of the laminate (y-direction) by applying a standard tensile test.

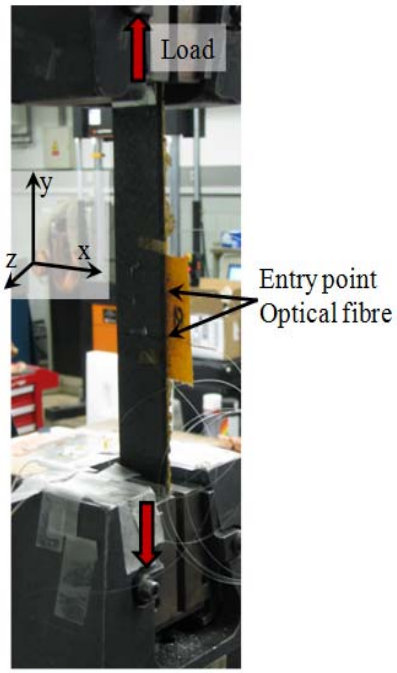

Figure 5-30: The test set-up used to transversally apply load to a MAxS-sensor and in the plane of the test specimen.

Uni-directional laminates

For the uni-directional laminates, this can only be achieved by testing a $[90]_n$-sample. Figure 5-31 shows the results of the tensile test. The strain field at the core of the optical fibre and the strain components in the composite laminate are plotted against the applied tensile load. Again, the increment of the measured strain components can be compared to the increment of the simulated strains as function of the applied tensile stress. The resulting ratios are given in Table 5-8. Only small differences can be observed between both samples.

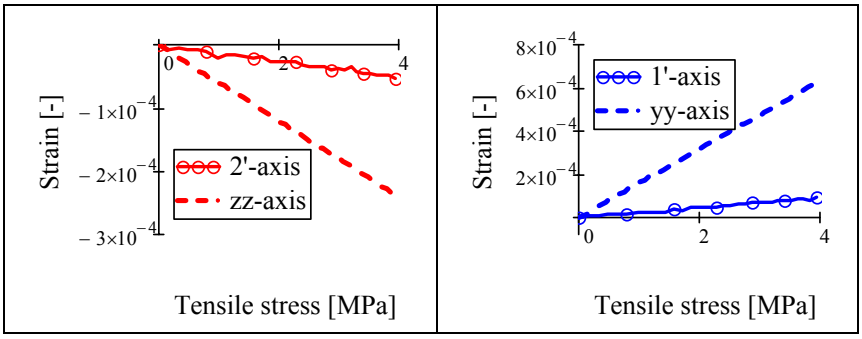

Figure 5-31: Results of the tensile tests for the samples $[0]_{24}$.

Table 5-8: Comparison of the strain field at the core of the optical fibre and the strain field of a $[90]_{24}$-laminate (in%)

	$[90]_{24}$		
	S 1	S 2	MEAN
$\frac{\Delta\varepsilon_{33'}(MAxS)}{\Delta\varepsilon_{xx}(Lam.)}$	100	100	100
$\frac{\Delta\varepsilon_{11'}(MAxS)}{\Delta\varepsilon_{zz}(Lam.)}$	19	18	18.5
$\frac{\Delta\varepsilon_{22'}(MAxS)}{\Delta\varepsilon_{yy}(Lam.)}$	14	15	14.5

Cross-ply laminates

For the cross-ply laminates, in-plane transverse loading is achieved by embedding the optical fibre sensor in a 90 deg ply and thus perpendicular to the load direction. The cross-ply is changed into a $[0_2,90_2]_{ns}$ laminate with, at the centre, an embedded sensor. Figure 5-32 shows the results of the tensile test. The strain field at the core of the optical fibre and the strain components in the composite laminate are plotted against the applied tensile load. The resulting ratios are given in Table 5-9.

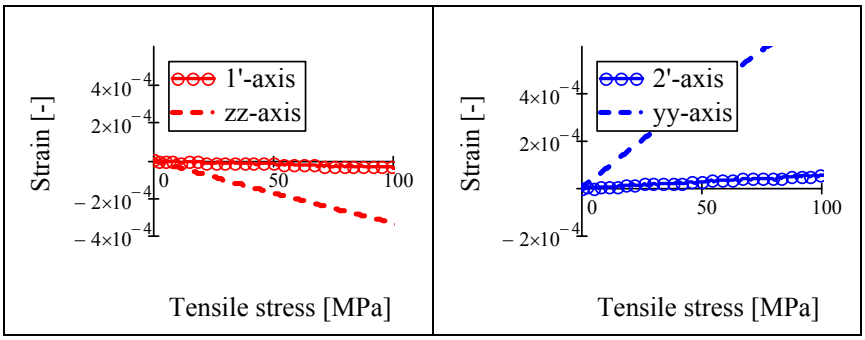

Figure 5-32: Results of the tensile tests for the $[0_2,90_2]_{2s}$ specimen

Table 5-9: Comparison of the strain field at the core of the optical fibre and the strain field of a $[0_2,90_2]_{ns}$-laminate (in%)

	$[0_2,90_2]_{ns}$	
	S 1	S 3
$\frac{\Delta\varepsilon_{33'}(MAxS)}{\Delta\varepsilon_{xx}(Lam.)}$	-	100
$\frac{\Delta\varepsilon_{11'}(MAxS)}{\Delta\varepsilon_{zz}(Lam.)}$	-	11
$\frac{\Delta\varepsilon_{22'}(MAxS)}{\Delta\varepsilon_{yy}(Lam.)}$	-	8

5. 4. 2. c. Longitudinal load – in-plane

In the third test, the load direction is chosen parallel to the embedding direction of the fibre. The fibre sensor is thus longitudinally loaded in the plane of the laminate. This can be achieved by applying a standard tensile test.

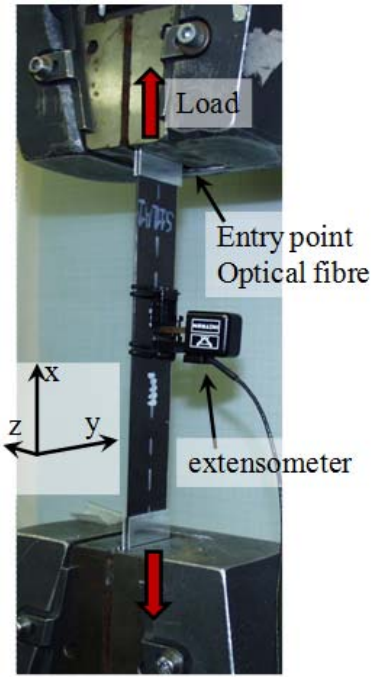

Figure 5-33: The test set-up used to longitudinally apply load along the x-direction of the test specimen (in-plane).

The strain field at the core of the optical fibre and the strain components in the composite laminate are plotted against the applied load. Once more, the increment of the measured strain components can be compared to the increment of the simulated strains as function of the applied load. Figure 5-34 shows the results of the tensile test for a $[0]_n$-specimen. The resulting ratios for all $[0]_n$-specimens are given in Table 5-10. Only small differences can be observed for the different samples.

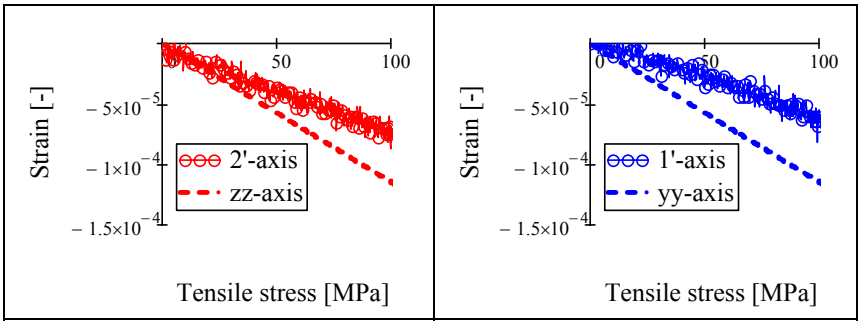

Figure 5-34: Results of the tensile tests for the samples $[0]_{16}$.

Table 5-10: Comparison of the strain field at the core of the optical fibre and the strain field of a $[0]_{48}$ and a $[0]_{16}$-laminate (ratios in%)

	$[0]_{48}$		$[0]_{16}$	S4A2		
	S 1	S 2	S 1	S 2	S 3	MEAN
$\frac{\Delta\varepsilon_{33'}(MAxS)}{\Delta\varepsilon_{xx}(Lam.)}$	100	-	100	-	100	100
$\frac{\Delta\varepsilon_{11'}(MAxS)}{\Delta\varepsilon_{yy}(Lam.)}$	44	-	55	-	50	49.7
$\frac{\Delta\varepsilon_{22'}(MAxS)}{\Delta\varepsilon_{zz}(Lam.)}$	63	-	65	-	63	63.7

Cross-ply laminates

Figure 5-35 shows the results of the tensile test for a $[90_2,0_2]_{2s}$-specimen. The resulting ratios of all specimens are given in Table 5-11. In the case of cross-ply laminates, no direct relation can be observed between the strain in the laminate and the strain at the optical fibre core. Strain in the direction of the sensor only gives rise to a small in-plane transverse strain of the laminate, since the stiffness of the optical fibre is much higher than the transverse stiffness of the prepreg layer. Therefore, the transfer ratio $\frac{\Delta\varepsilon_{22'}(MAxS)}{\Delta\varepsilon_{yy}(Lam.)}$ becomes very high, around 1000%. The non-linearity of the results for the strain along the 2'-axis becomes invisible when divided by one thousand, and matches the reference strain. For the $\frac{\Delta\varepsilon_{11'}(MAxS)}{\Delta\varepsilon_{zz}(Lam.)}$ ratio big variation is observed, which is due to the different sensor orientation in both specimens. Since the transfer of the transverse components are substantially different and therefore not in the same order of magnitude (~1000% vs. ~25%), the orientation of the optical fibre will be a sensitive parameter.

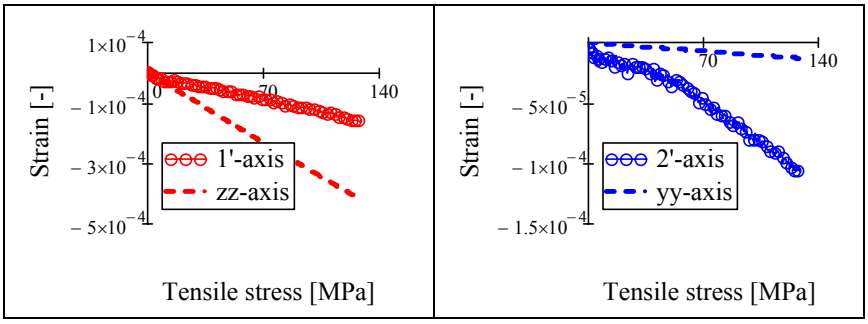

Figure 5-35: Results of the tensile tests for the samples S5A2 $[90_2,0_2]_{2s}$.

Table 5-11: Comparison of the strain field at the core of the optical fibre and the strain field of a $[90_2,0_2]_{2s}$ (in%),

	S 1	S 2	MEAN
$\frac{\Delta\varepsilon_{33'}(MAxS)}{\Delta\varepsilon_{xx}(Lam.)}$	100	100-	100
$\frac{\Delta\varepsilon_{11'}(MAxS)}{\Delta\varepsilon_{zz}(Lam.)}$	900	950	925
$\frac{\Delta\varepsilon_{22'}(MAxS)}{\Delta\varepsilon_{yy}(Lam.)}$	15	35	25

5. 4. 2. d. Optimized *TC*-matrix

Uni-directional laminates

The optimized *TC*-matrix can be calculated out of the above defined ratios for the three independent loading conditions of the uni-directional laminates,.

$$\begin{bmatrix}\Delta\varepsilon_{xx}\\ \Delta\varepsilon_{yy}\\ \Delta\varepsilon_{zz}\end{bmatrix}=\begin{bmatrix}1 & 0 & 0\\ 1.25 & 7.97 & 1.42\\ 0.34 & -0.65 & 3.77\end{bmatrix}\begin{bmatrix}\Delta\varepsilon_{33'}\\ \Delta\varepsilon_{11'}\\ \Delta\varepsilon_{22'}\end{bmatrix} \qquad \textbf{5-10}$$

The main difference compared to the theoretically determined *TC*-matrix, is the higher strain transfer (~1.8 times higher) for the strain component in the through-the-thickness direction of the laminate. The matrix is not symmetric and the effect of one transverse strain component on the other transverse component is opposite in sign.

Cross-ply laminates

The same procedure is applied with the results of the cross-ply laminates, to calculate the optimized *TC*-matrix.

$$\begin{bmatrix}\Delta\varepsilon_{xx}\\ \Delta\varepsilon_{yy}\\ \Delta\varepsilon_{zz}\end{bmatrix}=\begin{bmatrix}1 & 0 & 0\\ 1.09 & 10.35 & -2.00\\ -0.11 & -1.05 & 6.86\end{bmatrix}\begin{bmatrix}\Delta\varepsilon_{33'}\\ \Delta\varepsilon_{22'}\\ \Delta\varepsilon_{11'}\end{bmatrix} \qquad \textbf{5-11}$$

The main difference compared to the theoretically determined *TC*-matrix is the high value of TC_{22} which is almost 30% higher. This high value points to a very low strain transfer in the in-plane transverse direction of the laminate. Coefficient TC_{23} is doubled, which translates itself to a high influence of the opposite transverse strain component. The axial strain influence (TC_{31}) on the out-of-plane transverse strain component is very small. It should be noted that the optimization procedure to find the *TC*-matrix for a cross-ply laminate has been done on a small amount of

specimens. In the previous paragraphs, it was proven that the fibre orientation matters a lot; small differences already lead to high variations of the strain ratio.

5. 4. 2. e. Validation of the *TC*-matrix

In this paragraph, a few examples are given in which the optimized *TC*-matrix is used to relate the strain field at the optical fibre core to the one of the composite laminate. In the graphs, measured strains (MAxS-sensor) and reference strains (extensometer, FE-simulations) are compared.

Uni-directional laminates

The first sample has a uni-directional lay-up of $[0]_{48}$ in between the 40th and 41st layer (Figure 5-36). The sample was subjected to a transverse compression test and a tension experiment with the load parallel to the x-axis (respectively in Figure 5-37 and Figure 5-38).

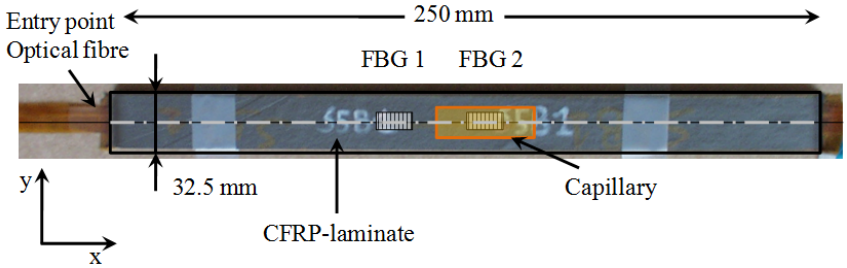

Figure 5-36: Uni-directional CFRP-specimen $[0]_{48}$ with a MAxS-sensor embedded in between the 40th and 41st CFRP-prepreg layer.

Figure 5-37 shows the transverse strain components measured by the MAxS-sensor (full line with symbol) and compares them with the reference strains (dashed lines) calculated using a FE-simulation. Up to 500με, both transverse strain components follow their proper reference strain component. At that point a kink can be noticed for both strain components. The resolving power of the sensor can be observed as the small leaps between the data points in the slopes; for the in-plane transverse strain (y-axis) this is maximally ~70 με, and for the out-of-plane transverse strain (z-axis) this is maximally ~15με.

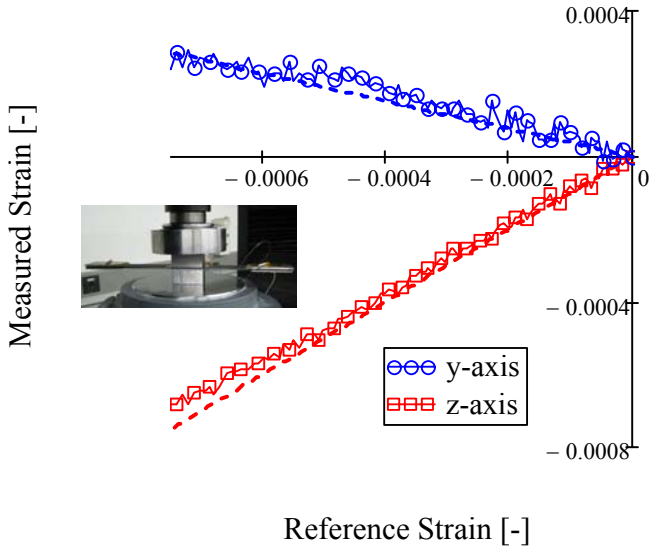

Figure 5-37: Strain measured with the MAxS-sensor embedded in a uni-directional $[0]_{48}$ CFRP-specimen during a transverse compression test

Afterwards, the sample was loaded in a tension experiment. Figure 5-38 shows the strain components measured by the MAxS-sensor (full line with symbol) and compares them with the reference strains (dashed lines) measured with an extensometer (x-axis) and calculated using the Poisson's coefficient of the laminate (y-axis and z-axis). The applied strain is lower than for the compression experiment, because for this experiment the stiffness in the load direction is ~50 times higher. A kink can clearly be observed for the measured axial strain component; it is also present in the graphs of the measured transverse strain components. In general, the slope of the measured strains are conform to the slope of the reference strains.
Again the resolving power of the sensor can be observed as the leaps between the data points in the slopes; for both transverse strain components this is maximally ~25 με.

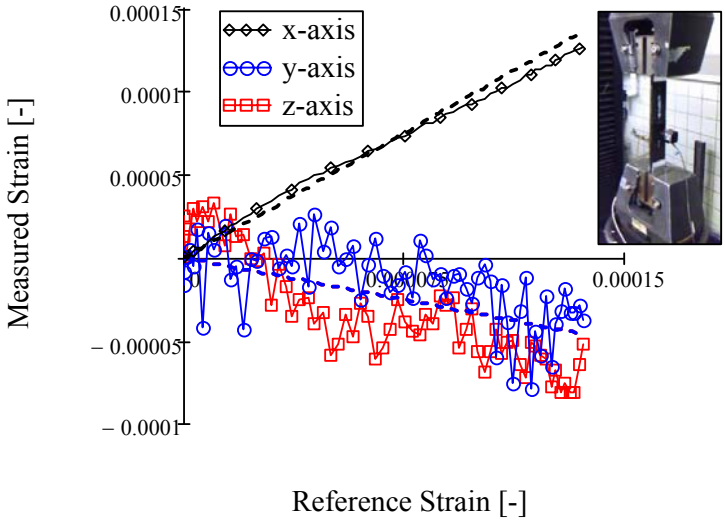

Figure 5-38: Strain measured with the MAxS-sensor embedded in a uni-directional $[0]_{48}$ CFRP specimen during a tension test

The second sample has a **$[90]_{24}$** lay-up with a MAxS-sensor embedded in between the 20th and 21st layer (Figure 5-39). Like the $[0]_n$ sample, this sample was also subjected to a transverse compression test and a tension experiment with the load parallel to the x-axis. For both experiments, very small strains were measured in the direction of the reinforcement fibres (y-axis) and are therefore not included in the graphs. Since the sensor is embedded parallel with the reinforcement fibres and thus perpendicular to the x-axis (Figure 5-39), the strain according to the x-axis is considered as a transverse strain component to the MAxS-sensor.

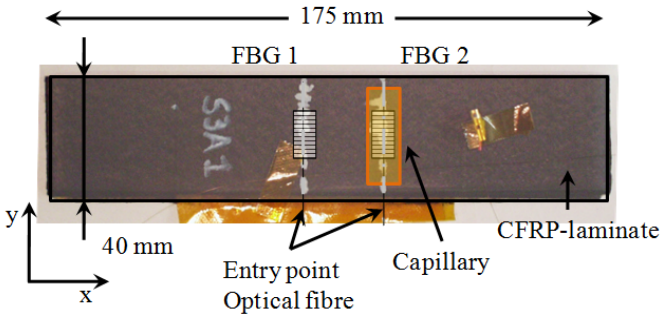

Figure 5-39: Uni-directional CFRP-specimen $[90]_{24}$ with a MAxS-sensor embedded in between the 20th and 21st layers.

First, the $[90]_{24}$ sample is loaded in compression. Figure 5-40 shows the transverse strain components measured by the MAxS-sensor (full line with symbol) and compares them with the reference strains (dashed lines) calculated using an FE-simulation. Both curves are quite linear. The slope of the measured (MAxS-sensor) strain component along the x-axis (black circle) is quite similar to that of the reference strain. However, the measured strain component along the z-axis is an underestimation of the reference strain calculated by FE-simulations. Once more, the resolving power of the sensor can be observed as the small leaps between the data points in the slopes; for the in-plane transverse strain (x-axis) this is maximally ~70 με, and for the out-of-plane transverse strain this is maximally ~50 με.

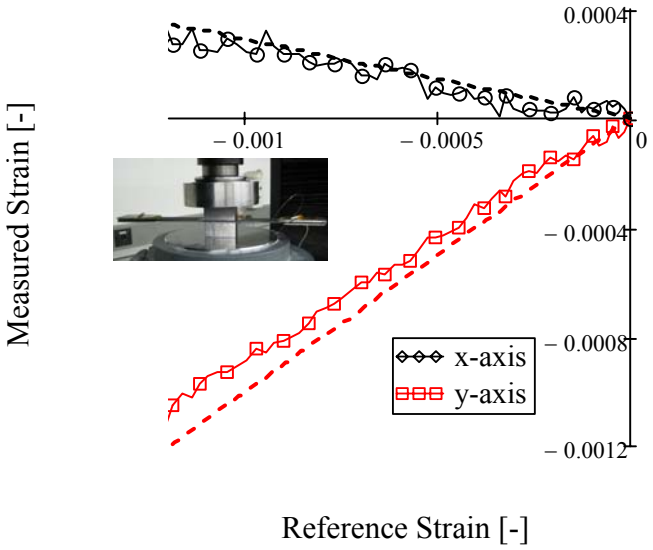

Figure 5-40: Strain measured with the MAxS-sensor embedded in a uni-directional $[90]_{24}$ CFRP specimen during a compression test.

Afterwards, the $[90]_{24}$-sample was loaded in a tension experiment. Figure 5-41 shows the transverse strain components measured by the MAxS-sensor (full line with symbol) and compares them with the reference strains (dashed lines) measured with an extensometer (x-axis) and calculated using the Poisson's coefficient of the laminate (z-axis). At the start, the measured in-plane transverse strain component measured by the MAxS-sensor is quite similar to the reference strain measured by the extensometer. Towards the end of the test, though, more differences can be noticed. From the start till the end, the out-of-plane transverse strain component matches well with the reference strain which is calculated by multiplying the Poisson's coefficient with the data of the extensometer.

The resolving power of the sensor for the in-plane transverse strain component is maximally ~80 με and for the out-of-plane transverse strain component this is maximally ~50 με.

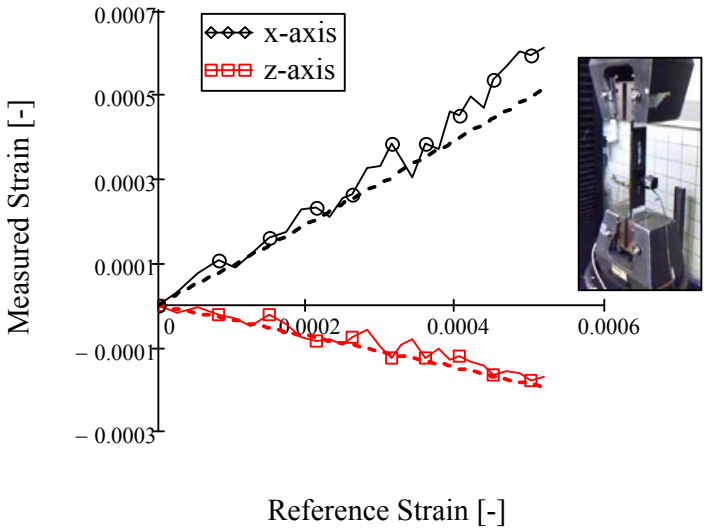

Figure 5-41: Strain measured with the MAxS-sensor embedded in a uni-directional $[90]_{24}$ CFRP specimen during a tension test

Cross-ply laminates

The **first cross-ply sample** has a lay-up of **$[0_2,90_2]_{2s}$;** the MAxS-sensor has been embedded in between the 8th and 9th layer (Figure 5-36). Since the FBG in the capillary only measures axial strain, it was replaced by a uni-axial draw tower grating (DTG). The sample was loaded in a tension experiment parallel with the x-axis and a transverse compression test (respectively in Figure 5-44 and Figure 5-43).

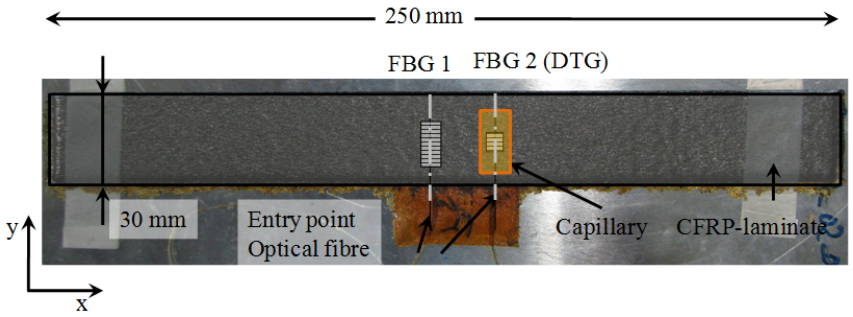

Figure 5-42: Cross-ply CFRP specimen $[0_2,90_2]_{2s}$ with a MAxS-sensor embedded in between the 8th and 9th layers.

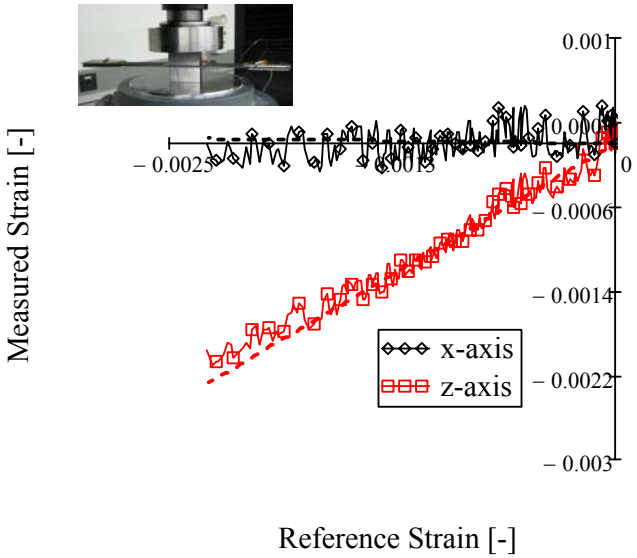

Figure 5-43: Strain measured with the MAxS-sensor embedded in a $[0_2,90_2]_{2s}$ CFRP specimen during a compression test.

In Figure 5-43, the measured transverse strain components (MAxS-sensor, full line with symbol) are depicted and compared to the reference strains (dashed lines) for the transverse compression test. Both measured components show equal increments with their respective reference measurement. At the far end (at 0.2% strain along the z-axis), a small shift from the reference strain arises for both strain components. This could be caused by the initiation of damage in the material.

Afterwards the sample was loaded in a standard tensile test of which the results are shown in Figure 5-44. It should be noted that the direction along which the sample is

tensioned (x-axis), is the in-plane transverse direction of the optical fibre sensor (2'-axis). Therefore, the strain transfer is not 100% and the measured curve can, as such, differ from the reference strain (in this case ~15%).

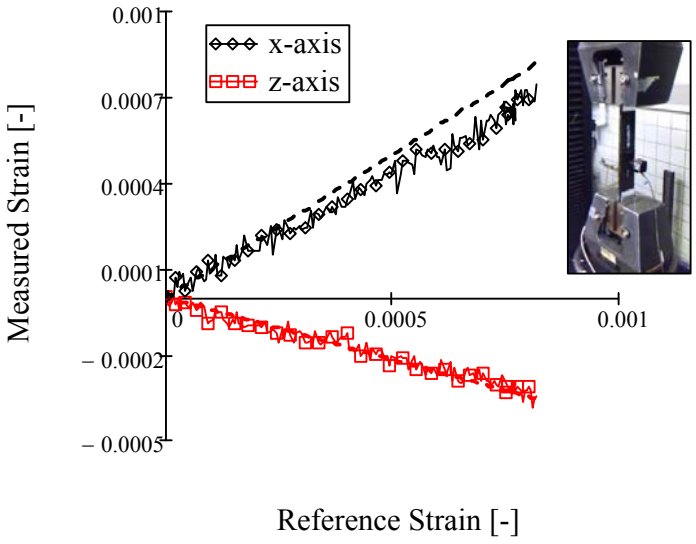

Figure 5-44: Strain measured with the MAxS-sensor embedded in a $[0_2,90_2]_{2s}$ CFRP-specimen during a tension test.

The **second sample** has a lay-up of **$[90_2,0_2]_{2s}$;** the MAxS-sensor has been embedded in between the 11th and 12th layer (Figure 5-45). The sample was loaded in a tension experiment parallel with the x-axis (Figure 5-46).

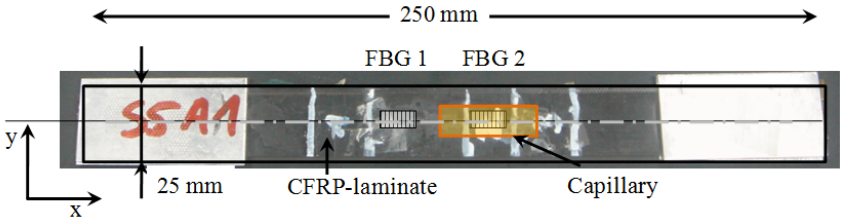

Figure 5-45: Cross-ply CFRP specimen $[90_2,0_2]_{2s}$ with a MAxS-sensor embedded in between the 11th and 12th layers.

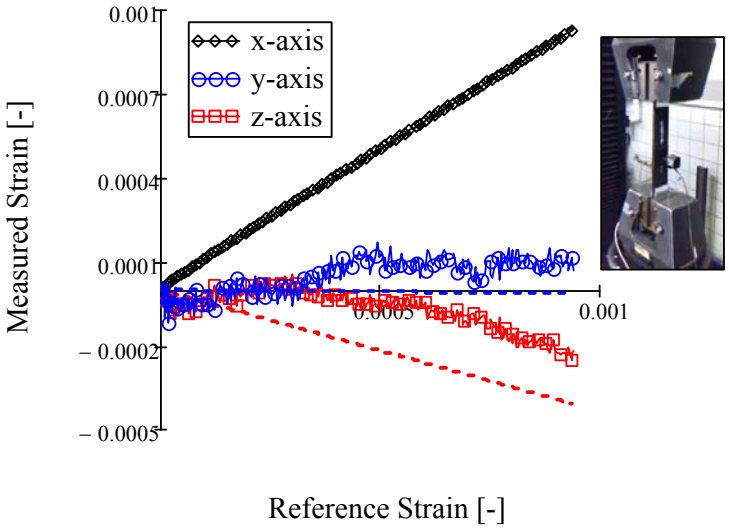

Figure 5-46: Strain measured with the MAxS-sensor embedded in a $[90_2,0_2]_{2s}$ CFRP specimen during a tension test.

Good agreement is found between the measured axial strain increment and its reference. The transverse strain components show high non-linearity at the beginning of the experiment. This non-linearity fades out at 0.035% of longitudinal strain. From this point on the increments match with those of the reference transverse strains. No valid explanation was found for this rather strange start of the experiment.

A third **sample** has a $[\mathbf{90_2,0_2}]_{6s}$ lay-up with the MAxS-sensor embedded in between the 3rd and the 4th layer (Figure 5-47). Unlike the other cross-ply laminate, the slow axis of the bow-tie has been oriented parallel to the surface of the laminate. The validity of the *TC*-matrix optimized for the previous cross-ply laminates (thin and 90 degree different fibre orientation) can be evaluated. The sample was loaded in a tension experiment, parallel to the x-axis.

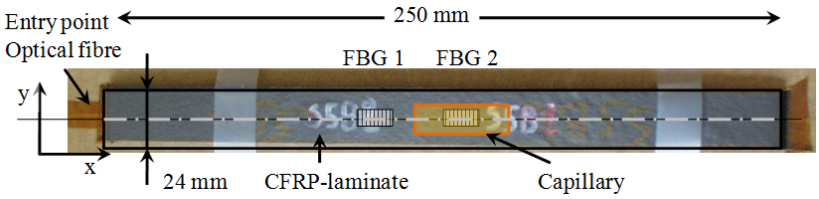

Figure 5-47: Cross-ply CFRP specimen $[0_2,90_2]_{6s}$ with a MAxS-sensor embedded in between the 3rd and 4th layers.

Figure 5-48 shows the measurement results (MAxS-sensor) and compares them with their respective reference strain. A small difference can be seen for the axial strain component. Remark that straining thick samples is not that straightforward; the discrepancy can be caused by inhomogeneous clamping of the sample in the grips. Strain at the left side of the loaded specimen will, as such, differ from that on the right side. Again a non-linear course of the transverse strain curves at the beginning of the experiment was noticed which could not be explained. From ~100 με (longitudinal strain) on, the increment of the measured in-plane transverse strain is equal to that of the reference strain (~0 με/ με). The increment of the measured out-of-plane strain differs 3.5 times from the reference strain. This preliminary experiment already indicates that a better strain transfer in the through-the-thickness direction is to be expected when embedding the slow axis of the bow-tie fibre parallel to the surface of the laminate. More experiments are needed to optimize the *TC*-matrix for such a combination of laminate and embedded MAxS-sensor.

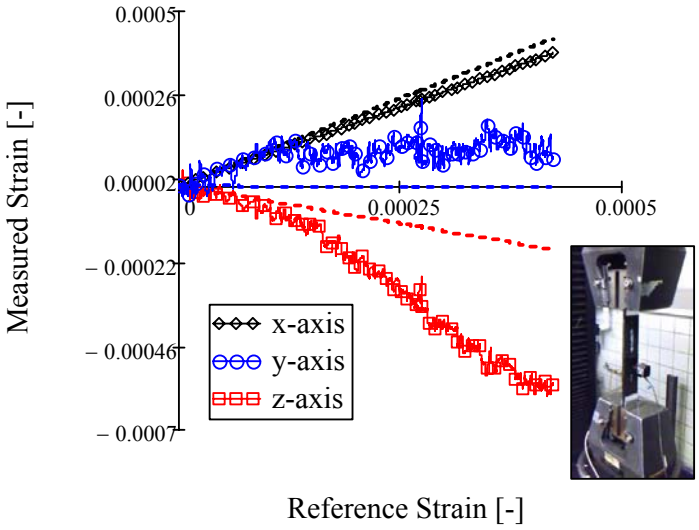

Figure 5-48: Strain measured with the MAxS-sensor embedded in a $[90_2,0_2]_{6s}$ CFRP specimen during a tension test.

5. 5. MAxS-SENSOR SUBJECTED TO A REPRESENTATIVE STRUCTURAL LOADING CONDITION

In the previously described results, the samples were subjected to a 'so-called' controlled load. In this section, a bending test was chosen as a representative for actual loading conditions. An example is the bending of an airplane wing as depicted in Figure 5-49).

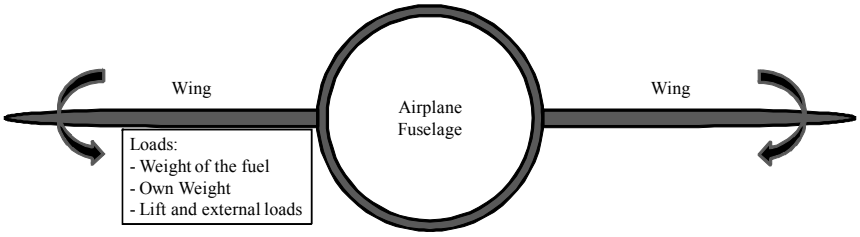

Figure 5-49: Schematic of the actual bending of an airplane wing (and the typical causes).

A four point bending configuration was chosen over a three point bending test, since for the first, a constant bending moment is created between the loading noses (load span). Further in this section, the opportunity to measure in-plane shear and temperature is evaluated. In the following discussions, several limitations and attention points of the MAxS-sensor will be addressed.

5. 5. 1. Four point bending experiment

5. 5. 1. a. Test results

Several samples were manufactured and subjected to a four point bending test. An overview of the samples is shown in Figure 5-50. Of each lay-up, two samples were created and tested. Depending on how the sample is mounted in the test set-up (Figure 5-15), the MAxS-sensor can be put in tension or compression.

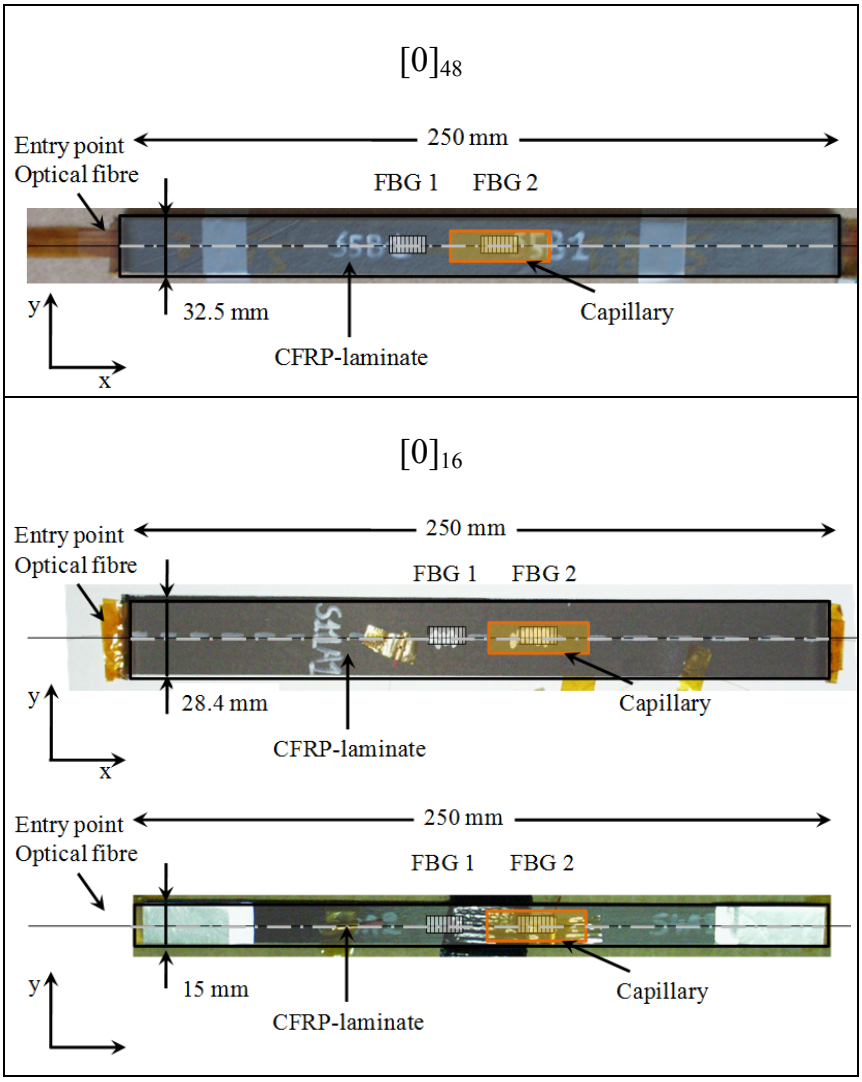

Figure 5-50: Detailed picture of the samples tested in four point bending

In Figure 5-51 and Figure 5-52, the results of the four point bending tests for two $[0]_{48}$ samples are depicted. For the first sample, the measured transverse strain components as function of the reference strain are depicted. The reference strain is measured by a surface mounted reference grating. In the first sample, the measured axial strain component was not available.

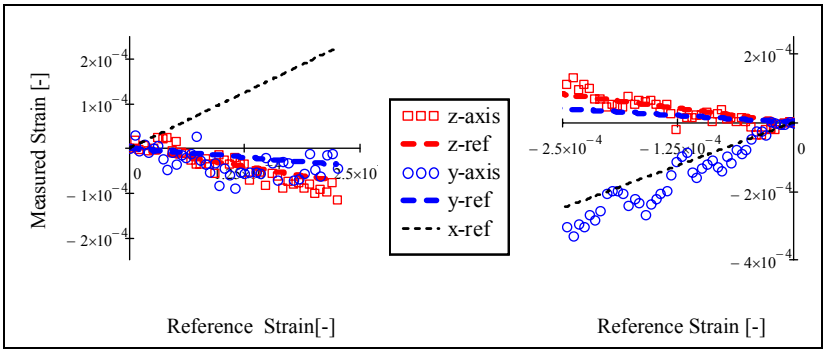

Figure 5-51: Results of the bending tests (sensor in tension at left and in compression at right) for the first $[0]_{48}$ sample

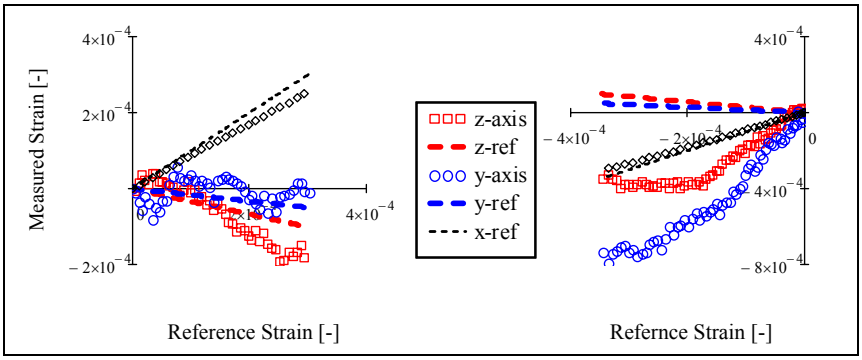

Figure 5-52: Results of the bending tests (sensor in tension at left and in compression at right) for the second $[0]_{48}$ sample

The measured transverse strain components for the first bending test and the sensor in tension, show very good agreement with the reference strain components. When the sensor is loaded in compression, the through-the-thickness strain shows good agreement, but the other component shows an unexpected positive shift. A reason could be the initiation of damage in previous tests (cracking of the fibre/epoxy interface). For the second sample and the sensor in tension, reasonable agreement was found for the transverse strain components as compared to the reference strain components. When the sensor is put in compression, unexpected shifts were noticed for both measured strain components. Notice also the small difference between the measured axial strain and the reference strain measured by the reference grating mounted on the surface. Possible reasons for the unexpected discrepancies are considered in Section 5. 5. 1. b.. The influence of the axial strain on the calculation of the transverse strain components and the influence of compressive stresses in the longitudinal direction are discussed in more detail.

In Figure 5-53 and Figure 5-54, the results of four point bending tests on two $[0]_{16}$ samples are depicted. As shown in Figure 5-50, the second sample has half of the width of the first sample. For both samples, the measured transverse strain components are depicted as function of the reference strain. The reference strain is measured by an external reference grating.

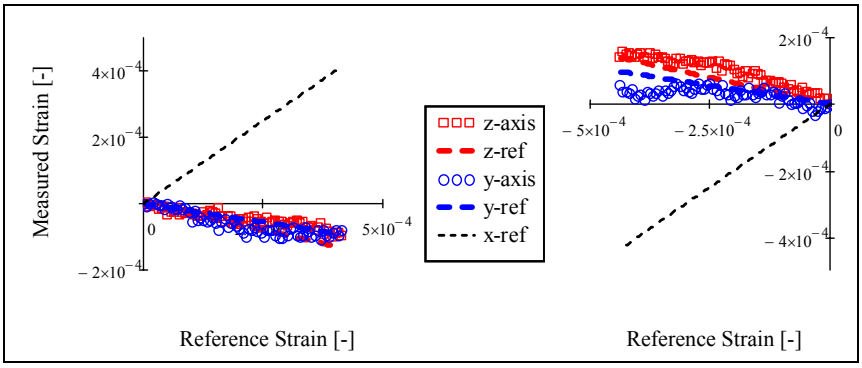

Figure 5-53: Results of the bending tests (sensor in tension on the left and in compression on the right) for the first $[0]_{16}$ sample.

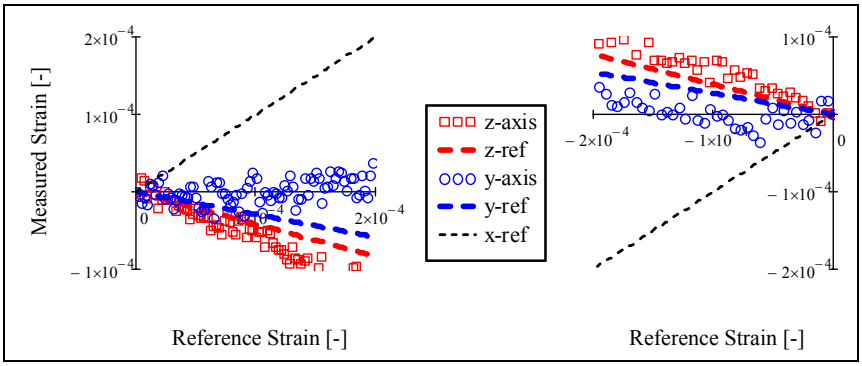

Figure 5-54: Results of the bending tests (sensor in tension on the left and in compression on the right) for the second $[0]_{16}$ sample.

The measured strain and the reference strain are very similar for the first sample when the sensor is loaded in tension. In compression, the in-plane transverse measured strain component follows its reference strain at the beginning of the experiment but starts to differ at approximately 300 με. Reasonable agreement between measured and reference value is found for the out-of-plane transverse strain component. The second sample shows a similar response for the sensor in tension and compression. The increment of the out-of-plane transverse strain component is slightly higher (respectively 25% and 30%) than the increment of its reference. On

the other hand, the increment of the in-plane transverse strain component is almost zero for the sensor loaded in tension and slightly positive when in compression. It should be noted that in this sample, the slow axis is oriented 75 deg with respect to the surface (the slow axis is almost the vertical axis). As was theoretically proven in Section 4. 5. 2. c., the same values of the *TC*-matrix can be used to calculate the strain components. However, the only difference is changing the 2nd and the 3rd row in the matrix. Experimentally this was not proven yet and can as such cause the differences in this set of experiments.

5. 5. 1. b. Pitfalls and solutions

Influence of the axial strain value on the calculation of transverse strains

One should be careful when using the axial strain determined from equation 5-6, to calculate the transverse strain components. If both FBGs of the MAxS-sensor do not have the same embedding depth in the laminate (e.g. because of differences in diameter of the bare fibre and the capillary, see Figure 5-55), this will lead to a different (axial) strain state sensed by both FBGs. It should be noted that the value of the axial strain has a big influence on the transverse strain components. When considering the theoretically determined *TC*-matrix of a $[0]_{48}$ laminate, a measurement error of the axial strain of 10% leads to a transverse strain component which is increased by ~8% of the axial strain value. Since in most loading conditions the axial strain is the highest component, the transverse strain will suffer from high measurement errors.

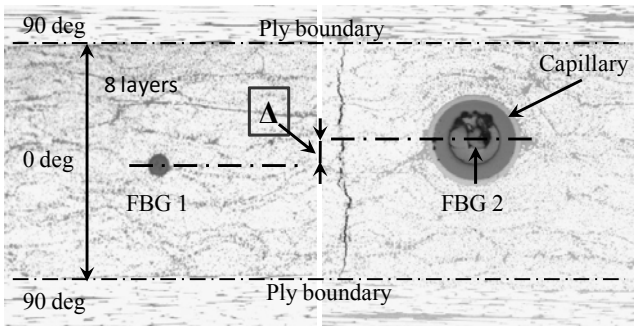

Figure 5-55: Micrographs for determining the difference in embedding depth of both FBGs.

Figure 5-56 repeats the results for the first $[0_{48}]$ sample loaded under four point bending. Two different values for the axial strain (the correct one and a 15% lower value) were used to calculate the transverse strain components. When FBG2 in the capillary measures the same axial strain as FBG 1, the transverse strain components

are in good agreement with the reference transverse strain components. However, when the capillary has an embedding depth which differs 15% from FBG1, the transverse strain components calculated using Equation 5-1 and Equation 5-6 will differ 750%!

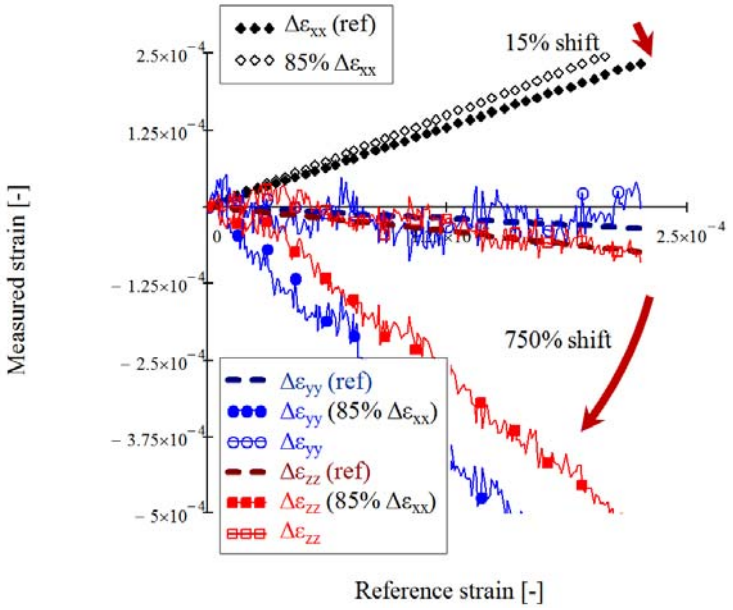

Figure 5-56: Results of the bending test on samples $[0]_{48}$ considering different embedding depths for FBG2 (capillary).

Compressive strains

To measure compressive strains with the MAxS-sensor, the grating in the capillary should have a certain pretension. In Figure 5-57, the Bragg wavelength shifts of a MAxS-sensor loaded in compression during a bending experiment are given. The grating outside the capillary exhibits a linear response, the one inside the capillary does not (the fibre is bent instead of compressed). The measured axial strain will therefore, not be correct and the transverse strain components will show large drifts for high axial strains during bending.

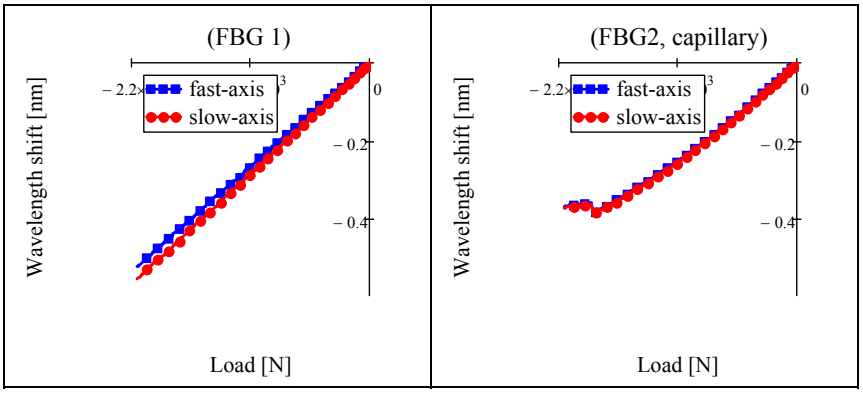

Figure 5-57: The Bragg wavelength shifts of a MAxS-sensor loaded in compression during bending.

5. 5. 2. Shear–tensile experiment

In this dissertation, the emphasis is on measuring the principal strains of a composite structure with embedded optical fibre sensors. A structure with a randomized lay-up in which 0 deg, 90 deg, +45 deg, and -45 deg layers are stacked, will always be subjected to shear strains when it is loaded. Theoretically it was already shown (Section 2. 2. 1.) that shear strains do not cause additional wavelength shifts. Performing a shear tensile test as described in Section 5. 2. 4. should prove the validity of this assumption. Four samples were produced: two $[+45_2,-45_2]_{6s}$ laminates (Figure 5-58) and two $[+45_2,-45_2]_{2s}$ laminates (Figure 5-59). For both lay-ups, the MAxS sensor is oriented along the -45 deg reinforcement layer. As such, the sample needs to be wider (minimum width is 30 mm) then described in the ASTM standard for this test.

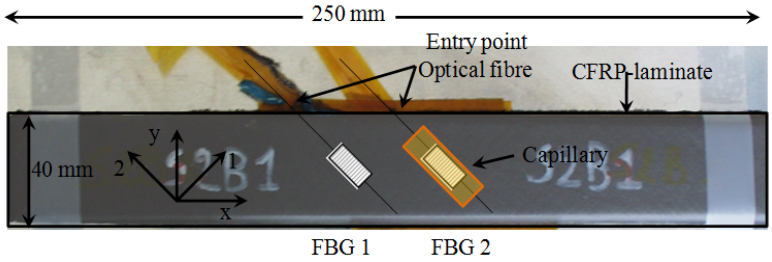

Figure 5-58: $[+45_2,-45_2]_{6s}$ CFRP specimen with a MAxS-sensor embedded in between the 3rd and 4th layer.

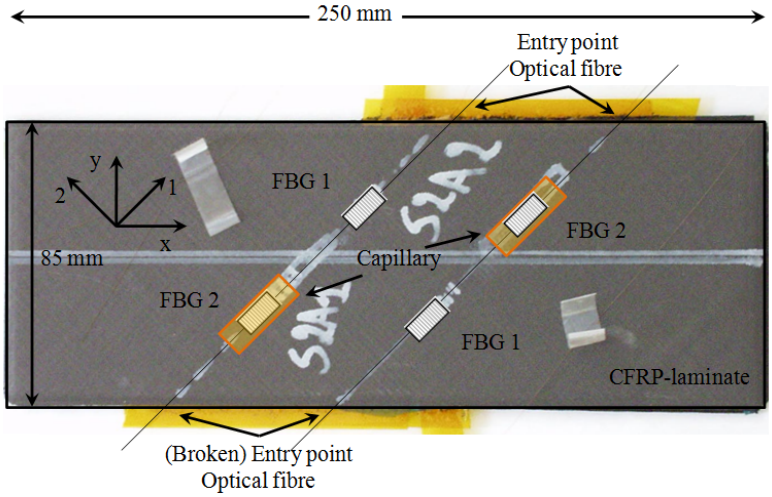

Figure 5-59: Two $[+45_2,-45_2]_{2s}$ CFRP specimens with a MAxS-sensor embedded in between the 11th and 12th layer.

For the case of the $[+45_2,-45_2]_{2s}$ laminates, we were obliged to test both samples at once without separating the samples, due to fibre breakage at the entry point at one side of the sample. Special metal tabs were used to easily mount the wide sample (~80 mm) in the grips of the universal materials testing machine (Figure 5-60, left). The samples were strained up to approximately 0.1% in the x-direction (Figure 5-60, right). In these samples, the optical fibre sensors are not embedded with the correct orientation (with the slow or fast axis parallel to the surface) (Table 5-4). This makes it difficult to relate the measured strain components (MAxS-sensor) with the reference strain (surface mounted reference grating combined with FE-simulations).

The results of the shear tensile test on a $[+45_2,-45_2]_{2s}$ laminate is given in Figure 5-61. Although the sample is strained up to 0.1% in longitudinal direction, the MAxS sensor (embedded along ±45°) measured a maximum strain of approximately 0.006% along the reinforcement fibres. This strain component shows good agreement with the reference strain measured by a surface mounted FBG. On the other hand, the measured in-plane transverse strain component is much higher and the out-of-plane strain component a bit lower than their respective reference strain component. This is caused by the wrong orientation (~50 deg) of the embedded optical fibre. The out-of-plane transverse strain component will, as such, affect both eigenaxes of the fibre, which can be seen in similar increments of the wavelength shift and measured strain values for both polarization modes. Notice that this type of experiment induces a shear strain in the optical fibre that has a

magnitude of ~10 times higher than the out-of-plane strain component and ~20 times higher than the induced axial strain component.

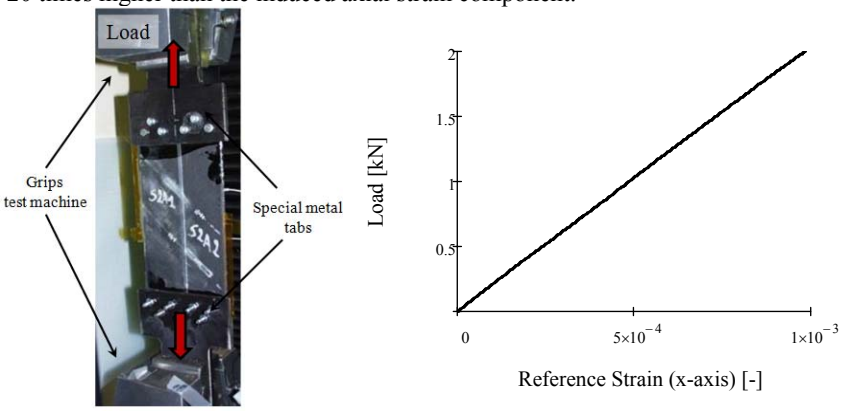

Figure 5-60: Two $[+45_2,-45_2]_{2s}$ CFRP-specimens mounted simultaneously in the grips of the test machine by using special metal tabs (left). The sample is strained up to 0.1% in the x-direction (right).

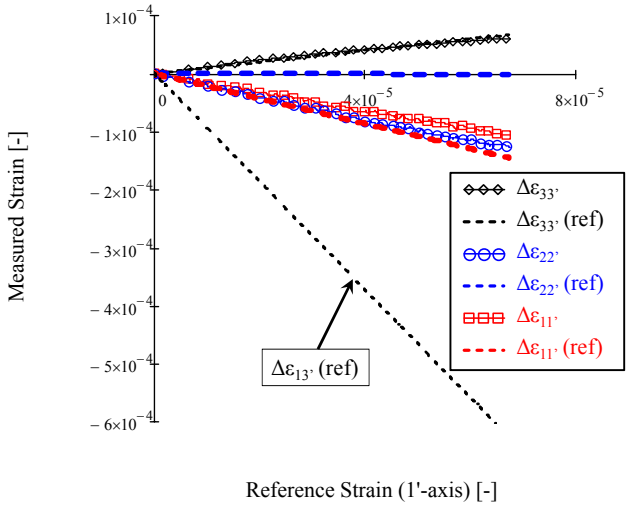

Figure 5-61: Results of the $[+45_2,-45_2]_{2s}$ specimen under a shear tensile load. The measured principal strains and the in-plane shear strain are given as function of the reference strain along the 1'-axis.

The results of the shear tensile test on a $[+45_2,-45_2]_{6s}$ laminate is given in Figure 5-63. Both laminates were tested separately and show similar results. Although the sample is strained up to 0.1% in longitudinal direction, the MAxS

sensor (embedded along +45 deg) measured a maximum strain of approximately 0.002% along the reinforcement fibres.

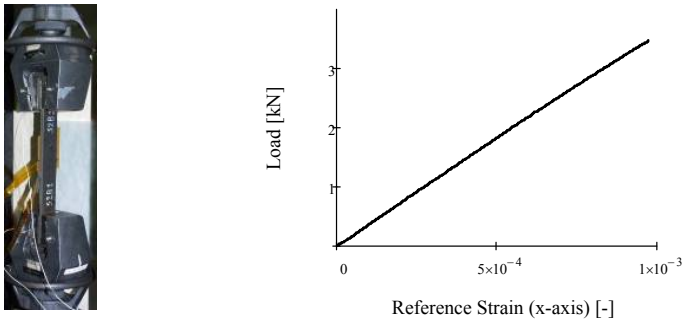

Figure 5-62: A $[+45_2,-45_2]_{6s}$ CFRP specimen mounted in the grips of the testing machine (left). The sample is strained up to 0.1% in the x-direction (right).

The strain measured parallel to the reinforcement fibres shows reasonable agreement with the reference strain calculated by FE-simulations. However, it shows decreasing increment during the test. This non-linear behaviour of the axial strain is caused by rotation of the reinforcement fibres towards the loading direction (i.e. the composite becomes stiffer during loading). Just like the thin samples and for the same sensor orientation reason, the measured in-plane transverse strain component is much higher and the out-of-plane strain component lower than their respective reference strain component.

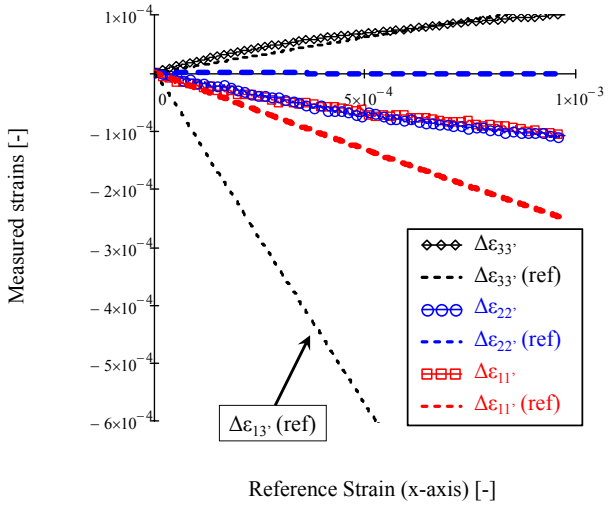

Figure 5-63: Results of the $[+45_2,-45_2]_{6s}$ specimen under a shear tensile load. The measured principal strains and the in-plane shear strain are given as function of the reference strain along the 1'-axis.

Although more research is necessary, one can already conclude that there exists no or limited influence of the shear strain on the strain measurements of a HiBi optical fibre sensor.

5. 5. 3. Thermal cycle testing

The internal strain field of structures can be measured with embedded FBGs whenever temperature is kept constant. In situ strain measurements, however, require a correction mechanism for the intrinsic temperature sensitivity of the Bragg grating sensors. Although a small difference exists in temperature sensitivity [13] for the Bragg peaks of FBGs written in classical birefringent fibres (bow-tie, panda, and elliptical cladding), discriminating axial strain and temperature remains very difficult [14, 15].

This is demonstrated in the following thermal cycle experiment on a $[+45_2,-45_2,90_2,0_2]_s$ laminate (Figure 5-64).

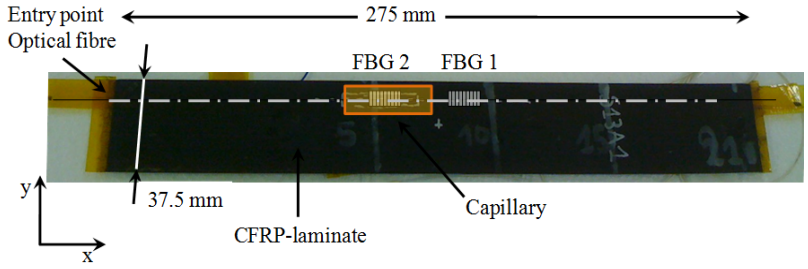

Figure 5-64: $[+45_2,-45_2,0_2,90_2]_s$ CFRP specimen with a MAxS-sensor embedded in between the 5th and 6th layer.

Figure 5-65 shows the temperature history of the thermal cycle test. A relative fast temperature rise of 3°C/min is followed by a very long cooling period (±6 hours). During the cooling phase, the temperature in the autoclave can be considered as homogeneous.

Figure 5-66 shows a clear difference between the FBG inside the capillary and the one fully surrounded by the host material. The difference in wavelengths of fast and slow axes remains more or less constant for the FBG in the capillary (FBG 2). This is a combined effect of intrinsic thermo-optic effects of the optical fibre and thermal strain (in longitudinal direction of the fibre) of the composite sample. The other FBG, however, senses these two effects and the transversal strain as well. The clear difference in sensor response results from the residual strain releasing during heating and building back up when cooling down.

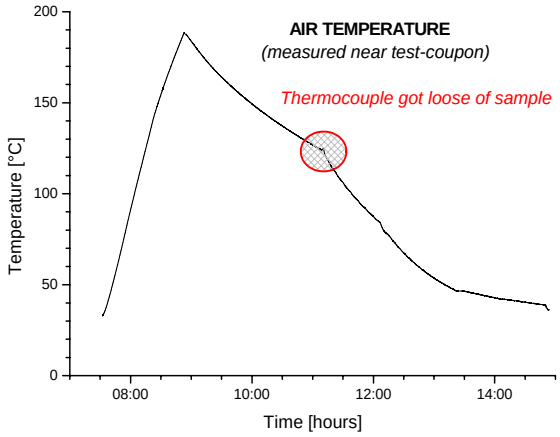

Figure 5-65: The temperature cycle applied during the thermal test inside the autoclave

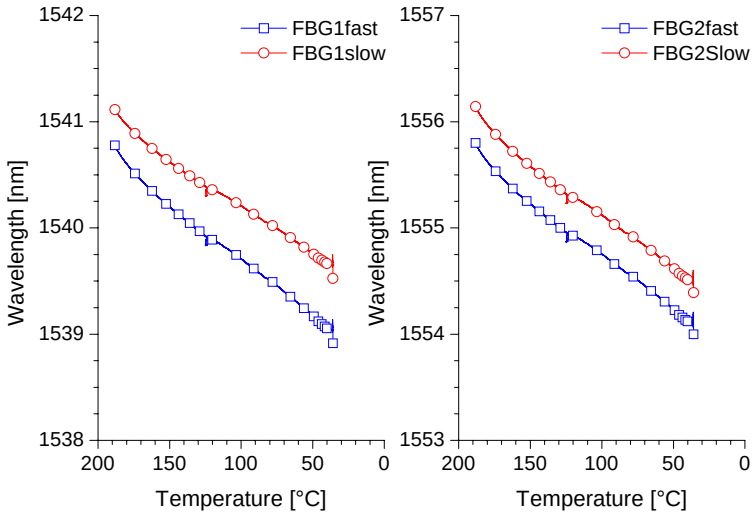

Figure 5-66: The wavelength shifts as function of temperature (cooling phase)

It should be remarked that decoupling of the thermal strains and intrinsic temperature effects is not at all straightforward. This is simply due to the fact that there is a fundamental difference in both phenomena. One can understand this fundamental difference by the observation that the fully embedded FBG notices "three dimensional" strain and temperature effects of the laminate and intrinsic thermal effects of the optical fibre. The FBG inside the capillary only notices intrinsic thermal effects (i.e. thermo-optic effect) and a pure longitudinal thermal

strain effect of the laminate. The three dimensional thermal strain effect of the laminate is determined by coefficients of thermal expansion in the longitudinal and transversal direction. As such, it is not possible to determine and decouple all effects with one MAxS sensor.
Instead, one typically relies on an additional embedded sensor to correct for temperature variations. This sensor should be isolated from the existing strain field by encapsulating it with a (glass, fused silica or metal) capillary (Figure 5-67) [14, 16, 17].

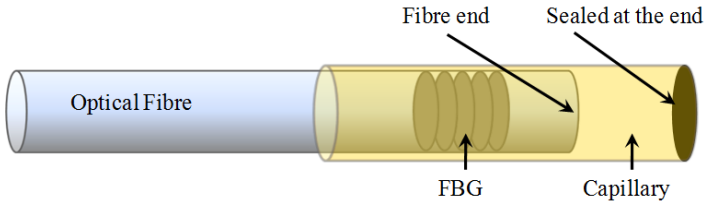

Figure 5-67: Schematic of an optical fibre Bragg grating embedded in a capillary to exclude all external stress/strain components.

An example of this method is illustrated in the following paragraph, using a composite sample with a uni-directional lay-up ($[0]_{16}$, Figure 5-68).

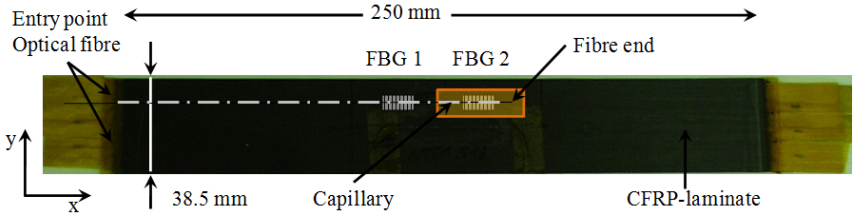

Figure 5-68: $[0]_{16}$ CFRP-specimen with a FBG 1 and FBG 2 as temperature sensor embedded in between the 3rd and 4th CFRP-prepreg layer.

The same thermal cycle as for the first sample is used. In order to evaluate more easily, the results are plotted as function of a rising temperature. Figure 5-69 shows the temperature variation against time: the duration of the thermal cycle is 16 h. This proves that the laminate is in a steady state of temperature at each moment.

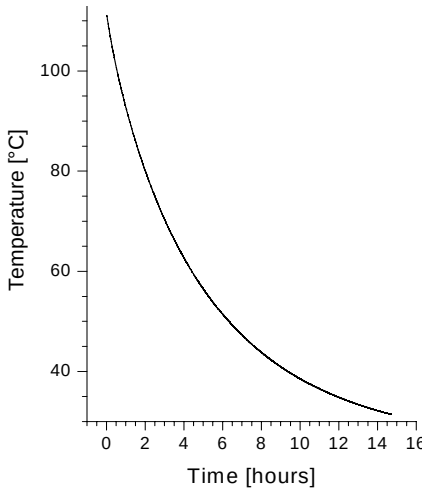

Figure 5-69: The temperature shift as function of time, during the thermal cycling of a $[0]_{16}$ laminate inside the autoclave.

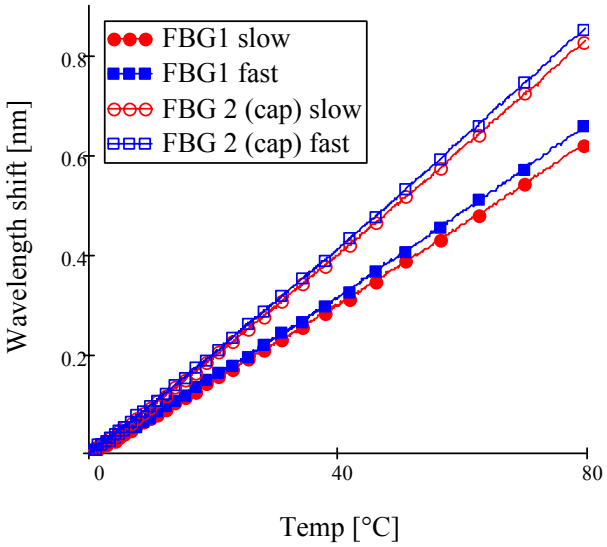

Figure 5-70: Wavelength shifts of the embedded MAxS-sensor (in a $[0]_{16}$ laminate) during thermal cycling

The plot in Figure 5-70 shows the wavelength shift of the two FBGs. The FBG inside the capillary (FBG 2), is subjected to the thermal expansion of the optical fibre, and the thermo-optic effect. In addition, FBG 1 is subjected to transverse strain imposed by the thermal expansion of the laminate in the transverse and axial

direction. One can notice a difference between the response of the fast and slow axis (FBG 1), indicating anisotropy in thermo-optic coefficients of the fibre caused by the bow-tie (i.e. SAPs). The curves are non-linear over the full range, which is caused by the non-linear temperature sensitivity of the grating (Figure 5-71, Section 2. 4. 3. a.).

Figure 5-71 indicates the good correspondence of the wavelength shifts of FBG 2 which is isolated from mechanical strain, and the wavelength shifts calculated using the calibrated temperature sensitivity (Equation 5-12).

$$\ln\left(\frac{\Delta\lambda_{fast}}{\lambda_{fast}}\right) = S_{2,fast}\cdot\Delta T^2 + S_{1,fast}\cdot\Delta T$$
$$\ln\left(\frac{\Delta\lambda_{slow}}{\lambda_{slow}}\right) = S_{2,slow}\cdot\Delta T^2 + S_{1,slow}\cdot\Delta T \qquad \textbf{5-12}$$

$S_{2,fast}$, $S_{1,fast}$, $S_{2,slow}$, and $S_{1,slow}$ are the temperature sensitivities determined in Section Section 2. 4. 3. c.)

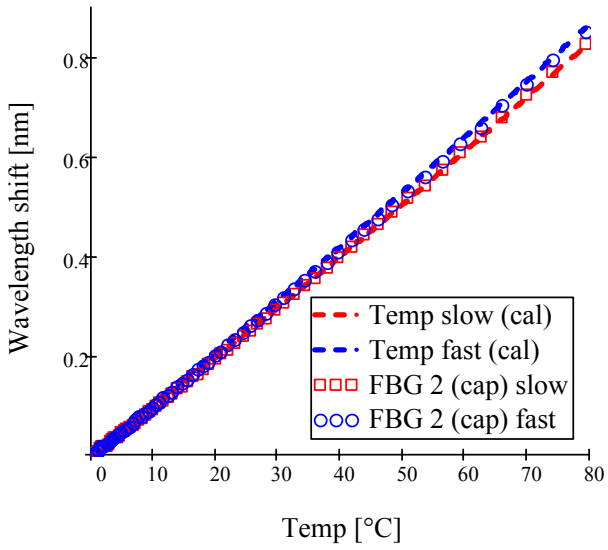

Figure 5-71: Wavelength shifts of FBG 2 which is isolated from mechanical strain, and the shifts calculated using the calibrated temperature sensitivity.

Subtracting the results of Figure 5-71 from the total wavelength shifts (Figure 5-70), one can find the wavelength shifts solely caused by thermal strain.

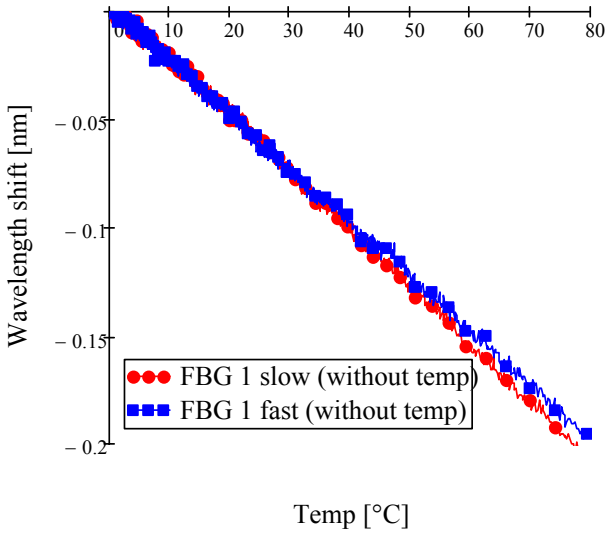

Figure 5-72: Wavelength shifts of the embedded FBG (in a $[0]_{16}$ laminate) under thermal cycling caused by thermal expansion only.

By applying the gauge factors on these wavelength shifts together with the expected axial strain, the transverse strain components present at the core of the optical fibre can be calculated.

$$\begin{bmatrix} \Delta\varepsilon_{11'} \\ \Delta\varepsilon_{22'} \\ \Delta\varepsilon_{33'} \end{bmatrix} = K^{-1} \begin{bmatrix} \Delta\lambda_{B1,1'} \\ \Delta\lambda_{B1,2'} \\ \Delta\lambda_{B2,2'} \end{bmatrix} \qquad \textbf{5-13}$$

The axial strain was calculated using the longitudinal expansion coefficients of the CFRP laminate (α_{axial} = -0.55*10^{-6} [1/°C]). The transverse reference strain components were calculated using the transverse expansion coefficient ($\alpha_{transverse}$ = 34*10^{-6} [1/°C]).

The same order of magnitude was found for the measured strains with FBG 1 and the ones calculated using the thermal expansion coefficients. The differences are most probably attributed to unknown values of the thermal expansion coefficient for the CFRP production process at the UGent facility. It can also be partially assigned to the fact that a small part (~10%) of the wavelength shift of the strain free FBG 2 is related to the free thermal expansion of the fibre, which is not allowed for FBG 1.

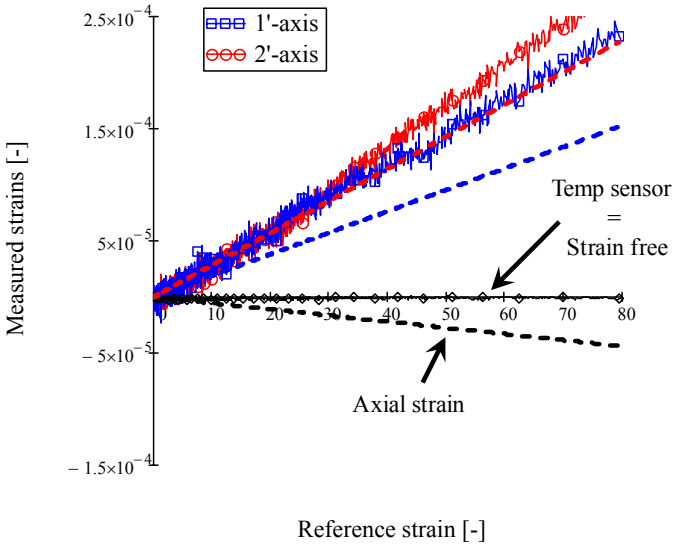

Figure 5-73: Transverse strain components measured with an HiBi bow-tie FBG embedded in a CFRP specimen under temperature load.

5. 6. CONCLUSIONS

In this chapter, the author embedded several MAxS-sensors in carbon reinforced thermosetting plastic samples. The samples have been manually laminated, which eased the embedment of the sensor. After embedment, the carbon/epoxy samples were cured using an optimized curing cycle. Although most of the mechanical properties were available from the manufacturer and from other authors, the actual properties (proper to our optimized autoclave curing cycle) have been determined during a master's thesis at Ghent University. Big differences were found for two sets of samples with a unidirectional lay-up in which the reinforcement fibres are oriented in the 0 deg-direction. It has been explained in literature that, in case of carbon-fibres, material properties are highly dependable on the fibre direction. Even the slightest deviation from the 0 deg direction causes a significant change in material properties.

Samples with different lay-ups and embedded MAxS-sensor were manufactured. For the samples which had the MAxS-sensor embedded in the 90 deg layer or the ± 45 deg layers of the sample, the two separate gratings of the sensor had a separate optical connector. For all other samples, the gratings could be embedded in series (one optical connector). Five different types of experiments were proposed. A transverse tension-compression test, a tensile test, a four point bending test, a shear tensile test, and a thermal cycle test were executed. Reference strains, wavelength shifts, load and displacement of the test rig were measured simultaneously. The

wavelength shifts were measured using a commercially available spectrum analyzer with an interrogation rate of 1/s and a wavelength resolution of 1 pm. Therefore, the load increment of the experiments was kept as low as necessary to obtain a quasi-static experiment.

A discrepancy between the measured strains (MAxS-sensor) and the reference strains exists when using the theoretically determined *TC*-matrix (Chapter 4). Therefore, the *TC*-matrix was optimized for two different stackings of the laminates (a $[0]_x$ and a $[0_4,90_4]_{xs}$ lay-up). During the optimization procedure, it was experimentally proven that both lay-ups should have a different *TC*-matrix. This optimized strain transfer coefficient-matrix was used to calculate the strain data of the composite samples under controlled loading via the wavelength shifts of the MAxS-sensor.

The **combined transverse tension-compression experiment** proved that the response of the embedded FBG is equal in tension and compression. As such, the *TC*-matrix for a particular lay-up can be generalized for all the samples with similar lay-up. No strain data was compared with the reference strain data since the test set-up had too many imperfections. The **transverse compression experiments** proved the feasibility of the sensor; it is capable of measuring the through-the-thickness strains. Because of that, this type of sensor could be used to serve as reference strain measurement in such an experiment. The **tensile tests** proved that the sensor is able to measure transverse strains, even though, they are very small in such experiments. Large scatter was observed for the small transverse strain components. It was shown that the magnitude of these components approximates the resolution of the MAxS-sensor. In order to create a uniform longitudinal strain field in the thick and wide composite samples, the tensile test is not that straightforward. It is very important to clamp the test-sample over its complete width with the same clamping pressure (e.g. with hydraulic grips, which were not available at the time). **The four point bending experiments** introduced several disadvantages and imperfections of the MAxS-sensor. For most samples, the measured strains are in good correspondence with the reference strains when the sensor is loaded in tension. For some samples, the in-plane transverse component does not react as it should (possibly due to damage at the position of the sensor). One of the imperfections is the large influence of the axially measured strain in determining the transverse strain components. It was shown that a small error on the axial strain (for example 15%) could lead to a big error (of 750%) on the transverse strain components. This 15% error can, for example, be caused by a different embedding height of FBG 1 and FBG 2. A solution could be a recoating of the sensor as a whole, so that the sensor has a uniform diameter over its length. The recoating should have high Young's modulus to minimize the buffering effect of the coating on the transverse strain components, and should be kept as small as possible to minimize distortion effects. A second

imperfection was found during compressive loading of the samples. Instead of compressing the fibre, it bends in the capillary, leading to an underestimation of the axial strain. Because of the first imperfection, this underestimation leads to a very high overestimation of transverse strains. Pretensioning of the fibre in the capillary should overcome this imperfection. **The shear tensile tests** have proven that the gratings are almost insensitive to shear strain, which proves the definition of the *K*-matrix in chapter 2. **Thermal cycle tests** have indicated the need for additional research in the field of temperature compensation for HiBi-fibre sensors. An extra sensor embedded in a capillary isolated from any stress or strain whatsoever, could be a solution and is evaluated in a preliminary test.

In the following chapter, an embedded MAxS-sensor will be used to follow up its autoclave curing cycle. Further, the sensor will be embedded in a T-joint to prove the feasibility of using it in a real composite structure. At last, FBGs written in a relatively new type of HiBi-fibre (micro-structured optical fibres) will be tested and their strain sensitivities will be compared with FBGs in bow-tie fibre.

5. 7. REFERENCES

1. Vlekken, J., *MASSFOS: full proposal GSTP3-project*. 2005: Geel, BELGIUM.
2. Available from: http://www.hexcel.com/.
3. Herakovitch, C.T., *Mechanics of fibrous composites*. 1998, New York: John Wiley and Sons inc.
4. Available from: http://www.hexcel.com/NR/rdonlyres/7E68292D-4EDE-4CA7-A73D-AFA4C8CE0248/0/HexPly_M18_eu.pdf.
5. Tavernier, B. and Verbeke, T., *Health Monitoring of Carbon-Epoxy Laminates Used in Space Applications by Means of Embedded Optical Fibres*, 2005-2006: Master Thesis at Gent University, Gent, BELGIUM.
6. ASTM, *D3039: Standard Test Method for Tensile Properties of Polymer Matrix Composite Materials.* 2002: USA.
7. Available from: http://www.toraycfa.com/pdfs/M55JDataSheet.pdf.
8. Jose, S., Kumar, R.R., Jana, M.K., and Rao, G.V., *Intralaminar fracture toughness of a cross-ply laminate and its constituent sub-laminates.* Composites Science and Technology, 2001. **61** (8): p. 1115-1122.
9. Degrieck, J., *Composieten I.* 2004-2005, Master Course at Ghent University: Gent, BELGIUM.

10. ASTM, *D6272: Standard Test Method for Flexural Properties of Unreinforced and Reinforced Plasticsand Electrical Insulating Materials by Four-Point Bending.* 2002: USA.

11. ASTM, *D3518: Standard Test Method for In-Plane Shear Response of Polymer Matrix Composite Materials by Tensile Test of a ±45° Laminate.* 1994: USA.

12. Available from: http://www.Fos-s.com.

13. Chehura, E., Ye, C.C., Staines, S.E., James, S.W., and Tatam, R.P., *Characterization of the response of fibre Bragg gratings fabricated in stress and geometrically induced high birefringence fibres to temperature and transverse load.* Smart Materials & Structures, 2004. **13** (4): p. 888-895.

14. Luyckx, G., De Waele, W., Degrieck, J., Van Paepegem, W., Vlekken, J., Vandamme, S., and Chah, K., *Three-dimensional strain and temperature monitoring of composite laminates.* Insight, 2007. **49** (1): p. 10-16.

15. Abe, I., Frazao, O., Schiller, M.W., Nogueira, R.N., Kalinowski, H.J., and Piinto, J.L., *Bragg gratings in normal and reduced diameter high birefringence fibre optics.* Measurement Science & Technology, 2006. **17** (6): p. 1477-1484.

16. Montanini, R. and D'Acquisto, L., *Simultaneous measurement of temperature and strain in glass fiber/epoxy composites by embedded fiber optic sensors: I. Cure monitoring.* Smart Materials & Structures, 2007. **16** (5): p. 1718-1726.

17. Mulle, M., Zitoune, R., Collombet, F., Olivier, P., and Grunevald, Y.H., *Thermal expansion of carbon-epoxy laminates measured with embedded FBGS - Comparison with other experimental techniques and numerical simulation.* Composites Part a-Applied Science and Manufacturing, 2007. **38** (5): p. 1414-1424.

Chapter 6 : PERSPECTIVES IN MULTI-AXIAL STRAIN SENSING WITH EMBEDDED FBGS

The feasibility of the MAxS-sensor has been evaluated in the previous chapter by conducting tests on coupon level. In this chapter, some perspectives are given to use this sensor type in several "real-life" applications (*Figure 6-1).*

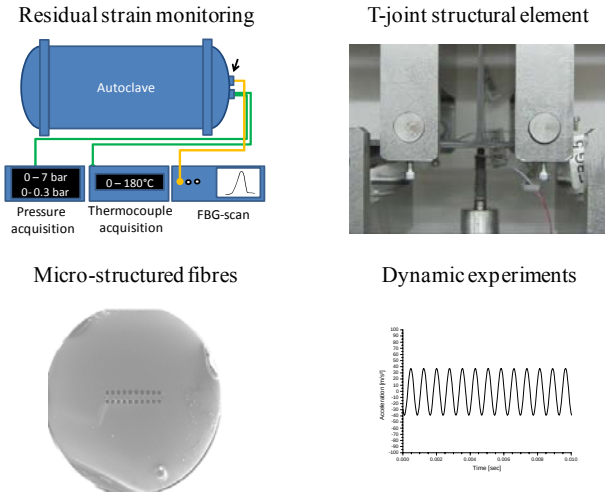

Figure 6-1: Overview of 4 perspectives in multi-axial strain sensing with embedded FBGs.

The first is following up the development of residual stresses and strains in composite laminates and structures. This is done by monitoring the sensor's response during the cure cycle of the composite element. A second perspective is the monitoring of a real structural element during its service life. In section 6.2, the MAxS-sensor is embedded in a scale model of a T-joint. An experimental set-up was designed and fabricated to test this type of structure. Instead of using conventional HiBi-fibre to measure the transverse strain components, one can switch to so-called micro-structured fibres (MSFs). As discussed in the third perspective, FBGs written in such a fibre hold a promising solution for transverse strain measurements without the need for temperature compensations.

6. 1. CURE CYCLE MONITORING

6. 1. 1. Origin of the cure residual strains

Residual strains are strains which exist in a structure in the absence of any external load (mechanical, and thermal). For composite structures in general, these strains play a significant role in their future mechanical performance. On microscopic level they arise from the mismatch in material properties between the (stiff) reinforcement fibres and the (soft) resin. For instance, the coefficient of thermal expansion is $-1.1 \cdot 10^{-6}$ $1/K^{-1}$ [1] and $55 \cdot 10^{-6}$ $1/K^{-1}$ [2], for fibre and epoxy resin respectively. On macroscopic level, they can arise from ply anisotropy (e.g. non balanced, non symmetric laminate) which can lead to mechanical instability of the structure (e.g. deformed structures). On both levels, the MAxS-sensor can play a role in understanding and characterizing these residual strains. With the MAxS-sensor, the cure cycle of composites can be monitored. In this section we focus on the microscopic level of residual strains.

6. 1. 2. Monitoring of residual strains using optical fibre sensors

Several authors have already tried to evaluate the curing process using optical fibre sensors. In what follows, a chronological overview is given.

Huang et al. [3] applied an embedded distributed fibre sensor based on Brillouin scattering to monitor the strain and temperature variation during the curing process of a carbon fibre/epoxy composite. Without going into detail, the used sensors measure the Brillouin frequency shift within the fibre, and determine the strain and temperature at different locations using the Brillouin loss technique. For more details, the author refers to more specialized literature [4]. The optical fibre was embedded within the mid-ply of a 16-ply panel. The used method could obtain data points for each 5cm of the fibre with a resolution of 17με. It was observed that the net strain change during curing was 255 με. It should be mentioned that the method only measures the combination of the longitudinal and transverse strain components, without making any distinction between them. Guemes and Menéndez [5] embedded two uni-axial FBGs in a carbon/epoxy laminate with a quasi-isotropic configuration ($[45,-45,0,90,0,-45,45,0,90,45,-45]_{2s}$). The fibres were embedded in between two intermediate plies parallel to the reinforcing fibres. Guemes and Menéndez observed that the shape of the spectrum remained unaltered during the heating process. However, at the beginning of the cooling process, the residual stresses promoted by the thermal contraction appear, affect the spectrum and even lead to a splitting of the Bragg peak. This splitting indicates that a certain transverse strain component ($\Delta\varepsilon_{yy}$-$\Delta\varepsilon_{zz}$) has developed during the curing. However, with the use of a single grating, one cannot distinct all individual strain components. Without making this distinction,

Guemes and Menéndez found the longitudinal strain during compression of the laminate to be approximately 600 με. Due to thermal contraction, the strain in longitudinal direction was observed to be about 1000 με. Okabe et al. [6] compared the influence of the occurring residual curing stress on uncoated, polyimide coated normal and polyimide coated small diameter FBG sensors. The fibres were embedded in a cross ply laminate $[0_2,90_4,0_2]$ in the 0 degree ply, in contact with the 90 degree ply. This embedment position should be appropriate for the detection of transverse cracks in the 90 degree ply. Goal of their research was the minimization of the effect of non-axisymmetric thermal residual stress on the spectrum of these FBG sensors. For the uncoated FBG sensor, birefringence effects are induced in the optical fibre, leading to a spectrum with two distinct peaks (Figure 6-2). This spectral splitting was not observed for the polyimide coated FBGs. Indeed, the coating acts as a buffer for the occurring non-axisymmetric residual stresses. However, the sensor will become less sensitive for measuring transverse cracks.

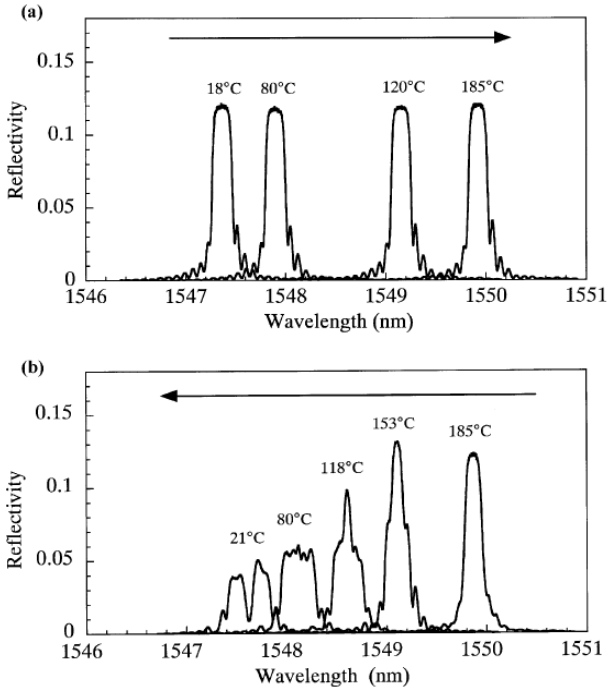

Figure 6-2: Reflection spectra from an uncoated uni-axial FBG sensor, which was embedded into a CFRP laminate, measured during the cure cycle. (a) During the heating process and (b) during the cooling process [6].

Kuang et al. [7] and Li et al. [8] removed the cladding of the optical fibre to keep the fibre core in contact with the host polymer. The technique used to monitor the

melting and solidification process in this study, is based on monitoring the modulation of the refractive index of the polymer matrix. This refractive index variation varies the amount of light transmitted through the optical core, which makes it possible to follow up the solidification process of the polymer matrix. Residual strains cannot be measured using this technique. Sorensen et al. [9] embedded uni-axial FBG sensors to observe the residual strain development during the consolidation of a thermoplastic composite (AS4/PPS). The wavelength shifts and spectral form changes induced by the contraction of the composite during cooling were measured. The spectrum splits in two overlapping peaks during cooling, which makes it difficult to simultaneously measure both Bragg wavelengths (using for example a '3db width' procedure [10]). A tuneable laser with polarization control was helpful in separately measuring both Bragg wavelengths (Figure 6-3). From the measurements before and after consolidation, a transverse strain difference (in-plane - out-of-plane) of maximum 273 με was found.

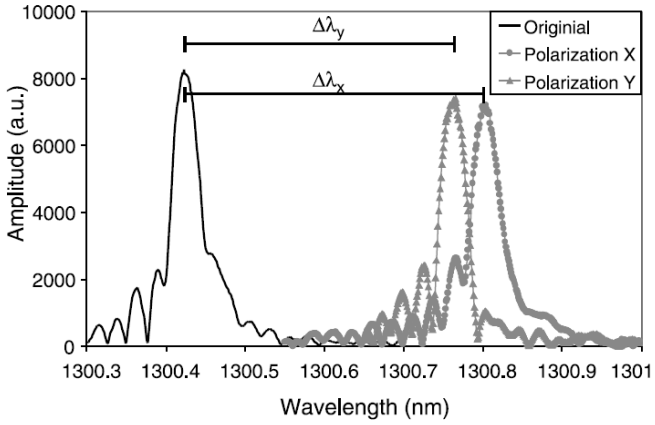

Figure 6-3: Spectral measurements of an embedded FBG before and after consolidation. The two right-hand peaks represent the two major polarization axes [9].

Jung et al. [11] braided several nylon fibres with the 3D-reinforcement of a composite laminate. Afterwards, these nylon fibres were replaced by optical fibres containing FBGs. This made it possible for the authors to monitor the expansion and contraction caused by the matrix cure, as well as the temperature changes during a resin transfer moulding process. A maximum strain of 410 με was measured in the longitudinal direction of the fibre. Jung et al. [12] also estimated the build-up of residual stress and strain in a hybrid carbon/phenolic composite using embedded fibre Bragg grating sensors. The composite is partially delaminated with a releasing film. Both regions were monitored during curing; the differences in strain between

hybrid and delaminated regions were assumed to be the residual strains in the hybrid region. Only a longitudinal strain component could as such be observed.

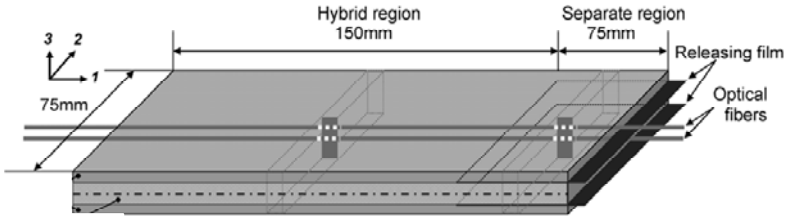

Figure 6-4: Partially delaminated hybrid composite [12].

Kim et al. [13] embedded an array of FBG sensors in a carbon laminate $[0,45,90,-45]_{2s}$ which was cured using an out-of-autoclave process (Quickstep process). During curing, a broadening of the spectrum could be observed, which indicates the occurrence of transverse stress. Mulle et al. [14] embedded FBG sensors in two different plies of a $[0_8]$ laminate to monitor the cure cycle during fabrication. The various phases during the cure cycle are well visualized (Figure 6-5). At the end of the cure cycle, the residual strains (longitudinal) were estimated to be 75 με at a specific point in the laminate.

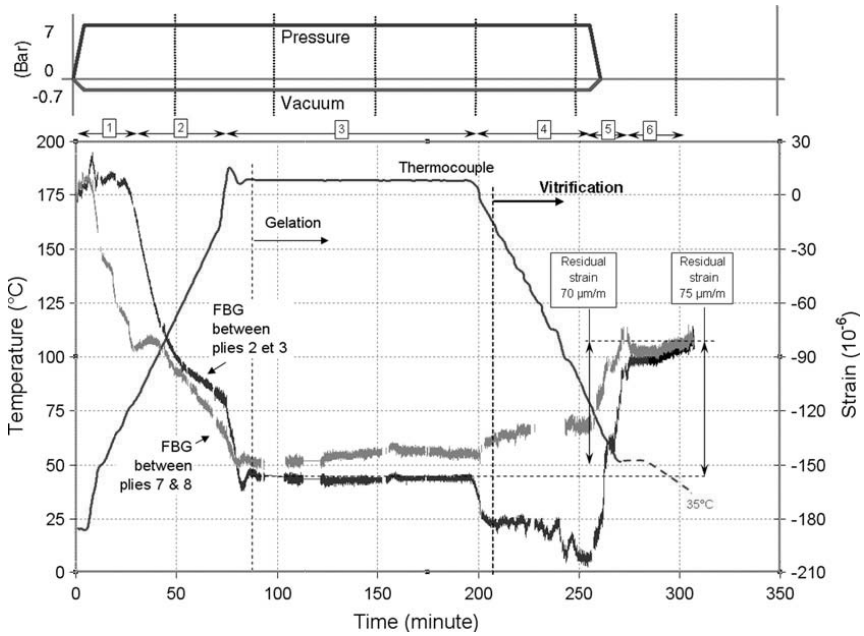

Figure 6-5: Longitudinal strain changes measured in a $[0_8]$ laminate during a cure cycle.

In the following sections, the MAxS-sensor is embedded in a carbon/epoxy laminate panel. During the cure cycle, the wavelength shifts of the sensor are monitored.

6. 1. 3. Materials and method

MAxS-sensors were embedded in a composite laminate $[\pm 45_2, 0_2, 90_2]_s$ in between and parallel to the 0 deg [15]. Figure 6-6 depicts the positions of the sensors. Only the sensor in the middle was monitored during curing of the composite panel. The panel was cured in the UGent autoclave which had to be modified with fibre through-puts (Figure 6-7). During the curing cycle, temperature (thermocouple), pressure (P-sensor), vacuum (P-sensor), and wavelength shifts (FBGs) have been measured and plotted as function of time.

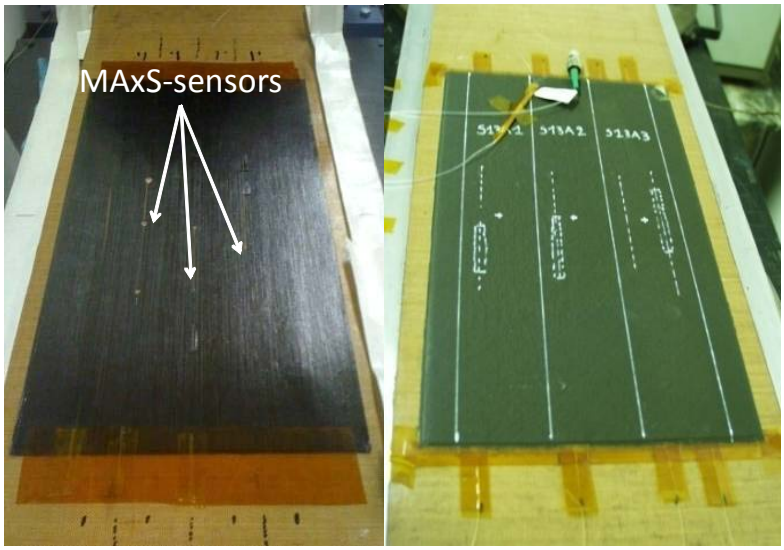

Figure 6-6: The composite laminate (lay-up $[\pm 45_2, 0_2, 90_2]_s$) which has been monitored during curing. On the left, the embedding of the MAxS-sensor in between two layers with the reinforcement fibres in the 0 deg direction is shown and on the right, the resulting laminate after curing[15].

6. 1. 4. Results and discussion

Figure 6-8 shows the results (pressure, vacuum, temperature, and wavelength shifts) as function of the curing time. The cure cycle can be divided into five phases, which is clearly indicated at the bottom of the figure. At first, vacuum is already on the laminate and temperature is raised until it reaches 120°C. In this phase, the wavelengths of both FBGs (red and black in the graph) change linearly with temperature. On the one hand, this is caused by the thermal dependency of the FBG, and on the other hand, it is caused by the thermal expansion of the uncured lamina.

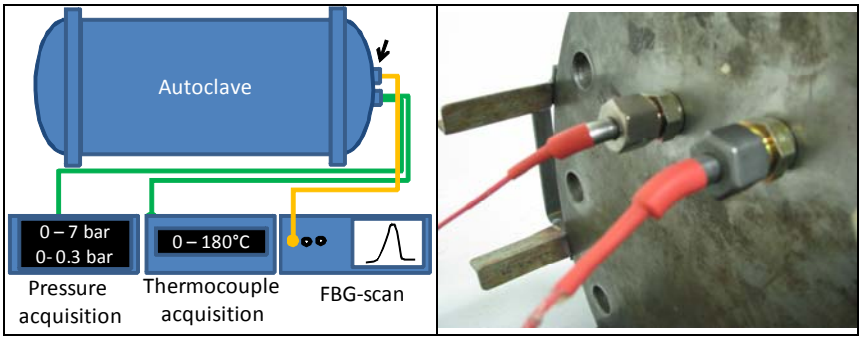

Figure 6-7: A schematic drawing of the set-up for measuring the cure cycle during manufacturing of a composite, using the autoclave production technique (left). Detail of the fibre through put at the UGent autoclave (right).

The second phase is the isothermal dwell phase in which temperature is kept constant at 120°C. In Section 5. 1 it was shown that this dwell step of constant temperature is done at the level of optimal epoxy viscosity of the matrix material [16], allowing the epoxy resin to flow and the layers to stick together. During this dwell step, the wavelengths slightly decrease, which corresponds to the settlement of the material due to the vacuum. This is a decrease of the wavelengths since the dependency of the sensor to transverse pressure is negative. In the third phase, firstly, pressure is put on top of the sample. This leads to a small drop of the wavelengths due to the reason mentioned before. Secondly, the temperature is raised up to 180°C (cure temperature); again all wavelengths are equally raised as function of temperature. At that point we enter the fourth phase in which the epoxy curing starts. This process leads to a chemical and thermal interaction of the sensor and its host material. In this phase, a different wavelength behaviour can be noticed for both FBGs. The wavelengths of the FBG in the capillary increase, while the other ones decrease. The FBG in the capillary is only exposed to axial stress during the settlement of the structure under the pressure and temperature conditions, while the other FBG is exposed to transverse stress components as well. The fifth phase starts when the heating is stopped and the inside of the autoclave can cool down under atmospheric conditions. The residual strains for the FBG outside the capillary - caused by the mismatch in CTE of epoxy and reinforcement fibres- appear in a peak separation of the spectrum.

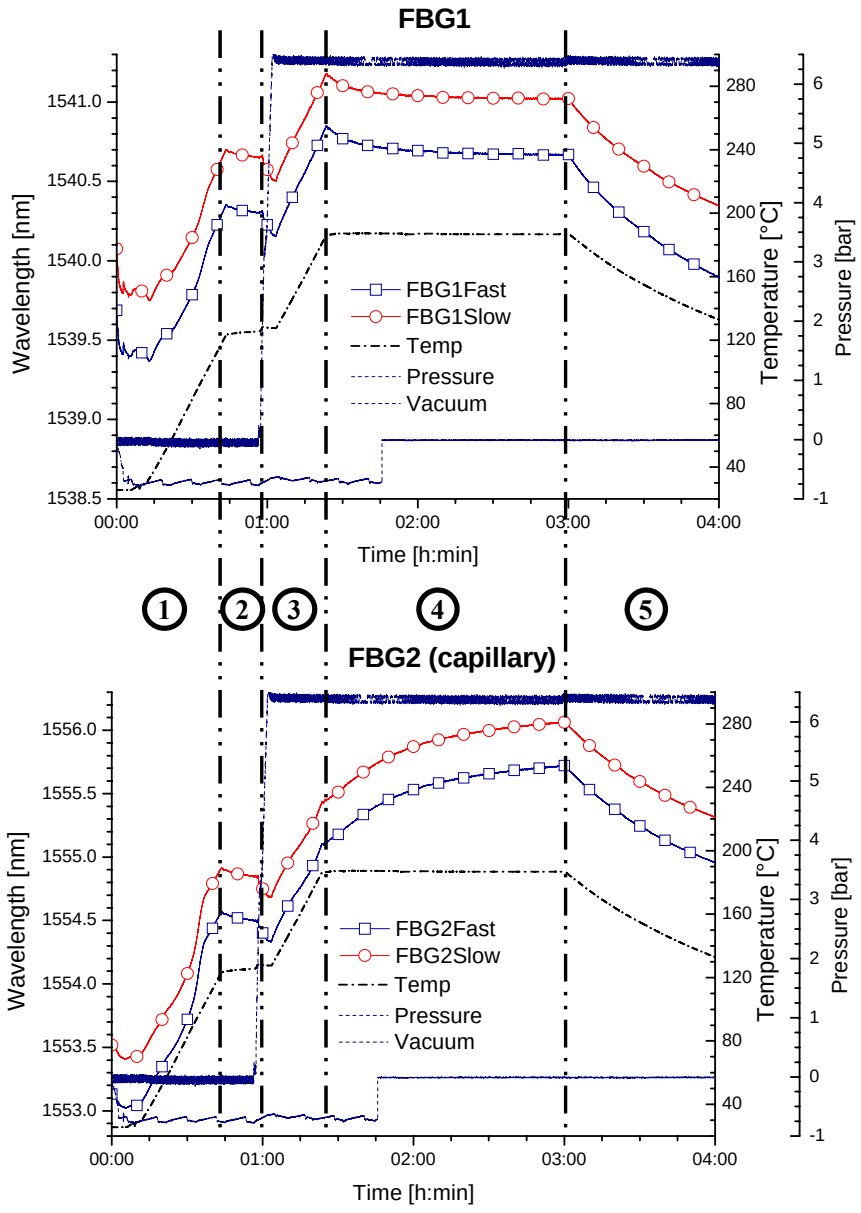

Figure 6-8: The measured temperature, external pressure, vacuum pressure, and Bragg wavelengths during the cure cycle of a $[\pm 45_2, 0_2, 90_2]_s$ laminate [15].

In Figure 6-9, all wavelength shifts are plotted as function of time on one graph to have a clear view on the different behaviour of both FBGs. During temperature increase, the encapsulated FBG exhibits a larger increase in wavelength shift since it

is sealed from transverse influences during expansion (increasing temperature) and shrinkage (decreasing temperature) of the laminate. This is because the gauge factors of these transverse influences are negative (pressure leads to an increasing wavelength shift). During cooling phase, the nominal wavelength decrease happens in a similar way for both sensors,. The most striking in this figure, is the Bragg peak separation during the cooling phase of the spectrum of the FBG which is not encapsulated. This Bragg peak separation is the visualization of the developing residual stresses and strains in the composite panel while curing. Note also that the four Bragg wavelength shifts move towards an asymptotic value while the temperature is kept constant at 180°C. The asymptote is not reached yet, which could be explained by assuming that the curing process (solidification) is incomplete.

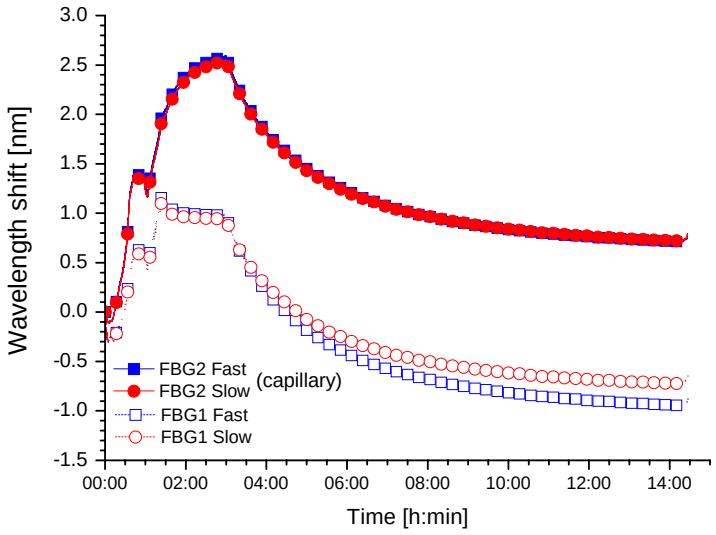

Figure 6-9: Wavelength shifts of both FBGs during the curing cycle of a $[\pm 45_2, 0_2, 90_2]_s$ laminate.

To have a better understanding of the curing process, the wavelengths of both FBGs are delineated as function of temperature in Figure 6-10. It is clear that during the whole curing process, the first FBG got a total negative wavelength shift of ~1.0 nm, while the encapsulated FBG got a total positive wavelength shift of ~1.0 nm. The first drop, observed in both graphs, is due to the application of the necessary pressure to enhance the flow of the resin throughout the laminate. At the constant curing temperature (dwell step), the differences for both sensors are clearly visible.

The first wavelength shift of the first FBG decreases less than the wavelength shift of the encapsulated FBG increases. During cooling, the FBG covered from transverse strains is only affected by the negative CTE of the lamina. As such, the wavelengths of both polarization modes of this FBG will change homogeneously. The other FBG is also affected by the mismatch in CTE between epoxy resin and reinforcement fibres. Since the CTE of the epoxy resin is a lot bigger than that of the fibres, the FBG will sense a certain pressure, which results in lower wavelengths. As temperature decreases, the pressure will rise and a peak separation will occur.
Because the FBG response is affected by the strain and temperature change simultaneously, the strain needs to be calculated by subtracting the temperature portion from the total Bragg wavelength shift. In order to determine the temperature portion, an external temperature measurement is necessary (section 5. 4. 3).
It is difficult to quantitatively measure the residual strains during the curing cycle. After curing, the initial and final wavelengths could be used to determine the residual strains in a composite lamina. Therefore, the exact TC-matrix needs to be determined (Section 5. 3). Though, with the MAxS-sensor a clear qualitative view is obtained of the occurring phenomena during the curing process.

6. 1. 5. Conclusions

It is generally known that during the fabrication process of composite laminates and structures, the build-up of residual stresses and strains can be significant, caused by the mismatch of the CTE of the reinforcing fibres and the epoxy matrix. By embedding the MAxS-sensor in a composite laminate $[\pm 45_2, 0_2, 90_2]_s$ (fabricated using the autoclave technique) it was possible to visualize the separate effects of axial strain and transverse strain components during the curing process. The difference in response between the FBG inside the capillary (homogeneous shift of the Bragg peak spectrum) and the one surrounded by the host material (shift with an extra Bragg peak separation), shows a clear residual strain development during the cooling phase.

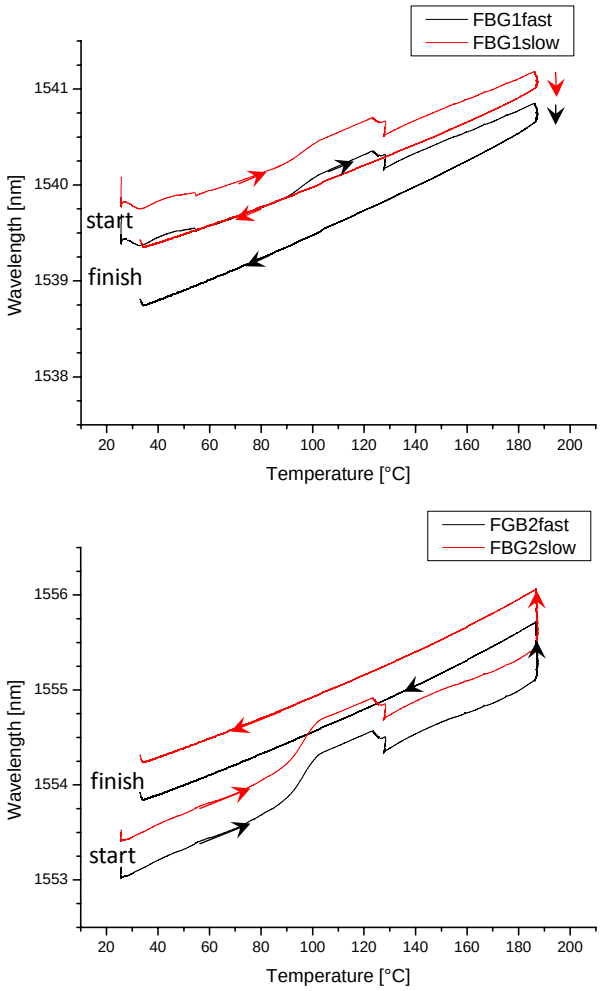

Figure 6-10: Dependency of the four Bragg wavelengths on temperature. FBG 1 is 'normally' embedded in the laminate and FBG 2 is the sensor inside the capillary.

6. 2. MAxS-SENSOR EMBEDDED IN A REPRESENTATIVE SCALE MODEL OF A T-JOINT STRUCTURE

6. 2. 1. Background

T-joints are frequently used as blade stiffeners. The T-section mostly carries in-plane shear loads from the stiffener plane to the skin-plane [17]. Such a structural element presents major advantages compared to sandwich structures. For example, absence of the core material with its problems in sorption and pressure balance inside/outside of the core, potting of fasteners, edge closure, and shape limitations (thickness variations, curvatures). Currently, T-joints are also finding increased application in 3-D structures e.g. to transfer all kinds of loads from one plane (e.g. X, Y) to another plane (e.g. Y, Z). A specific weakness of T-joints is their limited pull-off loads [17].
In this section, we will embed the MAxS-sensor into a scale model of a T-joint structure, and afterwards load the sample in four point bending and with a pull-off load.

6. 2. 2. Manufacturing process of T-joint structures with embedded FBGs

6. 2. 2. a. T-joint fabrication

In Figure 6-11 an overview is given of the production process of a T-joint scale model. Such T-sections are typically manufactured by laying up and debulking two angled parts on a mould and the rest of the skin on a flat table (1). Then the angled parts are assembled into a T-section (2) and the triangular UD stack of plies are inserted in the hole of the T-assembly. Finally, the assembly is finished with the (rest of the) skin lay-up and is put in a vacuum bag to cure in the autoclave (3). The resulting T-joint is depicted as well (4). It should be mentioned that the same base material as was used for the coupons (M55J/M18 prepreg) was used to manufacture the scale model.

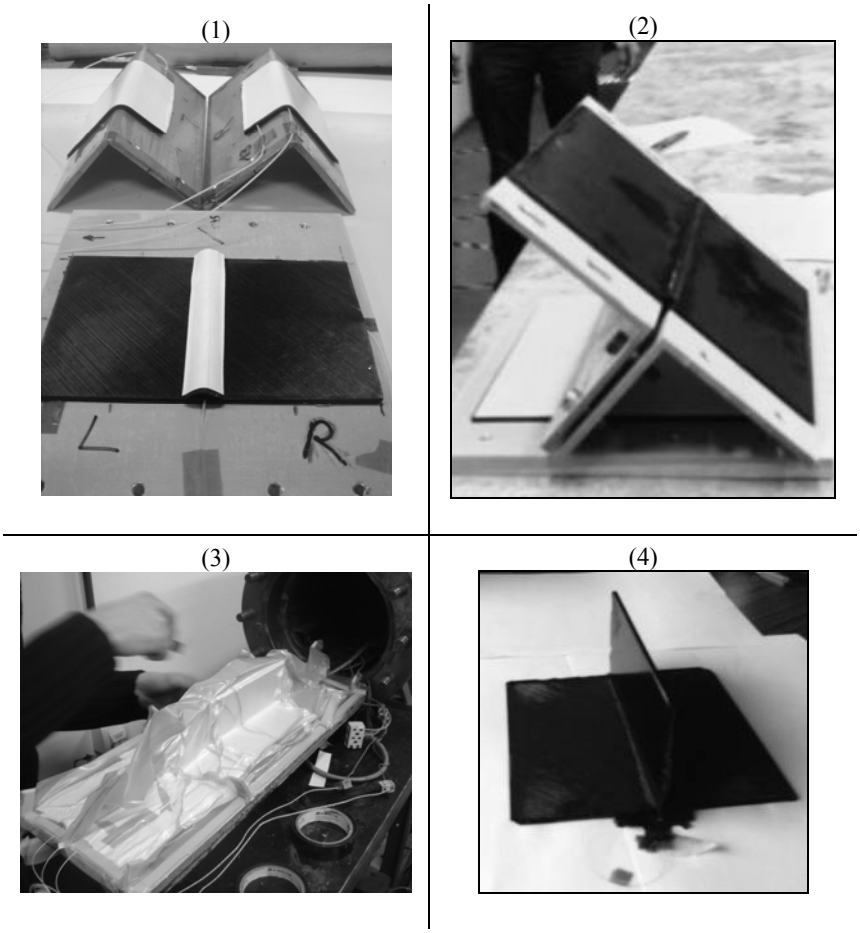

Figure 6-11: Production process of the T-joint demonstrator (1-3) and a resulting scale model (4).

The following geometry was used to manufacture the scale model of the T-joint structure (Figure 6-12):

- A (flange) = $[\pm 45_2, 0_4, 90_4]_s$ (thickness=2.4 mm)
- B (web) = $[\pm 45_2, 0_4, 90_4, 90_4, 0_4, \pm 45_2]_s$ (thickness =4.8 mm)
- Radius = 5 mm, d_1 = 2.4mm, $d_2 = d_3$ = 4.8mm
- Height (B) = 65 mm, Width = 100 mm, Length (A) = 150 mm

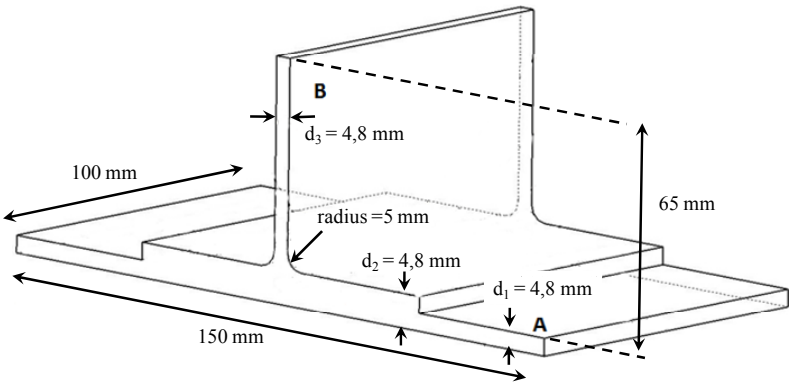

Figure 6-12: Geometry of the fabricated scale model of a T-joint structure

6. 2. 2. b. Sensor placement

In order to determine the optimal positions of the FBGs (zones in which large, preferably constant, longitudinal and transverse strain arises), detailed finite element analyses have been performed on a T-joint FE-model. One fourth (because of symmetry reasons) of the T-joint with lay-up was modelled for the four point bending load case. 128.000 hexahedral elements of type C3D8R, and in the bent zone 9.000 linear wedge elements of type C3D6, were used to model the T-joint.

An obvious result of the four point bending simulations, was the observation of a region in which a constant strain field was created during the experiment (Figure 6-13). This region is very well suited to embed a multi-axial strain sensor. Since very small strains in the in-plane transverse direction of the T-joint were to be expected, no capillary was embedded along this direction.

No continuous strain field region was observed for the simulation of the T-joint under pull-off load. However, very large strain gradients were observed in the bend section of the web, which leads to damage initiation. Cartié et al. [18] have done tests on various T-joints under pull-off load, in which they observed damage initiation in that particular region (Figure 6-14). Damage detection is not an issue in this work, however, embedding a multi-axial strain sensor in this region would be appropriate. At higher loads, damage propagates to completely pull off the web from the flange. This makes the middle between web and flange also an interesting region to embed a multi-axial strain sensor.

This knowledge leads to the definition of the position of five sensors which were embedded in the sample (Figure 6-15 and Figure 6-16). (1) One sensor was covered in a capillary sensor (FBG 1) and embedded in between layer six and seven of the flange (0 deg plies) to be able to measure the strain in the longitudinal direction of the sample. (2)-(3) Two sensors were embedded in the plateau of the T-joint (FBG 2 & FBG 5) and one in the bending region of the web (FBG4), in the tenth layer of the

web between two 90 deg plies. (4) FBG 3 is embedded under the triangular filling of the assembled web in between the web and the flange. Due to epoxy flow inside of the PTFE buffering during curing, the fibre of FBG 3 did not survive the process. In addition, during set-up of the four point bending experiment, FBG 4 broke.

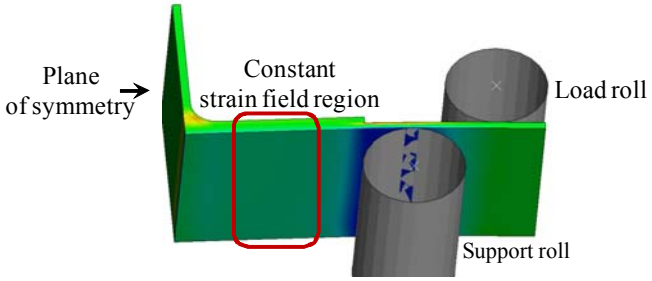

Figure 6-13: Finite element analysis of four point bending loading of a T-joint with indication of the principal strains

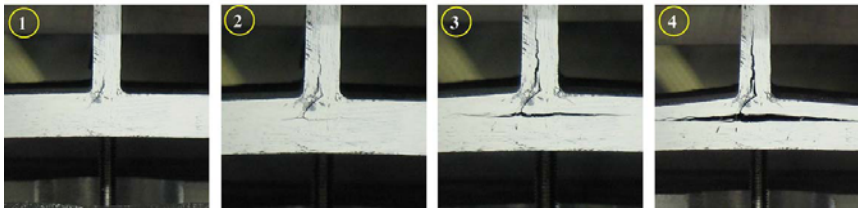

Figure 6-14: Observation of damage initiation in the web at the bending region during a pull-off testing of a T-joint[18].

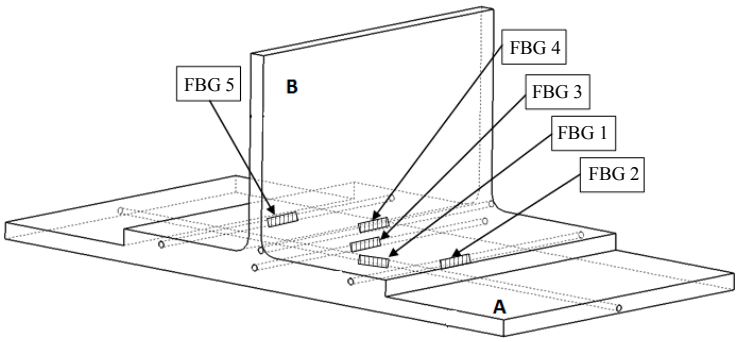

Figure 6-15: Schematic representation of the T-joint and the location of 5 embedded optical fibre sensors.

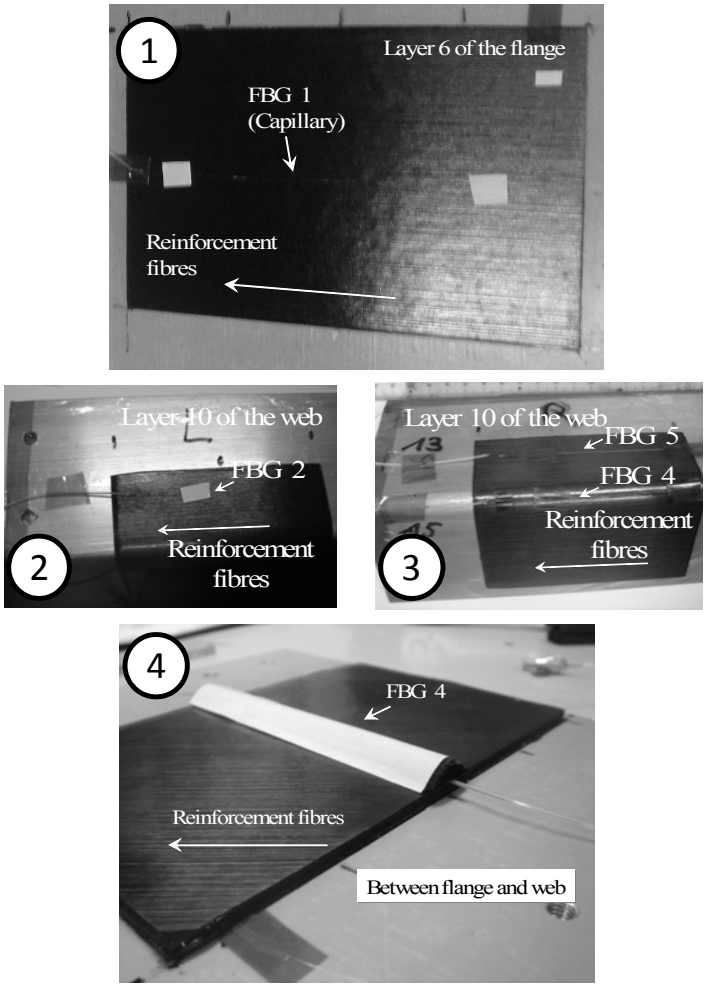

Figure 6-16: The several FBG sensors embedded in the scale model of the T-joint.

6. 2. 2. c. Post manufacturing sensor analysis

Due to a malfunctioning of the inlet valve of the autoclave, the pressure was twice the desired value during the curing cycle. Therefore, a lot of epoxy resin matrix was pressed out of the prepreg, and even some of the carbon fibres were pushed out of the laminate. This led to very high residual stresses inside the T-joint, which is clearly visible in the spectra of the FBGs that survived the manufacturing process (Figure 6-17). FBG 2 and FBG 4 experience a high differential transverse residual strain which can be observed in the spectrum because of a negative Bragg peak separation. For FBG 2, the Bragg peak of both polarization modes of the fibre are

almost joined in a single peak. The spectrum of FBG 1 (capillary) shifted homogeneously to higher wavelengths, which indicates that the capillary is well sealed.

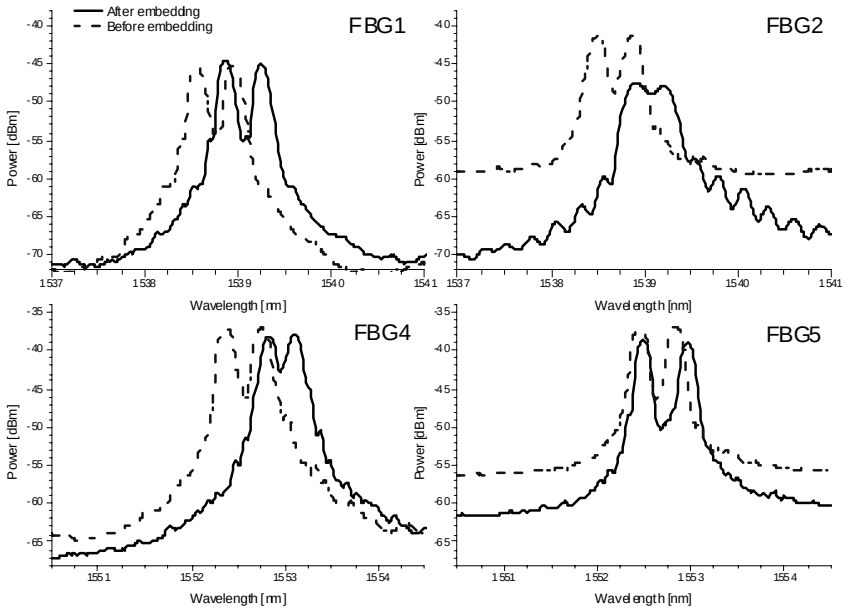

Figure 6-17: Spectra of the bow-tie FBGs before and after embedding.

To compare the sensor responses, the orientation of the FBGs that survived the process, needs to be known. The manufacturing process (high pressure) can have changed the orientation of the FBGs. In Figure 6-18, we observe that the fast axis of FBG 2 makes an angle of 24 degrees with the vertical axis, and the fast axis of FBG 5 an angle of 50 degrees. The totally different orientation makes it impossible to directly compare the wavelength shifts of both sensors. The results are discussed in the following section.

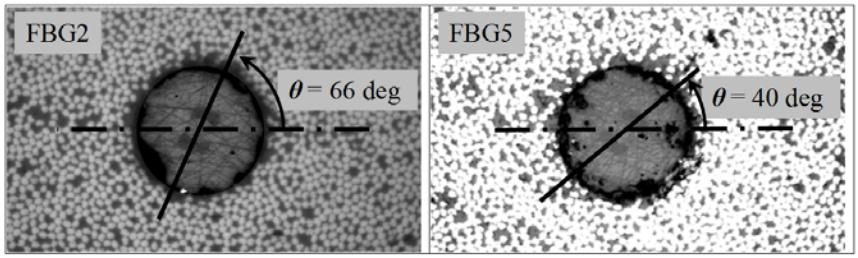

Figure 6-18: Orientations of FBG 2 and FBG 5 of the T-joint structure.

Another important fact if one wants to compare the wavelength shifts of both sensors (and the FBG in the capillary), is the embedding depth of the sensors (Table 6-1).

Table 6-1: Embedding depth of FBG 1, FBG 2 and FBG 5 in the T-joint structure with respect to the bottom of the flange.

FBG 1	FBG 2	FBG 5
586 µm	670 µm	640 µm

The embedding depth of FBG 1 differs a lot from the other FBGs since it has been embedded in the 0 deg plies, while the other two have been embedded in the 90 deg plies. In order to compare the results of the FBG sensors, the embedding depth of the sensors will be taken into account.

6. 2. 3. Test method and results

6. 2. 3. a. FBG interrogation test set-up

In Figure 6-19, the used interrogation test set-up is depicted. Every FBG needs to be exposed to the same depolarized light source. Therefore, the light of the source is first sent to a 2x2 coupler which splits the amount of light in two. The first part goes to a circulator and then to FBG 1. This circulator is necessary to block the unpolarized light sent by the FBG interrogator. The second part of the light first goes to a circulator for the same reason as above, and is then split up in two, to equally expose FBG 2 and FBG 5.

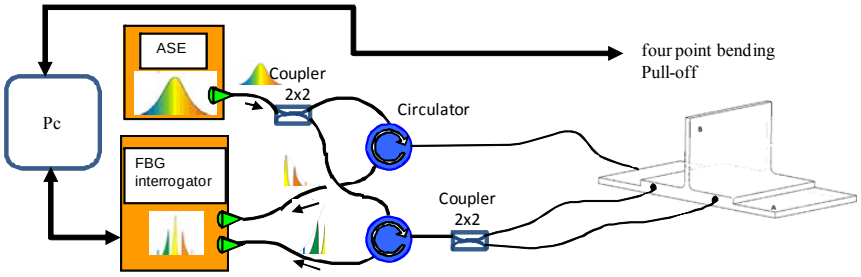

Figure 6-19: The interrogation set-up used during the experiments on the T-joint.

During the experiments (four point bending and pull-off), the wavelength measurements can be combined with load and displacement measurements (LVDT), and external reference strain gauges.

6. 2. 3. b. Four point bending experiment

Test set-up

The scale model of the T-joint structure was first exposed to a four point bending experiment as depicted in Figure 6-20. As shown in the FE-simulations (Figure 6-13), this experiment creates a constant strain field in the plateau of the structure.

Figure 6-20: The four point bending set-up, designed to test structural elements up to 150 mm in width.

Test results

The wavelength shift due to four point bending of the T-joint structure is depicted in Figure 6-21 and Figure 6-22. At the beginning of the experiment, the wavelength shifts for FBG 2 and FBG 5 are non-linear because only one roll of the load span touches the structure. Thus, the structure will first be loaded according to a three point bending set-up. It should be mentioned that at a certain load, large inelastic deformations were induced and cracking was initiated in the sample. This was clearly audible during the experiment.

Due to the high pressure (times 2) during the curing cycle, the T-joint had no homogeneous geometry. This makes it difficult to compare the wavelength shift of FBG 1 (which is, as discussed before, covered with a capillary), with the simulated reference longitudinal strain. However, by taking the embedding depth of the capillary into account, good agreement should be found. In Figure 6-22, a detail of the resulting wavelength shifts of FBG 2 and FBG 5 is shown. Both sensors have an opposite effect compared to the mean shift of the four wavelengths. This opposite effect can be explained by the different orientation and the different embedding depths of both sensors. It should be noted that the longitudinal strain acts as an in-plane transverse strain onto the optical fibre, which causes the opposite shift.

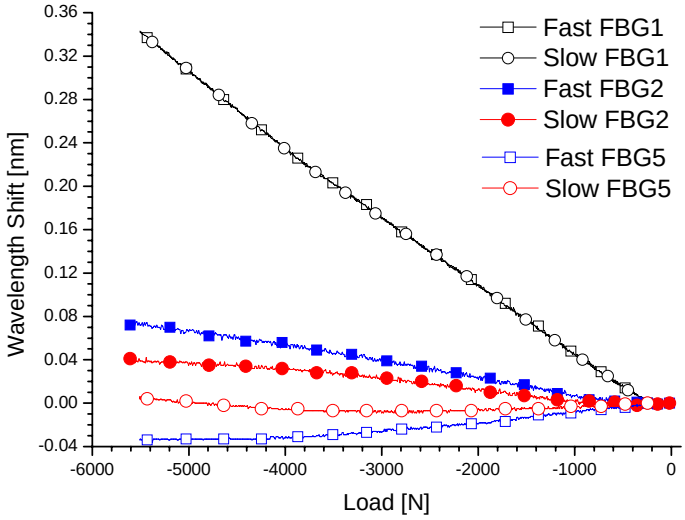

Figure 6-21: Results of the four point bending test with wavelength shifts of FBG 1, FBG 2 and FBG 5.

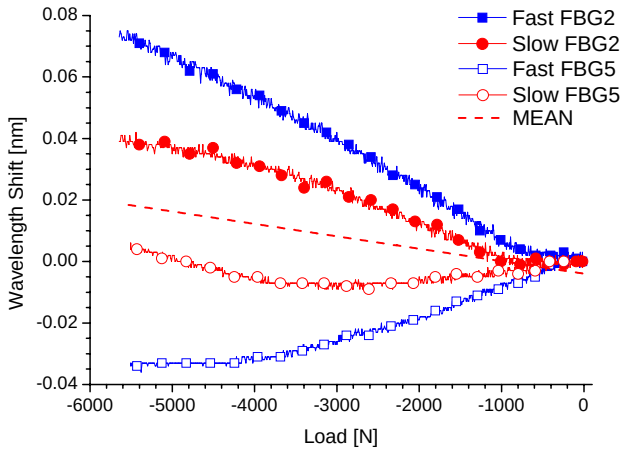

Figure 6-22: Detail of the results of the four point bending test for FBG 2 and FBG 5

6. 2. 3. c. Pull-off experiment

With respect to aircraft construction, pull-off refers to the tendency of joints between wing skins and spars to separate under aggressive loading conditions. An example of such a loading condition would be the fuel pressure loading on the internal surface of a wing skin when the aircraft experiences a rapid rolling manoeuvre [17].

Test set-up

In Figure 6-23, the test set-up for the pull-off of the web from the flange of a T-joint structure, is depicted. The web is clamped and pulled while the flange is at a fixed position in vertical direction.

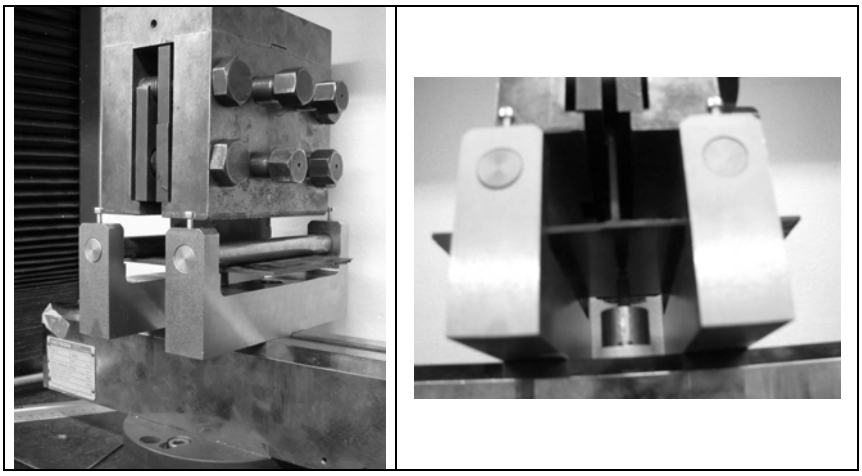

Figure 6-23: The pull-off test set-up available at Ghent University

Test results

The results of the experiments are depicted in Figure 6-24. It should be noted that the most interesting FBG, the one in the bend of the web, broke during manufacturing. During the pull-off load, the T-joint is more or less loaded according to a three point bending. Due to a possible movement of the FBGs, and the large (inelastic) deformations of the four point bending with the initiation of damage, it is difficult to compare the wavelength shifts of the individual sensors.

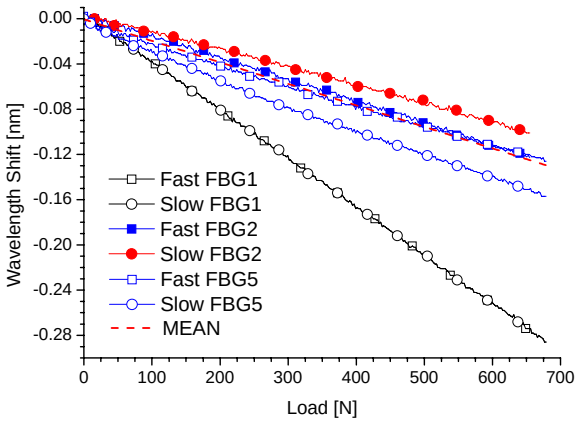

Figure 6-24: Wavelength shifts of FBG 1, FBG 2 and FBG5 during pull-off.

6. 2. 4. Conclusions

In this section, a representative scale model of a T-joint structure was manufactured with embedded sensors in several plies of the structure. FE-simulations showed the possible interesting positions of the sensors when the structure is loaded in four point bending. However, due to a malfunctioning of the inlet pressure valve, too much pressure was applied on top of the structure, leading to an inhomogeneous geometry of the structure. Wavelength shift and decreased Bragg peak separation was observed for several of the FBGs which survived the production process. In order to compare the results of the different tests better, the orientation and embedding depth of the FBGs were measured in a post mortem analysis. The FBGs in the plateau of the flange showed a different orientation and had, as such, also a different response for both loading conditions. During the four point bending experiment, the T-joint was subjected to large inelastic deformations which resulted in non-linear wavelength shifts during the experiment. Damage was initiated in the material, which was clearly audible during the experiment. The pull-off experiment was more difficult to compare since a movement of the sensor occurred during manufacturing. It could only be stated that the results were plausible.

If the fibre would be oriented correctly in the structure, the procedure as mentioned in Chapter 5 could be used to determine the strains in the structure. At first, the strain at the core of the optical fibre sensor should be calculated. Then, these strains of the core should be transformed into the strains of the structure by multiplying them with the inverse of the optimized *TC*-matrix for this particular lay-up. Since the T-joint is only a shell element, the fibre embedding should happen in a very precise manner. Otherwise, large fluctuations are to be expected on the measured strain values.

6. 3. STRAIN AND TEMPERATURE SENSITIVITY OF MICRO-STRUCTURED OPTICAL FIBRES VERSUS THOSE OF BOW-TIE FIBRES

6. 3. 1. Introduction

To monitor the structural health of composite materials, it is necessary to map all strain components inside the material. The former chapters of this dissertation proved the working principle of an embedded multi-axial strain sensor consisting of two FBGs written in a bow-tie birefringent fibre. This MAxS-sensor is well-suited for this task, because of its distinguishing response to axial and transverse strain components. However, the sensor has a couple of drawbacks for which the author, together with researchers from the VUB-TONA, is searching a solution. One is replacing the bow-tie fibre by a dedicated micro-structured optical fibre (MSF). Therefore, the MSF sensor should have similar strain response as a bow-tie fibre.
In this section, the response to mechanical and thermal loading of embedded FBGs written in three different fibre technologies is compared: draw tower fibre Bragg gratings (DTG FBG), micro-structured optical fibre Bragg gratings (MSF FBG) and fibre Bragg gratings in bow-tie fibre (bow-tie FBG). First, we introduce the MSF technology more in detail, for the other technologies the author refers to section 2. 3 of this work, in which the different fibre technologies and their FBG reflection spectra are shown. Afterwards, we explain how the fibres are embedded into a thermosetting composite. Finally, the monitored shift in Bragg peak wavelengths of the different FBGs for various controlled loading conditions is discussed.

6. 3. 2. Micro-structured optical fibres

Micro-structured optical fibre configuration

The optical fibre sensors used during the first 5 chapters of this book always relied on conventional glass optical fibres (either birefringent or not) consisting of a solid glass core, surrounded by a solid glass cladding material. MSFs consist of a solid glass core too, but their cladding is formed by a periodic lattice of air holes that run along the length of the fibre and that allow confining and guiding light in and through the fibre. The defect in the centre of the lattice then serves as fibre core (Figure 6-25).

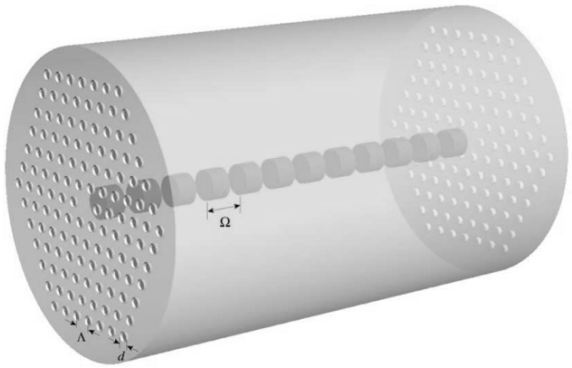

Figure 6-25: Illustration of an MSF with d = hole diameter and Λ = pitch. The FBG in the core of the MSF is also shown [19].

Adapting the particular features of the micro-structure, such as the air filling fraction and the lattice period, allows obtaining optical fibres with very particular properties in terms of dispersion, mode-field confinement, endlessly single-mode behaviour, birefringence etc. The optical and mechanical properties of MSFs can also be controlled by changing the size, shape and location of the air holes. Hence, MSFs bring along unprecedented design flexibility and unique sensing features, including the possibility to achieve very high birefringence levels and to operate in a temperature-insensitive way [20-22]. The birefringence levels can be of the order of several 10^{-3} and therefore, one order of magnitude higher than conventional highly birefringent fibres. The polarimetric response to temperature in standard non-embedded highly birefringent fibres is associated mostly with residual thermal stress induced by different thermal expansion coefficients in the fibre core and the cladding (Chapter 2). The thermal response of MSFs is related to the temperature induced variation of the refractive index (thermo-optic effect) of the glass and of the air filling the holes, and also to the thermal expansion of the fibre. The contribution of these effects to the overall temperature sensitivity depends on the guiding mechanism, fibre geometry, wavelength, and material used to manufacture the fibre. The effect of temperature on index guiding MSF has been numerically analyzed for a number of MSF structures [23].

The microstructure of the MSF used in this work consists of three rows of air holes and a central Germanium-doped core, as depicted in Figure 6-26. The diameter of the MSF is 125 μm, the Germanium-doped core is circular and the lattice constant of the microstructure was measured to be 3.9 μm. The phase modal birefringence in this MSF was measured to be about 8 10^{-4} at 1550 nm as a result of the asymmetric shape of the microstructure [24].

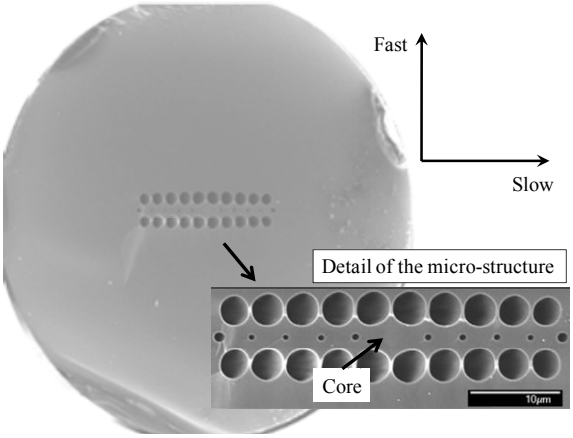

Figure 6-26: Configuration of the MSF with a detail of the microstructure as inset. The orientation of the fast and slow axis is depicted.

FBGs written in an MSF

The fabrication of FBGs in micro-structured fibres is not always straightforward, because the numerous air-silica interfaces can compromise the ability to form an interference pattern in the core with transverse laser inscription beams. Nevertheless, the compatibility of this particular type of micro-structured fibres with conventional UV FBG inscription set-ups has been described in [25, 26].

As discussed in section 2.3, the MSF is birefringent. When unpolarized light is launched into the MSF, it yields a Bragg peak for each of the two orthogonally polarized modes, that propagate in the fibre. The peak separation is related to the phase modal birefringence *B* by

$$\lambda_{B,fast} = 2\left(n_{eff} - \frac{B}{2}\right)\Lambda$$
$$\lambda_{B,slow} = 2\left(n_{eff} + \frac{B}{2}\right)\Lambda \qquad \textbf{6-1}$$

These FBGs will encode birefringence and therefore strain information into the wavelength of the Bragg resonance peaks. These peaks are very well separated and can be straightforwardly identified because of large birefringence. Since the fibre birefringence can be made insensitive to temperature, the spectral distance between both Bragg peaks will remain constant during temperature changes and will only change with applied strain. This leads to the sensing principle illustrated in Figure 6-27 [27].

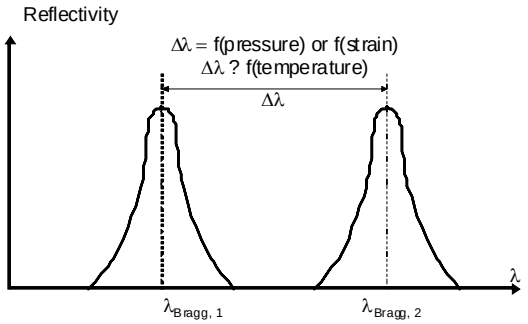

Figure 6-27: Sensing principle of an FBG inscribed in highly birefringent MSF [27].

Owing to the temperature insensitivity, the sensors will not require temperature correction mechanisms. This is in contrast to conventional optical strain sensors, which require compensation schemes for temperature cross-sensitivity. First measurements by Geernaert et al. [26] revealed that the differential temperature sensitivity $\Delta\lambda/\lambda$ (temperature) can be around 0.25 %, which is at least one order of magnitude lower than in conventional birefringent fibres. So far, only a few papers have been published which examine the possibility of applications of MSFs as hydrostatic pressure, strain or bend sensors. These works concentrate rather on investigations of the fibre sensing characteristics than on the modelling and on the design of sensor structures [28, 29].

In microstructured optical fibres, the air holes in the cladding can have a significant influence on the Bragg peak wavelength shifts, and the centre of strain approximation [30] is not necessarily valid. In general, when an external load is applied, a distribution of strain will exist in the core region of the MSF, which is not always accurately represented by the strain in the centre of the core. In order to rigorously assess the change of the effective refractive indices by strain distributions in an MSF, a 3-dimensional simulation of the fibre needs to be considered in which both the mechanical loading and the optical wave equations can be solved. Such simulations demand a high computing capacity, especially when embedded fibres are considered, and rely on an accurate knowledge of all the relevant optical and mechanical material parameters of the fibre. Instead of such a theoretical approach, we have chosen to compare the 3 FBG technologies experimentally and embedded them in composite test samples.

Calibration of FBGS written in MSF

Axial strain sensitivities for FBGs in various micro-structured fibres have already been reported [31, 32] and the transverse strain sensitivity for the MSF used in this paper was investigated in [24]. The transverse line load sensitivity for an FBG in this MSF was characterized experimentally up to a transverse load of 3 N/mm

(Figure 6-28) between two parallel plates in a test bench for the calibration of FBG-sensors (a modified set-up of Fernandez et al. [33] was used for this calibration, see Section 2. 4. 1. b.). The FBG spectra were measured with an amplified spontaneous emission (ASE) source, a circulator, and an optical spectrum analyzer (OSA). The Bragg peak wavelengths were detected with the built-in peak detection of the OSA. Reasonable agreement with the outcome of the FEM simulations was observed(Figure 2-21). Nevertheless, the possibility of controlling the applied load and its uniformity over the length of the FBG was limited.

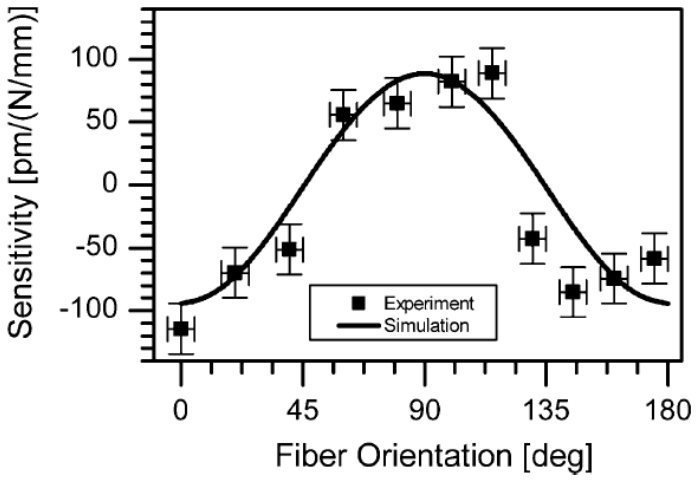

Figure 6-28: Transverse line load sensitivity for the Bragg peak separation of an FBG in a bare MSF versus MSF orientation. Zero degrees corresponds to a vertical load parallel to the slow axis of the MSF.

6. 3. 3. MSF and bow-tie fibre technology embedded in carbon epoxy samples

6. 3. 3. a. Optical fibre technologies

The first type of Bragg grating is written in a**n 80 µm birefringent bow-tie fibre** (bow-tie FBG) from Fibercore inc.. As discussed in section 2. 3., the birefringence in this fibre is induced by stress applying parts (SAPs) of boron-doped silica present in the fibre cladding (Figure 6-29, (A)). The temperature expansion coefficient of these 10 mol% boron-doped parts differs significantly from the temperature expansion coefficient of the fibre core and cladding. This results in temperature induced stresses during the cooling down of the fibre, which induces material birefringence in and around the core. At 1550 nm, the phase modal birefringence in this bow-tie fibre is $3\ 10^{-4}$.

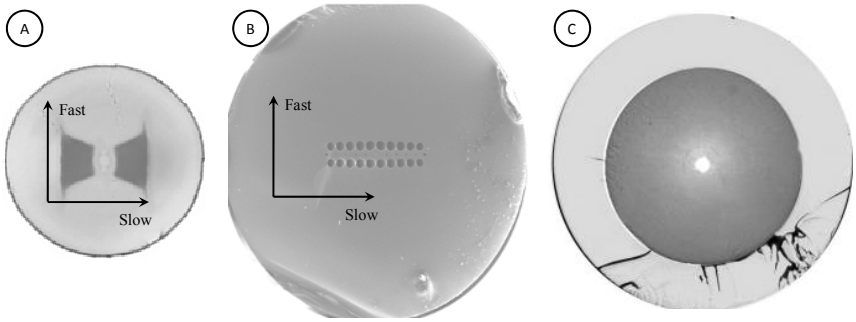

Figure 6-29: Overview of the different fibre technologies used in this section. For the birefringent fibres, the orientation of the slow and fast axis is shown.

The second grating type is an FBG written in the 125 µm **micro-structured optical fibre** (MSF FBG) as discussed in the previous paragraphs.
Finally, the response of these technologies is compared with a reference high strength draw tower grating (provided by FBGs Technologies in Jena, Germany). An **80 µm draw tower fibre Bragg grating** (DTG) technology has been used (Figure 6-29, (C)). Without going into detail, a DTG is written directly during the drawing process of the optical fibre, using one single laser pulse with a special FBG inscription set-up which is mounted onto the fibre draw tower. The FBG is inscribed in the fibre core before any primary coating material is applied. This avoids stripping of the coating to inscribe the FBG, which results in fibre optic sensors with very high tensile strength [34]. We used a single-mode fibre with a highly Germanium doped core (approx. 18 mol %) with a diameter of 6 µm and an 80 µm cladding. The coating material is a special ORMOCER® (Organic Modified Ceramic) that features excellent adhesion with both the fibre glass and the composite material. The total diameter of the coated fibre is approximately 120 µm.

6. 3. 3. b. Carbon fibre reinforced plastic sample preparation

Manufacturing and sensor placement

The three fibre types of Bragg sensors have been embedded in a carbon fibre epoxy laminate (M55J/M18 material from Hexcel inc.), fabricated using the autoclave technology. The composite sample had a $[0]_{16}$ lay-up with a total thickness of 1.54 mm. The optical fibres were embedded between the 2nd and the 3rd layer of a total of 16 layers (thickness: 0.1 mm/layer) (see Figure 6-30). The dimensions and positions of the fibres are depicted in Figure 6-31. All FBGs had a length of 8 mm. The slow axis of the MSF and the bow-tie fibre were both oriented parallel with the

surface of the composite panel (axis y). This orientation was established during a qualitative calibration procedure of each sensor as discussed in Section 4. 2. 2. d.

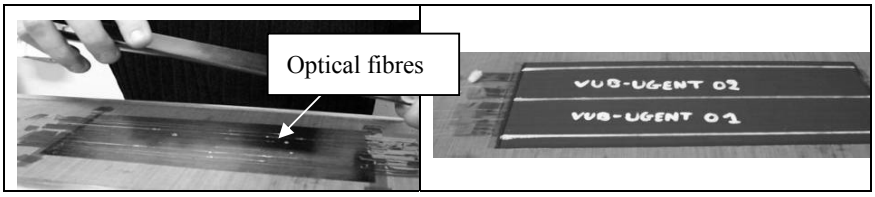

Figure 6-30: Left: lay-up of the samples, embedding the sensors between layer 2 and 3. Right: the samples fabricated by the autoclave technology before cutting.

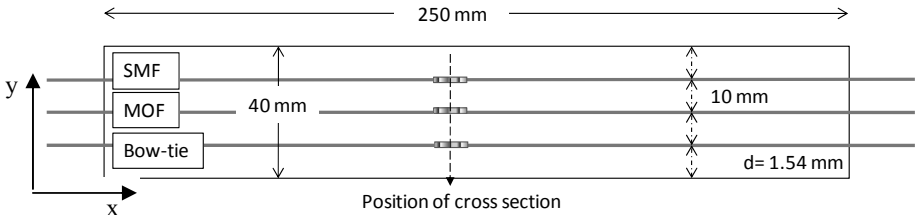

Figure 6-31: Position of the different types of fibres/FBGs along the width of the sample, with a distance of 10 mm in between the different fibres

Post fabrication sample evaluation

The reflection spectra of the bow-tie and MSF FBG after and before embedment, can be found in Figure 6-32 and Figure 6-33.

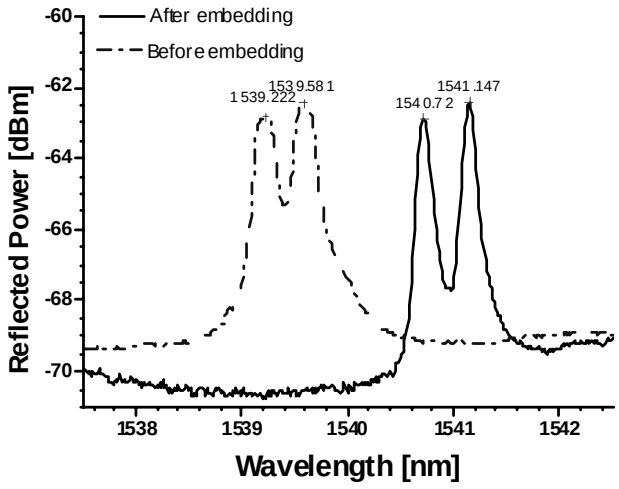

Figure 6-32: Spectra of the embedded bow-tie FBG.

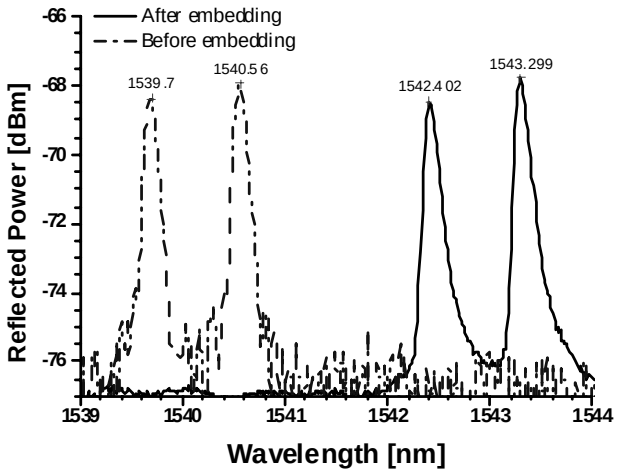

Figure 6-33: Spectra of the embedded MSF.

All spectra in Figure 6-32 and Figure 6-33, indicate no distortion of the Bragg peaks. After all experiments had been finished, the orientation and the embedding depth of all the optical fibres were determined at the FBG location. Figure 6-34 shows the microscopic images of the embedded micro-structured fibre technology. No distortion (e.g. resin eye) of the host material can be observed. It is clear that the optical fibres are homogeneously surrounded by reinforcement fibres. Scratches on the pictures are due to the polishing process and do not stem from any induced damage in the composite material. Similar results were found for the bow-tie fibre and for the reference draw tower fibre.

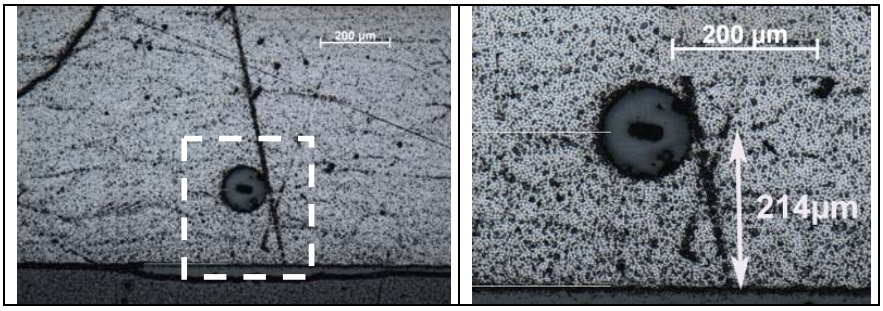

Figure 6-34: Microscopic images of the cross section of the first sample at the FBG location, showing the depth and orientation of the embedded MSF in sample 1 at the position of FBG 1.

In Table 6-2 and Table 6-3, the embedding depths and the orientations of the slow axes with respect to the sample's (x, y)-plane are noted. The embedding depth was measured as the distance between the bottom surface of the sample to the core of the optical fibre. A difference in embedding depth can be noticed for the bow-tie FBG and the MSF FBG in both samples. On the one hand, this is caused by the size differences between both optical fibres (80-125 µm), and on the other hand by the size difference of the optical fibres compared to the reinforcement fibres (3-5 µm) of the composite laminate. As such, when placing the fibre sensors during lay-up, there is a tendency to press the smallest fibre deeper into the reinforcement fibres. The orientation of bow-tie and micro-structured fibre is almost the same for the first sample, but differ a lot for the second sample 2 (the bow-tie FBG was accidentally oriented according to the fast axis). This was taken into account when analyzing the results of the transverse load test.

Table 6-2: Embedding depth of the optical fibres.

	Reference DTG [µm]	bow-tie FBG [µm]	MSF FBG [µm]
Sample 1	182	150	214
Sample 2	228	161	240

Table 6-3: Orientation of the optical fibres

	bow-tie FBG [deg]	MSF FBG [deg]
Sample 1	13	15
Sample 2	60	12

Since no deformed Bragg peaks (Figure 6-32 and Figure 6-33) and no local distortion of the composite sample (Figure 6-34) was observed, we can state that the embedding of the fibres was conducted successfully.

6. 3. 3. c. The response of the embedded FBGs under various loading conditions

Similar tests, as described in Chapter 5, were used to compare the response of the different sensors. Three different loading conditions were used: a bending test, a transverse load test, and a thermal test. Since different fibre technologies were embedded in the same sample, the width of the sample (40 mm) became too large to perform a reliable standard tensile test. Therefore, a four point bending test was chosen instead. Moreover, this test is representative for an actual load condition of a structural component such as an airplane wing. The transverse load test allows comparing the transverse sensitivities of the different sensor technologies. Finally,

the composite panel has been thermally cycled to assess the differences in cross-sensitivity to temperature. In all experiments, the repetition rate of the grating measurements was much higher than the time scale of the loading. As a result, all measurements are considered to be static.

For the mechanical loading experiments, the applied load was measured via an electrical load cell. The FBG spectra and Bragg peak wavelengths were measured with an ASE-source (Amplified Spontaneous Emission, non-flattened) and a commercial FBG interrogator with a resolution of 1 pm. The embedded fibres were spliced to fibre pigtails. (Figure 6-35)

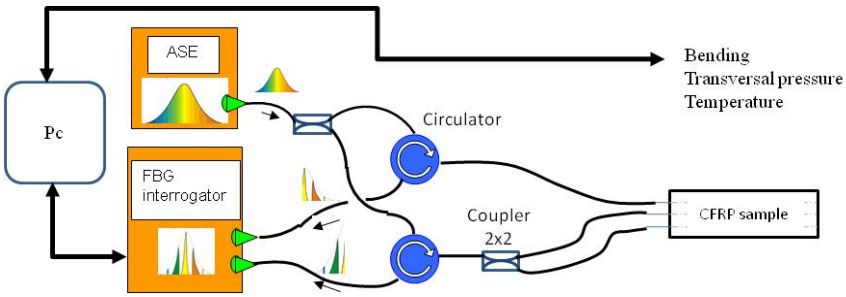

Figure 6-35: The interrogation set-up. The FBG spectra and the Bragg peak wavelengths are detected with a commercial FBG interrogator

6. 3. 3. d. Four point bending test

The maximum stress can be found at the outer surface of the sample. For ease of comparison, the embedding depth has been considered already in Figure 6-36. The curves show similar slopes for both sensors. The MSFs have the same orientation in both samples (Table 6-3) and show equal sensitivities during bending (fitted values in Table 6-4). The orientation of the bow-tie gratings, however, is different. The sensitivity of the less favourably oriented bow-tie in sample 2 is ~10% lower than in the first sample. Where both bow-tie and micro-structured fibre almost have the same orientation in sample 1, the sensitivity is slightly different (~8%).

Table 6-4: FBG sensitivities versus axial bending strain of the composite material

	Sample 1 [pm/με]	Sample 2 [pm/με]
Bow-tie slow axis	1.115	0.998
Bow-tie fast axis	1.103	0.996
MSF slow axis	1.020	1.029
MSF fast axis	1.011	1.023

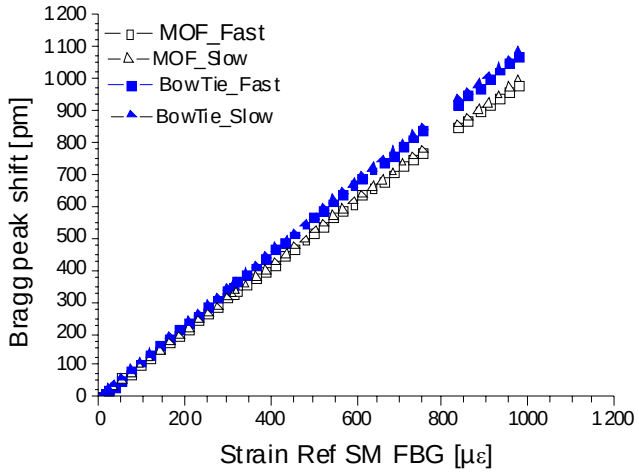

Figure 6-36: Wavelength shifts measured during the four point bending test for the different embedded FBGs vs. the strain measured by the reference DTG for Sample 1.

6. 3. 3. e. Transverse pressure test

In this test, metal blocks were fixed to the surfaces of the test samples and pressed between two polished metal plates of a universal testing machine (as discussed in Section 5. 5.). A rubber slice was put between the metal plates and the metal pressure blocks to improve the homogeneity of the transverse pressure over the surface of the composite sample.

The transverse strain response of the two grating types shows moderate differences (Figure 6-37). The transverse strain is derived from the applied transverse load and the material's transverse Young modulus of 6.3 GPa (Table 2-).

Table 6-5: FBG sensitivities versus transverse strain of the composite material

	Sample 1 [pm/με]	Sample 2 [pm/με]
Bow-tie slow axis	0.089	0.061
Bow-tie fast axis	0.068	0.052
MSF slow axis	0.058	0.047
MSF fast axis	0.043	0.036
Bow-tie peak separation	-0.022	-0.010
MSF peak separation	-0.014	-0.010

The transverse sensitivities of the FBG in the bow-tie fibre are slightly higher. This difference can be partly attributed to the smaller cladding diameter of the bow-tie fibre. For the Bragg peak separation, the sensitivities of the MSF FBG and the bow-

tie FBG are in reasonable agreement (Figure 6-37). The current differences between the MSF FBG and the bow-tie FBG can be related to the different orientation of the polarization axes at the FBG location.

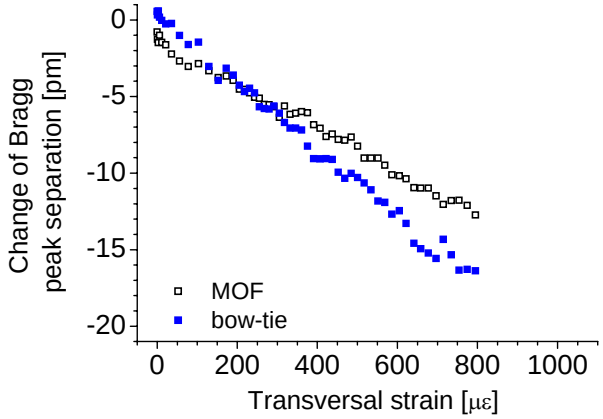

Figure 6-37: Change of the peak separation vs. transversely applied strain in the FBG for the MSF and bow-tie fibres in sample 1.

6. 3. 3. f. Temperature test

When the temperature change ΔT is considered zero, Equation 2-11 can be adapted in such a way that the normalized peak separation can be seen as a measure for the transverse strain difference.

$$\frac{\Delta\lambda_{B,fast} - \Delta\lambda_{B,slow}}{\lambda_{B,0}} = \frac{1}{2} n_{eff}^2 (p_{12} - p_{11})(\varepsilon_{fast} - \varepsilon_{slow}) \qquad \textbf{6-2}$$

This difference in transverse strain leads to strain-induced phase modal birefringence in the fibre core, which leads to a Bragg peak separation. However, whenever temperature is not constant, this measurement is compromised. Since the phase modal birefringence in both fibres has a different origin, the thermal behaviour of the Bragg peak wavelength separation is also different. The stress-induced material birefringence in a Bow-tie fibre is inherently temperature dependent, whereas the geometrical birefringence in the MSF is far less temperature sensitive and can even be zero at a given wavelength [23].

To evaluate the possibility of such a sensor, one of the samples was heated in an oven up to 120°C and then slowly cooled down. During this cooling phase, the Bragg peak wavelength separation for the MSF FBGs and the bow-tie FBGs were monitored (Figure 6-38).

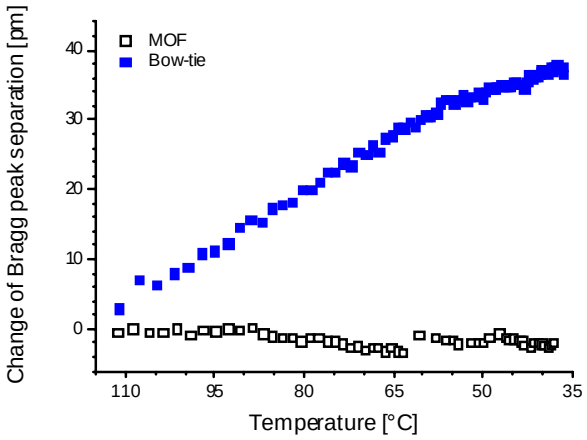

Figure 6-38: Change of the Bragg peak separation in the FBG in the MSF and Bow-tie vs. temperature.

Figure 6-38 shows that the linear change of the Bragg peak separation due to temperature is much smaller in the micro-structured fibre (0.026 pm/°C) than in the Bow-tie fibre (-0.42 pm/°C).
Therefore, it can be stated that the Bragg peak separation in a highly birefringent micro-structured fibre can provide a temperature independent measurement of transverse strain in the composite material.

6. 3. 4. Conclusion

The response of FBGs written in conventional birefringent fibre and in highly birefringent micro-structured optical fibre embedded in a composite material, was compared.
First, the embedding procedure was evaluated and evidenced that it is possible to embed the different fibre technologies into fibre reinforced thermosetting composites without distorting the material significantly. No resin rich areas were created in the samples, and the optical fibres were homogeneously surrounded by the reinforcement fibres.
Then, the mechanical axial bending strain sensitivities of the fibres' Bragg wavelengths were determined and were found to be slightly different for the micro-structured fibre and the Bow-tie fibre (approx. 8%). The micro-structured fibre reported here was not optimized yet to feature high sensitivities to axial or transverse strain, but has nevertheless already similar sensitivities as conventional birefringent fibres.

Thirdly, the response to temperature changes show important differences (Bow-tie FBG: -0.42 pm/°C, MSF FBG: 0.026 pm/°C), which is well known to stem from the different origin of the birefringence in the different fibre types. The MSF FBG can be tuned to operate almost independently of temperature.

Thus, it was evidenced that micro-structured fibres can be applied for structural integrity monitoring purposes in composite materials. The design flexibility of micro-structured fibres can now be exploited to obtain fibres containing Bragg grating sensors which are sensitive to single or to multiple stress components, while being almost insensitive to temperature. For example, a pre-defined *TC*-matrix (Chapter 4 and 5) can be the start point of designing a micro-structured fibre with Bragg grating to conduct in-situ high resolution strain field mapping inside composite structures.

6. 4. DYNAMIC TESTING

Up to this point, this work only contains quasi-static experiments, which is sufficient in terms of calibrating and proving the feasibility of a multi-axial strain sensor. However, for real time structural monitoring of e.g. spacecraft structural elements, one has to switch to dynamic measurements. Therefore, a dynamic interrogator system has been designed by XenIC's during the MASSFOS-project. The schematic representation of this interrogator is shown in Figure 6-39. It consists of two spectrometers with a 512 pixel array, one for each polarization mode. The light is generated by a depolarized SLED and travels towards the sensor on which it diffracts; part of the light is back-reflected towards the interrogator. The system has a wavelength range of 70 nm (from 1515 to 1585 nm) and the wavelength resolution is ~5pm. It should be noted that for this system, every part should have the polarization maintaining label.

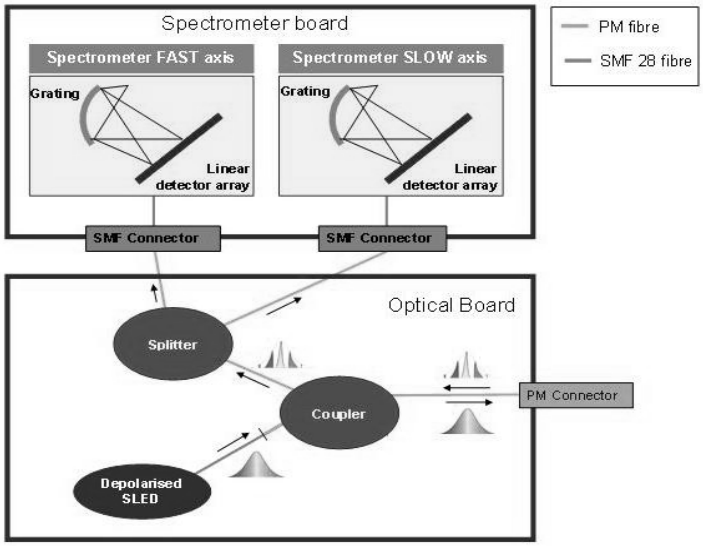

Figure 6-39: Design of the dynamic interrogator

Several preliminary experiments have been executed and some of these are discussed in the following paragraphs. Figure 6-40 and Figure 6-41 respectively, show recorded Bragg spectra for the '512 pixel array' system and the commercial interrogation system (FBG scan 607) used throughout this work. For the MASSFOS interrogator, the Bragg spectrum is represented by a limited number of measurement points. Using the best possible settings of this interrogator, a difference in Bragg

peak separation of about 40pm till 50pm is obtained, compared to the FBG scan unit.
To overcome this problem, a 1024 array is presently being built by XenIC's.

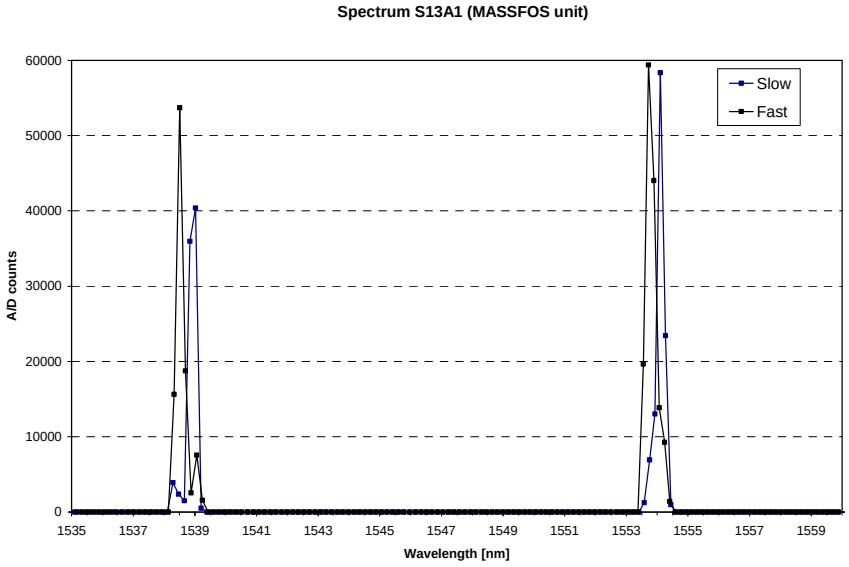

Figure 6-40: Spectrum measured with the MASSFOS unit (512 pixel array)

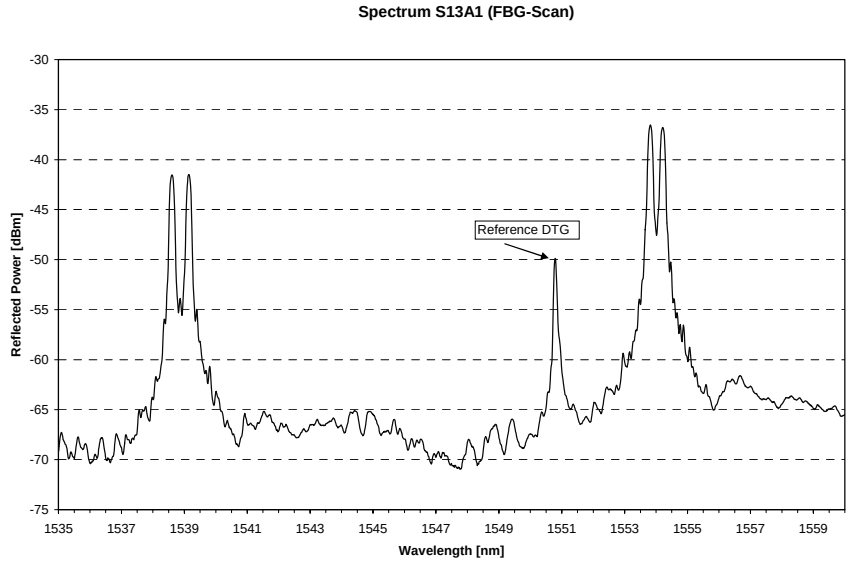

Figure 6-41: Spectrum measured with the FBG-Scan unit from FOS&S.

Due to the poor resolution, the emphasis of these experiments is mainly put on the possibility of measuring high frequency signals and less on quantitatively determining the different strain components.

6. 4. 1. Resonance search track and dwell

The experiments, discussed in this section, were carried out on a $[0_2,90_2]_{6s}$ and $[\pm45_2,0_2,90_2]_s$ sample with embedded MAxS-sensor clamped at one side in a shaker set-up. The shaker set-up from Ling Dynamic Systems (LDS V406/8 PA 100E, see Figure 6-42) has a frequency range of 5 to 9000Hz and a maximum acceleration sine peak of 100g. The applied load is a so-called 'resonance search track and dwell' (RSTD) from 5Hz till 2000Hz. The actuator acceleration was held constant at 1g.
Fast Fourier Transformation (FFT) is performed on data obtained from the MAXs sensors at these high loading frequencies. The highest traceable eigenfrequency beneath 2kHz of both (thin and thick) samples was approximately 1.4kHz.

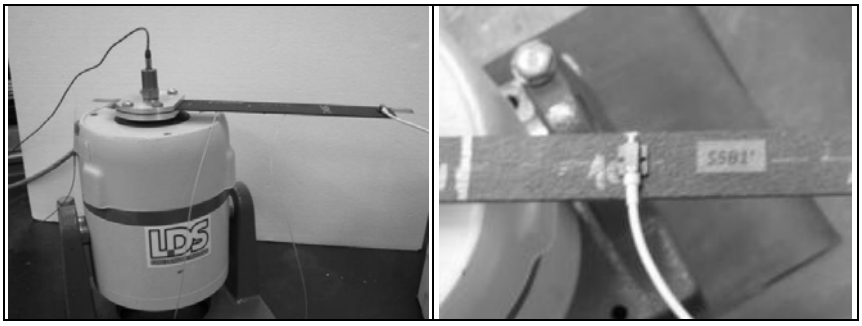

Figure 6-42: Set-up of the high dynamic tests with the composite test sample clamped at one side (left). Detail of the miniature dynamic accelerometer (right).

As reference measurement, a miniature accelerometer is positioned at a distance of 10 cm from the clamp, on top of the composite sample (Figure 6-42, left). The acceleration was registered together with the wavelength data (measured with the MASSFOS unit). Figure 6-43 shows the signals measured with the accelerometer on top of the $[0_2,90_2]_{6s}$ sample, and the MAxS sensor embedded in the sample. The sampling rate of the MASSFOS unit was set at approximately 10kHz (i.e. maximum sampling frequency). For each measurement, i.e wavelength shifts, and acceleration, the frequency of the signals was derived by executing an FFT.

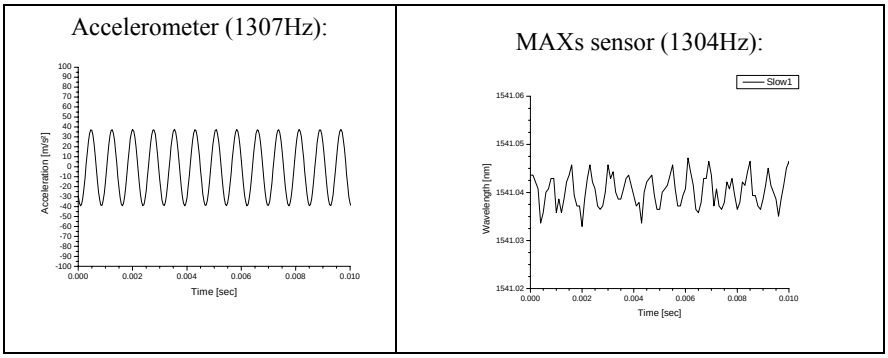

Figure 6-43: Example of the raw signal of the MAxS-sensor (right) and the accelerometer (left) for a sample with lay-up $[0_2,90_2]_{6s}$ and the accelerometer positioned at 10 cm from the clamp.

Table 6-6: Summary of eigenfrequencies determined with an accelerometer and with the MAXs sensor for the $[0_2,90_2]_{6s}$ sample

Distance accelerometer	10 cm			
Freq. Accelerometer [Hz]	57	174	306	1306
Freq. MAxS sensor [Hz]	57	174	305	1305

As shown in Table 6-6, the frequencies, calculated based on the MAxS-sensor's wavelength data and the accelerometer data, match very well. A very small difference can be seen for the higher frequencies, since these vibrations have a rather low amplitude which leads to small wavelength shifts.
Similar results were obtained for the second sample. The MAxS sensor can be used to measure (maximum) eigenfrequencies in the order of magnitude of 1.4 kHz.

6. 4. 2. Shock loading response

Using the same experimental set-up, a shock load has been applied on the composite samples. The structural response of a $[\pm 45_2,0_2,90_2]_s$ sample during a 15g shock loading has been examined with the MASSFOS unit. The response is clear and shows that when monitoring at 10 kHz, it is possible to reproduce the same signal as measured with the accelerometer (Figure 6-44). In addition, the MAxS-sensor is able to reproduce the strains induced during such a test. During this shock response an axial strain of approximately ±110 με appeared.

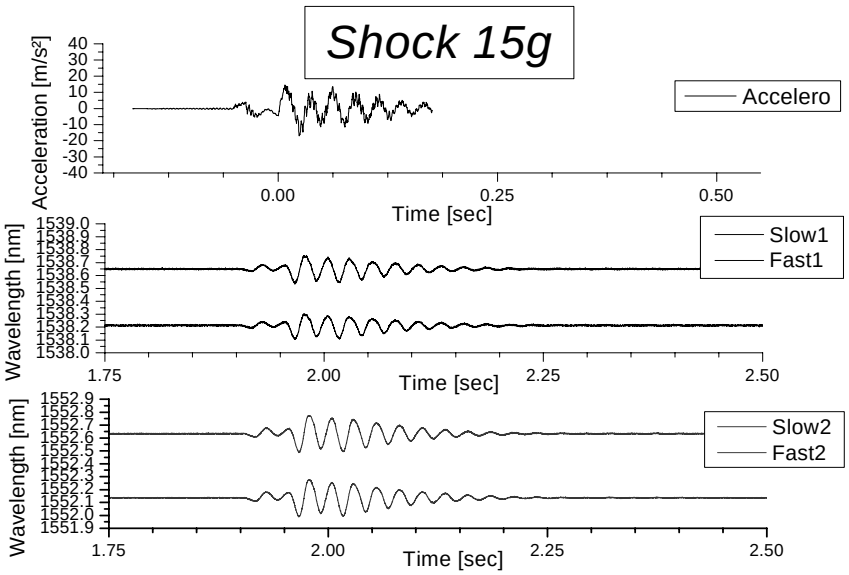

Figure 6-44: Example of the response to a shock of 15g for a $[\pm 45_2, 0_2, 90_2]_s$ sample with the accelerometer positioned at 7.5 cm from the clamp.

6. 4. 3. Conclusions

For real time structural monitoring one has to switch to dynamic measurements. This section did not had the intention to give an thorough overview of existing dynamic interrogators. However, a dynamic interrogator system has been designed during the MASSFOS-project with which several preliminary experiments were conducted. The system has a wavelength range of 70 nm (from 1515 to 1585 nm), a wavelength resolution of ~5pm, and a Bragg spectrum which is represented by a limited number of measurement points. The last two properties are the limited factors in terms of strain resolving power, especially for the transverse strain components. During the writing of this dissertation, both properties were improved by the use of a 1024 pixel array instead of the present 512 pixel array.

The scope of the experiments was put on frequency measurements during a 'search track and dwell' procedure for determining the eigenfrequencies of a composite sample with embedded MAxS-sensor. Similarities between the frequency measurement of the MAxS-sensor and the externally mounted accelerometer could be found for all eigenfrequencies up to 2 kHz. During a shock loading response the measured signal is more complicated, though, the same frequency content was found in the signal of the accelerometer and the MAxS-sensor.

6. 5. REFERENCES

1. Available from: http://www.hexcel.com/.
2. Fibercore, *Factnote 4.1.2: The Physical properties of Silica and UV Cure Axrylate Coating Packages*. 2004: Chilworth, UK.
3. Huang, C., Bao, X., Zeng, X., Arcand, A., and Lee-Sullivan, P. *Simultaneous temperature and strain monitoring of composite cure using a Brillouin-scattering-based distributed fiber optic sensor*. in *Proceedings of the Smart Structures and Materials 2001 Conference*. 2001. Newport Beach, Ca (USA).
4. Bao, X., Dhliwayo, J., Heron, N., Webb, D.J., and Jackson, D.A., *Experimental and theoretical studies on a distributed temperature sensor-based on Brillouin scattering.* Journal of Lightwave Technology, 1995. **13** (7): p. 1340-1348.
5. Guemes, J.A. and Menendez, J.M., *Response of Bragg grating fiber-optic sensors when embedded in composite laminates.* Composites Science and Technology, 2002. **62** (7-8): p. 959-966.
6. Okabe, Y., Yashiro, S., Tsuji, R., Mizutani, T., and Takeda, N., *Effect of thermal residual stress on the reflection spectrum from fiber Bragg grating sensors embedded in CFRP laminates.* Composites Part a-Applied Science and Manufacturing, 2002. **33** (7): p. 991-999.
7. Kuang, K.S.C. and Cantwell, W.J., *In situ process monitoring of a thermoplastic-based fibre composite using optical fibre sensors.* Smart Materials & Structures, 2002. **11** (6): p. 840-847.
8. Li, C.S., Cao, M.S., Wang, R.G., Wang, Z.P., Qiao, Y.J., Wan, L.B., Tian, Q., Liu, H.T., Zhang, D.Q., Liang, T.X., and Tang, C.H., *Fiber-optic composite cure sensor: monitoring the curing process of composite material based on intensity modulation.* Composites Science and Technology, 2003. **63** (12): p. 1749-1758.
9. Sorensen, L., Gmur, T., and Botsis, J. *Residual strain development in an AS4/PPS thermoplastic composite measured using fibre Bragg grating sensors*. in *2nd International Conference on Composites Testing and Model Identification (CompTest 200)*. 2004. Bristol, UK.
10. *personal communications* with FOS&S
11. Jung, K. and Kang, T.J., *Cure monitoring and internal strain measurement of 3-D hybrid braided composites using fiber Bragg grating sensor.* Journal of Composite Materials, 2007. **41** (12): p. 1499-1519.
12. Jung, K., Kang, T.J., Lee, B., and Kim, Y., *Estimation of residual strain and stress in interply hybrid composite using fiber bragg grating sensor.* Fibers and Polymers, 2007. **8** (4): p. 438-442.

13. Kim, B., Nesbitt, A., Walker, W., and P.J., W. *Optimization and Strain Measurements of FBG Sensors Embedded in Carbon Composites*. in *Proceedings of ECCM 13, 13 th European Conference on Composite Materials*. 2008. Stockholm, SWEDEN.

14. Mulle, M., Collombet, F., Olivier, P., and Grunevald, Y.H., *Assessment of cure residual strains through the thickness of carbon-epoxy laminates using FBGs, Part I: Elementary specimen.* Composites Part a-Applied Science and Manufacturing, 2009. **40** (1): p. 94-104.

15. Luyckx, G. and Voet, E., *MASSFOS: Summary report*. 2009: Gent, BELGIUM.

16. Available from: http://www.hexcel.com/NR/rdonlyres/7E68292D-4EDE-4CA7-A73D-AFA4C8CE0248/0/HexPly_M18_eu.pdf.

17. Gosse, J.H., *Strain invariant failure criteria for fiber reinforced polymeric composite materials*. 2009.

18. Cartie, D.D.R., Dell'Anno, G., Poulin, E., and Partridge, I.K. *3D reinforcement of stiffener-to-skin T-joints by Z-pinning and tufting*. in *4th Conference on Fracture of Polymers, Composites and Adhesives*. 2005. Les Diablerets, SWITZERLAND.

19. Florous, N.J., Saitoh, K., Varsheney, S.K., and Koshiba, M., *Fluidic sensors based on photonic crystal fiber gratings: Impact of the ambient temperature.* Ieee Photonics Technology Letters, 2006. **18** (21-24): p. 2206-2208.

20. Nasilowski, T., Berghmans, F., Geernaert, T., Chah, K., Van Erps, J., Statkiewicz, G., Szpulak, M., Szewski, J., Golcjuch, G., Martynkien, T., Urbanczyk, W., Mergo, P., Makara, M., Wqicik, J., Chojetzki, C., and Thienpont, H. *Sensing with photonic crystal fibres*. in *Proceedings of the IEEE International Symposium on Intelligent Signal Processing*. 2007. Alcala de Henares, SPAIN.

21. Urbanczyk, W., Martynkien, T., Szpulak, M., Statkiewicz, G., Olszewski, J., Golojuch, G., Wojcik, J., Mergo, P., Makara, M., Nasilowski, T., Berghmans, F., and Thienpont, H. *Photonic crystal fibers: new opportunities for sensing - art. no. 66190G*. in *Proceedings of the 3rd European Workshop on Optical Fibre Sensors*. 2007. Naples, ITALY.

22. Szpulak, M., Olszewski, J., Martynkien, T., Urbanczyk, W., and Wojcik, J., *Polarizing photonic crystal fibers with wide operation range.* Optics Communications, 2004. **239** (1-3): p. 91-97.

23. Martynkien, T., Szpulak, M., and Urbanczyk, W., *Modeling and measurement of temperature sensitivity in birefringent photonic crystal holey fibers.* Applied optics, 2005. **44** (36): p. 7780-7788.

24. Geernaert, T., Luyckx, G., Voet, E., Nasilowski, T., Chah, K., Becker, M., Bartelt, H., Urbanczyk, W., Wojcik, J., De Waele, W., Dearieck, J., Terryn, H., Berghmans, F., and Thienpont, H., *Transversal Load Sensing With*

Fiber Bragg Gratings in Microstructured Optical Fibers. Ieee Photonics Technology Letters, 2009. **21** (1-4): p. 6-8.

25. Geernaert, T., Nasilowski, T., Chah, K., Becker, M., Rothhardt, M., Szpulak, M., Olszewski, J., Poturaj, K., Wojcik, J., Urbanczyk, W., Terryn, H., Bartelt, H., Berghmans, F., and Thienpont, H. *The fabrication and characterization of Fiber Bragg Gratings in highly birefringent Photonic Crystal Fibers for sensing applications - art. no. 69900C*. in *Proceedings of the Conference on Photonic Crystal Fibers II*. 2008. Strasbourg, FRANCE.

26. Geernaert, T., Nasilowski, T., Chah, K., Szpulak, M., Szewski, J., Statkiewicz, G., Wojcik, J., Poturaj, K., Urbanczyk, W., Becker, M., Rothhardt, M., Bartelt, H., Berghmans, F., and Thienpont, H., *Fiber Bragg gratings in germanium-doped highly birefringent microstructured optical fibers.* Ieee Photonics Technology Letters, 2008. **20** (5-8): p. 554-556.

27. Berghmans, F., Degrieck, J., De Waele, W., and Landuyt, S., *proposal FWO-project: Multi-axial multi-parameter embedded sensors for strain mapping and damage detection in thermoset composite materials based on micro-structured optical fibres*. 2009: Brussel, BELGIUM.

28. Statkiewicz, G., Martynkien, T., and Urbanczyk, W., *Measurements of modal birefringence and polarimetric sensitivity of the birefringent holey fiber to hydrostatic pressure and strain.* Optics Communications, 2004. **241** (4-6): p. 339-348.

29. Szpulak, M., Martynkien, T., and Urbanczyk, W., *Effects of hydrostatic pressure on phase and group modal birefringence in microstructured holey fibers.* Applied optics, 2004. **43** (24): p. 4739-4744.

30. Lawrence, C.M., Nelson, D.V., Udd, E., and Bennett, T., *A fiber optic sensor for transverse strain measurement.* Experimental Mechanics, 1999. **39** (3): p. 202-209.

31. Martelli, C., Canning, J., Groothoff, N., and Lyytikainen, K., *Strain and temperature characterization of photonic crystal fiber Bragg gratings.* Optics Letters, 2005. **30** (14): p. 1785-1787.

32. Frazao, O., Carvalho, J.P., Ferreira, L.A., Araujo, F.M., and Santos, J.L., *Discrimination of strain and temperature using Bragg gratings in microstructured and standard optical fibres.* Measurement Science & Technology, 2005. **16** (10): p. 2109-2113.

33. Fernandez, A.F., Ottevaere, H., Van Ierschot, C., Panajatov, K., Berghmans, F., and Thienpont, H. *Multi-parameter force sensing with fiber Bragg grating sensors*. in *Proceedings of Symposium IEEE/LEOS Benelux Chapter*. 2002. Amsterdam, THE NETHERLANDS.

34. Rothhardt, M., Chojetzki, C., and Mueller, H.R. *High mechanical strength single-pulse draw tower gratings*. in *International Conference on Applications of Photonics Technology*. 2004. Ottawa, CANADA.

Chapter 7 : CONCLUSIONS AND RESEARCH PERSPECTIVES

7. 1. OVERVIEW OF THE WORK

The optical fibre Bragg grating sensor can be considered as the optical counterpart of electrical resistance strain gauges. A lot of advantages favour the use of this optical alternative. Therefore, optical fibre Bragg grating sensors have found wide acceptance as reference strain measurements in research applications, and for monitoring of all kind of structures. A standardized method to mount this type of sensor on top of structures is already available on the market.

There are numerous publications addressing the use of FBGs for strain monitoring in a direct or indirect way (with transduction mechanism). Most of these publications consider the FBG sensor as a uni-axial sensor. This approach is justified for surface mounted sensors; however, it is not applicable for embedded sensors. Embedded sensors have the advantage of being integrated in the structure at the region of interest (smart materials), and of being protected from external influences by the structure. These advantages explain the high interest of several research groups worldwide towards embedded sensors.

Notwithstanding the advantages of embedded sensors, a lot of difficulties remain. For example, the impact of the sensor on the host material in terms of strain field disturbance and host material distortion needs to be considered profoundly. A uni-axial sensor does not give sufficient insight in the size and type of impact on the host material. A multi-axial strain sensor can possibly help to investigate and explain these effects.

In this work, all aspects of non-embedded as well as embedded optical fibre Bragg gratings were considered. It is the first time that bow-tie FBGs are considered in depth.

- Calibration procedures from literature were critically evaluated and optimized based on analytical formulations (e.g. rotation of the optical and mechanical eigenaxes).
- By diametrical loading of the fibre and relating the induced strain with the resulting wavelength shift, the strain optic coefficients of a LoBi fibre were determined.
- After a critical review of multi-axial strain sensors discussed in literature, a novel design of a multi-axial strain sensor was proposed, using two FBGs at different wavelengths. One of the FBGs was covered with a capillary to isolate it from transversal stress. The resolution of this sensor met the requirements of the aircraft and spacecraft industry.
- It was clearly demonstrated theoretically and experimentally that the strain field present inside the composite material and this inside the embedded

optical fibre sensor are different. The relation between both strain fields is determined by a strain transfer coefficient matrix (*TC*-matrix).

- The theoretical influence of several mechanical properties of the composite material and the type of optical fibre sensor with Bragg grating on the *TC*-matrix was considered. An experimentally optimized matrix was proposed.
- An extended test program confirmed the feasibility of using the strain transfer coefficient matrix to relate the strain field in the core of the optical fibre Bragg grating with that present in the composite material.

An overview of the different chapters in this book and main realisations and conclusions is given below.

7. 1. 1. Advanced strain sensing using optical fibre Bragg gratings

The spectral response of an FBG exposed to a multi-axial strain field was theoretically determined using the photo-elastic effect. The photo-elastic effect describes the changes in optical properties (refractive index) of a transparent dielectric when it is subjected to mechanical strain. For low birefringent fibres with Bragg grating, axial strain and thermal loading cause the Bragg spectrum to homogenously shift to higher wavelengths, transverse strains cause a broadening of the Bragg spectrum which will eventually split in two separate Bragg peaks. Thus, the optical fibre is becoming highly birefringent. The same effects were also observed for fibres which are already highly birefringent. However, these FBGs already have a spectrum with two separate peaks in the unloaded condition. Transverse strain components will cause a change in separation distance of both peaks. In both cases, the change in spectrum contains information on the strain components present at the core of the optical fibre.

To clearly understand the influence of each individual strain component on the refractive index of the optical fibre, and thus on the spectrum of the FBG, calibration was needed.

In this work, the strain optic coefficients were experimentally determined. The design of the transverse calibration set-up was based on the difficulties and shortcomings of other set-ups found in literature. It was proven that this transverse strain calibration works fine for isotropic fibres with Bragg grating (the so-called uni-axial FBGs). The experimentally determined strain optic coefficients of the calibrated FBGs showed good similarities with literature. However, this method was not accurately enough for high birefringent fibres with Bragg grating, due to the unknown mechanical and optical properties of the SAPs. Several disadvantages and difficulties (rotation of the optical eigenaxes, load transfer,…) were discussed, together with a viable solution.

7. 1. 2. Multi-axial strain sensor

As discussed in chapter 2, a HiBi-fibre with Bragg grating enables the measurement of two Bragg-wavelengths and hence yields the potential of determining two strain components. However, to determine the three normal strain components in the direction of the main axes of the fibre, at least 2 sensors of this type are required. Two FBG sensors yield 4 measurable wavelengths, which theoretically allows the determination of the three strain components and a fourth parameter (e.g. the temperature).

Internationally, a lot of research has been performed on trying to design such a sensor. However, no optimal solution was found in this matter and in most cases the **resolving power** of the **embedded sensor** was not even considered. In this work, the author has proposed and studied several sensor configurations consisting of two FBGs in a bow-tie fibre. Several configurations did not achieve the desired strain resolution or were not suitable for embedding purposes. In the final configuration (MAxS-sensor), the second grating has been isolated from transverse stress by placing it inside a capillary. The first grating remains sensitive to longitudinal stress as well as transverse stress. The theoretical strain resolution of this configuration was good and the composite distortion was kept as low as possible. This theoretical strain resolution was based on assumptions which were proven during an experimental and numerical (FEM) feasibility study. If the temperature sensitivity of both gratings is sufficiently different, it would be possible to use a MAxS-sensor without the need for external temperature compensation.

7. 1. 3. Embedded fibre Bragg grating sensors

Embedding a fibre Bragg grating sensor in carbon fibre thermosetting composites seems quite straightforward. However, it involves some vital issues (embedding procedure, composite distortion, composite strain disturbance) which need to be considered. A lot of attention was paid to the development of a robust **embedding procedure**. In- and egress points of the optical fibre were reinforced with Kapton foil or Teflon tubing. This makes the fibres robust and lets them survive the harsh manufacturing and lab environment. It should be mentioned that these solutions are not very well suited for industrial application. The coating and size of an embedded optical fibre, together with the relative orientation of the sensor with respect to the reinforcement fibres, have an impact on the distortion of the surrounding composite material. It was shown that when a sensor is embedded parallel to the reinforcement fibres, no visible distortion of the composite could be observed and even the composite strength properties remained unaltered.

Theoretically it is straightforward to design a multi-axial optical fibre strain sensor and determine the strain resolution of a non-embedded sensor. However, when embedded, **the interaction of the sensor** and its host material needs to be taken into

account. Because of the different mechanical properties of both materials (optical fibre and host material), the resolving power of the sensor will be significantly lower than its theoretical resolution. In this work it was proven both theoretically and experimentally that the strain measured with an embedded sensor is not necessarily the one present in the structure. This observation is pronounced when the material properties of the optical fibre and the host structure are significantly different. The specific strain transfer for an optical fibre embedded in a transversally loaded laminate was determined by using FE-simulations for several lay-ups and varying mechanical properties of the composite. This strain transfer method was validated by a transverse load experiment on a composite with a 'well-known' (in terms of mechanical properties) embedded uni-axial FBG sensor. However, for the multi-axial FBGs, a difference was found between the theoretical and experimental strain transfer coefficient matrices because of the unknown properties of the stress applying parts of the HiBi-fibre. An experimental calibration led to an optimized strain transfer coefficient matrix.

7. 1. 4. Feasibility of the embedded MAxS-sensor

The feasibility of the MAxS-sensor has been studied by means of an extensive experimental program. MAxS-sensors have been embedded in carbon reinforced epoxy samples during manual lamination. The carbon/epoxy samples were cured using an optimized autoclave curing cycle.

The samples have been subjected to five different experiments: a transverse tension-compression test, a tensile test, a four point bending test, a shear tensile test, and a thermal cycle test. Each test was designed to create a homogeneous strain field at the sensor location.

The **combined transverse tension-compression experiment** proved that the response of an embedded FBG is opposite but equal in magnitude for tensile and compressive loading. The **transverse compression experiments** proved the feasibility of the MAxS-sensor to measure the through-the-thickness transverse strain components. The **tensile test** proved that the sensor is able to measure the longitudinal strain along with the transverse strain components, which are very small (tens of microstrain was shown to be the limit). **The four point bending experiments** highlighted several disadvantages and imperfections of the MAxS-sensor. One example is the large influence of the axially measured strain in calculation of the transverse strain components. However, for most of the samples, the measured strains were in good correspondence with the reference strains when the sensor was loaded in tension. Pretensioning of the fibre in the capillary is needed when the sensor is to be used in compression. **The shear tensile tests** have proven that the gratings are almost insensitive to shear strain.

7. 2. STRUCTURAL HEALTH MONITORING USING THE MAXS-SENSOR

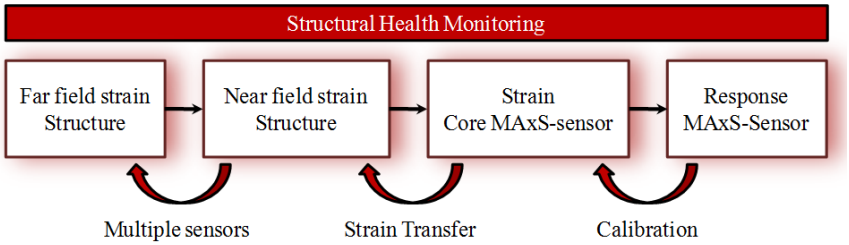

Figure 7-1: Flow chart of the different steps necessary for structural health monitoring using an embedded optical fibre sensor.

An overview of the different steps necessary to monitor the health of a structure is given in Figure 7-1. Supposing that several sensors are embedded at key locations in the structure, the depicted flow chart can be described as follows: (from left to right). When a structure is loaded, a certain strain field is created within. This (possibly disturbed) strain field exists near the embedded MAxS-sensor. Since the fibre is embedded, it will sense a strain in its core at the position of the grating which eventually leads to the shift of the four wavelengths of the MAxS-sensor.
Starting from the measured wavelength shifts, the structural strain can be determined by applying the following steps (from right to left in Figure 7-1). The spectral response of the MAxS-sensor can be related to the strain at the core of the optical fibre by conducting a qualitative calibration for all strain components. This leads to the definition of the strain gauge matrix (*K*-matrix). Next, the strain at the core of the optical fibre can be related with the one in the structure close to the sensor, by defining a strain transfer matrix (*TC*-matrix). If the mechanical material properties of the structure and the sensor are known within reasonable precision, FE-simulations are the solution in determining this matrix. However, an optimized matrix can be defined by testing the embedded MAxS-sensor for small specimens under controlled loading conditions. Finally, if several of these MAxS-sensors are embedded, the total strain field in a structural element can be remodelled. FE-simulations can again play a key role in this last step.

7. 3. EXPLORATORY RESEARCH IN MULTI-AXIAL STRAIN MONITORING

7. 3. 1. Curing

It is generally known that during the fabrication process of composite laminates and structural elements, residual stresses and strains develop because of a mismatch in the coefficient of thermal expansion of the reinforcing fibres and of the epoxy matrix.

In this work, the MAxS-sensor was embedded in a composite laminate $[\pm 45_2, 0_2, 90_2]_s$ and the author was able to visualize the separate effects of axial strain and transverse strain components during the autoclave curing process. Monitoring during curing demonstrated a clear residual strain build up during the cooling phase of the curing cycle. In the future, it will be a challenge to quantitatively determine temperature and strain during the curing process.

7. 3. 2. T-joint demonstrator

A representative scale model of a T-joint structure was manufactured with embedded sensors in several plies of the structure. FE-simulations revealed possible interesting positions of the sensor when the structure is loaded in four point bending or with pull-off loads. Due to practical problems during curing, an inhomogeneous composite structure was obtained. This made it difficult to relate the measured strains (MAxS-sensor) with those actually present in the T-joint structure. In the future, similar T-joint structures could be made with embedded sensors to investigate the monitoring capabilities of the MAxS-sensor. A four point bending test will be used to completely define the interaction between sensor and host material. Surface mounted FBGs will be taken as reference measurements. Since a specific weakness of T-joints are pull-off loads, this experiment will be executed with special attention to monitoring damage initiation. The author believes that, transverse strain components play a significant role in this damage initiation, the sensor can become very valuable. A MAxS-sensor is most probably the only sensor able to directly measure the transverse strain components.

7. 3. 3. Micro-structured fibre Bragg gratings

In this work, the author compared **the response of FBGs** written in **conventional birefringent** optical fibre and in highly birefringent **micro-structured** optical fibre. Firstly, the embedding procedure was evaluated and it was shown that it is possible to embed the different fibre technologies into fibre reinforced plastic without significantly distorting the material. Then, the sensitivity to mechanical strain of both types of FBG was compared. The micro-structured fibre reported here was not

optimized yet to feature high sensitivities to axial or transverse strain, but nevertheless it has already similar sensitivities as conventional birefringent fibres (bow-tie). The response to temperature changes shows important differences which could lead to the development of a MSF FBG sensor which is insensitive to temperature.
It was evidenced that micro-structured fibres can be applied for monitoring the structural integrity of composite structures. The design flexibility of micro-structured fibres allows the development of sensors which are sensitive to single or multiple strain components while being almost insensitive to temperature. This gives the opportunity to conduct effective in-situ full strain field mapping inside composite material structures.

7. 3. 4. Dynamic testing

A dynamic interrogator system has been designed during the MASSFOS-project. The interrogator consists of two spectrometers with a 512-pixel array, one for each polarization mode. The system has a wavelength range of 70 nm (from 1515 to 1585 nm) and the wavelength resolution is ~5 pm. Several preliminary experiments have been executed. At first, the recording of the Bragg spectrum of a HiBi FBG, by using respectively the '512 pixel array' system and the commercial interrogation system (FBG scan 607), revealed a difference in Bragg peak separation of ~40 to 50 pm. This was caused by the limited number of measurement points (512-pixel array) to capture the back-reflected spectrum of an FBG. A 1024-pixel array, which is presently being built, should improve this.

A $[0_2,90_2]_{6s}$ and $[\pm45_2,0_2,90_2]_s$ sample with embedded MAxS-sensor were clamped at one side in a shaker set-up and loaded according to a swept sine from 5Hz up to 2000Hz, (at 1g). Fast Fourier Transformation (FFT) performed on data obtained from the MAXs sensors and from the reference accelerometer matched very well. Even small wavelength shifts could be measured.
Using the same shaker set-up, a shock load has been applied on the composite samples. The structural response of a $[\pm45_2,0_2,90_2]_s$ sample during a 15g shock loading has been examined with the MASSFOS unit. The response is clear and the same signal as measured with the accelerometer could be reproduced. In the future, the MAxS-sensor will make it possible to measure the (rather small) dynamic strains induced during such a test. During this shock response, an axial strain of ~110 με was measured.

7. 4. FUTURE RESEARCH OPPORTUNITY

All the issues mentioned above – together with the author's confidence that MSF offers great, but unexplored potential for the targeted application – have led to the definition of a **research proposal**. This proposal contains the following challenges.

The first challenge is the **modelling of the thermal and mechanical response** of a micro-structured optical fibre. The MSF should be designed as such, that it matches the requirements of the multi-axial sensing concept. This concept relies on highly birefringent MSF in which FBGs need to be inscribed. The MSF should be made in such a way that its core is photosensitive and allows the inscription of Bragg gratings with conventional UV laser set-ups. The micro-structure should not compromise the writing of the grating. In addition, the birefringence in this MSF should exhibit almost zero temperature sensitivity in the wavelength region of interest, to avoid the effect of temperature changes interfering with mechanical strain measurements. In addition, the whole geometry should enhance the transverse strain transfer to the core of the optical fibre.

A second challenge is using this MSF-model as input for **determining the strain transfer** of the host material onto the MSF sensor. A structural model should be built using finite elements. Carbon or glass fibre reinforced plastics can be taken as host material system with a silica glass MSF integrated in between two layers of the laminate. This multi-physical model will take into account the general geometry and material properties of the host material and of the MSF sensor. If necessary, the anisotropic nature of the MSF will be included by a predefined strain field imposed on the model. Based on the simulated strain and temperature distributions, the response of the MSF based sensor can be developed in analytical form. An adequate amount of test specimens should be used to validate the macro-mechanical as well as the micro-mechanical/photonic model.

The concept of the newly fabricated sensors should be **validated** in two phases. In a **first phase,** the sensors will be embedded in small composite samples with particular attention paid to the fragile ingress and egress parts of the fibre leads and to the perturbation of the composite material. The response of the MSF sensor will be characterized for thermally induced stress (due to differences in thermal expansion coefficients) and for internal strain within the composite material induced by pre-defined loading on the composite sample. MSF sensor measurements should be compared with conventional techniques such as strain gauges, extensometers, surface mounted uni-axial FBGs, or embedded FBGs written in standard birefringent fibre (bow-tie type).

In a **second phase,** small scale structural elements should be manufactured (e.g. guiding mechanisms of wing flaps). Realistic loading conditions, which should reproduce real aerodynamic loads, will be applied to these elements. An FE-model

of the structure, together with the measurements of the MSF sensor, will lead to mapping of the total strain field in the structure.